National Library
of Canada

Acquisitions and
Bibliographic Services Branch

395 Wellington Street
Ottawa, Ontario
K1A 0N4

Bibliothèque nationale
du Canada

Direction des acquisitions et
des services bibliographiques

395, rue Wellington
Ottawa (Ontario)
K1A 0N4

Your file Votre référence

Our file Notre référence

NOTICE

The quality of this microform is heavily dependent upon the quality of the original thesis submitted for microfilming. Every effort has been made to ensure the highest quality of reproduction possible.

If pages are missing, contact the university which granted the degree.

Some pages may have indistinct print especially if the original pages were typed with a poor typewriter ribbon or if the university sent us an inferior photocopy.

Reproduction in full or in part of this microform is governed by the Canadian Copyright Act, R.S.C. 1970, c. C-30, and subsequent amendments.

AVIS

La qualité de cette microforme dépend grandement de la qualité de la thèse soumise au microfilmage. Nous avons tout fait pour assurer une qualité supérieure de reproduction.

S'il manque des pages, veuillez communiquer avec l'université qui a conféré le grade.

La qualité d'impression de certaines pages peut laisser à désirer, surtout si les pages originales ont été dactylographiées à l'aide d'un ruban usé ou si l'université nous a fait parvenir une photocopie de qualité inférieure.

La reproduction, même partielle, de cette microforme est soumise à la Loi canadienne sur le droit d'auteur, SRC 1970, c. C-30, et ses amendements subséquents.

Canada

THE UNIVERSITY OF ALBERTA

EXPERIMENTAL STUDY OF TRANSVERSELY LOADED CONTINUOUS STEEL PLATES

by

KURT PAUL RATZLAFF ©

A THESIS
SUBMITTED TO THE FACULTY OF GRADUATE STUDIES AND RESEARCH IN
PARTIAL FULFILMENT OF THE REQUIREMENTS FOR THE DEGREE OF
DOCTOR OF PHILOSOPHY
IN STRUCTURAL ENGINEERING

DEPARTMENT OF CIVIL ENGINEERING

EDMONTON, ALBERTA
SPRING 1995

National Library of Canada

Acquisitions and Bibliographic Services Branch

395 Wellington Street
Ottawa, Ontario
K1A 0N4

Bibliothèque nationale du Canada

Direction des acquisitions et des services bibliographiques

395, rue Wellington
Ottawa (Ontario)
K1A 0N4

Your file Votre référence

Our file Notre référence

THE AUTHOR HAS GRANTED AN IRREVOCABLE NON-EXCLUSIVE LICENCE ALLOWING THE NATIONAL LIBRARY OF CANADA TO REPRODUCE, LOAN, DISTRIBUTE OR SELL COPIES OF HIS/HER THESIS BY ANY MEANS AND IN ANY FORM OR FORMAT, MAKING THIS THESIS AVAILABLE TO INTERESTED PERSONS.

L'AUTEUR A ACCORDE UNE LICENCE IRREVOCABLE ET NON EXCLUSIVE PERMETTANT A LA BIBLIOTHEQUE NATIONALE DU CANADA DE REPRODUIRE, PRETER, DISTRIBUER OU VENDRE DES COPIES DE SA THESE DE QUELQUE MANIERE ET SOUS QUELQUE FORME QUE CE SOIT POUR METTRE DES EXEMPLAIRES DE CETTE THESE A LA DISPOSITION DES PERSONNE INTERESSEES.

THE AUTHOR RETAINS OWNERSHIP OF THE COPYRIGHT IN HIS/HER THESIS. NEITHER THE THESIS NOR SUBSTANTIAL EXTRACTS FROM IT MAY BE PRINTED OR OTHERWISE REPRODUCED WITHOUT HIS/HER PERMISSION.

L'AUTEUR CONSERVE LA PROPRIETE DU DROIT D'AUTEUR QUI PROTEGE SA THESE. NI LA THESE NI DES EXTRAITS SUBSTANTIELS DE CELLE-CI NE DOIVENT ETRE IMPRIMES OU AUTREMENT REPRODUITS SANS SON AUTORISATION.

ISBN 0-612-01750-8

Canada

THE UNIVERSITY OF ALBERTA

RELEASE FORM

NAME OF AUTHOR: KURT PAUL RATZLAFF

TITLE OF THESIS: EXPERIMENTAL STUDY OF TRANSVERSELY LOADED CONTINUOUS STEEL PLATES

DEGREE: DOCTOR OF PHILOSOPHY

YEAR THIS DEGREE GRANTED: SPRING 1995

Permission is hereby granted to the UNIVERITY OF ALBERTA LIBRARY to reproduce single copies of this thesis and to lend or sell such copies for private, scholarly or scientific research purposes only.

The author reserves other publication rights, and neither the thesis nor extensive extracts from it may be printed or otherwise reproduced without the author's written permission.

(Student's Signature)

5504 Centre Street North
(Permanent Address)

Calgary, Alberta

Canada

T2K 0T3

Date: April 21, 1995

THE UNIVERSITY OF ALBERTA

FACULTY OF GRADUATE STUDIES AND RESEARCH

The undersigned certify that they have read, and recommend to the Faculty of Graduate Studies and Research for acceptance, a thesis entitled EXPERIMENTAL STUDY OF TRANSVERSELY LOADED CONTINUOUS STEEL PLATES submitted by KURT PAUL RATZLAFF in partial fulfilment of the requirements for the degree of DOCTOR OF PHILOSOPHY in Structural Engineering.

D. J. Laurie Kennedy (Supervisor)

J. J. R. Cheng (Co-supervisor)

D W Murray
D. W. Murray

T. Hrudey
T. M. Hrudey

B. M. Patchett

Mu Hosain
M.U. Hosain (External Examiner)

W. Sproule (Committee Chairman)

Date: April 21, 1995

This thesis is dedicated to my mother and father,

Mary and David Ratzlaff

ABSTRACT

Structures such as bottom-founded petroleum exploration and production platforms and ice-breaking vessels are required to resist extreme loads. The loads, primarily due to ice, must be resisted by the hull or exterior wall that is generally made up of a rectangular grid of frames and stiffeners covered by steel plate. The results of the experimental work reported here, supported by the predictions of various analyses, show that thin steel plates with span to thickness ratios of between 65 and 155 are indeed suitable to resist extreme transverse loads without the need for stiffening elements when the resistance provided by membrane behaviour is utilized.

Four tests were carried out on plates with nominal thicknesses between 6 mm and 16 mm and having an aspect ratio, width/length, of 0.34. The plates were loaded transversely by fluid pressure until failure occurred. Deflections and strains at numerous locations were recorded throughout the loading history. The plates all failed at the edge near mid-length where the greatest bending occurred. Although they were considered to have failed prematurely within the heat affected zone of the weld at the plate edges, the plates were loaded for the most part into the inelastic flexural membrane range of behaviour. The failure loads were many times that corresponding to yield-

line collapse mechanisms. Three failure mechanisms have been identified.

ACKNOWLEDGEMENTS

Completion of this work can be attributed in large part to a number of individuals and institutions that require mention.

A guiding and patient supervisory role through the many years by my supervisor, D.J. Laurie Kennedy, is gratefully acknowledged. His many efforts alongside me, exemplifying the philosophy of results through team-work, has again, with this work, brought about a successful and recognizable effort for which I am eternally grateful. The initial supervisory committee of J.J.R. Cheng, D.W. Murray, and A. Scanlon who all gave of their time and knowledge during this work are personally and gratefully acknowledged.

The experimental work was carried-out in the I.F. Morrison Structural Engineering Laboratory at the University of Alberta. Its use and the assistance of laboratory technicians Larry Burden and Richard Helfrich are gratefully acknowledged. Office space, computers, and other essentials for carrying out and documenting this work were provided by the Dept. of Civil Engineering, University of Alberta. Clark Bicknel and B. Patchett of the Dept. of Mining & Metallurgical Engineering gave valuable assistance with the welding and metallurgical aspects of the work.

Major funding for this work was provided by the Natural Sciences and Engineering Research Council of Canada (NSERC) and the Dept. of Civil Engineering, University of Alberta, through Kennedy. Personal funding was provided also by Kennedy through NSERC and through Graduate Student Teaching Assistantships within the Department of Civil Engineering.

A special acknowledgement to Mary Ann M^{c}Clees, a dear friend, who provided the computer and software to prepare the final work. David Playdon, a schoolmate for many years, provided assistance with the finite element analyses and in producing the many figures throughout the text. Time off from my present regular duties was provided by Omega Joists Inc., Nisku, Alberta. A great deal of thanks is extended to you all!

Table Of Contents

Chapter **Page**

ABSTRACT v

ACKNOWLEDGEMENTS vii

Table of Contents ix

List of Tables xii

List of Figures xiv

List of Symbols xxii

1. INTRODUCTION 1
   1.1 General 1
   1.2 Objectives 2
   1.3 Scope 2

2. LITERATURE REVIEW 5
   2.1 General 5
   2.2 Elastic and Elasto-Plastic Behaviour 8
      2.2.1 Theoretical Behaviour 8
      2.2.2 Experimental Behaviour 11
   2.3 Behaviour Considering Strain Hardening 12
   2.4 Other Work 13

3. EXPERIMENTAL PROGRAM 21
   3.1 General 21
   3.2 Plate Tests 23
      3.2.1 General 23
      3.2.2 Test Specimens 23
      3.2.3 Reaction Plate 24
      3.2.4 Welding Materials And Procedures 26
      3.2.5 Test Set-Up 27
      3.2.6 Instrumentation And Measurement 28
         3.2.6.1 Strain Measurements 28
         3.2.6.2 Load Measurements 29
         3.2.6.3 LVDT Measurements 29
         3.2.6.4 Surface Level Indicator (SLI) Measurements 30

Chapter Page

3.2.7 Test Procedure 30

3.3 Calibrations 31

3.3.1 LVDT's And Potentiometers 31

3.3.2 Pressure Transducer 32

4. MATERIAL PROPERTIES AND BEHAVIOUR 61

4.1 Tension Tests 61

4.2 Weld Tests 63

4.3 Bending Tests 64

5. TEST RESULTS AND OVERALL BEHAVIOUR 86

5.1 General 86

5.2 Deflections 88

5.2.1 Deflections Across The Width At Mid-Length 88

5.2.2 Continuous Deflection Measurements 90

5.3 Strain Measurements 90

5.3.1 Strains Across The Width At Mid-Length .. 90

5.4 Behaviour Near The Corners 94

5.5 Reaction Plate Behaviour 95

6. FINITE ELEMENT ANALYSES 138

6.1 Program 138

6.2 Models 139

6.2.1 Discretizations 140

6.2.2 Material Properties 140

6.2.3 Loading 143

6.3 Results 143

7. ANALYSES OF TEST RESULTS 158

7.1 Overall Behaviour 158

7.2 Deflections 162

7.2.1 Deflections Across The Width At Mid-Length 162

7.2.2 Deflections Across The Width At Other Locations 163

Chapter **Page**

7.2.3 Deflections At Mid-Length As A Function Of Load 165
7.3 Strain Variation With Load 166
7.3.1 Test P6-2 166
7.3.1.1 Summary 171
7.3.2 Test P12 174
7.3.3 Test P6-1 178
7.3.4 Test P16 179
7.4 Strains Across The Width At Mid-Length 180
7.5 Membrane Behaviour 183
7.6 Longitudinal Strains 186
7.7 Behaviour At Edges 187
7.8 Failure Loads And Deflected Shapes 188
7.9 Failure Mechanisms 192

8. SUMMARY, OBSERVATIONS, CONCLUSIONS AND APPLICATIONS 259
8.1 Summary 259
8.2 Observations 260
8.3 Conclusions 262
8.4 Applications 263

REFERENCES 269

APPENDIX A 273

List of Tables

Table Page

3.1 Test plate designation 34

3.2 Chemical composition and mechanical properties from mill reports 35

3.3 Strain gauge reference code 36

3.4 Strain gauges on test plate P6-1 37

3.5 Strain gauges on test plate P6-2 38

3.6 Strain gauges on test plate P12 39

3.7 Strain gauges on test plate P16 40

3.8 LVDT characteristics 41

4.1 Tensile coupon identification 68

4.2 Tensile coupon test results for specimen P6-1 steel plate 69

4.3 Tensile coupon test results for specimen P6-2 steel plate 70

4.4 Tensile coupon test results for specimen P12 steel plate 71

4.5 Tensile coupon test results for specimen P16 steel plate 72

4.6 Ceramic weld backing configurations 73

4.7 Weld backing tests 73

5.1 Maximum pressures, deflections and measured fracture lengths 96

6.1 Features of the ADINA program 146

6.2 ADINA program material models 147

7.1 ADINA strain differences, model 1, $q/q_C = 17.7$ 197

7.2 ADINA strain differences, model 2, $q/q_C = 6.6$ 198

7.3 Failure loads based on Ratzlaff-Kennedy model and test (measured) geometry 199

7.4 Failure loads based on Ratzlaff-Kennedy model and ADINA geometry 200

Table Page

7.5 Comparison of maximum strains based on Ratzlaff-Kennedy model using test load and geometry, with ADINA strains 201

7.6 Failure loads based on Ratzlaff-Kennedy model and ADINA strains in HAZ at test failure load 202

7.7 Actual and predicted failure loads 203

7.8 Failure loads based on Ratzlaff-Kennedy model and linear strains in HAZ 203

List of Figures

Figure Page

1.1 Plate having aspect ratio of one-third and thickness, h 4

2.1 Bilinear stress-strain relationships 15

2.2 Elasto-plastic moment-curvature relationship 16

2.3 Behavioural domain without strain hardening 17

2.4 Test results of Young (1959) and behavioural domain ..18

2.5 Load-deflection behaviour of inelastic membrane (Ratzlaff and Kennedy, 1986) 19

2.6 Test and predicted load-deflection curves (Ratzlaff and Kennedy, 1986) 20

3.1 Partial cross-section through test and reaction plates at edge 42

3.2 Machined steel piping plug 43

3.3 Reaction plate edge preparations 44

3.4 Edge preparations, backing bars and welding sequences 45

3.5 Edge preparations, backing bars and welding sequences 46

3.6 Clamping frames on specimen P6-1 and reaction plate assembly 47

3.7 Clamped assembly elevated at one end, before welding 48

3.8 End view of test set-up 49

3.9 Partial cross-section at edge of test apparatus 50

3.10 Grid lines for strain gauge locations on test specimen P6-1 51

3.11 Grid lines for strain gauge locations on test specimen P6-2 52

3.12 Grid lines for strain gauge locations on test specimen P12 53

Figure **Page**

3.13 Grid lines for strain gauge locations on test specimen P16 54

3.14 Stain gauges blanketed with silicon on specimen P6-1 55

3.15 LVDT's in support frame above test plate 56

3.16 LVDT locations in support frame above test plate 57

3.17 Surface Level Indicator (SLI) above test plate 58

3.18 Schematic diagram of Surface Level Indicator (SLI) .. 59

3.19 Path of surface level indicator (SLI) 60

4.1 Location and identification of tensile coupons 74

4.2 Tension coupon in Baldwin testing machine 75

4.3 Stress-strain curves for tension coupons 6P10-1 and 6P10-2 76

4.4 Stress-strain curves for tension coupons 12P7 and 16P7 76

4.5 Strain ratio versus axial strain for several 6 mm tension coupons 77

4.6 Strain ratio versus axial strain for several 12 mm tension coupons 77

4.7 Strain ratio versus axial strain for several 16 mm tension coupons 78

4.8 Weld test set-up, fabrication and evaluation 79

4.9 Test frame for bending specimens 1 and 2 80

4.10 Beam test specimens and instrumentation 81

4.11 Sections along x-axis through test frames with loading method 82

4.12 Test frame for bending specimen 3 83

4.13 Load-displacement diagrams for bending tests 1, 2, and 3 84

4.14 Longitudinal section of bending specimen 1 after failure 85

Figure **Page**

4.15 Longitudinal section of bending specimen 2 after failure 85

4.16 Longitudinal section of bending specimen 3 after failure 85

5.1 Load-deflection curves 97

5.2 Nondimensional load-deflection curves 98

5.3 Specimen P6-1 during testing 99

5.4 Rupture at edge prior to failure of plate specimens . 100

5.5 Fracture region of specimen P6-1 101

5.6 Fracture region of specimen P6-2 102

5.7 Fracture region of specimen P12 103

5.8 Fracture region of specimen P16 104

5.9 Rupture development at plate edge 105

5.10 Rupture development at plate edge 106

5.11 Deflections at mid-length, test P6-1 107

5.12 Deflections at mid-length, test P6-2 108

5.13 Deflections at mid-length, test P12 109

5.14 Deflections at mid-length, test P16 110

5.15 SLI deflections for plate P6-2 at q/qc = 6.0 111

5.16 SLI deflections for plate P6-2 after failure 112

5.17 SLI deflections for plate P16 at q/qc = 2.7 113

5.18 SLI deflections for plate P16 after failure 114

5.19 SLI deflections for specimens P6-2 and P16 after failure 115

5.20 Strains across the width at mid-length, q/qc = 1.0, specimen P6-1 116

5.21 Strains across the width at mid-length, q/qc = 1.0, specimen P6-2 117

Figure **Page**

5.22 Strains across the width at mid-length, q/qc = 1.1, specimen P12 118

5.23 Strains across the width at mid-length, q/qc = 1.0, specimen P16 119

5.24 Strains across the width at mid-length, q/qc = 17.4, specimen P6-1 120

5.25 Strains across the width at mid-length, q/qc = 17.9, specimen P6-2 121

5.26 Strains across the width at mid-length, q/qc = 6.6, specimen P12 122

5.27 Strains across the width at mid-length, q/qc = 5.5, specimen P16 123

5.28 Strains across the width at mid-length, q/qc = 5.9, specimen P6-1 124

5.29 Strains across the width at mid-length, q/qc = 5.4, specimen P6-2 125

5.30 Strains across the width at mid-length, q/qc = 3.0, specimen P12 126

5.31 Strains across the width at mid-length, q/qc = 2.5, specimen P16 127

5.32 Strains across the width at mid-length, q/qc = 11.2, specimen P6-1 128

5.33 Strains across the width at mid-length, q/qc = 10.9, specimen P6-2 129

5.34 Strains across the width at mid-length, q/qc = 5.1, specimen P12 130

5.35 Strains across the width at mid-length, q/qc = 3.9, specimen P16 131

5.36 Longitudinal strains at mid-length, test P6-1 132

5.37 Longitudinal strains at mid-length, test P6-2 133

5.38 Longitudinal strains at mid-length, test P12 134

5.39 Longitudinal strains at mid-length, test P16 135

Figure **Page**

5.40 Deflections along diagonal and strains along diagonal, test P6-2 136

5.41 Reaction plate strains at mid-width and mid-length, test P16 137

6.1 Finite element model 1 148

6.2 Finite element model 2 149

6.3 True stress-strain curves for steel plates used in the analyses 150

6.4 True stress-strain curve for weld metal 151

6.5 Strains at plate edge, model 1, 6 mm plate 152

6.6 Strains at plate edge, model 2, 12 mm plate 153

6.7 Deformed mesh at plate edge, model 1, plate P6-2, $q/q_c = 51.6$ 154

6.8 Deformed mesh at plate edge, model 2, plate P12, $q/q_c = 40.0$ 155

6.9 Model 1 load-deflection results 156

6.10 Model 2 load-deflection results 157

7.1 Load-deflection relationships, specimen P6-1 204

7.2 Load-deflection relationships, specimen P6-2 205

7.3 Load-deflection relationships, specimen P12 206

7.4 Load-deflection relationships, specimen P16 207

7.5 Model 1 (test P6-2) midsurface nodal displacements, $q/q_c = 17.7$ 208

7.6 Model 2 (test P12) midsurface nodal displacements, $q/q_c = 6.6$ 209

7.7 Model 1 (test P6-2) mid-surface deflections at test failure load 210

7.8 Model 2 (test P12) mid-surface deflections at test failure load 211

Figure **Page**

7.9 Deflection at toe of weld by LVDT's and ADINA model 1, test P6-2 212

7.10 Deflection at 87 mm from toe of weld by LVDT's and ADINA model 1, test P6-2 213

7.11 Deflection at 174 mm from toe of weld by LVDT's and ADINA model 1, test P6-2 214

7.12 Deflection at 348 mm from toe of weld by LVDT's and ADINA model 1, test P6-2 215

7.13 Deflection at toe of weld by LVDT's and ADINA model 2, test P12 216

7.14 Deflection at 87 mm from toe of weld by LVDT's and ADINA model 2, test P12 217

7.15 Deflection at 174 mm from toe of weld by LVDT's and ADINA model 2, test P12 218

7.16 Deflection at 348 mm from toe of weld by LVDT's and ADINA model 2, test P12 219

7.17 Locations for strain comparisons at mid-length between ADINA and test P6-2 220

7.18 Locations for strain comparisons at mid-length between ADINA and test P12 220

7.19 Strains at location X given by ADINA and gauges on plate P6-2 221

7.20 Strains at location A given by ADINA and gauges on plate P6-2 222

7.21 Strains at location B given by ADINA and gauges on plate P6-2 223

7.22 Strains at location C given by ADINA and gauges on plate P6-2 224

7.23 Strains at location D given by ADINA and gauges on plate P6-2 225

7.24 Strains at location E given by ADINA and gauges on plate P6-2 226

7.25 Strains at location F given by ADINA and gauges on plate P6-2 227

Figure Page

7.26 Strains at location G given by ADINA and gauges on plate P6-2 228

7.27 Strains and free body diagrams from location A to location G, model 1, $q/q_c = 17.7$ 229

7.28 Strains at location X given by ADINA and gauges on plate P12 230

7.29 Strains at location A given by ADINA and gauges on plate P12 231

7.30 Strains at location B given by ADINA and gauges on plate P12 232

7.31 Strains at location C given by ADINA and gauges on plate P12 233

7.32 Strains at location D given by ADINA and gauges on plate P12 234

7.33 Strains at location E given by ADINA and gauges on plate P12 235

7.34 Strains at location F given by ADINA and gauges on plate P12 236

7.35 Strains at location G given by ADINA and gauges on plate P12 237

7.36 Locations of strain measurements, test P6-1 238

7.37 Locations of strain measurements, test P16 238

7.38 Strains at location X, test P6-1 239

7.39 Strains at location A, test P6-1 240

7.40 Strains at location B, test P6-1 241

7.41 Strains at location C, test P6-1 242

7.42 Strains at location D, test P6-1 243

7.43 Strains at location E, test P6-1 244

7.44 Strains at location F, test P6-1 245

Figure Page

7.45 Strains at location G, test P6-1 246

7.46 Strains at location X, test P16 247

7.47 Strains at location A, test P16 248

7.48 Strains at location B, test P16 249

7.49 Strains at location C, test P16 250

7.50 Strains at location D, test P16 251

7.51 Strains at location E, test P16 252

7.52 Strains at location F, test P16 253

7.53 Strains at location G, test P16 254

7.54 Deflected shapes, P6-1 255

7.55 Deflected shapes, P6-2 256

7.56 Deflected shapes, P12 257

7.57 Deflected shapes, P16 258

8.1 Partial section through ice-resisting wall 268

A.1 Free body diagrams 278

List of Symbols

A = initial cross-sectional area

A_f = final cross-sectional area

d = distance

e = eccentricity

D = flexural rigidity = $Eh^3/12(1-\nu^2)$

E = modulus of elasticity

h = plate thickness

L = length

L_o = initial or original length

L_f = final length

M = bending moment per unit length

M_o = bending moment per unit length at plate edge

M_p = fully plastic moment per unit length

M_u = fully plastic ultimate moment per unit length

M_y = yield moment per unit length

N = axial force per unit length

P = P_o = horizontal component of force S

P_u = $\sigma_u h$ = ultimate force per unit length

q = uniform load per unit area

q_c = critical value of uniform load per unit area = $16\ M_p/L^2$

Q = total load per unit area due to q

S = axial membrane force per unit length

U = nondimensional membrane stress parameter = $[SL^2/4D]^{1/2}$

V = vertical (shear) component of S

w = transverse deflection

$[W_m]_y$ = maximum transverse deflection at load corresponding to first yielding

W_m = maximum transverse delflection

x, y, z = cartesian coordinates

ε = engineering strain

ε_f = engineering strain at fracture

ε_p = engineering strain corresponding to P_o

ε_s = axial strain corresponding to S

ε_{st} = engineering strain at onset of strain hardening

ε_t = true strain

ε_u = engineering strain corresponding to σ_u

ε_y = uniaxial yield strain

θ = angle of inclination, degrees

ν = Poisson's ratio

ν_p = 0.5 = inelastic strain ratio with zero volume change

ν_s = inelastic strain ratio = absolute value of ratio of lateral strain to longitudinal strain

σ = engineering stress

σ_t = true stress

σ_u = engineering ultimate stress in uniaxial tension

σ_y = engineering yield stress in uniaxial tension

ρ = radius of curvature

ρ_c = critical radius of curvature corresponding to ε_u

ρ_{min} = minimum radius of curvature

φ = curvature $\approx d^2w/dx^2$

φ_y = curvature corresponding to My

1. INTRODUCTION

1.1 General

In the design of transversely loaded flat plates which are continuous over a rectangular grid of beams and stiffeners the structural usefulness of the system is often considered to be the flexural strength of the plate panels alone. This flexural strength may be even limited to that based on first yield, neglecting the strength developed when a mechanism forms, where for the latter the strength is taken as that given by classical yield-line theory. Such limits are irrelevant for any system in which the deflections are not critical and in which the increase in strength due to membrane action can be considered.

Some of the structures that have been designed or proposed for oil exploration and production in the Arctic Ocean consist of steel caissons clad with continuous thin steel plating. Interior plate panels are continuous over the support grillage on all four edges and can therefore by modelled as being rotationally and translationally fixed along the edges. Because the skin plates may be subjected to enormous local lateral forces from the floe ice, economic design requires that the full strength of the plating be utilized.

To benefit from the increased strength provided by the development of membrane behaviour, a complete understanding of the load-deflection behaviour to failure of the system is required. Of particular significance are: (i) the material characteristics of the steel plate, (ii) the geometry and strength characteristics of the supporting grillage, (iii) the method of construction of the system, (iv) the type and severity of loading, and (v) the determination of possible failure modes and loads. With this knowledge advantage can be taken of the increased load-carrying capacity provided by membrane action while still providing any desired level of safety. At present, no clear design procedures are available. Such procedures should be confirmed experimentally.

1.2. Objectives

The overall objective of this work was to provide experimental evidence on the behaviour of transversely loaded continuous steel plates to failure and to develop analytical models to predict this behaviour. Failure modes were to be investigated.

1.3 Scope

The literature has been reviewed and the assumptions and limitations of the analyses and the results of experimental work discussed. In particular the previous work of the author with Kennedy (Ratzlaff and Kennedy, 1985; 1986) is thoroughly reviewed. It describes the behaviour throughout loading and predicts some failure modes and loads.

Four large scale tests that included an extensive array of measurements were performed. The tests were done by subjecting commonly available mild structural steel plates with an aspect ratio (defined as the width divided by the length) of about one-third to fluid pressure. A plate having an aspect ratio of one-third and thickness, h, is shown in Fig. 1.1. Two finite element models that modelled the behaviour of two of the experimental plates are presented and the results compared with those of the tests.

In this work only long and initially flat plates with aspect ratios that can be considered to approach zero are considered. The effects of restraint at the edges and material strain hardening have been included and are shown to be of significance.

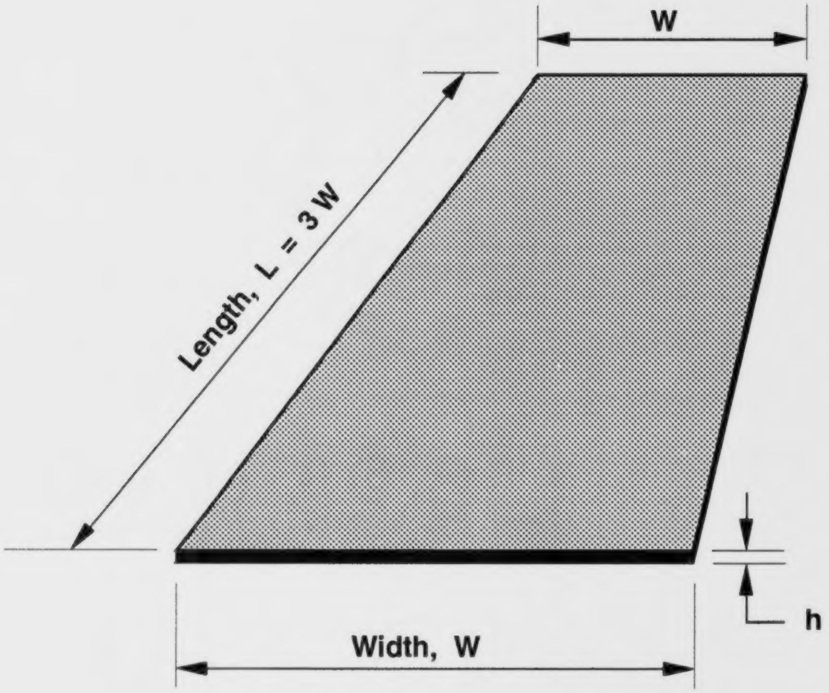
W
Length, L = 3 W
h
Width, W

Figure 1.1 Plate having aspect ratio of one-third and thickness, h

2. LITERATURE REVIEW

2.1 General

Analyses to predict the load-deflection behaviour of transversely loaded continuous plates have considered steel plates of varying aspect ratios. These analyses have commonly assumed the stress-strain characteristics of the plate material to be elasto-plastic, ignored strain hardening, and have neglected the contribution to load-carrying of the membrane forces that develop when the edges of the plate are restrained translationally.

Boobnoff (1902) determined the exact closed form solution to the differential equations describing the large elastic deflection behaviour of uniformly loaded clamped rectangular flat infinitely long plates. The aspect ratio, the ratio of the width to the length, is therefore zero. The differential equations for plates of any aspect ratio were first determined by von Karman in 1910.

It would be expected that the maximum deflection that occurs at mid-width and mid-length would not be significantly different for a plate with an aspect ratio of less than about 1/2 than that for a plate with an aspect ratio of zero (Clarkson, 1956; Hooke, 1970).

For an infinitely long flat plate the elastic load-deflection equation of von Karman, when shear deformations are neglected, becomes

$$[2.1] \qquad \frac{q}{D} = \frac{d^4w}{dx^4} - \frac{N_x}{D}\frac{d^2w}{dx^4}$$

If the term containing the membrane force N_x in [2.1] is neglected, the equation reduces to the elastic small deflection equation of Lagrange (1811). Some approximate solutions to the large deflection equations of von Karman for rectangular plates with different boundary or edge conditions were first presented by Way (1938). Levy (1942) used a Fourier series method to solve the same equations for a plate with an aspect ratio of 1. To the author's knowledge, no closed-form solution to the complete von Karman equations exists for a plate with an aspect ratio other than zero. A multitude of approximate solutions exist for the load-deflection behaviour of transversely loaded clamped plates of any aspect ratio when the plate material is assumed to exhibit elasto-plastic behaviour. These solutions are generally considered too rigourous mathematically for use in design. One of these analyses, for example, is the well known upper-bound yield line method of Ingerslev (1923) and Johansen (1943,1946).

For the elastic and elasto-plastic analyses that follow, it is assumed that the tensile and compressive characteristics of the plate are bilinear as shown in Fig. 2.1. This results in a moment-curvature relationship for a rectangular cross-section of unit width, although curved as shown dotted in Fig. 2.2, that may be idealized as being bilinear. Because a plate with an aspect ratio approaching zero is restrained under load from deforming in the direction of its length the state of stress is one of plane strain or constrained plane stress (Lay, 1982). With restraint the yield stress and corresponding yield strain are increased above the uniaxial values and depend on Poisson's ratio. If it is assumed that the maximum principal strain theory is valid and Poisson's ratio is taken as 0.30, the yield stress under plane strain conditions is $\sigma_Y/(1-\nu^2) = 1.099\ \sigma_Y$. The corresponding yield strain remains unchanged from that found in a uniaxial state of stress and is equal to ε_Y. The tensile and compressive stress-strain curves based on the transformed values of yield strain and yield stress are shown in Fig. 2.1 and exhibit larger stresses for a given strain than for the condition of uniaxial tension or compression. Although other yield theories are not considered in this study, the maximum principal strain theory gives a yield stress under plane strain conditions, and taking Poisson's ratio to be 0.30, that is about 2% above that given by the maximum energy of distortion theory formulated by von Mises.

Yielding occurs because of shear distortions. If it is assumed, upon yielding, that the inelastic strain ratio is 0.50, consistent with zero volume change, the stress-strain curve would rise to 1.333 σ_Y as shown in Fig. 2.1. Ratzlaff et al. (1988) show, however, that after yielding the inelastic strain ratio may reach values of 0.40 to 0.45, somewhat less than the zero volume change value of 0.50, and with subsequent straining there is a gradual reduction to a value of about 0.35.

2.2 Elastic and Elasto-plastic Behaviour

2.2.1 Theoretical Behaviour

Many analyses are based on the simplifying assumptions that the stress-strain relationship is bilinear, neglecting strain hardening, and also that the moment-curvature relationship is bilinear. As well, the effect of the variation in Poisson's ratio in the inelastic range is neglected.

Figure 2.3 developed by Ratzlaff and Kennedy (1985) presents nondimensionalized load-deflection responses based on different assumptions in behaviour of transversely loaded flat plates. To nondimensionalize the curves, the load intensity per unit width, q, has been divided by that corresponding to a plastic collapse mechanism, q_c, and the mid-width deflections, w_m, divided by the initial plate thickness, h. The curves are drawn for a steel plate of zero aspect ratio subject to a load of uniform intensity, q, with a span to depth ratio, L/h, equal to 100 (h = 10 mm). The steel is characterized by a yield strain of 1500 $\mu\varepsilon$ and a modulus of elasticity of 200000 MPa . With the exception discussed subsequently both the stress-strain and moment-curvature relationships are assumed bilinear. Poisson's ratio is assumed to be 0.30 and on yielding the inelastic strain ratio is taken as 0.50 as discussed previously.

Curve F in Fig. 2.3 gives the first two of the three segments of the load-deflection response when the plate is assumed to carry loads in flexure only. The formation of the last hinge at midspan leading to mechanism formation occurs at a deflection greater than the maximum shown. The load to cause the collapse mechanism to form, q_c, (used to nondimensionalize the load intensity) equals $16M_p/L^2$.

When the edges of a plate are restrained against translation as well as rotation the flexural behaviour as given by curve F must represent a lower-bound.

Another lower-bound solution, established by considering elastic membrane action only and neglecting bending, is given by curve M_e. The deflections result solely from the elastic straining of the plate. The curve terminates at point B when the maximum membrane stress at the edges reaches yield.

Curve M_i, extending beyond point B, gives the inelastic membrane response as yielding gradually progresses from the plate edges towards the mid-width when Poisson's ratio is assumed to be 0.30. The increased load-carrying capacity results from the increasing inclination of the membrane forces at the edges. Not entirely consistent with the assumption of a bilinear stress-strain curve, this analysis requires the membrane stress at the edge, for the plate characteristics given, to rise to about 1.05 σ_Y at a value of q/q_c equal to 12.4. Curve M_i projects backward to the origin.

Curve N in Fig. 2.3 represents the inelastic membrane response based on the same assumptions as those for curve M_i except that the inelastic membrane response is based on an inelastic strain ratio of 0.50. Beyond point B there is no flexural action and the response would be expected to gradually move from curve M_i towards curve N as yielding progresses from the edges towards the centre and the inelastic strain ratio applies to more and more of the membrane.

The closed-form solution by Timoshenko (1940) for elastic flexural membrane behaviour is shown as curve E in Fig. 2.3 and in reality should not be drawn beyond point A' representing the onset of yielding of the extreme fibres at the edges of the plate in combined tension and flexure. Point A represents the onset of yielding if the moment-rotation curve in the presence of axial load is assumed to be elasto-plastic . The extension of curve E beyond point A assumes that yielding has not occurred. Curve E, taking both membrane and flexural contributions into account is an upper-bound.

If it is assumed that a collapse mechanism forms with zero deflection and then that deflections occur due to inelastic membrane action, as suggested by Kennedy and Hafez (1984), curve Y joining M_i asymptotically, results.

Within the limits of the assumptions made the shaded areas in Fig. 2.3 represent a permissible domain of behaviour as the curves provide, in general, upper and lower-bound solutions. Curve R is a possible response drawn from the point representing full yielding at the edge, partially in tension and partially in compression, to point B representing full yielding in tension at the edges due to membrane action. Beyond point B there is no flexural action and the response would be expected to move gradually from curve M_i towards curve N as yielding progresses from the edges towards the centre and the inelastic strain ratio applies to more and more of the membrane. When straining beyond the strain hardening strain occurs, the response could rise above curve N.

2.2.2 Experimental Behaviour

Plotted in Fig. 2.4 are test results of Young (1959) for a plate with an aspect ratio of 1/3 and a width to thickness ratio of 57.1. These data are in good agreement with curves E and R for a plate having an aspect ratio of zero. Although falling slightly below point B, to the right of point B the experimental results gradually move from curve M_i to N and even exceed it. The data that fall below and to the right of point B can be attributed to the assumption that the moment-rotation curve is elasto-plastic and to the fact that to get full yielding of the plate in membrane action (curves M_i and N) a small portion of the plate near the edge must be strained into the strain hardening region. The consequent inelastic straining would therefore increase the deflections beyond those assumed.

2.3 Behaviour Considering Strain Hardening

In Fig. 2.5 inelastic membrane behaviour beyond point B, as described by Ratzlaff and Kennedy (1986), is depicted for a variety of assumptions. Curves M_i and N have been described in the previous section and are both drawn for a uniformly loaded membrane. Curve V is similar to curve N but is drawn for a plate subjected to fluid pressure.

Curve U in Fig. 2.5 predicts the load-deflection behaviour under uniform loading when the stress-strain curve beyond the onset of strain hardening is approximated by five linear segments as given by Ratzlaff and Kennedy (1986). At point B the plate is fully yielded in tension. With increased loading and as yielding progresses from the edges towards the mid-width, the inelastic strain ratio is computed based on the dilitation that occurs as suggested by Stang et al. (1946). The curve bends sharply upward at a value of W_m/h of about 8.2 when the membrane strains enter the strain hardening region and the corresponding stresses increase. Curve U continues until the ultimate tensile strain is achieved at some location in the plate.

The results of 2 tests reported by Ratzlaff and Kennedy (1986) are shown in Fig. 2.6 together with curves V and U as well as curve U' taking into account the contribution of observed shear deformations to the total deflection, and the results of a finite element analysis. Ratzlaff and Kennedy (1986) suggested two possible failure modes as indicated by the maximum strain limit and shear limit on curve U. The maximum tensile strain occurs at the edges of the plate on the loaded side but could not be reached if the shear limit governs. The proposed shear limit is reached when the average shear stress along the edges equals the ultimate shear stress, taken as $0.577\sigma_u$. Specimen 2 failed prematurely due to loss of restraint while an examination of the failure surface along one edge of specimen 1 revealed that it failed in shear (Vitovec, 1984, 1989). For test 1 the test-to-predicted load ratio was 0.97 and the test-to-predicted deflection ratio based on curve U' was 1.08.

The finite element analysis, which did not model the shear limit, follows curve U closely but does not exceed it at high loads. This difference is attributed to the use of a limited number of elements through the thickness at the edge, increasing the restrain there.

2.4 Other Work

In a series of tests, Taylor (1986) tested six plates under lateral fluid pressure. The load-deflection behaviour into the inelastic membrane range followed closely the predictions of Ratzlaff and Kennedy (1985) but unfortunately the plates were not loaded to failure.

Kennedy and Cheng (1992a,b) tested a series of steel-concrete sandwich panels, essentially completely restrained at the edges, with 5 transverse loads. The behaviour was dominated by membrane action with failure initiating in one or both of the steel plates at the support, in what was described as a shear-tension failure. Based on an extension of the von Mises-Huber-Hencky yield condition to ultimate and assuming an inelastic strain ratio in this condition of 0.50 the mean test-to-predicted ratio for 6 tests was 1.13 with a coefficient of variation of 0.037. As the authors state, however, the test points are clustered because only one load configuration was used. Moreover the failure criterion was based on only axial force and shear acting at the edge of the membrane, i.e., no bending moments were considered to exist there.

2.5 Summary

The literature review reveals that those tests that have been conducted were generally of relatively small scale when compared to actual structures in which membrane behaviour could be utilized effectively. Moreover, with the exception of tests by the author (Ratzlaff and Kennedy, 1986) laterally loaded steel plate tests have not been taken to failure, not have failure mechanisms been proposed. Therefore the need exists for tests on plates of substantial scale and with a range of width/thickness ratios. These would serve to confirm the failure mechanisms that have been proposed or suggest others and to establish preferred proportioning of membrane structures, i.e. the ratio of the distance between supporting frames and the plate thickness. Implied in this is whether intermediate stiffeners and orthogonal frames should be used at all.

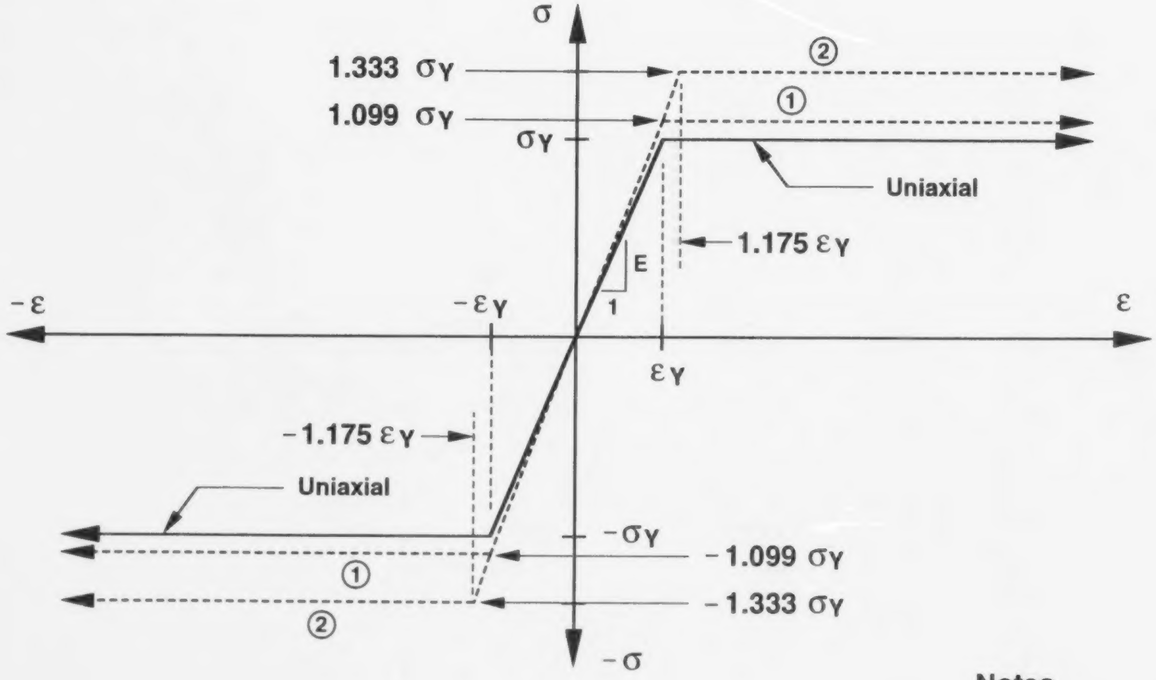

Notes

① Plane strain stress state, $\nu = 0.3$

② Plane strain stress state, $\nu_p = 0.5$

Figure 2.1 Bilinear stress-strain relationships

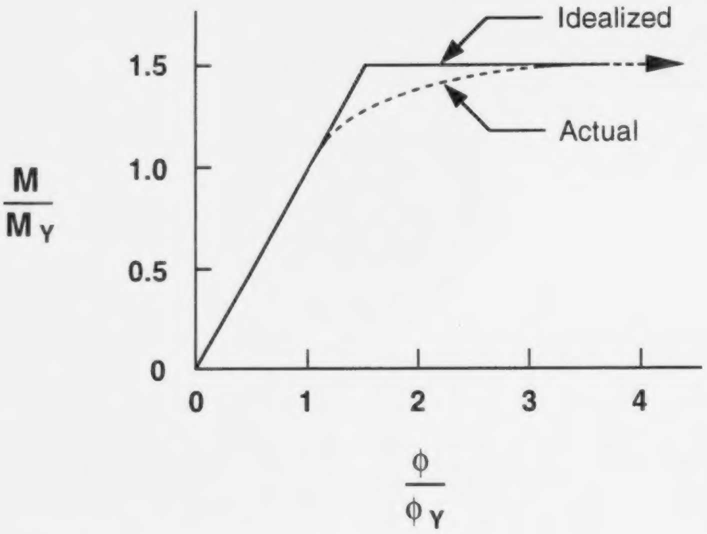

Figure 2.2 Elasto-plastic moment-curvature relationship

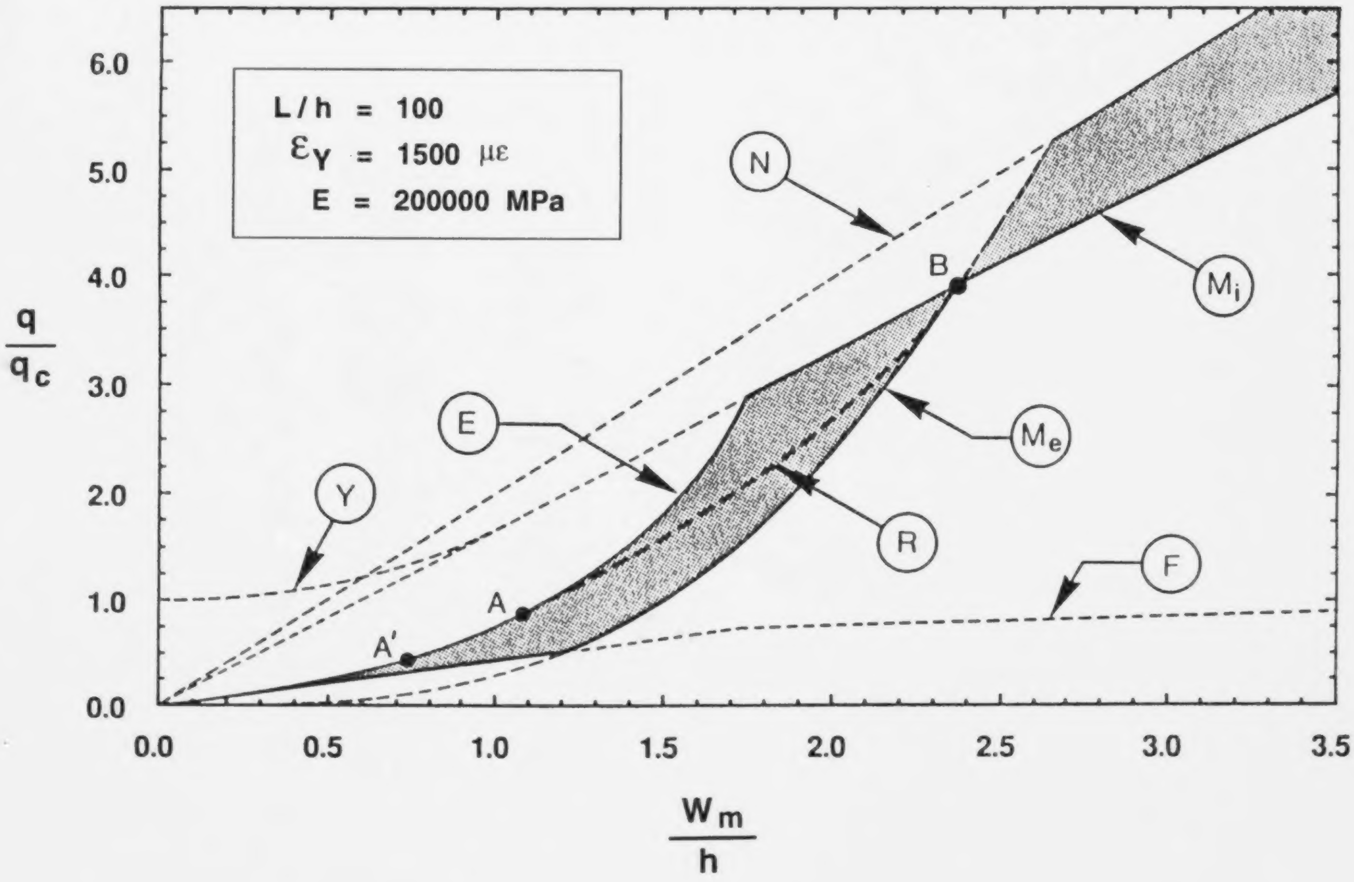

Figure 2.3 Behavioural domain without stain hardening

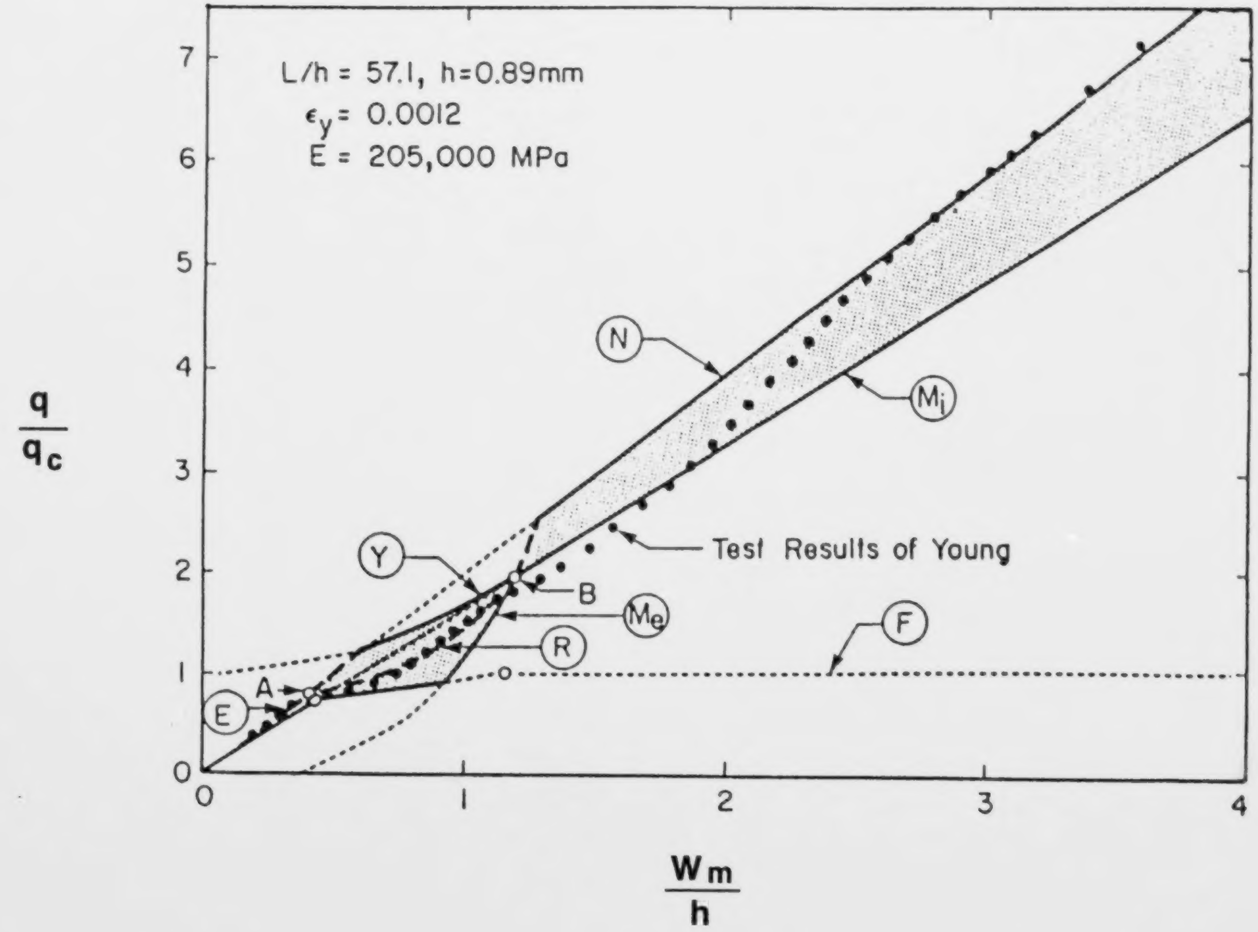

Figure 2.4 Test results of Young (1959) and behavioural domain

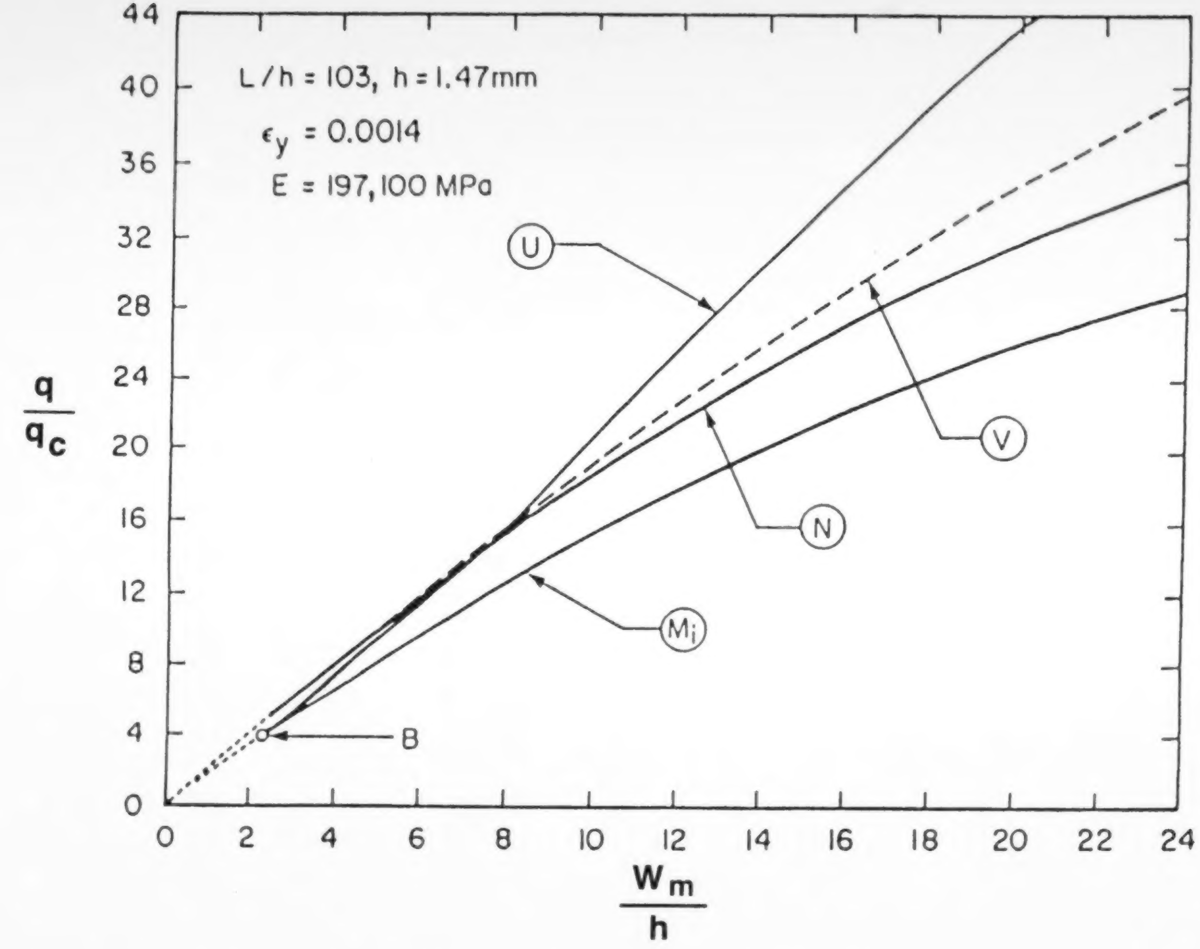

Figure 2.5 Load-deflection behaviour of inelastic membrane (Ratzlaff and Kennedy, 1986)

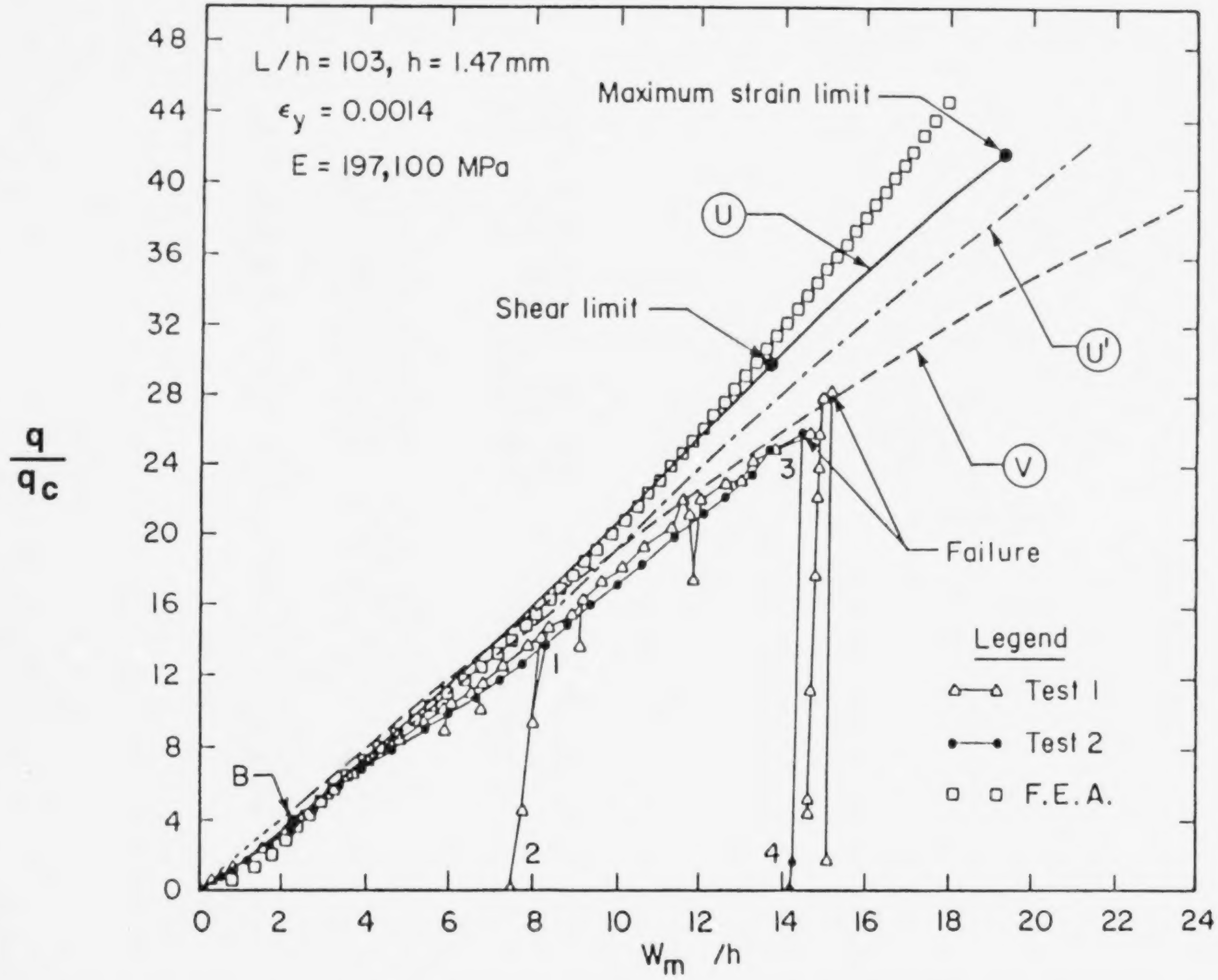

Figure 2.6 Test and predicted load-deflection curves (Ratzlaff and Kennedy, 1986)

3. EXPERIMENTAL PROGRAM

3.1 General

The primary objectives of the experimental program were:

1. to verify the predicted load-deflection behaviour of full-scale transversely loaded continuous flat steel plates;
2. to determine the influence of the corners on the overall behaviour;
3. to investigate failure modes.

Four tests were performed on steel plates having nominal thicknesses of 6, 12 and 16 mm. The overall width and length, out-to-out of welds, of all specimens were 1064 mm and 3064 mm, respectively, giving an aspect ratio of the loaded surface after deducting the size of the edge welds of about 1/3. With this aspect ratio it was anticipated that the stress condition, across the width at the middle of the long sides, would approach that of plane strain. The geometry chosen provided nominal width-to-thickness ratios of about 174, 86, and 64 for the three plate thicknesses. The width/thickness ratio of ship hull plating between intermediate stiffeners varies between 30 and 80 (Hughes, 1981). This range is also common in caisson-type steel ice-resisting walls in offshore structures used for oil exploration in the Arctic ocean (Comyn, 1985). The greater width/thickness ratios of plates used in the tests were selected in anticipation that, with increased spacing of intermediate stiffeners, the local behaviour would be satisfactory for steel caisson-type structures such as ships and other offshore structures.

Material properties of the test plates were determined by means of a series of uniaxial tension tests. The effect of welding on the geometry and microstructure of the restraint zone near the edges of the plates was investigated in small-scale welding tests and small-scale bending tests.

The chronological sequence of tests that developed follows. The ancillary tests to determine the stress-strain properties of the steels, Poisson's ratio and the inelastic strain ratio were first carried out. Plate test P6-1, tested first, failed at a lower load than expected and examination of the fracture surface showed copper contamination from the copper backing bar. This led to a series of weld tests using ceramic backing bars to develop a procedure to give contaminant-free welds with superior profiles and characteristics.

After completion of the weld tests, plate specimens P6-2, P12 and P16 were tested in that sequence. Because even these tests failed at lower than expected loads, a series of small scale bend tests were conducted to examine the ductility of the heat-affected zones and to determine the effect of the heat-affected zone on the failure loads and modes.

3.2 Plate Tests

3.2.1 General

In all tests the four edges of the test plates were fixed against rotation and translation by groove welding the edges of the specimens to a 152 mm thick reaction plate as shown in Fig. 3.1. The depth of the groove weld, made from one side, was 1.5 times the nominal test plate thickness. The multipass weld was designed to contain the oil under pressure and to transmit bending moments, shear forces and in-plane axial forces from the plate specimens to the relatively rigid reaction plate. The thickness of the reaction plate was determined such that its behaviour would be elastic when the test plates acting as membranes with a 30 degree inclination at the edges failed in shear. The reaction plate was re-used from test to test.

The measured thicknesses of the test plates is given in Table 3.1.

3.2.2 Test Specimens

The 4 test specimens, sheared from larger plates, were supplied by C.W. Carry Ltd., Edmonton, Alberta. Specimen P6-2 was hot rolled by Altos Hornos De Mexico S.A. whereas the 3 others were hot rolled by Stelco Inc., Hamilton, Ontario. All plates were specified to conform with CSA Standard CAN3-G40.21-M81 "Structural Quality Steels", (CSA, 1981), grade 300W. Chemical analyses, mill test reports, and the requirements of CSA Standard CAN3-G40.21-M81 are given in Table 3.2. Additional material from each heat was supplied to obtain material properties.

After identifying and marking each test plate the ancillary test material was sheared from one end and the test plate geometry determined. Electrical resistance strain gauges were applied to the lower surface and, as this surface was to be the loaded surface, the strain gauges were protected with flowable silicon (see Fig. 3.1). The lead wires were then passed through holes in the reaction plate into which copper tubes had been threaded to protect the wires during welding of the test plate to the reaction plate. After transporting the test plate-reaction plate assembly to the structural engineering laboratory at the University of Alberta, the strain gauges were placed on the top (free) surface of the test plate and a few on the lower surface of the reaction plate.

3.2.3 Reaction Plate

The mechanical properties of the reaction plate, hot-rolled by Stelco Inc., exceeded the requirements of ASTM A36-84A plate with a yield strength of 336 MPa and an ultimate tensile strength of 510 MPa as given on the mill test certificates.

Twelve 12.7 mm diameter holes were drilled through the thickness of the reaction plate to accommodate pressure piping fittings and plugs so that strain gauge wires could be brought from the underside of the test specimens, as discussed previously, and to provide ports for injecting or releasing oil and bleeding off air. Four lifting lugs were attached to the side of the reaction plate.

To seal the holes in the reaction plate through which the lead wires from the strain gauges passed, the lead wires were threaded through machined piping plugs as shown on Fig. 3.2. The wires were twisted counter clockwise and the conical hole filled with "5-minute" epoxy which was allowed to harden. The piping plugs were then threaded into the reaction plate holes.

The edges of the reaction plate were prepared for welding by flame cutting as shown in Fig. 3.3. Figures 3.4 and 3.5 show the backing bars used in the four tests. To maintain the gap between the test plate and the reaction plate additional backing bars were placed between the two plates. The copper backing bar used in test P6-1 was fastened to the reaction plate by counter sunk machine screws. Because in the first plate test P6-1 copper from the backing bar had infiltrated into the weld metal and was evident on the failure surface, after extensive testing and experimentation, ceramic backing bars were used for the remainder of the tests. To hold the ceramic backing in place, continuous thin steel plates were tack welded to the reaction plate as shown in Fig. 3.4(b) and Fig. 3.5.

3.2.4 Welding Materials And Procedures

All shielded metal arc welding used for the root passes was performed using type E48018 covered electrodes meeting the requirements of AWS A5.1-81, specification for Carbon Steel Covered Arc Welding Electrodes, (American Welding Society, 1981). Type E 48018 electrodes provide a minimum specified yield strength of 480 MPa and an ultimate tensile strength of between 550 MPa and 650 MPa. The flux cored welding was done with type LA T-9 flux cored electrode supplied by Liquid Air Canada Ltd., Montreal, Quebec, to meet the requirements of AWS A5.20-79 class E70T-1, specification for Carbon Steel Electrodes for Flux Cored Arc Welding (American Welding Society, 1979). The LA T-9 electrode is specified to have a minimum yield strength of 450 MPa and a minimum ultimate tensile strength of 550 MPa. Both filler metals were chosen for their strength and similarity in chemical composition to the base metal of the reaction plate and test plates. The weld deposit sequences are shown on Figs. 3.4 and 3.5.

Welding for test P6-1 was done in the shop of C.W. Carry Ltd., Edmonton. A number of steel frames were welded to the reaction plate to hold the test plate in position. These frames are shown in Fig. 3.6. Before welding began, the reaction plate was preheated using, acetylene gas flame, to a global temperature of 180°C with local temperatures occasionally exceeding 250°C. The first and second root passes were made in the horizontal position and the steel frames removed. The root passes were started at opposite corners of the assembly and were deposited along the long sides first. The surfaces of the first two root passes were ground before making additional passes to minimize slag entrapment. With the test assembly in the vertical position, while maintaining the preheat temperature, the remaining four passes of the groove weld were placed in the downhand position.

The procedures used for welding specimens P6-2, P12 and P16 were the same, with the root pass made at the University of Alberta and subsequent flux cored welding at C.W. Carry Ltd. Mechanical clamps were used to hold the test plate against the backing bars for the root passes. The reaction plate was preheated to 150° C to 200° C. The root pass was placed with the clamped assembly in a vertical plane but with one end 22° above the other as shown in Fig. 3.7. Welding proceeded from the lower to the upper corner. The long sides were again welded first. Based on the results of small scale tests done at the Welding Research Lab, Dept. of Mining and Metallurgical Engineering, University of Alberta, a welding speed of about 60 mm/min. and welding machine settings of 170 Amps and 22 Volts were used for the root pass.

3.2.5 Test Set-Up

The test set-up consisted of the self equilibrating test -reaction plate assembly, support columns, a pneumatically activated hydraulic oil pump with reservoir and control valves, an enclosure structure, mechanical and electronic instrumentation, and data acquisition systems. A number of the components can be seen in Fig. 3.8. An enclosure, visible in Fig. 3.8, was provided to limit the area of the laboratory sprayed by oil when rupture occurred. The enclosure was placed along the long sides of the test assembly where rupture was anticipated. Figure 3.9 shows schematically a partial cross-section of the test-reaction plate assembly.

3.2.6 Instrumentation And Measurement

3.2.6.1 Strain Measurements

Assuming symmetrical behaviour, the bulk of the strain gauges were placed in one quadrant only. Strain gauges were generally applied at the same locations on each surface of the plate. The strain gauge alphanumeric reference code, described in detail in Table 3.3, specifies the location, the orientation, the type of gauge and the surface upon which the gauge was mounted.

The location of grid lines for test plates P6-1, P6-2, P12 and P16 are given in Figs. 3.10, 3.11, 3.12, and 3.13, respectively, and the strain gauge codes, in Tables 3.4, 3.5, 3.6, and 3.7, respectively.

The strain gauges were applied using Armstrong type A-12 epoxy adhesive and subsequent to lead wire attachment protected with Dow Corning flowable silicon type RTV-340 . In Fig. 3.14 are shown a pair of strain gauges on the loaded surface of specimen P6-1 and blanketed with silicon. The free ends of lead wires were connected to the data acquisition system to form a 1/4 Wheatstone bridge configuration. The remaining 3/4 of the bridge configuration was made up of electrical resistances contained within the data acquisition equipment.

Prior to tests on plates P12 and P16, three strain gauges were mounted vertically on the outside of weld metal located at the centre of the long side to measure the strains in the weld.

3.2.6.2 Load Measurements

Fluid pressure, measured by an electronic pressure transducer on-line between the test set-up and the pump, was monitored by the data acquisition equipment.

3.2.6.3 LVDT Measurements

Nine linear variable displacement transformers (LVDT's) were mounted directly across the width at the centre of the long sides, as shown in Figs. 3.15 and 3.16, to measure the vertical displacement of the centreline of the plate. The LVDT output signals were recorded electronically. The LVDT located at the mid-width together with the pressure transducer were connected to an x-y plotter to give a visual display of the load-deflection behaviour during testing.

3.2.6.4 Surface Level Indicator (SLI) Measurements

The surface level indicator (SLI),(see Figs. 3.17 and 3.18), bolted to the lifting lugs of the reaction plate, was fabricated using steel channels, hard rubber wheels with steel axles, plastic chains, gears and bearings, two electrical motors, a spring-loaded cable LVDT, two electrical potentiometers, a power supply, control switches, and numerous other pieces. At any load step the SLI traversed the width of the test specimen at 14 locations along the half length as shown in Fig. 3.19 to provide continuous displacement measurements of the plate surface from one long edge to the long edge opposite. The LVDT and potentiometer gave horizontal and vertical displacement readings that were recorded graphically with an x-y plotter.

3.2.7 Test Procedure

The testing procedure generally consisted of the following steps:

1. Oil was pumped into the pressure cavity between the reaction plate and test plate while allowing entrapped air to escape;
2. Initial surface levels were recorded with the SLI at zero oil pressure. The spindles of the LVDT's were checked to ensure they were in contact with and in the correct location on the test plate surface;
3. Initial strain gauge reading, pressure readings and LVDT readings were taken and stored in the data acquisition system;

4. Up to the theoretical collapse pressure, q_c, the oil pressure was increased in increments of about 0.05 q_c, taking pressure, strain and LVDT readings at each step. SLI profiles were recorded at a pressure of q_c;
5. Beyond the pressure q_c, increments of about 0.1 q_c were used and the corresponding electronic readings were recorded. Profiles of the plate surface and photographs were taken at random pressure levels;
6. After fracture, photographs were taken and the surface profiles were recorded.

Each test took about 8 hours to complete. Due to the volume of oil required to fill the pressure cavity as the test plate deformed, it was necessary to add oil periodically to the reservoir . Except for one occurrence while testing plate P12, the pressure was increased continuously or maintained and not reduced during the test. Visual inspection of the test set-up was made periodically to ensure that all test equipment and instrumentation were performing as planned.

3.3 Calibrations

3.3.1 LVDT'S And Potentiometers

The LVDT's were calibrated at a near constant supply voltage against a linear micrometer having a resolution of 0.001 mm. These calibrations also defined the linear range of the LVDT's. The relevant data are given in Table 3.8.

After installing the two potentiometers in the SLI (see Fig. 3.18) they were calibrated using a hand-held digital caliper. The 10-turn potentiometer used to determine transverse displacements in the x-z plane was found to have a constant of proportionality of 128.55 mm/V at a supply excitation voltage of 9.555 Volts. The spring-loaded cable potentiometer used to determine vertical displacements was found to have a calibration constant of 56.30 mm/V at a supply excitation of 9.555 Volts. These calibrations were then used to calibrate the x-y plotter that recorded graphically the pressure and displacement readings during testing.

3.3.2 Pressure Transducer

The electronic pressure transducer, used to monitor fluid pressure during testing and having a capacity of 13.8 MPa, was calibrated by 2 different methods.

First the transducer was attached on-line between a hand activated pump and a loading jack that was placed between the heads of a 1000 KN capacity MTS loading machine. A preset AC excitation voltage was used on the transducer. Using the effective area of the jack piston to translate the MTS load to a pressure, corresponding values of a pressure and the output voltage were determined. A linear least squares analysis of these data gave a calibration factor of 1415 kPa/V.

Second, a calibration was done using dead weights to give corresponding pressures and output voltages directly. The least squares fit of these data gave a calibration factor of 1418 kPa/V. The average of the two values was used during testing.

Table 3.1 **Test Plate Designation**

Plate Designation	Nominal Thickness (mm)	Measured Thickness			
		Number of Measurements	Mean (mm)	Standard Deviation (mm)	Coefficient of Variation, V
P6-1	6	27	6.8	0.07	0.011
P6-2	6	18	7.1	0.06	0.008
P12	12	30	13.4	0.10	0.008
P16	16	30	16.8	0.04	0.003

Table 3.2 **Chemical Composition And Mechanical Properties From Mill Reports**

	Heat	Chemical Composition (%)					Mechanical Properties		
Plate	No.	C	Mn	P	S	Si	Yield Strength (MPa)	Tensile Strength (MPa)	% elongation in 200mm gauge
P6-1	316533	0.17	1.29	0.011	0.010	0.04	313.2	450.3	26.0
P6-2	78328	0.19	1.10	0.012	0.025	0.06	316.3	464.5	26.0
P12	621764	0.16	1.40	0.012	0.012	0.24	324.9	509.7	23.0
P16	346039	0.19	1.30	0.005	0.022	0.18	352.5	539.0	22.0
CSA G40.21-M81		>0.05 <0.22	<1.50	<0.04	<0.05	<0.40	>300	>450 and <620	>20.0

Table 3.3 Strain Gauge Reference Code

CODE : a b - c d e

Code letter designator	Options		Significance
a	**A** through **M**		Located on grid lines **A** through **M**
b	**1** through **7**		Located on grid lines **1** through **7**
c	**T** or **L**	**T** =	Oriented transverse to long side
		L =	Oriented parallel to long side
d	**H** or **P**	**H** =	High elongation foil strain gauge: Micro - Measurements type EP-08-250BG-120 [ε limits = ± 20 % or less]
		P =	foil strain gauge: Showa type N11-FA-5-120-11 [ε limits = ± 1.5 %]
e	**I** or **O**	**I** =	Mounted on loaded surface
		O =	Mounted on free surface

Example: **D3-THI** --- Located at intersection of grid lines **D** and **3**. Oriented in transverse direction. High elongation type gauge. Mounted on loaded surface.

Table 3.4 Strain Gauges On Test Plate P6-1

Longitudinal grid lines / trans. grid lines	A	B	C	D	E	F	G	H	I	J	K	L	M
1	A1-THI A1-THO A1-LHI AX-THO	B1-THI B1-THO	C1-THI C1-THO C1-LPI C1-LPO	D1-THI D1-THO	E1-THI E1-THO E1-LPI E1-LPO	F1-THI F1-THO	G1-THI G1-THO G1-LPI G1-LPO	H1-THI H1-THO	I1-THI I1-THO I1-LPI I1-LPO	J1-THI J1-THO	K1-THI K1-THO K1-LPI K1-LPO	L1-THI L1-THO	M1-THI M1-THO M1-LHI MX-THO
2	A2-THI A2-THO	B2-THI B2-THO		D2-THI D2-THO D2-LPI D2-LPO			G2-THI G2-THO G2-LPI G2-LPO		I2-THI I2-THO		K2-THI K2-THO		
3	A3-THI A3-THO A3-LHI			D3-THI D3-THO			G3-THI G3-THO G3-LPI G3-LPO						
4							G4-THI G4-THO G4-LHI G4-LHO						
5	A5-THI A5-THO A5-LHI			D5-THI D5-THO D5-LPI D5-LPO			G5-THI G5-THO G5-LHI G5-LHO						
6	A6-THI A6-THO			D6-THI D6-THO D6-LHI D6-LHO			G6-THI G6-THO G6-LHI G6-LHO						
7	A7-SHI A7-SHO						G7-LHI G7-LHO						

Table 3.5 Strain Gauges On Test Plate P6-2

Longitudinal grid lines	A	B	C	D	E	F	G	H	I	J	K	L	M
Trans. grid lines													
1	A1-THI A1-THO AX-THO	B1-THI B1-THO	C1-THI C1-THO C1-LPI C1-LPO	D1-THI D1-THO	E1-THI E1-THO E1-LPI E1-LPO	F1-THI F1-THO	G1-THI G1-THO G1-LPI G1-LPO	H1-THI H1-THO	I1-THI I1-THO I1-LPI I1-LPO	J1-THI J1-THO	K1-THI K1-THO K1-LPI K1-LPO	L1-THI L1-THO	M1-THI M1-THO MX-THO
2	A2-THI A2-THO	B2-THI B2-THO		D2-THI D2-THO D2-LPI D2-LPO			G2-THI G2-THO G2-LPI G2-LPO		I2-THI I2-THO		K2-THI K2-THO		
3	A3-THI A3-THO			D3-THI D3-THO			G3-THI G3-THO G3-LPI G3-LPO						
4							G4-THI G4-THO G4-LHI G4-LHO						
5	A5-THI A5-THO			D5-THI D5-THO D5-LPI D5-LPO			G5-THI G5-THO G5-LHI G5-LHO						
6	A6-THI A6-THO			D6-THI D6-THO D6-LHI D6-LHO			G6-THI G6-THO G6-LHI G6-LHO						
7	A7-SHI A7-SHO			D7-LHI D7-LHO			G7-LHI G7-LHO						

Table 3.6 Strain Gauges On Test Plate P12

Longitudinal grid lines	A	B	C	D	E	F	G	H	I	J	K	L	M
Trans. grid lines													
1	A1-THI A1-THO AX-THO	B1-THI B1-THO	C1-THI C1-THO C1-LPI C1-LPO	D1-THI D1-THO	E1-THI E1-THO E1-LPI E1-LPO	F1-THI F1-THO	G1-THI G1-THO G1-LPI G1-LPO	H1-THI H1-THO	I1-THI I1-THO I1-LPI I1-LPO	J1-THI J1-THO	K1-THI K1-THO K1-LPI K1-LPO	L1-THI L1-THO	M1-THI M1-THO MX-THO
2	A2-THI A2-THO	B2-THI B2-THO		D2-THI D2-THO D2-LPI D2-LPO			G2-THI G2-THO G2-LPI G2-LPO		I2-THI I2-THO		K2-THI K2-THO		
3	A3-THI A3-THO			D3-THI D3-THO			G3-THI G3-THO G3-LPI G3-LPO						
4							G4-THI G4-THO G4-LHI G4-LHO						
5	A5-THI A5-THO			D5-THI D5-THO D5-LPI D5-LPO			G5-THI G5-THO G5-LHI G5-LHO						
6	A6-THI A6-THO			D6-THI D6-THO D6-LHI D6-LHO			G6-THI G6-THO G6-LHI G6-LHO						
7	A7-SHI A7-SHO			D7-LHI D7-LHO			G7-LHI G7-LHO						

Table 3.7 Strain Gauges On Test Plate P16

Longitudinal grid lines	A	B	C	D	E	F	G	H	I	J	K	L	M
Trans. grid lines													
1	A1-THI A1-THO AX-THO	B1-THI B1-THO	C1-THI C1-THO C1-LPI C1-LPO	D1-THI D1-TPO	E1-THI E1-THO E1-LPI E1-LPO	F1-THI F1-TPO	G1-THI G1-THO G1-LPI G1-LPO	H1-THI H1-TPO	I1-THI I1-THO I1-LPI I1-LPO	J1-THI J1-TPO	K1-THI K1-THO K1-LPI K1-LPO	L1-THI L1-TPO	M1-THI M1-THO MX-THO
2	A2-THI A2-THO	B2-THI B2-THO		D2-THI D2-THO D2-LPI D2-LPO			G2-THI G2-THO G2-LPI G2-LPO		I2-THI I2-THO		K2-THI K2-THO		
3	A3-THI A3-THO			D3-THI D3-THO			G3-THI G3-TPO G3-LPI G3-LPO						
4							G4-THI G4-TPO G4-LHI G4-LPO						
5	A5-THI A5-THO			D5-THI D5-THO D5-LPI D5-LPO			G5-THI G5-TPO G5-LHI G5-LPO						
6	A6-THI A6-THO			D6-THI D6-THO D6-LHI D6-LHO			G6-THI G6-THO G6-LHI G6-LPO						
7	A7-SHI A7-SHO			D7-LHI D7-LHO			G7-LHI G7-LHO						

Table 3.8 LVDT Characteristics

Laboratory reference code	Location number in frame	Nominal operating range (mm)	Excitation Voltage (V)	Sensitivity (mm/V)	Calibration constant (mm/V)
7T0502	1	± 12.7	5.998	± 0.0003	3.875
6T1004	2	± 25.4	5.999	± 0.0005	4.977
6T3006	3	± 76.2	5.999	± 0.002	17.525
6T3005	4	± 76.2	5.999	± 0.002	17.305
6T3001	5	± 76.2	5.999	± 0.002	16.800
6T3016	6	± 76.2	5.999	± 0.002	17.732
6T3045	7	± 76.2	5.998	± 0.002	16.354
6T1006	8	± 25.4	5.999	± 0.0005	5.950
7T0501	9	± 12.7	5.998	± 0.0003	3.897

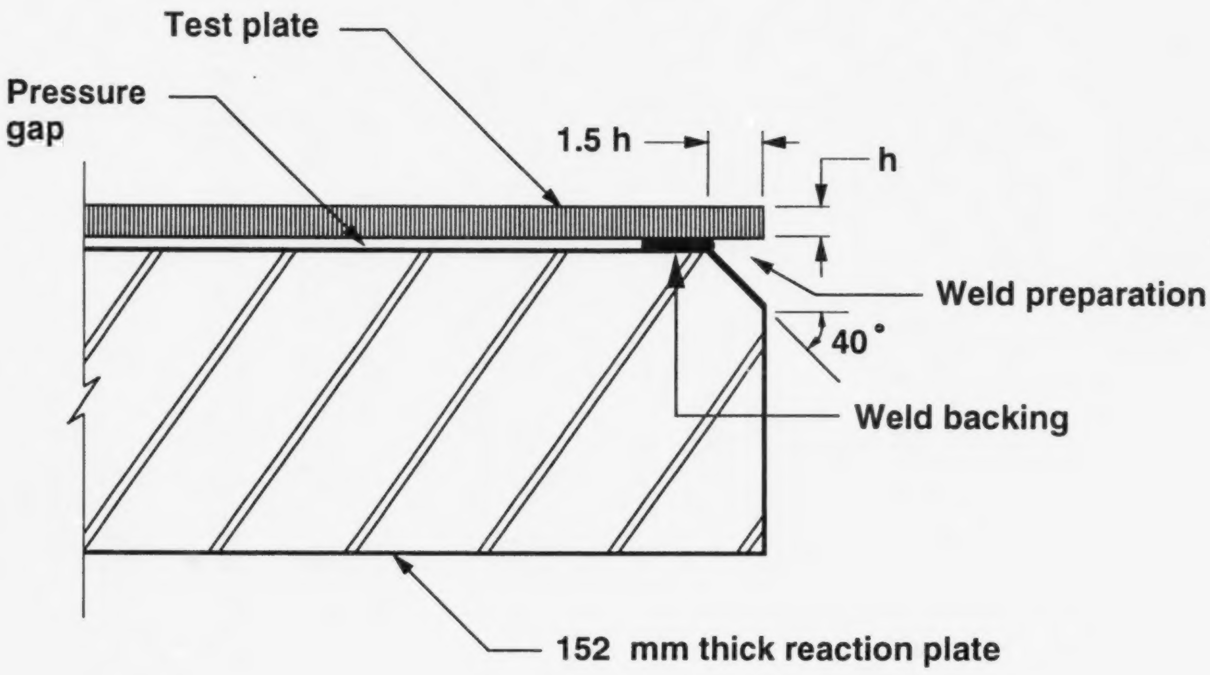
Test plate
Pressure gap
1.5 h
h
Weld preparation
40 °
Weld backing
152 mm thick reaction plate

Figure 3.1 Partial cross-section through test and reaction plates at edge

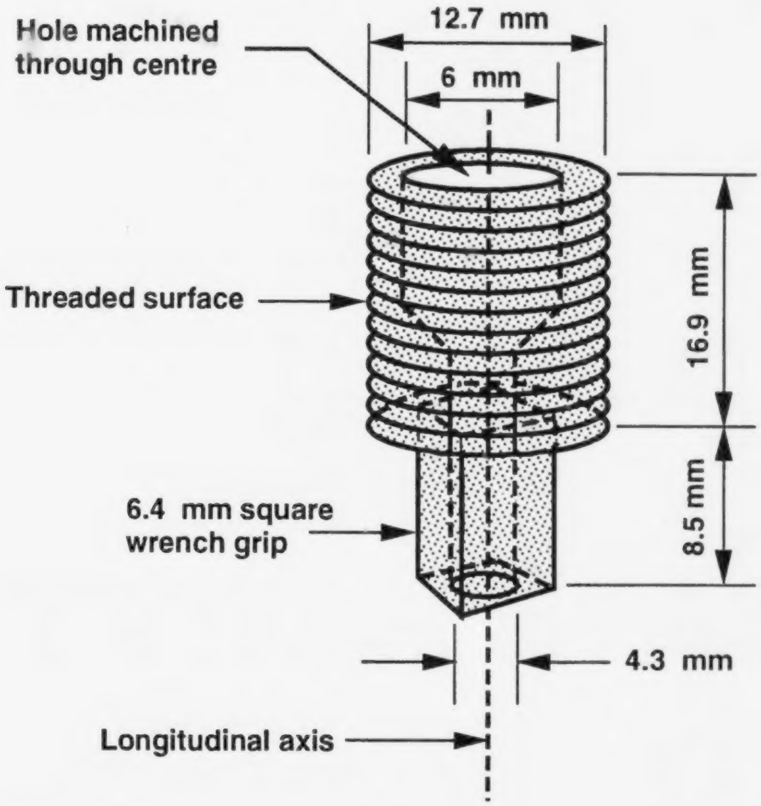
Hole machined through centre
12.7 mm
6 mm
Threaded surface
16.9 mm
6.4 mm square wrench grip
8.5 mm
4.3 mm
Longitudinal axis

Figure 3.2 Machined steel piping plug

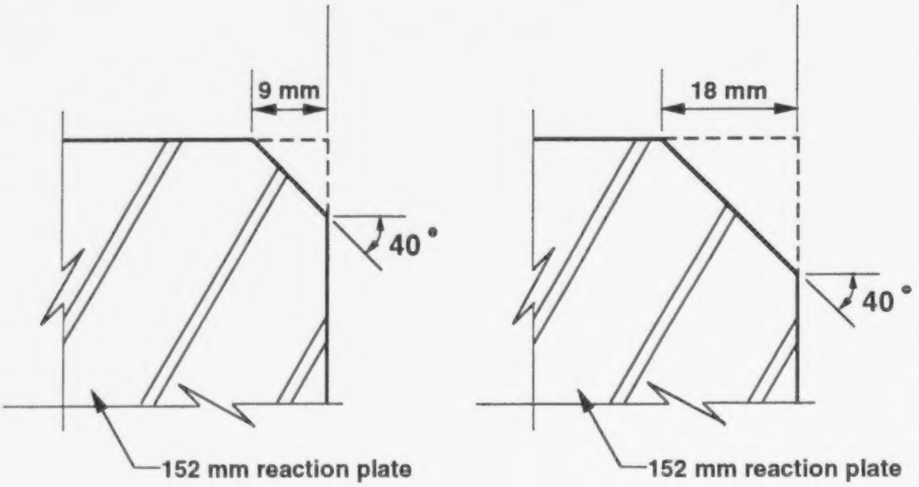
9 mm
40 °
152 mm reaction plate
18 mm
40 °
152 mm reaction plate

(a) Tests P6-1 and P6-2

(b) Test P12

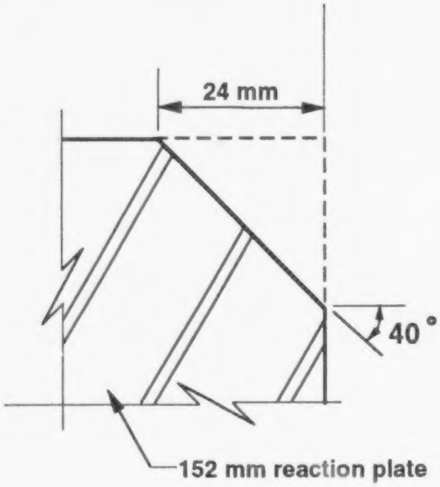
24 mm
40 °
152 mm reaction plate

(c) Test P16

Figure 3.3 Reaction plate edge preparations

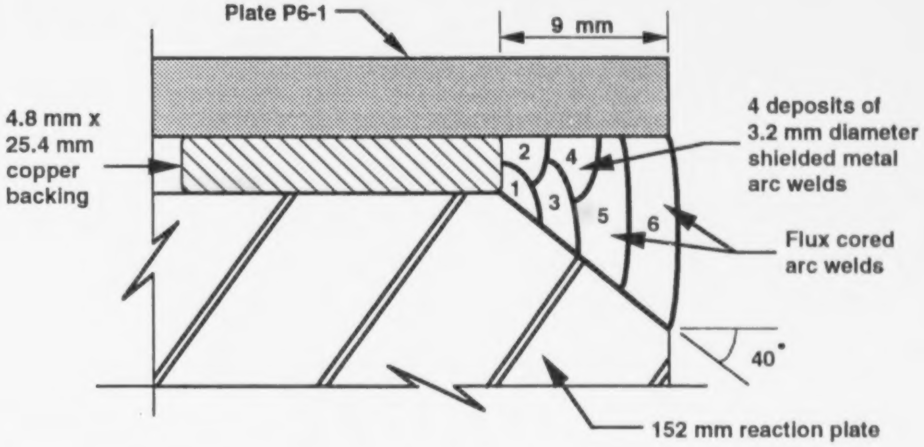
Plate P6-1
9 mm
4.8 mm x
25.4 mm
copper
backing
4 deposits of
3.2 mm diameter
shielded metal
arc welds
1
2
3
4
5
6
Flux cored
arc welds
40°
152 mm reaction plate

(a) Specimen P 6 - 1

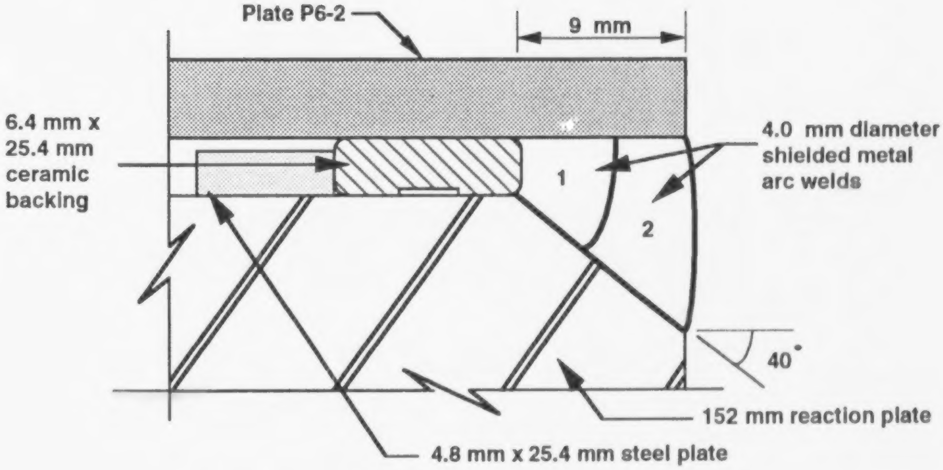
Plate P6-2
9 mm
6.4 mm x
25.4 mm
ceramic
backing
4.0 mm diameter
shielded metal
arc welds
1
2
40°
152 mm reaction plate
4.8 mm x 25.4 mm steel plate

(b) Specimen P 6 - 2

Figure 3.4 Edge preparations, backing bars and welding sequences

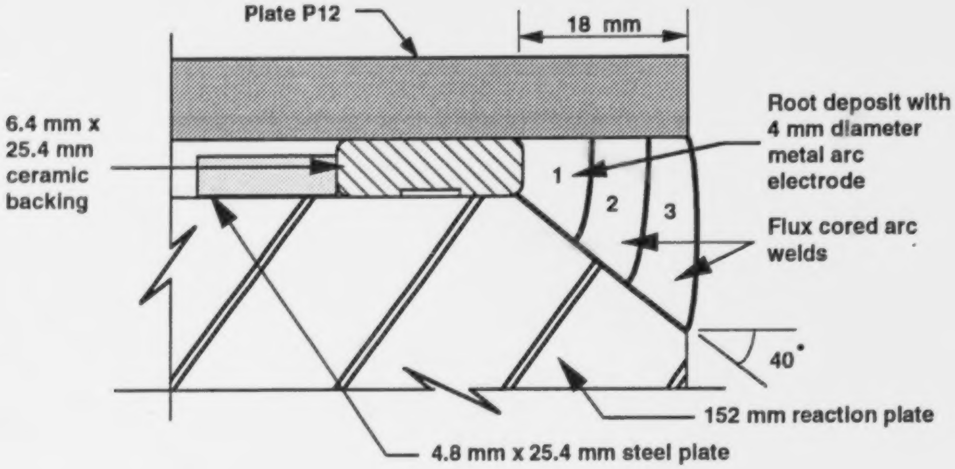
Plate P12
18 mm
6.4 mm x
25.4 mm
ceramic
backing
Root deposit with
4 mm diameter
metal arc
electrode
1
2
3
Flux cored arc
welds
40°
152 mm reaction plate
4.8 mm x 25.4 mm steel plate

(a) Specimen P 12

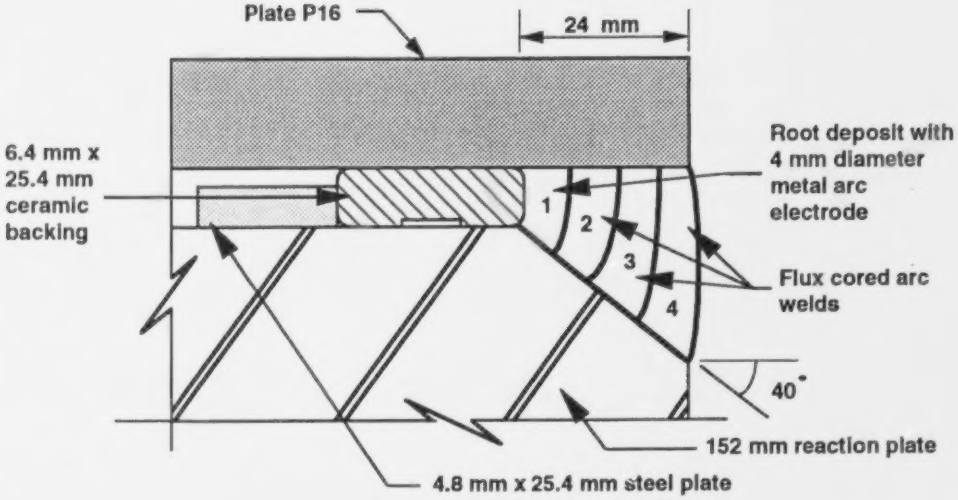
Plate P16
24 mm
6.4 mm x
25.4 mm
ceramic
backing
Root deposit with
4 mm diameter
metal arc
electrode
1
2
3
4
Flux cored arc
welds
40°
152 mm reaction plate
4.8 mm x 25.4 mm steel plate

(b) Specimen P 16

Figure 3.5 Edge preparations, backing bars and welding sequences

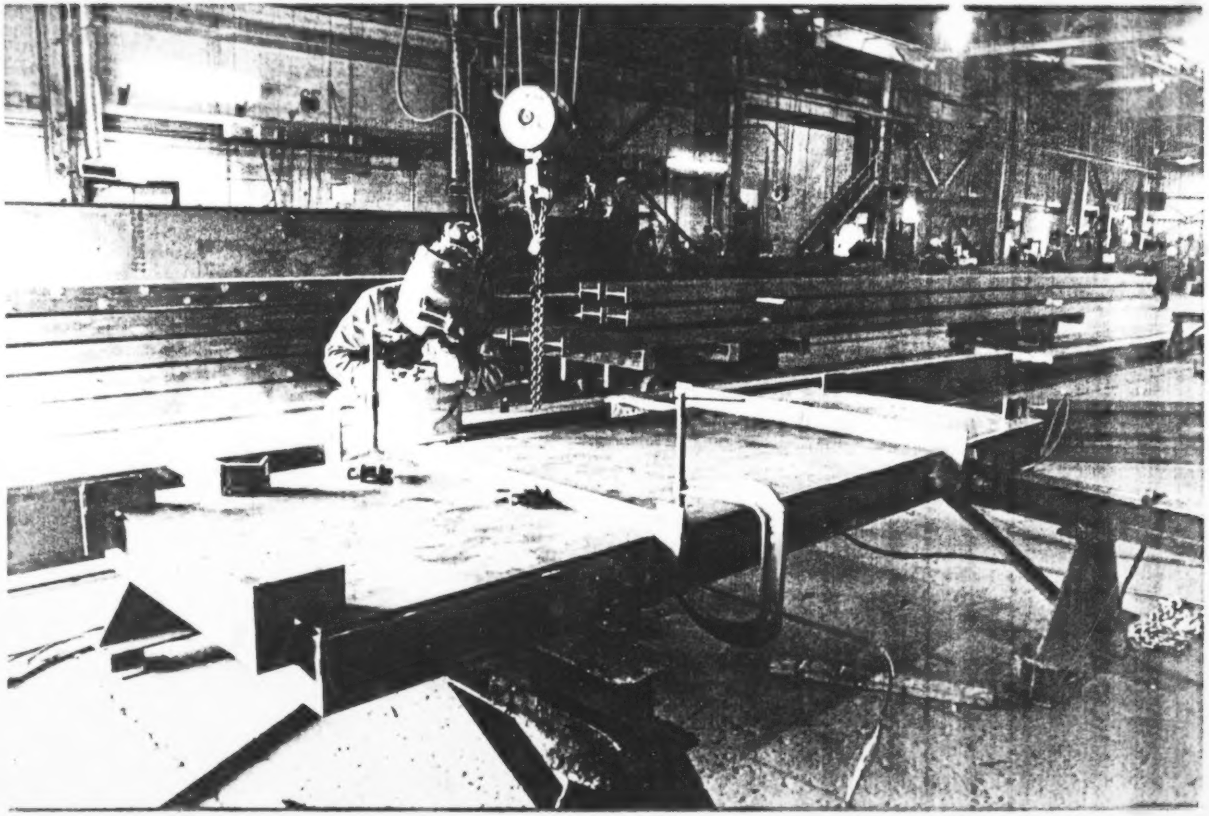

Figure 3.6 Clamping frames on specimen P6-1 and reaction plate assembly

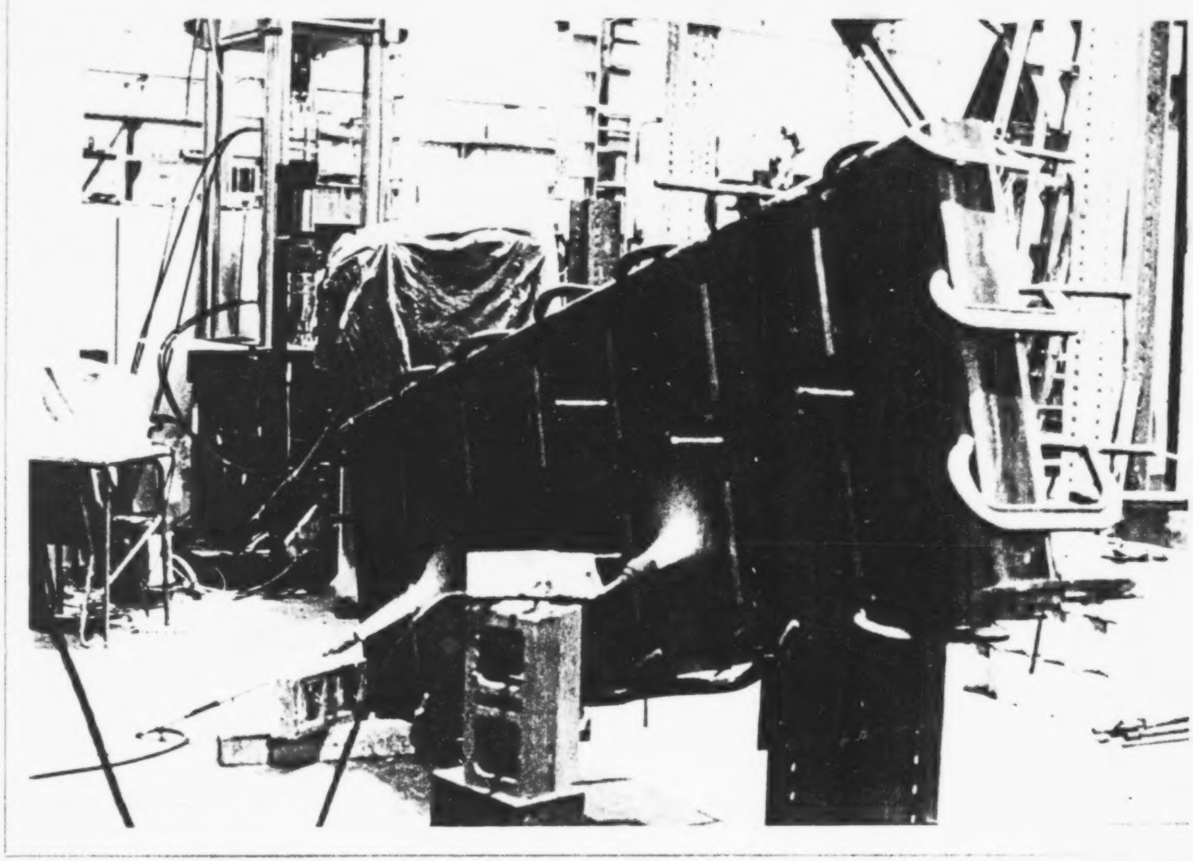

Figure 3.7 Clamped assembly elevated at one end, before welding

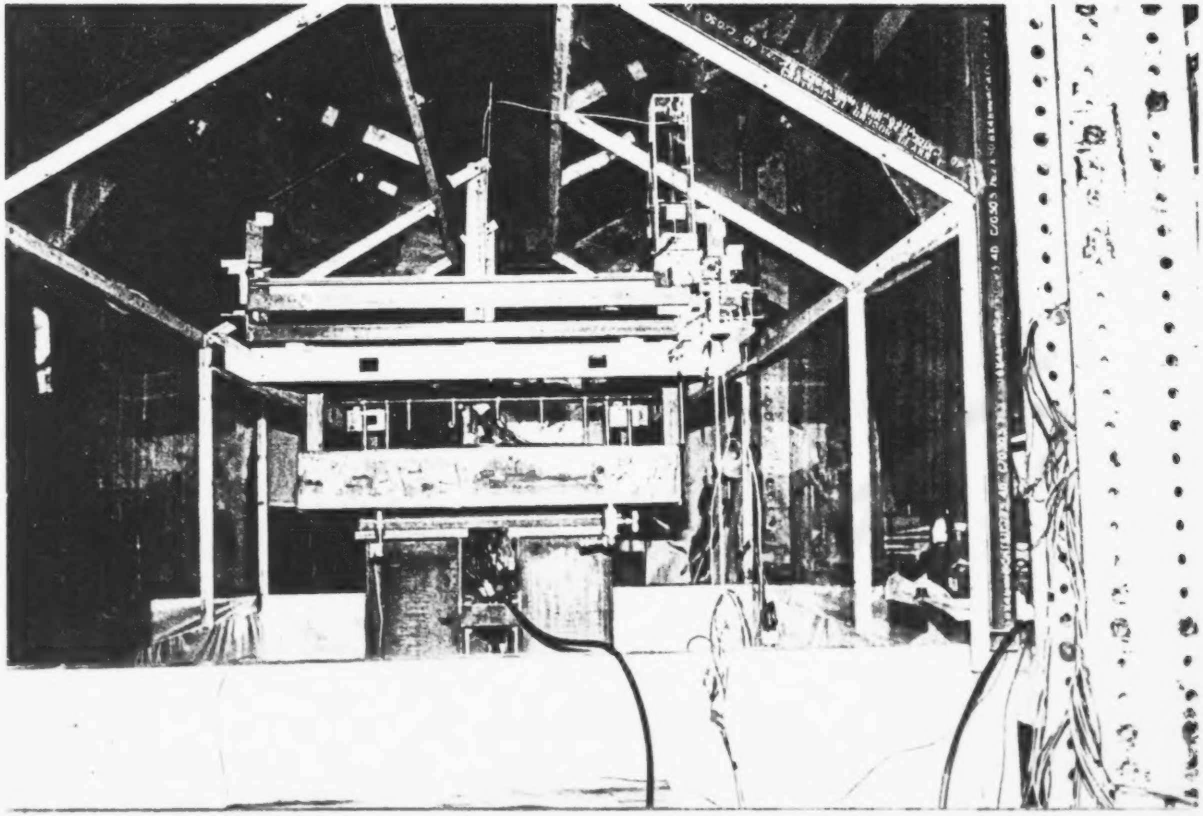

Figure 3.8 End view of test set-up

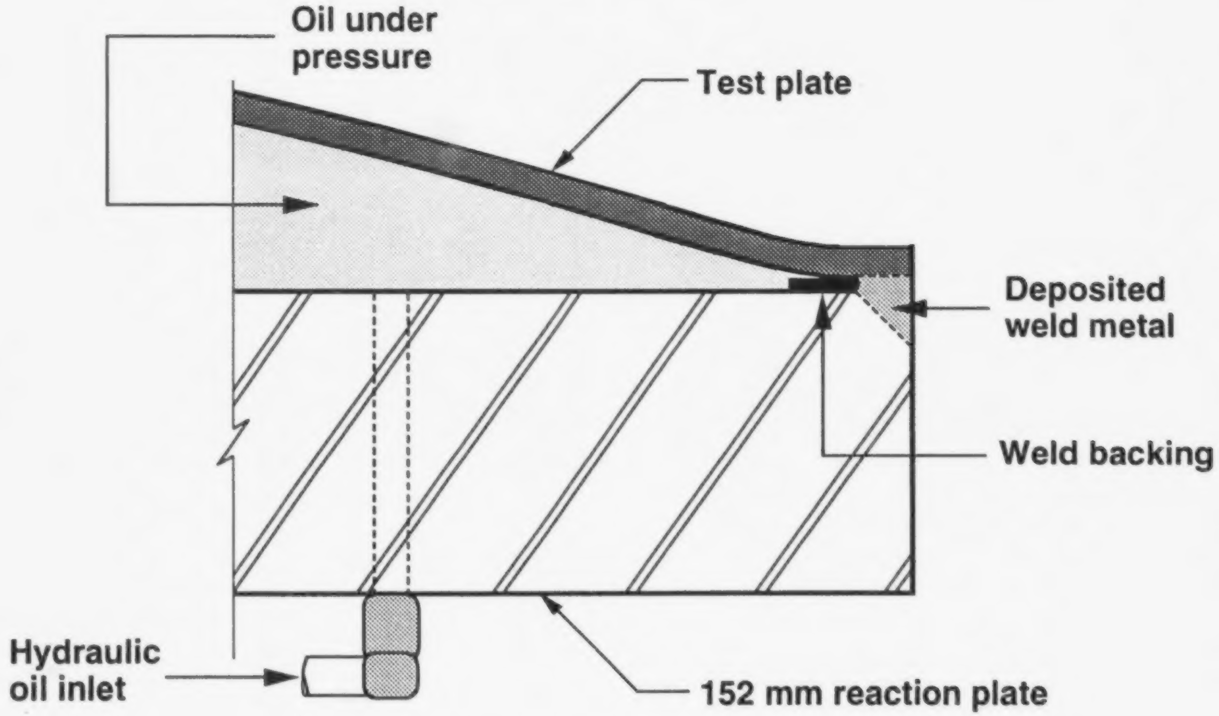
Oil under pressure
Test plate
Deposited weld metal
Weld backing
Hydraulic oil inlet
152 mm reaction plate

Figure 3.9 Partial cross-section at edge of test apparatus

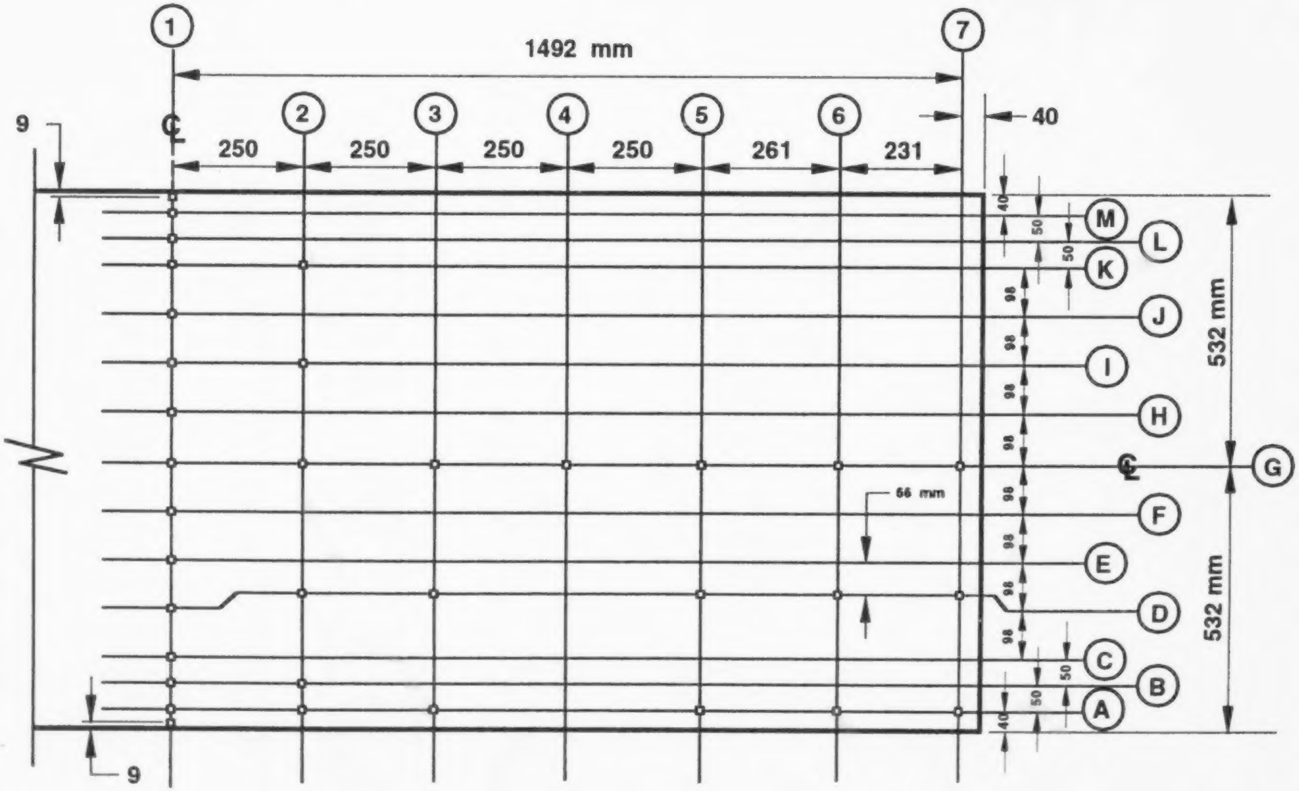
1
2
3
4
5
6
7
1492 mm
250
250
250
250
261
231
40
9
9
℄
℄
M
L
K
J
I
H
G
F
E
D
C
B
A
40
50
50
98
98
98
98
98
98
98
98
50
50
40
532 mm
532 mm
66 mm

All dimensions in mm

Figure 3.10 Grid lines for strain gauge locations on test specimen P6-1

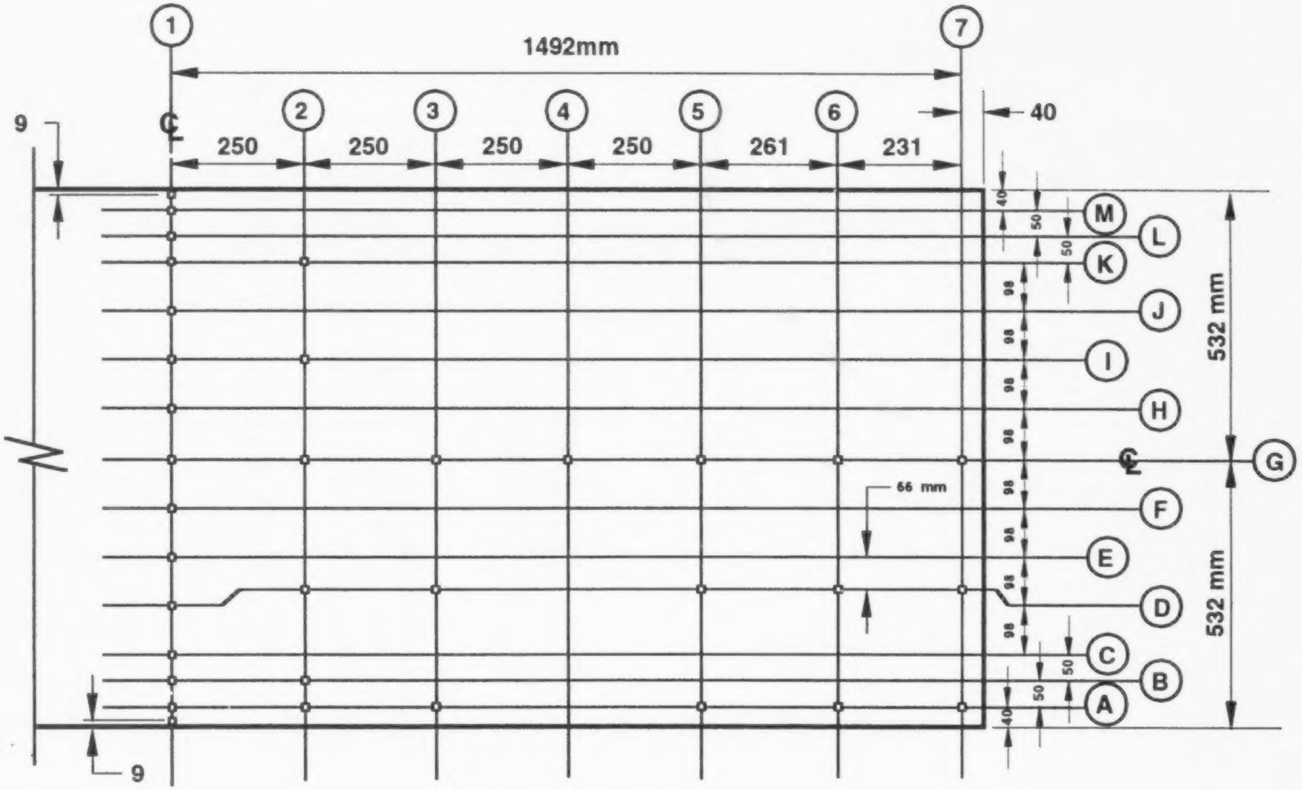
1492mm
250
250
250
250
261
231
40
9
9
66 mm
40
50
50
98
98
98
98
98
98
98
50
50
40
532 mm
532 mm
1
2
3
4
5
6
7
A
B
C
D
E
F
G
H
I
J
K
L
M

All dimensions in mm

Figure 3.11 Grid lines for strain gauge locations on test specimen P6-2

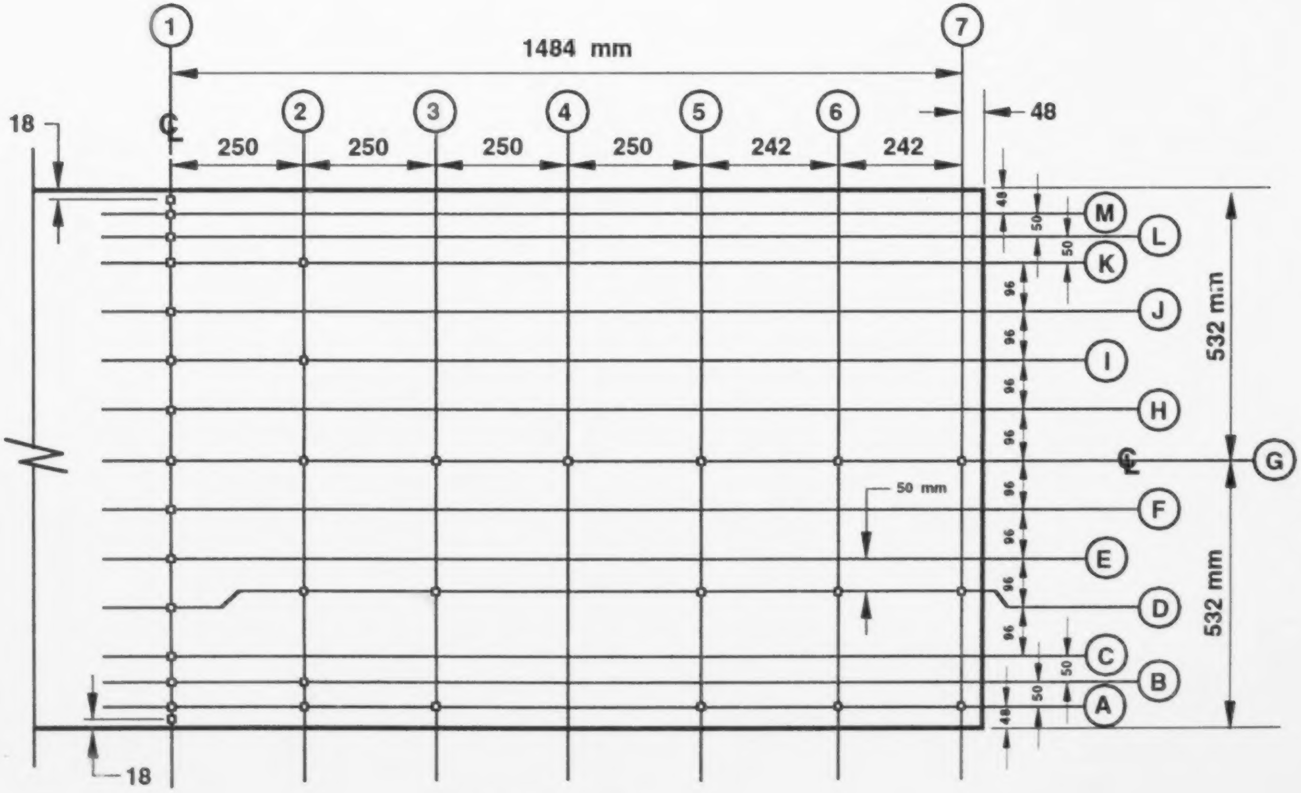
1
2
3
4
5
6
7
1484 mm
18
250
250
250
250
242
242
48
48
50
50
96
50 mm
532 mm
532 mm
M
L
K
J
I
H
G
F
E
D
C
B
A
18

All dimensions in mm

Figure 3.12 Grid lines for strain gauge locations on test specimen P12

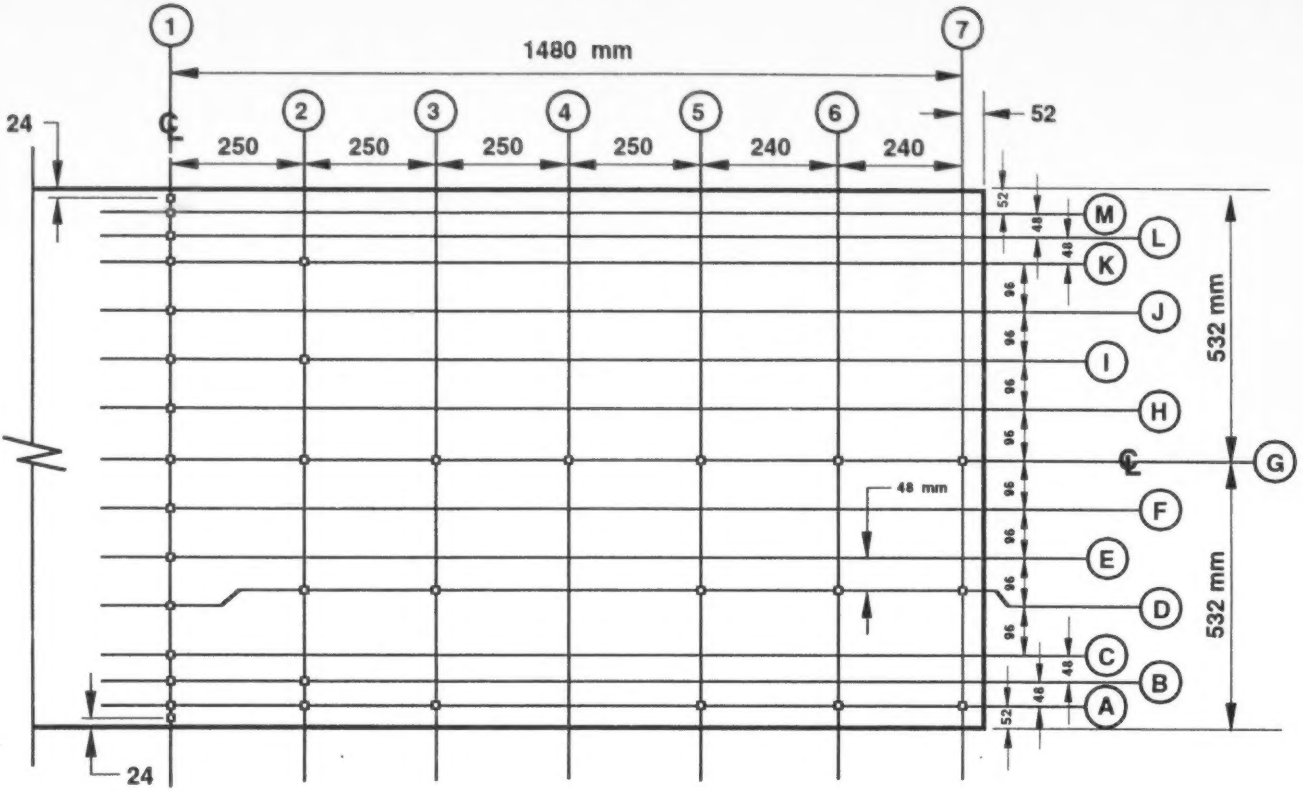
1
2
3
4
5
6
7
1480 mm
250
250
250
250
240
240
52
24
24
℄
A
B
C
D
E
F
G
H
I
J
K
L
M
52
48
48
96
96
96
96
96
96
96
96
48
48
52
532 mm
532 mm
48 mm

All dimensions in mm

Figure 3.13 Grid lines for strain gauge locations on test specimen P16

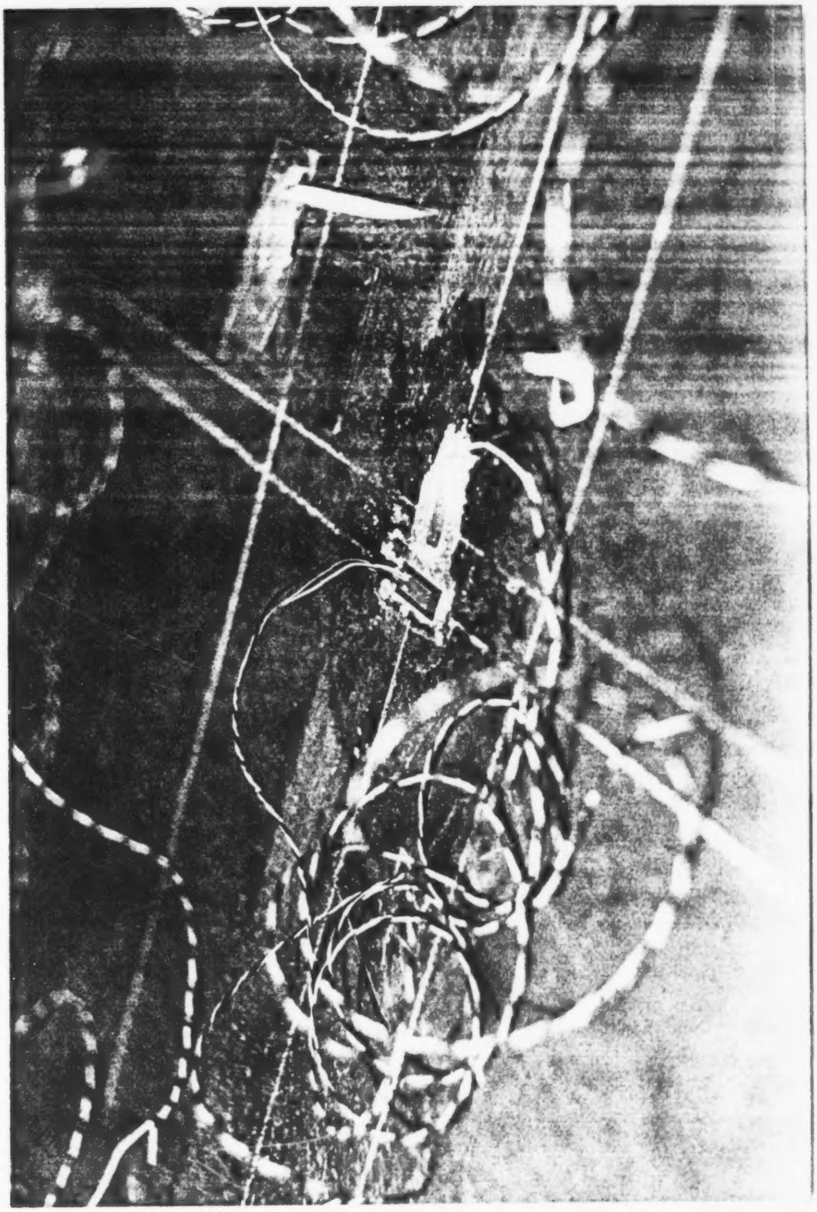

Figure 3.14 Strain gauges blanketed with silicon on specimen P6-1

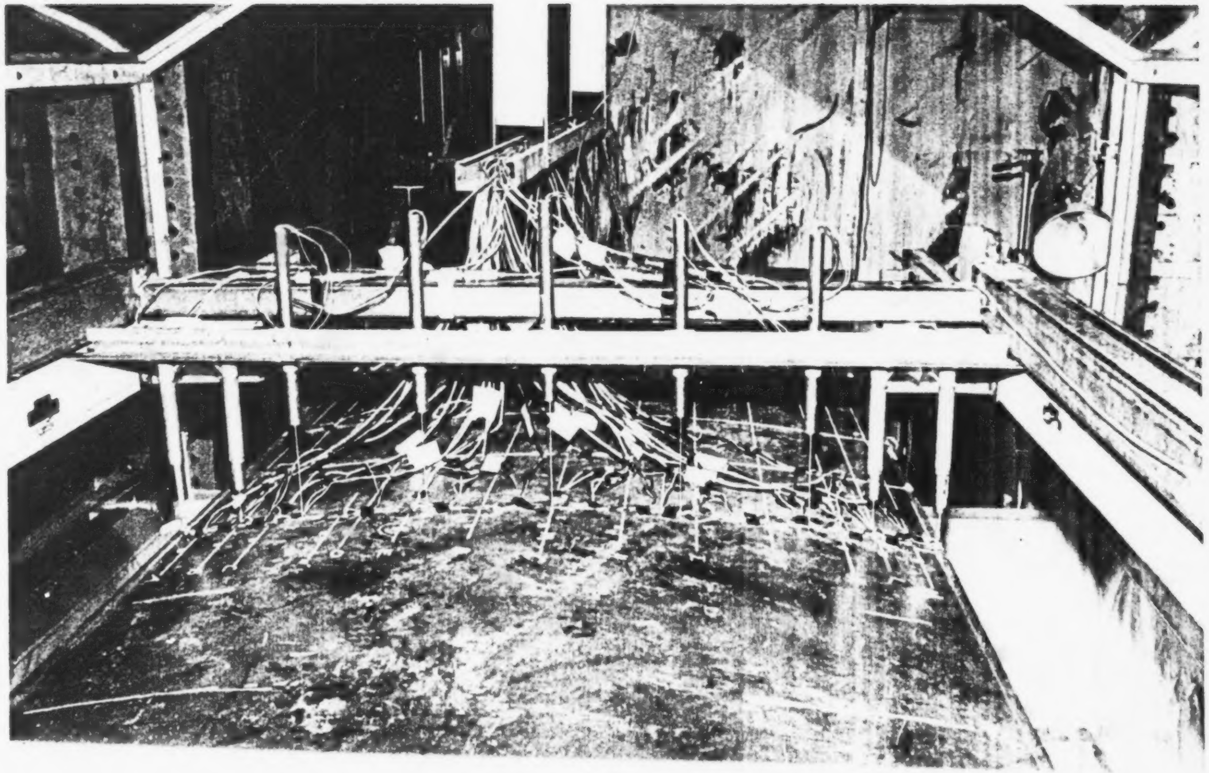

Figure 3.15 LVTD's in support frame above test plate

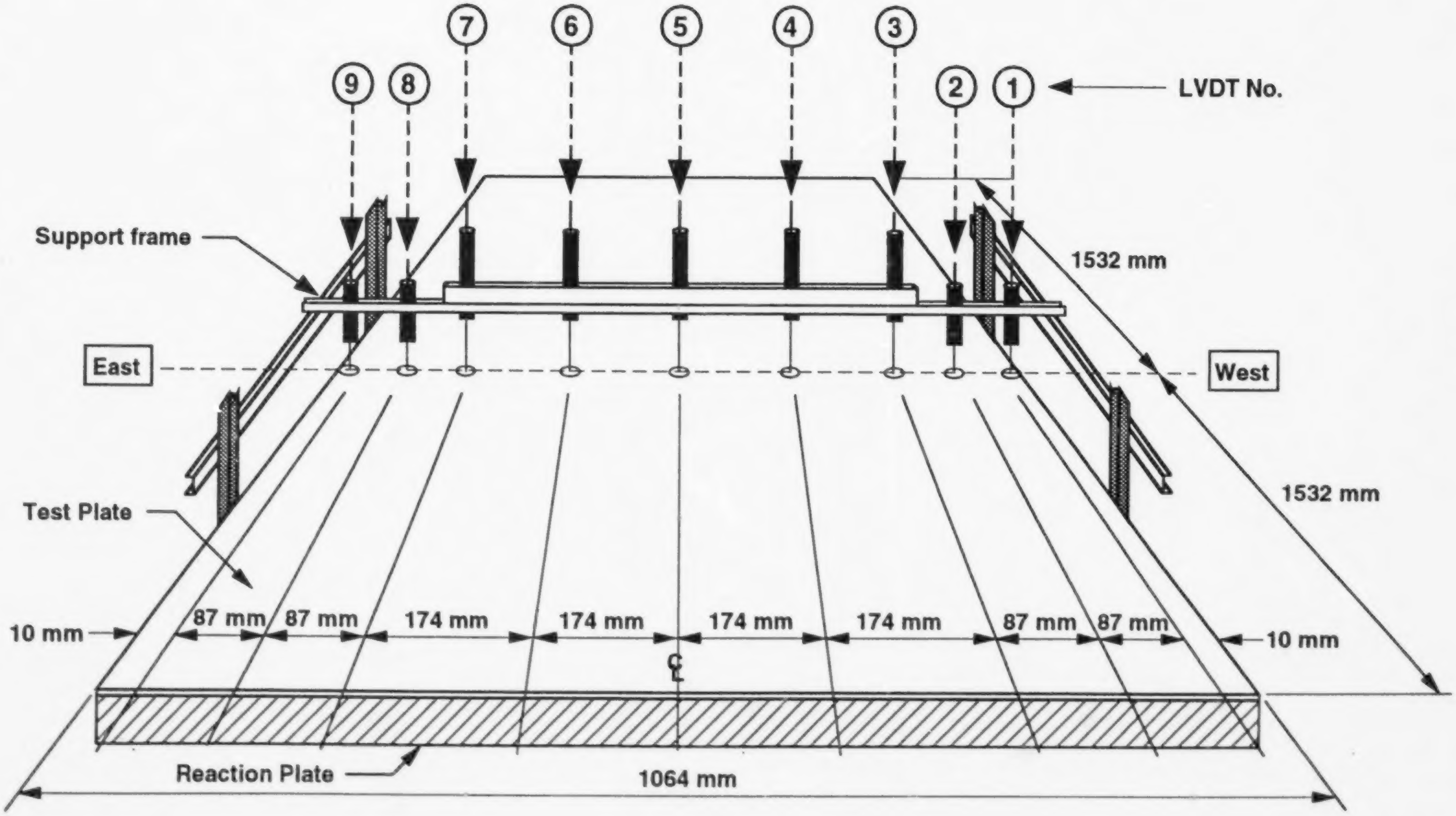

9
8
7
6
5
4
3
2
1
LVDT No.
Support frame
1532 mm
East
West
1532 mm
Test Plate
10 mm
87 mm
87 mm
174 mm
174 mm
174 mm
174 mm
87 mm
87 mm
10 mm
℄
Reaction Plate
1064 mm

Figure 3.16 LVDT locations in support frame above test plate

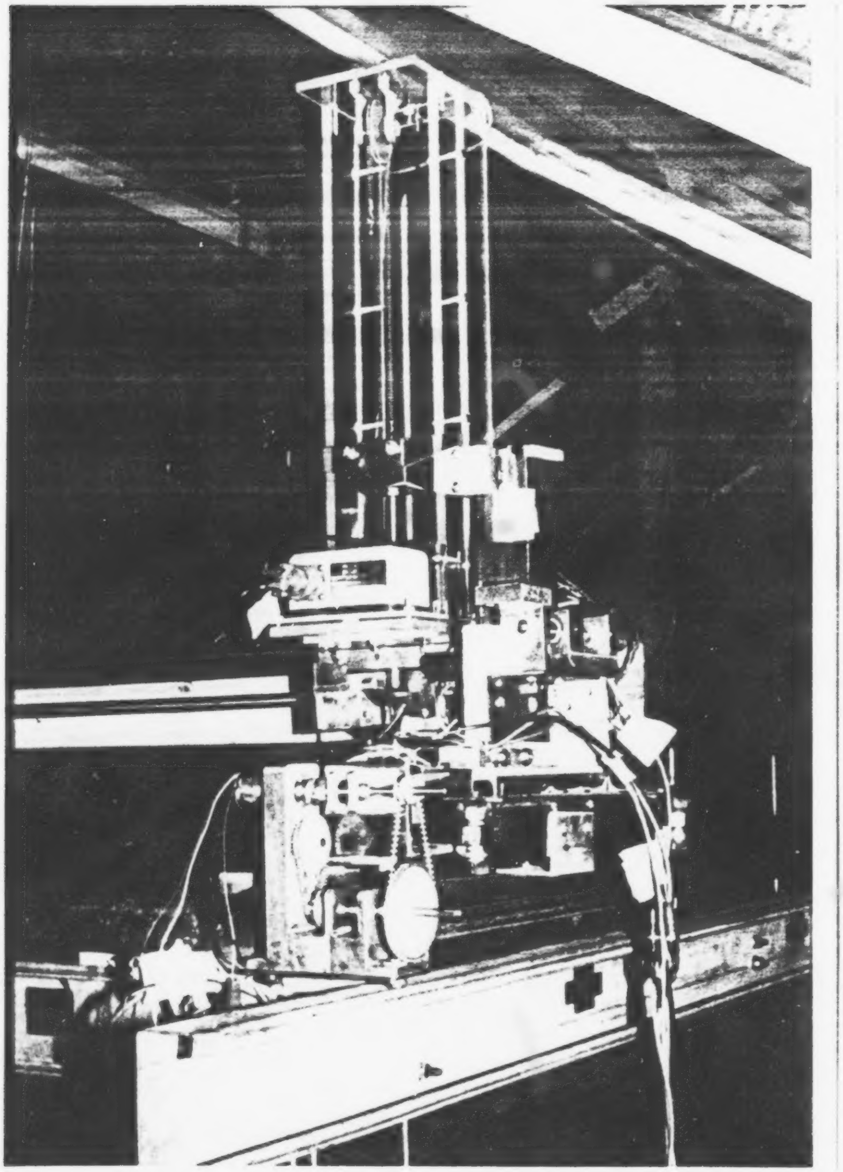

Figure 3.17 Surface level indicator (SLI) above test plate

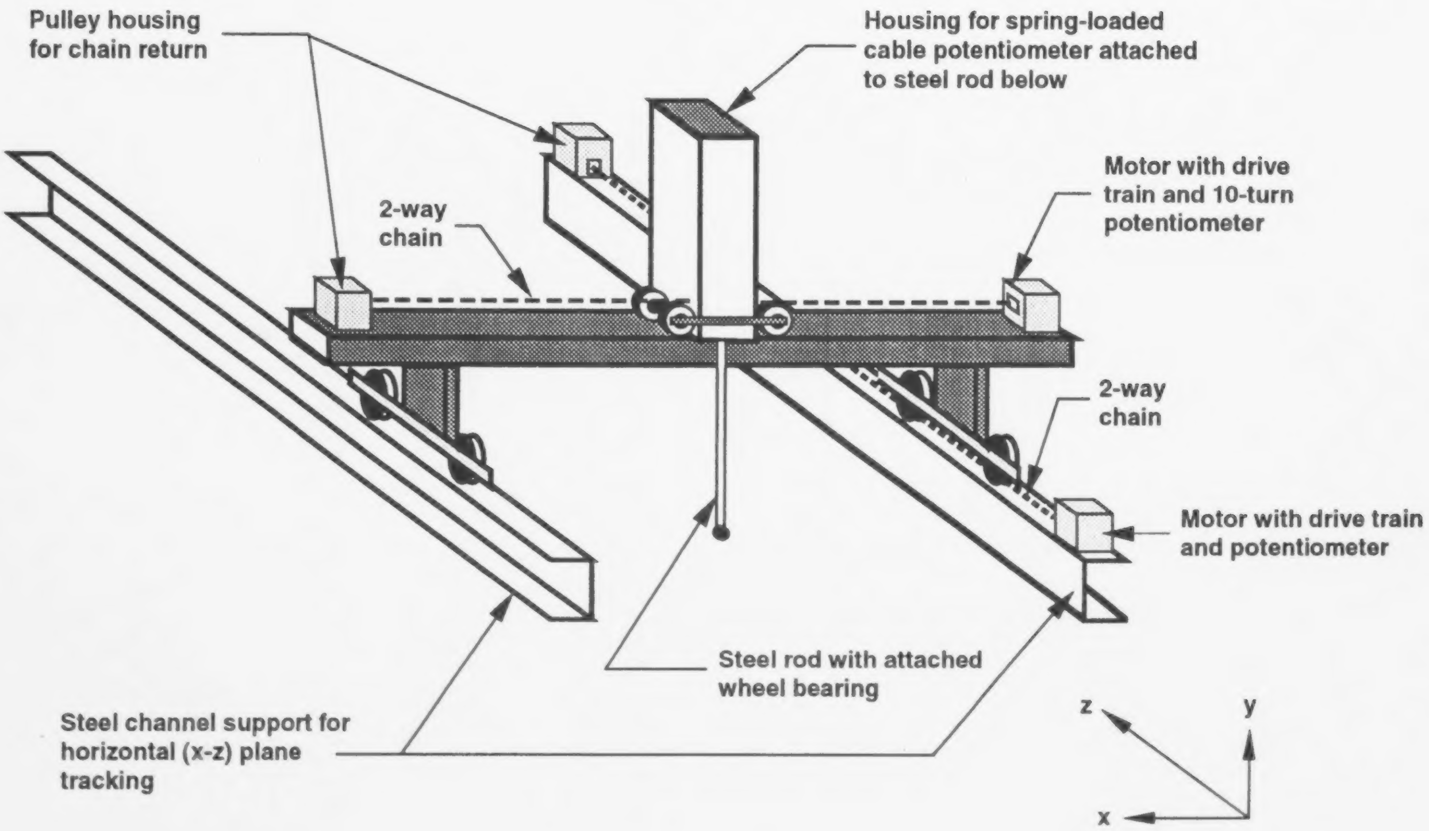
Pulley housing for chain return
Housing for spring-loaded cable potentiometer attached to steel rod below
Motor with drive train and 10-turn potentiometer
2-way chain
2-way chain
Motor with drive train and potentiometer
Steel rod with attached wheel bearing
Steel channel support for horizontal (x-z) plane tracking
z
y
x

Figure 3.18 Schematic diagram of Surface Level Indicator (SLI)

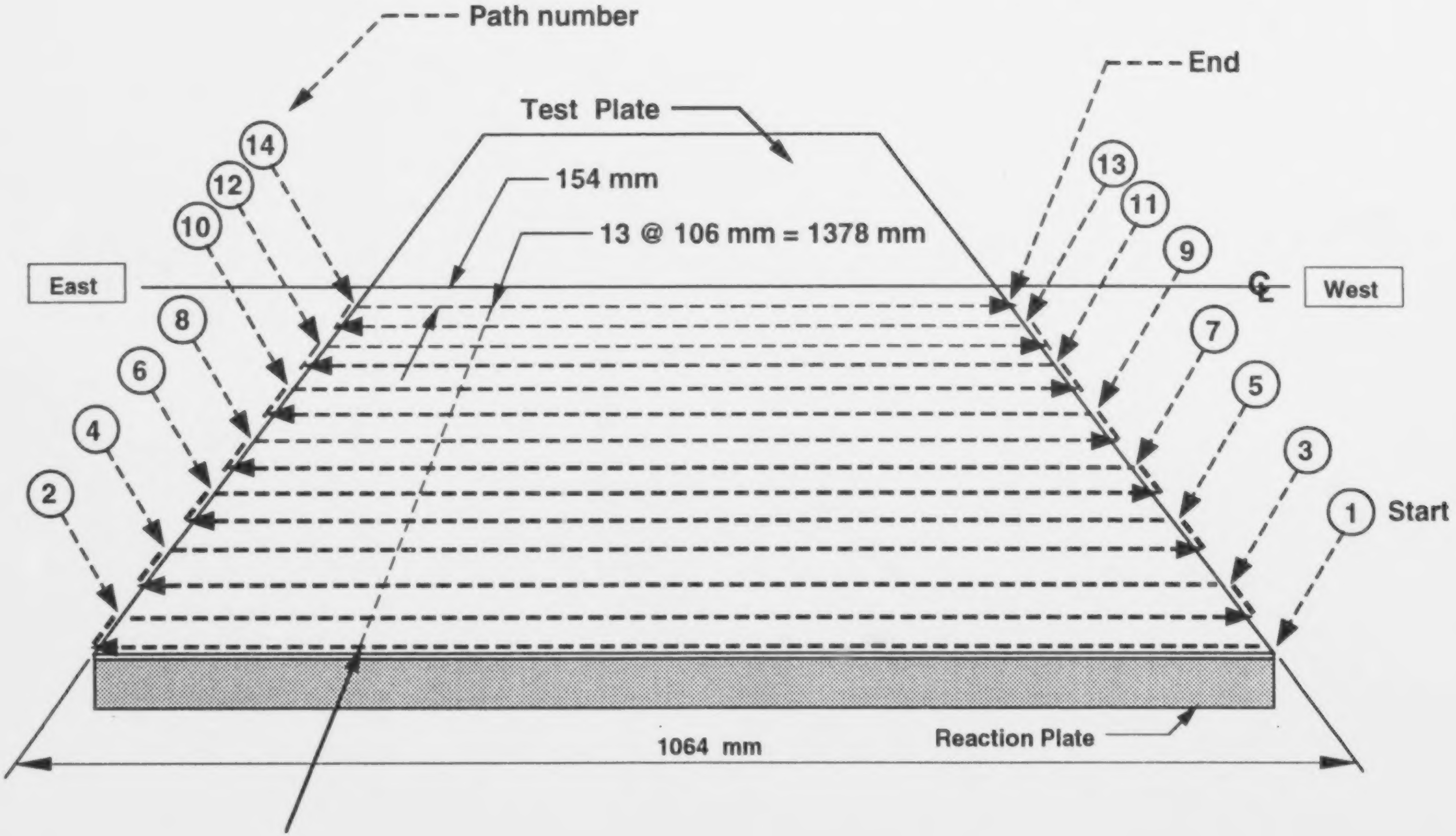
Path number
End
Test Plate
154 mm
13 @ 106 mm = 1378 mm
East
West
℄
14
12
10
8
6
4
2
13
11
9
7
5
3
1
Start
1064 mm
Reaction Plate

Figure 3.19 Path of Surface Level Indicator (SLI)

4. MATERIAL PROPERTIES AND BEHAVIOUR

4.1 Tension Tests

A total of 37 uniaxial tension coupon tests were performed on specimens from the four parent plates to establish the stress-strain characteristics, Poisson's ratio, and the inelastic strain ratio. With these data, the behaviour in other stress states could be determined. As shown in Fig. 4.1 five coupons were oriented parallel to and five transversely to the direction of rolling of the parent plate. Table 4.1 gives the alphanumeric identification of the test coupons. After cutting from the larger plate the full thickness coupons were milled to provide a reduced section.

Table 4.1 indicates which coupons were mounted with strain gauges to measure longitudinal strains on both faces and which had longitudinal and transverse gauges on both faces in order to determine Poisson's ratio. The table also notes which specimens had high elongation strain gauges so that inelastic strain ratios could be determined. As well, calipers were used to measure large strains. Figure 4.2 shows a tension coupon with longitudinal and transverse gauges in the Baldwin testing machine.

Figures 4.3 and 4.4 give typical stress-strain curves for the four test plates. The coupon test results are summarized in Tables 4.2 through 4.5 for plates P6-1, P6-2, P12 and P16, respectively. No significant difference exists in the material properties parallel and transverse to the direction of rolling.

In Figs. 4.5, 4.6 and 4.7, the strain ratio is plotted versus axial strain for the 6 mm, 12 mm and 16 mm plates, respectively. The strain ratio is defined as the absolute value of the mean transverse strain divided by the mean longitudinal strain. The strain ratio, so defined, is sometimes called the total strain ratio because it is based on engineering or total strains. In the elastic range, this ratio is, of course, Poisson's ratio. Because these strains could amount to as much as 20% the strain data were corrected for both the nonlinearity in electrical output of the one-quarter Wheatstone Bridge circuit and for the effect of transverse strains on the electrical resistance of the strain gauge.(Ratzlaff et al, 1988).

The value of Poisson's ratio obtained for the 6 mm and 12 mm plates was 0.28 and for the 16 mm plate, 0.29. In the yield plateau the strain ratio would appear to fluctuate widely. However, this is attributed to the fact that yielding is a discontinuous phenomenon and the gauges, of finite length, give average strains and not those at a point.

For the 6 mm and 12 mm plates the inelastic strain ratio beyond the yield plateau has a maximum value approaching 0.4 at a longitudinal strain of about 2% and then decreases almost linearly to a value of about 0.33 at an axial strain of about 20%. Beyond the yield plateau the inelastic strain ratio for the 16 mm plate begins at values as high as 0.47, decreases at first rapidly to about 0.44 and then linearly to about 0.37 at an axial strain of about 15%.

Instantaneous values of the inelastic strain ratio can be obtained by using true strains rather than engineering strains to determine this ratio. From Figs. 4.5, 4.6, and 4.7, instantaneous strain ratios so obtained were found to be from 0.5% to 5.7% greater than the total inelastic strain ratio, increasing as the longitudinal strain increases.

4.2 Weld Tests

After plate specimen P6-1 was tested it was determined that copper from the copper backing strips had infiltrated the weld metal during welding. As the copper had appeared on the fracture surface it was considered responsible for crack initiation and subsequent fracture of the plate. Therefore, a non-metallic chemically neutral non-hygroscopic ceramic backing bar was selected for subsequent use. Small scale shielded metal arc welding tests were done to establish a welding procedure that, when used for the plate tests, would provide a favourable geometry and microstructure at the heavily stressed weld root. As well, the procedure should minimize the possibility of entrapment of slag and allow the root weld to be completed in one pass. Figure 4.8 illustrates the test set-up, fabrication and evaluation procedures. The various ceramic weld backing configurations assessed and other test parameters are given in Table 4.6 and 4.7. The 6 mm plate came from the ancillary material of specimens P6-1 and P6-2.

All welding was performed using a constant excitation of 21 Volts and 4 mm diameter type E48018 shielded metal arc electrodes meeting the requirements of AWS A5.1-81 (AWS, 1981). Stop and start locations were marked on the edges of the plates. As shown in Fig. 4.8, each test specimen was cut into 4 or more smaller pieces, the sides of which were ground smooth and polished for visual inspection.

Ceramic weld backing bar 3, even at start and stop locations, gave a smooth weld root face and almost always complete root penetration. By inclining the test set-up at an angle θ of 20° to the vertical as shown in Fig. 4.8 (b) the root pass was deposited most easily.

Some of the pieces were pried apart as shown in Fig. 4.8 (c) to evaluate the performance of the welds. The welds were very ductile. Failure occurred through the heat-affected zone initiating at the root face of the weld as shown in Fig. 4.8(c) but not before the plate had been bent through an angle of more than 15°.

4.3 Bending Tests

Plates of tests P6-2, P12 and P16 all failed when cracks developed through the thickness of the plate at the toe of the weld in the mid-length of a long side, even though ceramic backing bars with a rounded nose had been used to eliminate the possibility of copper contamination and to provide a favourable weld profile. It appeared that the tensile and flexural straining at this location combined with the strain concentration due to the change in geometry exceeded the considerable ductility of the heat-affected zone next to the toe of the weld as established in the weld tests. Of the three small scale restrained bending tests that were performed on specimens fabricated using the 12 mm plate steel, two simulated the conditions of edge fixity in the plate tests. Figure 4.9 shows these latter test specimens in the restraining frame positioned for welding. After welding, the run-off tabs were removed. The dimensions and instrumentation of the three test specimens are given in Fig. 4.10. Figure 4.11 shows a longitudinal section. The long direction of the specimens were both parallel to and perpendicular to the rolling direction of the parent plate with the latter modelling the condition on the long side of the plate tests.

Figures 4.11(a) and 4.11(b) show how specimens 1 and 2, and specimen 3, respectively, were loaded. For specimen 3 it is noted that no weld exists on the upper side of the specimen at the point where the bending and tensile strains are a maximum as is the case for specimens 1 and 2. Figure 4.12 is an isometric view of the restraining frame for testing specimen 3. The restraining frames were quite rigid relative to the test specimens and therefore provided rotational and translational restraint at the ends. All welding was done with type E48018 shielded metal arc electrodes as was the case for the root pass in plate tests P6-2, P12 and P16.

Load-displacement curves for the three tests are given in Fig. 4.13. The maximum load of 63.3 kN for specimen 1 with the rolling direction parallel to the span was 11% greater than that for specimen 2 with the rolling direction transverse to the span. The curves are otherwise similar. Longitudinal sections of specimens 1 and 2 at failure, given in Fig.'s 4.14 and 4.15, show that failure initiated with cracks starting at the weld toe and progressed through the thickness. For specimen 1 the crack deflected longitudinally in a manner similar to lamellar tearing.

Specimen 3 attained a maximum load of 121 kN, about twice that of specimens 1 and 2 and ruptured on the tension side underneath the load point as shown in Fig. 4.16. The mean strains of gauges mounted on the convex side of beam 3, immediately adjacent to the support where the maximum tensile strains occurred, at loads corresponding to the failure of specimens 1 and 2, was about 5.4% as compared to a fracture strain of the plates of about 31% on a 150 mm gauge length. Fracture of specimens 1 and 2 is therefore considered to have occurred as the result of pre-necking cracking in the heat-affected zone due to a loss in relative ductility and exacerbated by the strain concentration due to a change in cross section. Lay (1982) relates the drop in ductility there to the reduction in the amount of ductile ferrite present because the relatively rapid cooling rate after welding increases the perlite percentage. Matic and Jolles

(1987) reported a critical fracture strain of 7% at one location in the heat-affected zone of an HY-100 steel.

Table 4.1 Tensile Coupon Identification

	Coupon direction	
Parent plate	Plate rolling direction	
	Transverse	Parallel
P6-1	6T1-1[2]	6P6-1[1]
	6T2-1	6P7-1[2]
	6T3-1	6P8-1
	6T4-1[2]	6P9-1[1]
	6T5-1	6P10-1[1]
P6-2	6T1-2[1]	6P6-2
	6T2-2	6P8-2[2]
	6T3-2[2]	6P10-2
	6T4-2[1]	
P12	12T1[2]	12P6[1]
	12T2	12P7[2]
	12T3	12P8
	12T4[2]	12P9[1]
	12T5	12P10[1]
P16	16T1[2]	16P6[1]
	16T2	16P7[2]
	16T3	16P8
	16T4[2]	16P9[1]
	16T5	16P10[1]

Notes: [1] Poisson's ratio determined using Showa type N11-FA-5-120-11 strain gauges.

[2] Poisson's ratio determined using Micro-Measurements type EP-08-250BG-120 strain gauges.

Table 4.2 Tensile Coupon Test Results For Specimen P6-1 Steel Plate

Coupon number or statistical parameter	σ_Y (MPa)	E (MPa)	ε_Y ($\mu\varepsilon$)	ε_{st} ($\mu\varepsilon$)	ε_u ($\mu\varepsilon$)	σ_u (MPa)	ε_f ($\mu\varepsilon$)	ν
6T1-1	-	-	-	12900	193000	485.2	306000	0.294
6T2-1	295.0	202700	1460	17600	194000	478.5	291000	-
6T3-1	296.2	201300	1440	13400	195000	481.2	305000	-
6T4-1	296.2	208800	1420	16400	192000	467.6	292000	0.282
6T5-1	293.0	205700	1420	13200	182000	473.6	279000	-
Mean	294.4	204600	1440	14700	191000	477.2	295000	0.288
Coefficient of variation	0.0093	0.0141	0.0116	0.1462	0.0246	0.0128	0.0340	0.0208
6P6-1	293.1	211500	1390	15800	196000	477.8	296000	0.302
6P7-1	288.9	210000	1380	16400	193000	467.8	293000	0.290
6P8-1	290.0	200300	1450	14200	189000	477.7	296000	-
6P9-1	289.9	200000	1450	11800	191000	473.3	291000	0.288
6P10-1	267.9	207200	1290	14700	192000	475.2	298000	0.281
Mean	286.0	205800	1390	14600	192000	474.4	295000	0.290
Coefficient of variation	0.0320	0.0234	0.0422	0.1093	0.0121	0.0077	0.0084	0.0261

Table 4.3 Tensile Coupon Test Results For Specimen P6-2 Steel Plate

Coupon number or statistical parameter	σ_Y (MPa)	E (MPa)	ε_Y ($\mu\varepsilon$)	ε_{st} ($\mu\varepsilon$)	ε_u ($\mu\varepsilon$)	σ_u (MPa)	ε_f ($\mu\varepsilon$)	ν
6T1-2	286.3	208300	1370	21800	227000	453.1	313000	0.287
6T2-2	-	209300	-	-	-	-	-	0.279
6T3-2	295.2	209600	1410	23700	205000	455.9	320000	-
6T4-2	296.1	207300	1430	23400	213000	451.9	313000	0.281
Mean	292.5	208600	1400	23000	215000	453.4	315000	0.282
Coefficient of variation	0.0151	0.0043	0.0214	0.0214	0.0423	0.0037	0.0105	0.0121
6P6-2	296.1	207000	1430	23600	244000	453.2	347000	0.282
6P8-2	293.2	208100	1410	22300	253000	453.5	333000	0.278
6P10-2	286.5	208200	1380	23700	233000	453.6	347000	0.280
Mean	291.9	207800	1410	23200	243000	453.3	342000	0.280
Coefficient of variation	0.0188	0.0026	0.0148	0.0275	0.0337	0.0004	0.0193	0.0058

Table 4.4 Tensile Coupon Test Results For Specimen P12 Steel Plate

Coupon number or statistical parameter	σ_Y (MPa)	E (MPa)	ε_Y ($\mu\varepsilon$)	ε_{st} ($\mu\varepsilon$)	ε_u ($\mu\varepsilon$)	σ_u (MPa)	ε_f ($\mu\varepsilon$)	ν
12T1	316.7	208700	1520	17400	193000	520.8	253000	0.273
12T2	316.0	205100	1540	17100	184000	524.9	258000	-
12T3	317.0	204800	1550	17000	193000	530.7	269000	-
12T4	325.1	208600	1560	19600	189000	513.0	269000	0.276
12T5	320.0	205800	1550	16600	193000	519.6	267000	-
Mean	318.9	206100	1540	17500	190000	521.8	263000	0.274
Coefficient of variation	0.0105	0.0083	0.0088	0.0605	0.0187	0.0112	0.0105	0.0055
12P6	317.4	206100	1540	27300	186000	528.9	306000	0.283
12P7	324.9	210000	1550	20000	196000	519.7	299000	0.278
12P8	307.0	204600	1500	16800	179000	524.3	306000	-
12P9	326.0	203700	1600	20000	200000	526.1	300000	0.281
12P10	321.7	204100	1580	19200	190000	529.4	297000	0.284
Mean	319.4	205700	1550	20700	190000	525.7	302000	0.282
Coefficient of variation	0.0216	0.0112	0.0221	0.1701	0.0388	0.0067	0.0123	0.0083

Table 4.5 Tensile Coupon Test Results For Specimen P16 Steel Plate

Coupon number or statistical parameter	σ_Y (MPa)	E (MPa)	ε_Y ($\mu\varepsilon$)	ε_{st} ($\mu\varepsilon$)	ε_u ($\mu\varepsilon$)	σ_u (MPa)	ε_f ($\mu\varepsilon$)	ν
16T1	306.0	211300	1450	15500	173000	510.0	267000	0.280
16T2	308.1	201300	1530	14100	189000	513.2	276000	-
16T3	309.3	205100	1510	11700	191000	514.4	264000	-
16T4	305.2	210700	1450	15800	189000	508.2	276000	0.272
16T5	308.2	201900	1530	15700	177000	515.8	258000	-
Mean	307.4	206000	1490	14600	184000	512.3	268000	0.276
Coefficient of variation	0.0049	0.0206	0.0245	0.1069	0.0398	0.0055	0.0261	0.0145
16P6	307.8	206100	1490	12100	187000	516.0	313000	0.287
16P7	302.2	208100	1450	13100	198000	508.4	311000	0.277
16P8	304.7	200600	1520	15100	186000	513.3	314000	-
16P9	309.6	207300	1490	23300	198000	520.3	324000	0.285
16P10	305.1	201600	1510	13500	198000	514.5	318000	0.283
Mean	305.9	204700	1490	15400	193000	514.5	316000	0.283
Coefficient of variation	0.0084	0.0150	0.0161	0.2631	0.0292	0.0075	0.0146	0.0132

Table 4.6 Ceramic Weld Backing Configurations

Notes: Ceramic weld backing manufactured by :

1. 3M Canada Inc.
   Montreal, Quebec
2. Gullco Int. Ltd,
   Toronto, Ontario

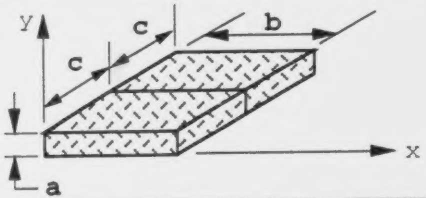

Configuration		1^1	2^2	3^1
Dimensions (mm)	**a**	6.4	3.2	6.4
	b	25.4	9.5	25.4
	c	25.4	19 - 25	25.4
Cross-section and notes		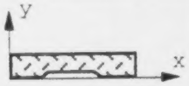 Sharp edges and smooth sides	 Rough, un-finished edges	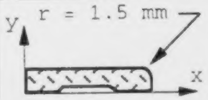 Sharp edges and smooth sides

Table 4.7 Weld Backing Tests

Configuration	Test	θ (degrees)	DC (Amps)	Estimated speed (mm/min.)
1	1	0	170	75
	2	0	180	105
	3	20	190	90
2	1	0	170	110
	2	15	170	102
3	1	0	170	64
	2	15	190	93
	3	20	170	58
	4	30	190	62

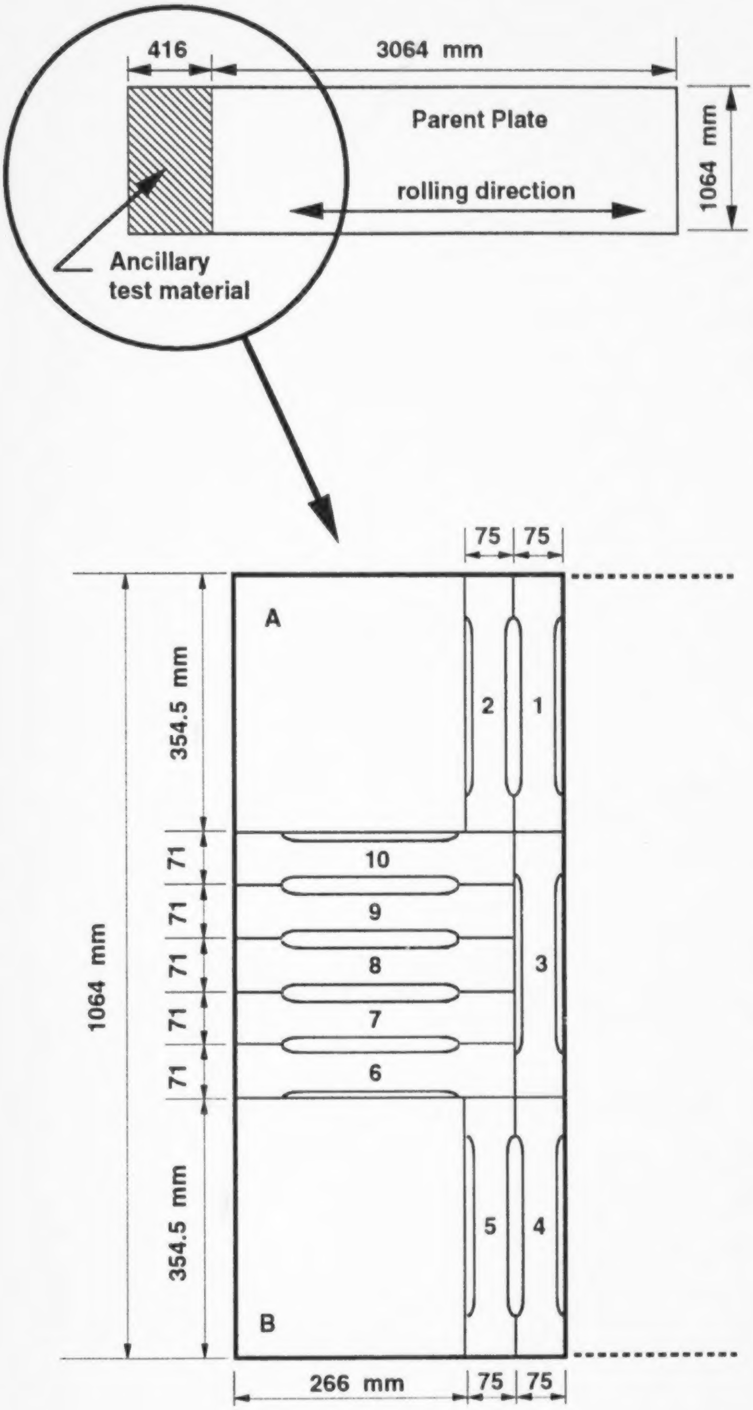
416
3064 mm
Parent Plate
rolling direction
1064 mm
Ancillary test material
75
75
A
354.5 mm
2
1
10
9
8
7
6
3
71
71
71
71
71
1064 mm
354.5 mm
5
4
B
266 mm
75
75

Figure 4.1 Location and identification of tensile coupons

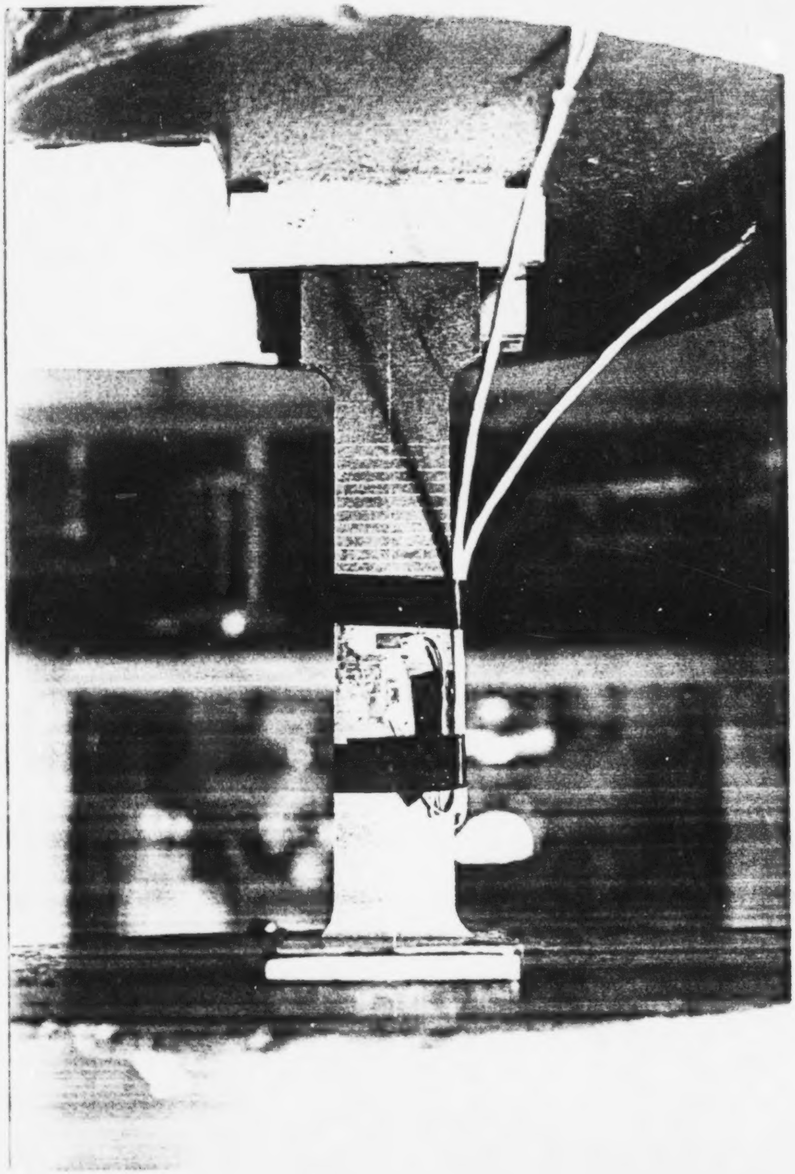

Figure 4.2 Tension coupon in Baldwin testing machine

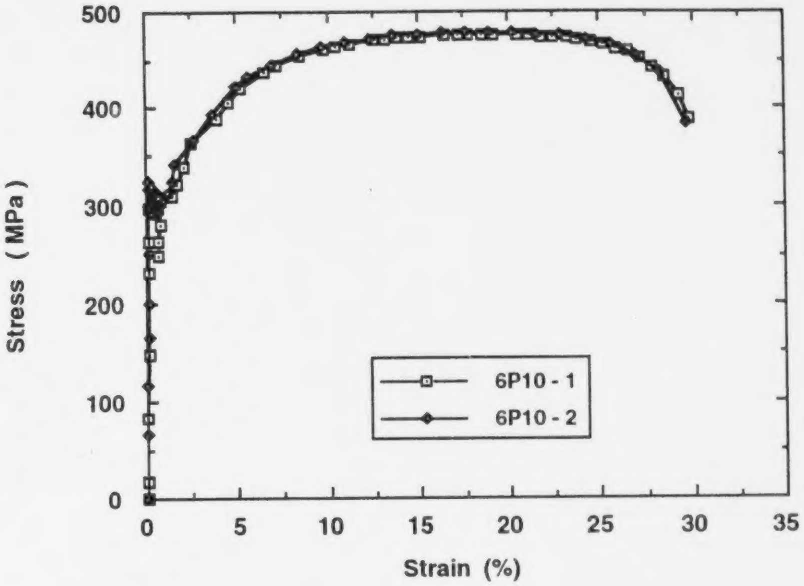

Figure 4.3 Stress-strain curves for tension coupons 6P10-1 and 6P10-2

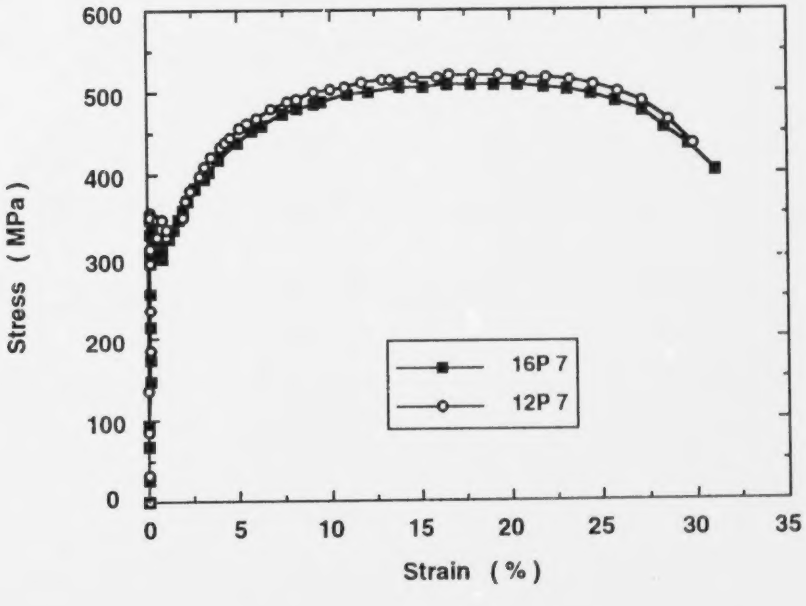

Figure 4.4 Stress-strain curves for tension coupons 12P7 and 16P7

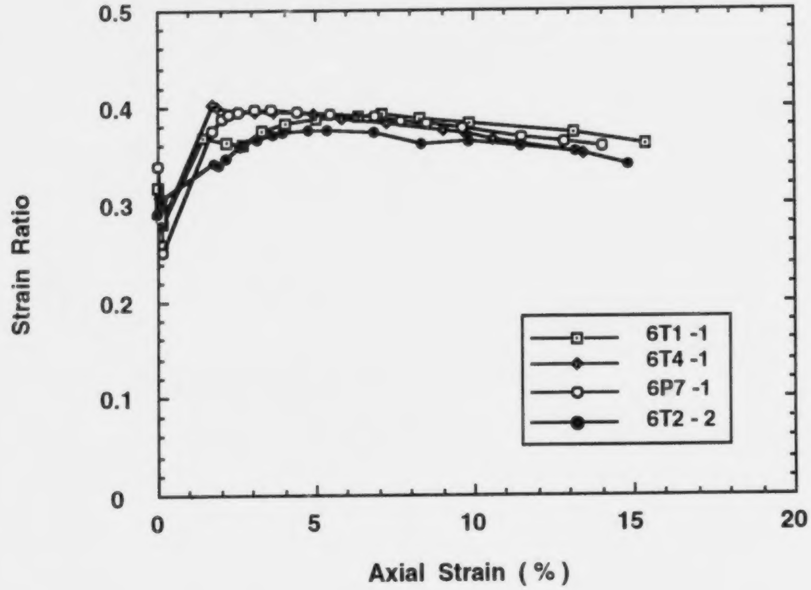

Figure 4.5 Strain ratio versus axial strain for several 6 mm tension coupons

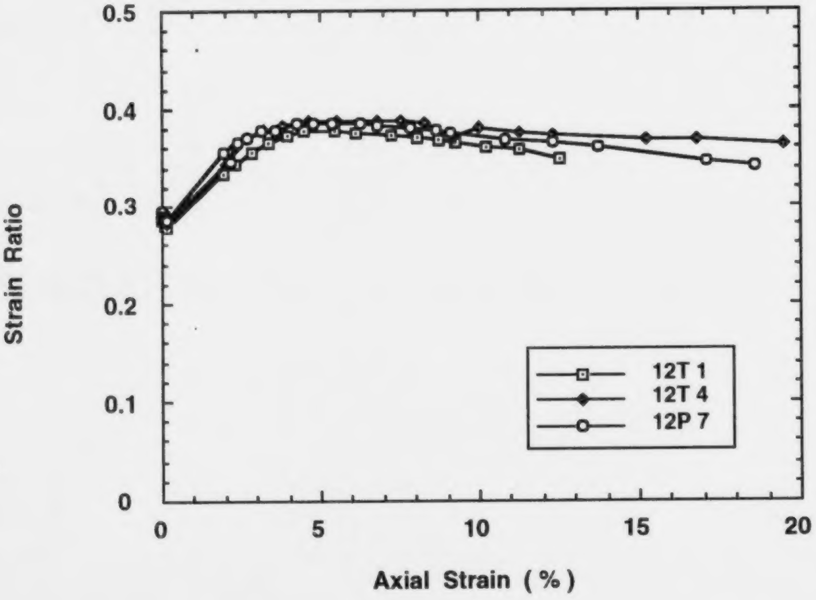

Figure 4.6 Strain ratio versus axial strain for several 12 mm tension coupons

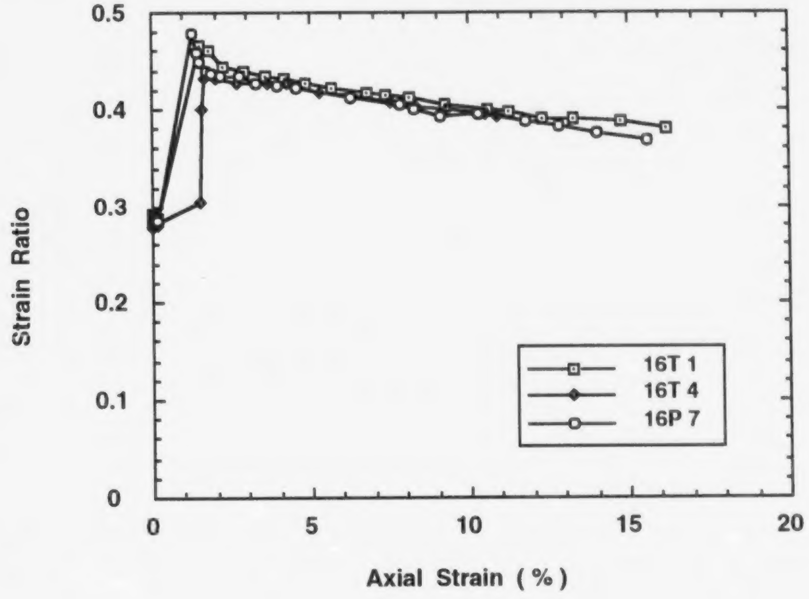

Figure 4.7 Strain ratio versus axial strain for several 16 mm tension coupons

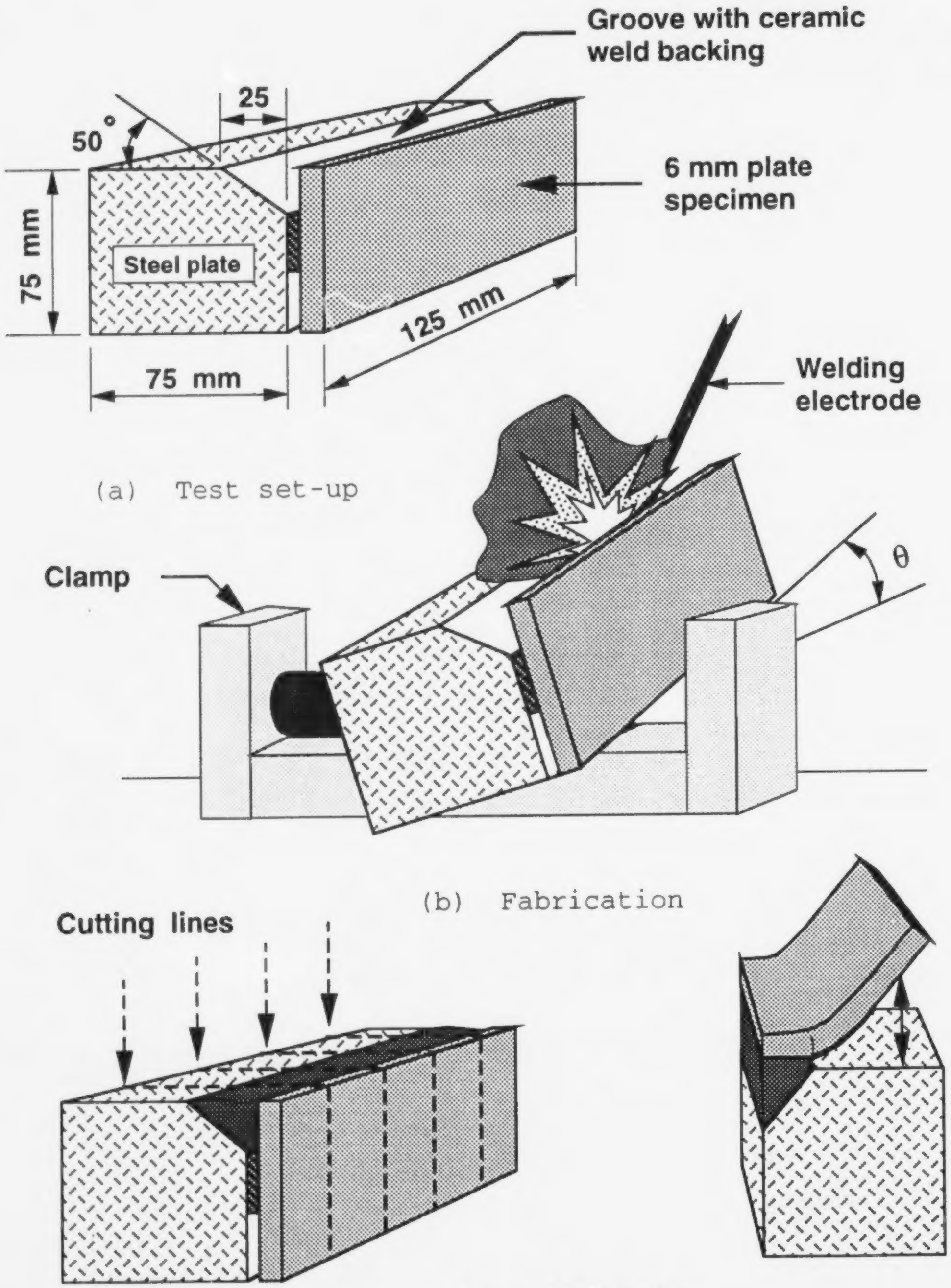
Groove with ceramic weld backing
25
50 °
6 mm plate specimen
75 mm
Steel plate
125 mm
75 mm
Welding electrode
Clamp
θ
Cutting lines

(a) Test set-up

(b) Fabrication

(c) Evaluation

Fig. 4.8 Weld test set-up, fabrication and evaluation

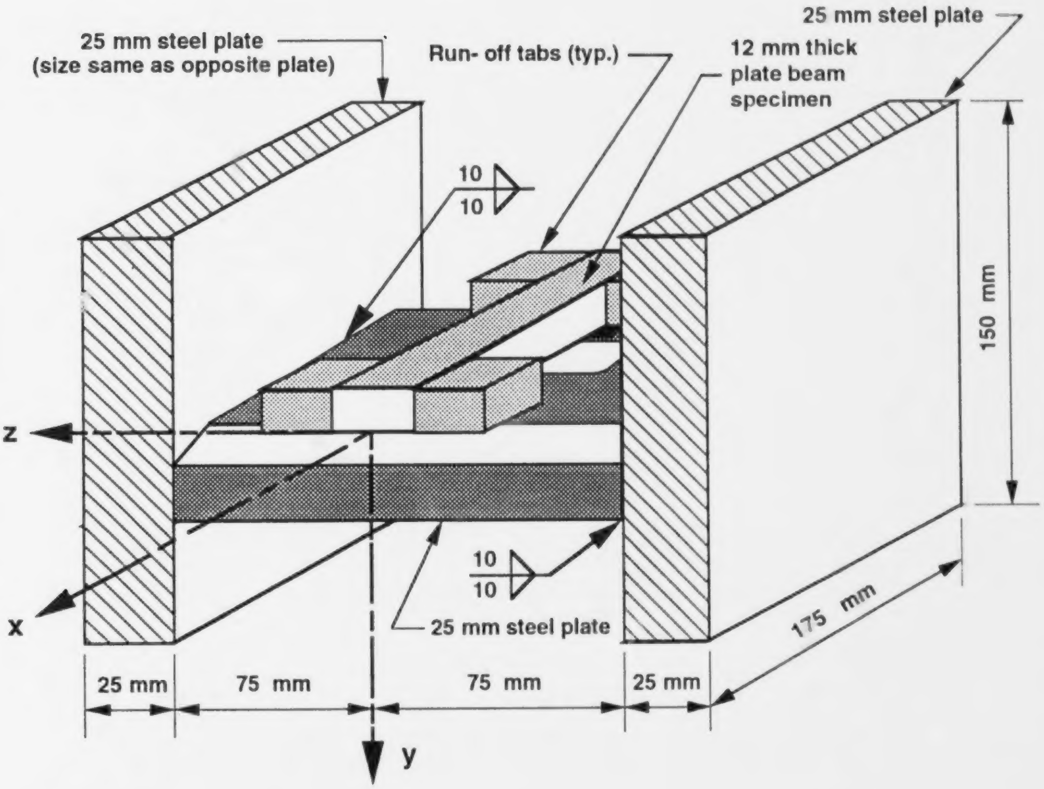
25 mm steel plate
(size same as opposite plate)
Run- off tabs (typ.)
12 mm thick plate beam specimen
25 mm steel plate
10
10
150 mm
z
x
10
10
25 mm steel plate
175 mm
25 mm
75 mm
75 mm
25 mm
y

Figure 4.9 Test frame for bending specimens 1 and 2

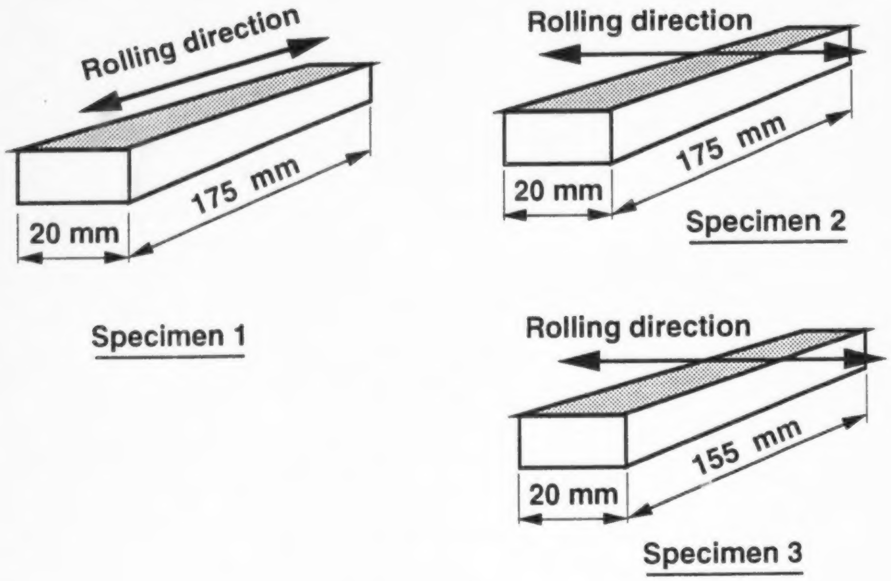
Rolling direction
175 mm
20 mm
Specimen 1
Rolling direction
175 mm
20 mm
Specimen 2
Rolling direction
155 mm
20 mm
Specimen 3

(a) Test specimens

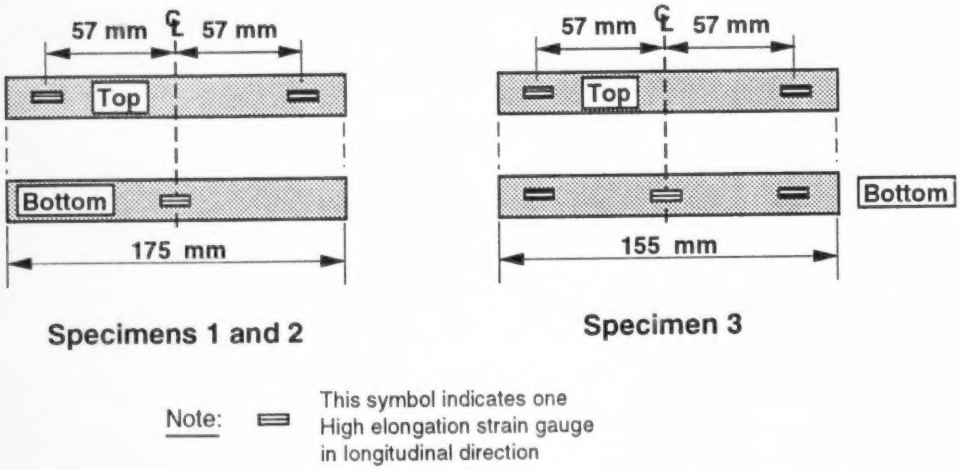
57 mm
℄
57 mm
Top
Bottom
175 mm
Specimens 1 and 2
57 mm
℄
57 mm
Top
Bottom
155 mm
Specimen 3
Note:
This symbol indicates one
High elongation strain gauge
in longitudinal direction

(b) Instrumentation

Figure 4.10 Beam test specimens and instrumentation

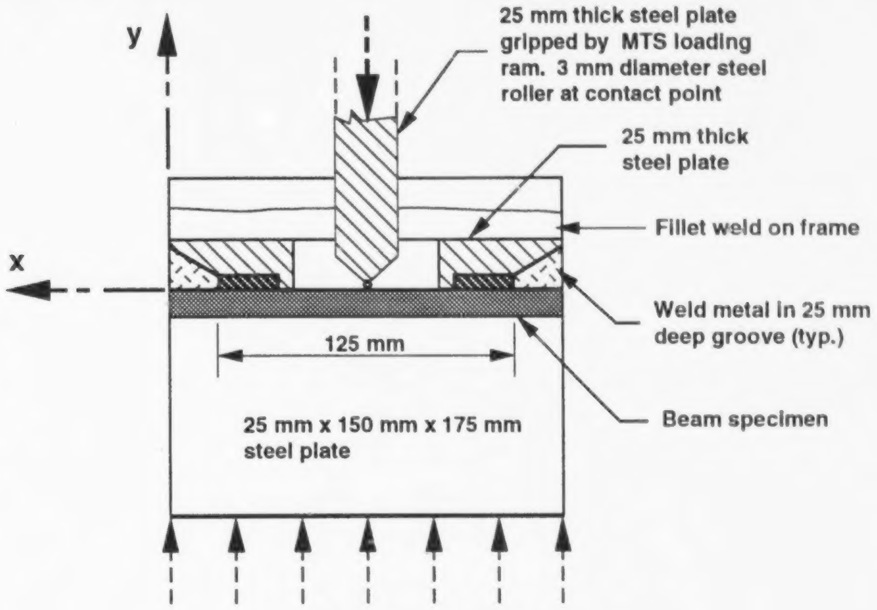
y
25 mm thick steel plate gripped by MTS loading ram. 3 mm diameter steel roller at contact point
25 mm thick steel plate
Fillet weld on frame
x
Weld metal in 25 mm deep groove (typ.)
125 mm
Beam specimen
25 mm x 150 mm x 175 mm steel plate

(a) Specimens 1 and 2

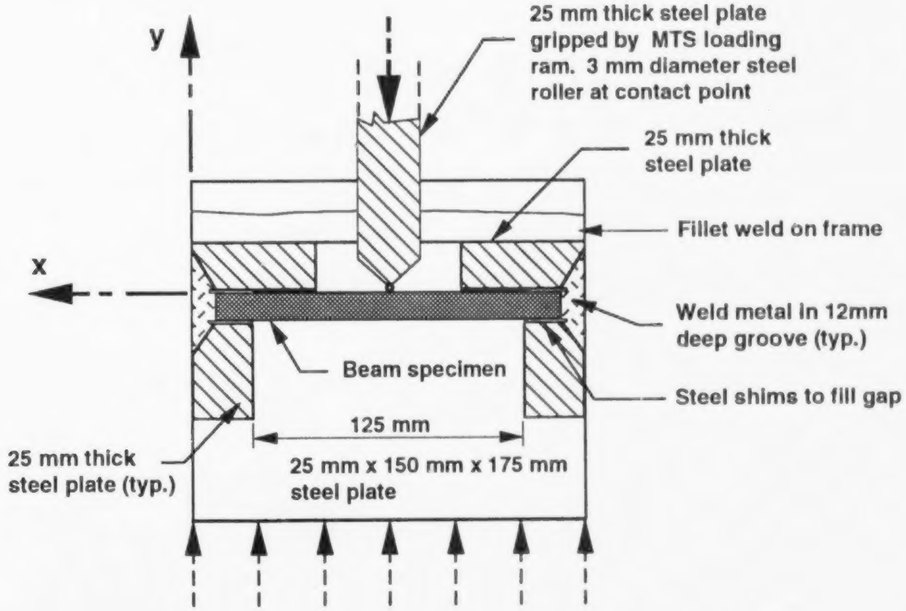
y
25 mm thick steel plate gripped by MTS loading ram. 3 mm diameter steel roller at contact point
25 mm thick steel plate
Fillet weld on frame
x
Weld metal in 12mm deep groove (typ.)
Beam specimen
Steel shims to fill gap
125 mm
25 mm thick steel plate (typ.)
25 mm x 150 mm x 175 mm steel plate

(b) Specimen 3

Figure 4.11 Sections along x-axis through test frames with loading method

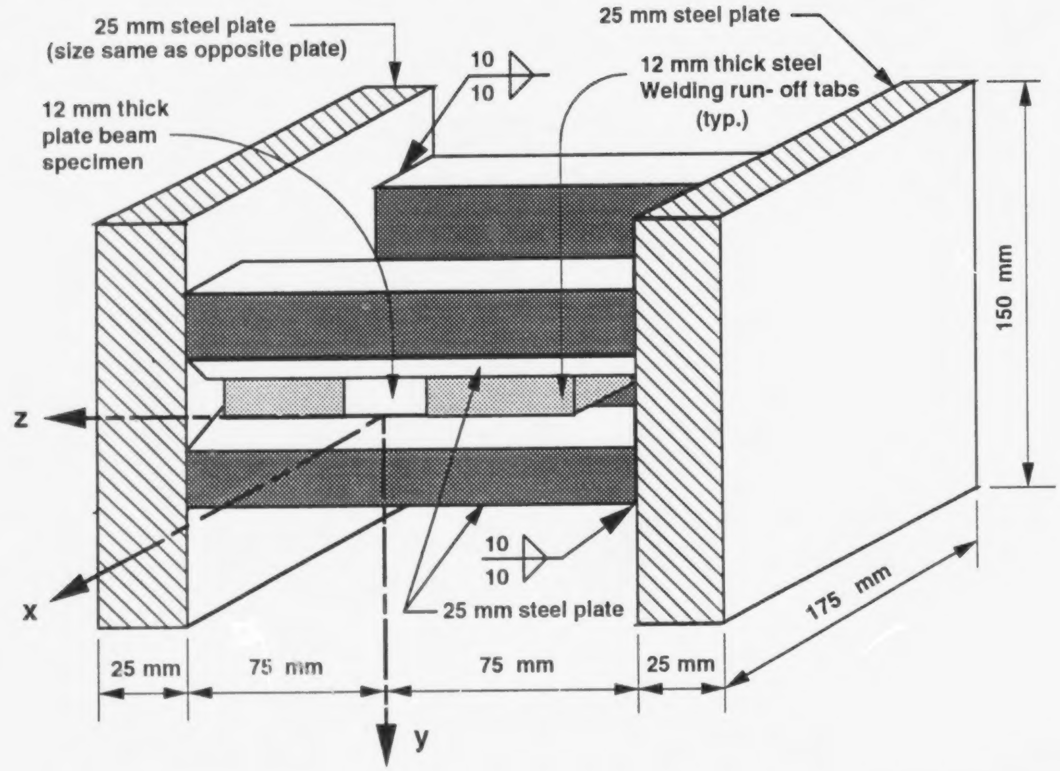
25 mm steel plate
(size same as opposite plate)
12 mm thick
plate beam
specimen
10
10
12 mm thick steel
Welding run- off tabs
(typ.)
25 mm steel plate
150 mm
z
x
10
10
25 mm steel plate
175 mm
25 mm
75 mm
75 mm
25 mm
y

Figure 4.12 Test frame for bending specimen 3

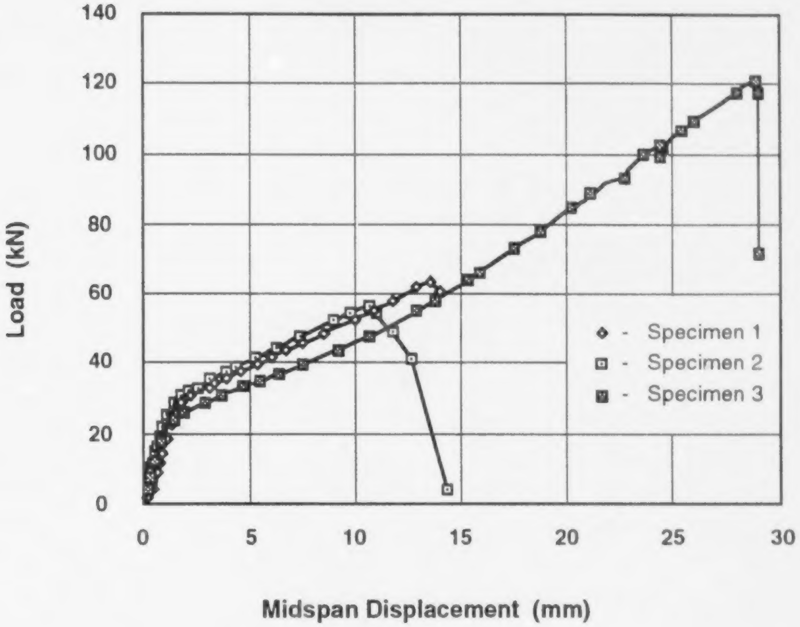

Figure 4.13 Load-displacement diagrams for bending tests 1, 2 and 3

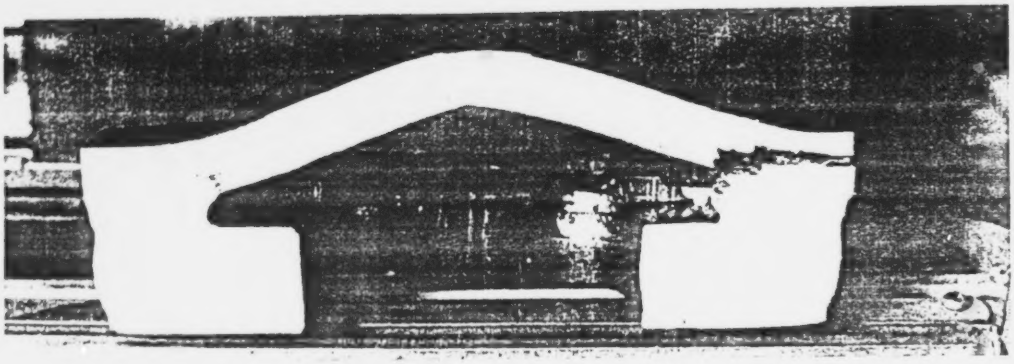

Figure 4.14 Longitudinal section of bending specimen 1 after failure

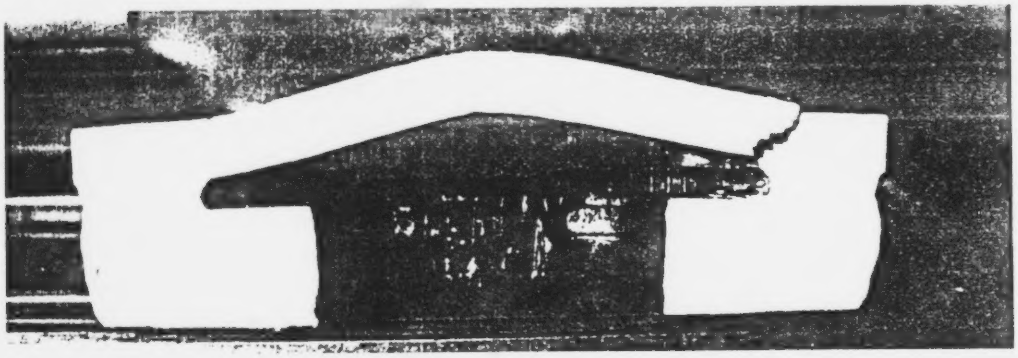

Figure 4.15 Longitudinal section of bending specimen 2 after failure

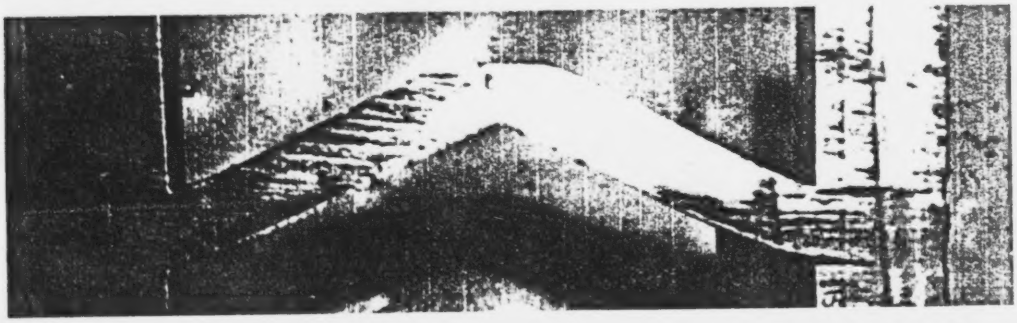

Figure 4.16 Longitudinal section of bending specimen 3 after failure

5. TEST RESULTS AND OVERALL BEHAVIOUR

5.1 General

This Chapter documents the test results and overall behaviour. Loads, deflections, strains, and failure modes and failure loads are presented. Comparisons between results of the ADINA finite element analyses (presented in Chapter 6) and the test results reported here are given in Chapter 7.

In Fig. 5.1 are plotted the load-maximum deflection curves for the four plate tests. The load is expressed in terms of the applied pressure, q, and the maximum deflection, W_m, is that at the centre of the plate. The load at failure, as can be expected, increases with increasing plate thickness and the deflections decrease. The data of Fig. 5.1 have been nondimensionalized in Fig. 5.2 by dividing the measured deflections by the measured plate thicknesses and by dividing the test pressures by the uniform transverse load per unit area, q_c, corresponding to the collapse load of an infinitely long plate (zero aspect ratio) with no membrane action (i.e., a three hinge mechanism).

In Table 5.1 the failure data for the 4 tests are summarized. The maximum pressures reached just prior to failure and the maximum deflections are given both in absolute and normalized values. Figure 5.3 of specimen P6-1, taken when the applied pressure was equal to 1000 kPa, shows the pillow-like shape of the plate surface that develops during loading.

In all tests, just prior to failure the applied pressure decreases slightly. This is attributed to the deformation increasing more rapidly than could be accommodated by the ability of the pumping system to supply oil to maintain the pressure. Tearing of the steel, initiating on the loaded surface, occurred at mid-length of one of the long edges. When the plates deform into the pillow-like shape, larger tensile strains develop at this location due to a combination of the membrane stresses and bending at the edge. Figure 5.4 shows schematically the development of the tensile failure. Failure occurred when the tensile straining capacity of the HAZ at the toe of the weld was exhausted.

At failure the plates ripped open and oil spurted out. Figures 5.5 through 5.8 show the fracture regions for the four plate tests. The lengths of the fracture surface for the 4 tests are given in Table 5.1. Samples of the plate material in the fracture region were taken, polished and acid-etched for microscopic examination. In specimen P6-1 microcracks in the weld metal with infiltrations of copper from the weld backing were visible. These initiated the development of the rupture through the plate thickness that led to failure. The crack development, shown in Figs. 5.9 and 5.10 perpendicular to the plate surface, appears to have travelled initially through the coarse grains of the HAZ.

For the 3 other tests, micrographs of the cross-section through the fracture plane indicate that tearing resulted when the strain capacity of the steel in the weld zone was reached as discussed in section 5.3.

Figure 5.1 shows that the load-deflection curves for the two 6 mm plates correspond closely. Although the maximum load for P6-2 is about 1.22 times that of P6-1, the ratio is only 1.03 when computed on a nondimensional basis. Specimen P6-2 did however develop about 1.14 times the maximum deflection, indicative of greater ductility. Thus, changing the welding procedure apparently increased the ductility but not the strength.

5.2 Deflections

5.2.1 Deflections Across The Width At Mid-length

Shown in Figs. 5.11, 5.12, 5.13 and 5.14 are the measured deflections across the width and at the mid-length for 4 values of the nondimensional pressure for tests P6-1, P6-2, P12 and P16, respectively. The deflections, determined from the finite element analysis for tests P6-2 and P12, at the indicated load levels, are also given. The first LVDT was located at 10 mm from the outside edge, directly above the weld fastening the test plate to the reaction plate, and therefore did not deflect appreciably. The lowest value of normalized pressure for which the deflection curves are drawn corresponds to a value of q/q_c of about 1 while the highest curve is at or near the failure load. The second level of q/q_c corresponds to the case when full yielding is assumed to occur along the long edges of the plate in tension. At this load if it is assumed that the stress-strain curve is elasto-plastic, tensile straining would obliterate the plastic hinge along the edge. The third curve is an intermediate one. The upper 2 curves in the figures, given that tensile yielding has occurred through the thickness near the edges, must represent cases where the load is being carried by inelastic tensile membrane action.

Figures 5.11 through 5.14 also show that double curvature persists and increases with increasing load levels as the points of zero curvature move towards the plate edges. This behaviour is most clearly evident for tests P12 and P16. The results of the ADINA finite element analyses as presented and discussed in Chapter 6 are also plotted on Figs. 5.12 and 5.13.

The overall deflection behaviour is generally consistent with the hypothesis that, as load is increased, the bending resistance of the plate at its fixed edges gradually reduces. Full yielding of the cross-section due to tensile straining develops and progresses from the edges towards the centre. The plate deformations are discussed further in Chapter 7 where comparisons are made with the postulated behaviour and with the results of finite element analyses.

5.2.2 Continuous Deflection Measurements

Typical deflection plots for one-half of the plate width, obtained using the surface level indicator (SLI), are given in Figs. 5.15, 5.16, 5.17 and 5.18. Deflections are symmetric about the mid-width. Each of the four figures give four curves that are identified by the distance measured along the length from one end of the plate. Figures 5.15 and 5.17 correspond closely to the load at which full tensile yielding along the long edges was anticipated and, as the curves of Figures 5.16 and 5.18 were determined after the the maximum load had been reached, some rebound due to the elastic recovery had occurred. Figure 5.19 shows the deflections across one half of the plate length at mid-width of specimen P6-2 and P16 after failure.

5.3 Strain Measurements

As the strains recorded here, with one exception, do not exceed 25000 $\mu\varepsilon$ no corrections have been made for nonlinearities that result due to transverse strains on the gauges or for excessively large strains. As well, no corrections have been made for in-plane shear stresses nor, in the case of gauges mounted on the loaded face of the test plate, for any effects of the fluid pressure on the gauges themselves.

5.3.1 Strains Across The Width At Mid-Length

In Figs. 5.20 through 5.23 the steel strains on a line across the width of the plate at mid-length are plotted for a load q/q_c of about 1.0 for tests P6-1, P6-2, P12 and P16, respectively. Strains obtained from the ADINA finite element analysis for specimens P6-2 and P12 are also shown on Figs. 5.21 and 5.22, respectively. Comparisons between the ADINA strains and the measured strains are made in Chapter 7. The strains indicate that the plate is bent concave upward at the edge and concave downward across the greater portion of the total width. The point of zero curvature lies about 160 mm - 200 mm from the toe of the weld for the 6 mm plates and at about 220 mm away for the thicker plates. This indicates that the bending action is more substantial for the thicker plates. The mean strain on the two surfaces is indicative of axial straining and for plates subjected to transverse fluid pressure with no bending resistance would be expected to be constant. For the 6 mm plates the axial strain is relatively constant across the width indicating that a tensile (membrane) force equivalent to a stress of 40 to 60 MPa exists in the plate. For the thicker plates with substantial bending resistance the average strain is positive near the edges and approaches zero at mid-width. Thus for these plates the tensile force has not developed substantially at this load level. The average positive tensile strain near the edge (above that in the remainder of the plate) indicates that the tensile strains on the loaded face exceed the corresponding compressive strains on the free face.

Figures 5.24 through 5.27 for tests P6-1, P6-2, P12 and P16, respectively, are plotted for the value of q/q_c at failure. On Figs. 5.25 and 5.26, strains based on the ADINA analysis are also plotted. Comparisons between the ADINA strains and the measured strains are made in Chapter 7. The figures show that the membrane action (average tensile strain) is a maximum for the thinner plates and is inelastic with strains of 12000 $\mu\varepsilon$ to 15000 $\mu\varepsilon$ that are quite uniform across the width with the exception of edge disturbances. For tests P12 and P16, greater variability of strains is exhibited but even here the average strains are in the inelastic range. Thus for all tests at maximum load, inelastic membrane action has developed, very strongly for the 6 mm plates and to a lesser extent for the thicker plates.

Figures 5.28 to 5.31 are drawn for the case when membrane action corresponding to tensile yielding of that portion of the plate between points of zero curvature, relatively near to the plate edges, has developed substantially, and in particular, in the thinner plates. ADINA strains are also plotted on Figs. 5.29 and 5.30. Comparisons between the ADINA strains and the measured strains are made in Chapter 7. From Fig. 5.28 for test P6-1 the average strain is remarkably close to the uniaxial tensile yield strain whereas from Fig. 5.29 for test P6-2, the average strain while sensibly constant across the width except for edge disturbances, is at about 80% of the uniaxial yield strain. For tests P12 and P16 in Figs. 5.30 and 5.31 respectively the average tensile strain across the width is only about 50% of the uniaxial yield strain.

Figures 5.32 through 5.35, drawn for load levels intermediate between those corresponding to full yielding at the edge and failure and therefore at load levels where inelastic membrane action would be expected to exist, do in fact indicate that this is the case. For tests P6-2 and P12 (Figs. 5.33 and 5.34) strains obtained by the ADINA analyses are also shown. Comparisons between the ADINA strains and the measured strains are made in Chapter 7. The axial and bending strains are intermediate between those of the corresponding two previous sets of figures. In the tests on thin (6 mm) plates the average tensile strains are greater within about 200 mm of the edge than elsewhere while for the 12 mm and 16 mm plates this was not found to be the case. In summary, the strains show that the transverse load is initially principally carried by flexural action with some membrane action that increases as the plate thickness decreases. At higher loads the flexural contribution is reduced or even nearly obliterated and the load is carried by inelastic membrane action. The transition to the latter behaviour occurs earlier for the thinner specimens.

Figures 5.36 through 5.39 give, for tests P6-1, P6-2, P12 and P16 respectively, distributions of the average strains for 4 load levels measured in the longitudinal direction of the plate, across the width at the mid-length.

These strains are therefore orthogonal to the strains presented in Figs. 5.20 to 5.35. None of the strains in Figs. 5.36 through 5.39 exceed the yield strain indicating that the longitudinal behaviour of the plates at mid-length remained in the elastic region. At the edge of the plates the longitudinal strains appear to approach zero, indicative of a plane strain condition there. This condition of plane strain is lost as one moves towards the mid-width of the plate.

5.4 Behaviour Near the Corners

Figure 5.40 (a) shows the deflection of plate P6-2 for 4 different load levels plotted along a 45 ° line from the corner extending to the mid-line of symmetry. The common characteristic of all curves is that there is a significant flat portion with little deflections near the corner. In Fig. 5.40 (b) strains at the same load levels are plotted. At about 57 mm from the corner the strains indicate significant bending of the plate with the loaded surface in tension and with the free surface in compression. The average strain indicates a small net tension on the section. The strains at 384 and 754 mm from the corner are for gauges mounted longitudinally and transversely. Because the corresponding strains are essentially equal in the two perpendicular directions (not shown on this figure) and at any load level, they show that the transverse load is being transferred equally in both directions. The difference between the strains of the top and bottom of the plate are related to the curvature of the membrane with the free surface strains consistently greater than the loaded surface strains.

5.5 Reaction Plate Behaviour

Reaction plate strains obtained from two strain gauges, one mounted longitudinally and the other transversely at the midpoint of the free face of the reaction plate, are shown in Fig. 5.41 for test P16 in which the reaction plate was subjected to the greatest pressure. The variation of strains in the transverse direction is essentially linear and the maximum value does not exceed about 1/3 the uniaxial yield strain of the plate. The longitudinal strains are about 0.29 times the transverse strains, ie. in the ratio of Poisson's ratio. The strains, on unloading, return to zero also indicating elastic behaviour of the reaction plate.

Table 5.1 Maximum Pressures, Deflections And Measured Fracture Lengths

Test Specimen	q_c (kPa)	Maximum Test Pressure, q_m (kPa)	Maximum Test Deflection, W_m (mm)	Normalized Pressure, q_m/q_c	Fracture Length (mm)
P6-1	66	1152	71.4	17.4	680
P6-2	79	1411	85.4	17.9	610
P12	289	1909	53.6	6.6	550
P16	433	2383	53.2	5.5	540

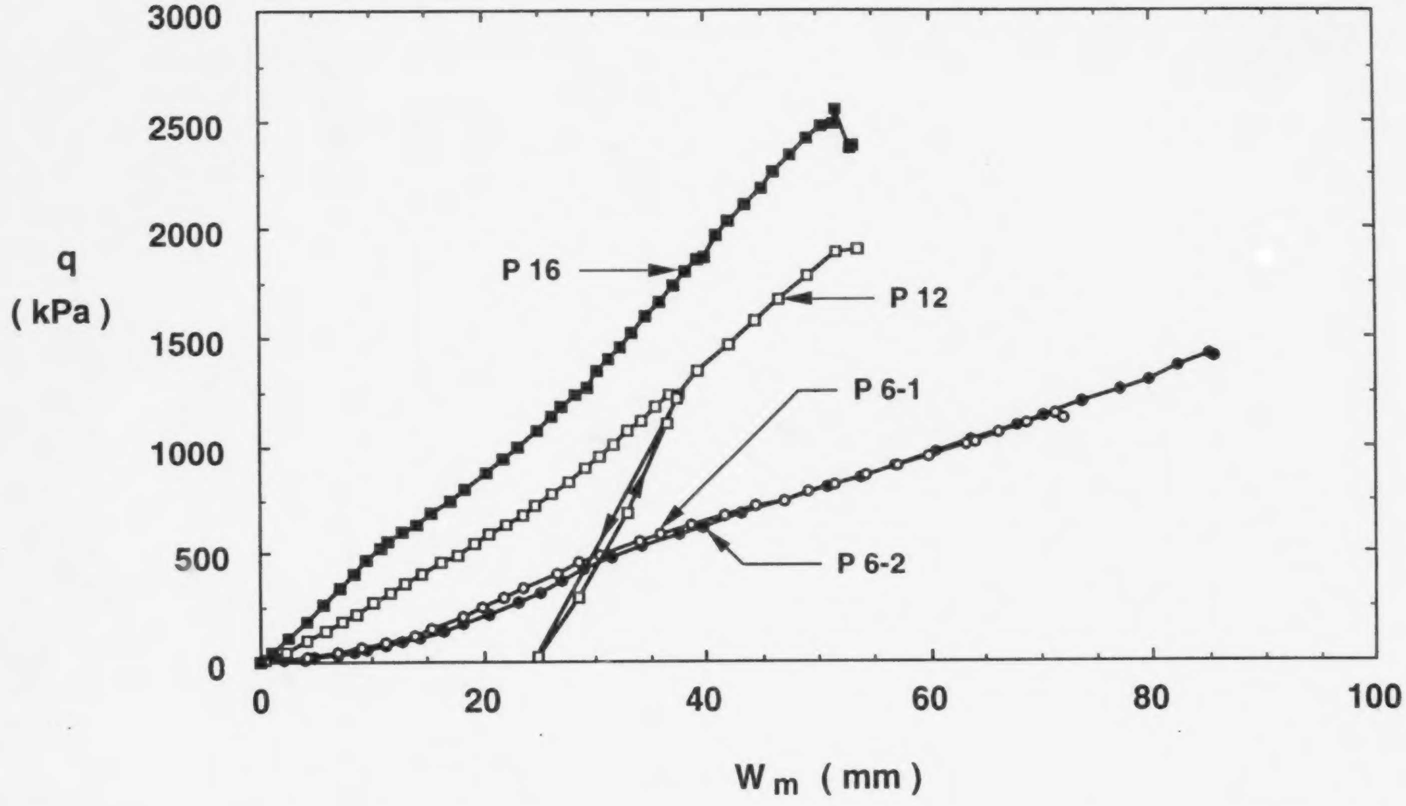

Figure 5.1 Load-deflection curves

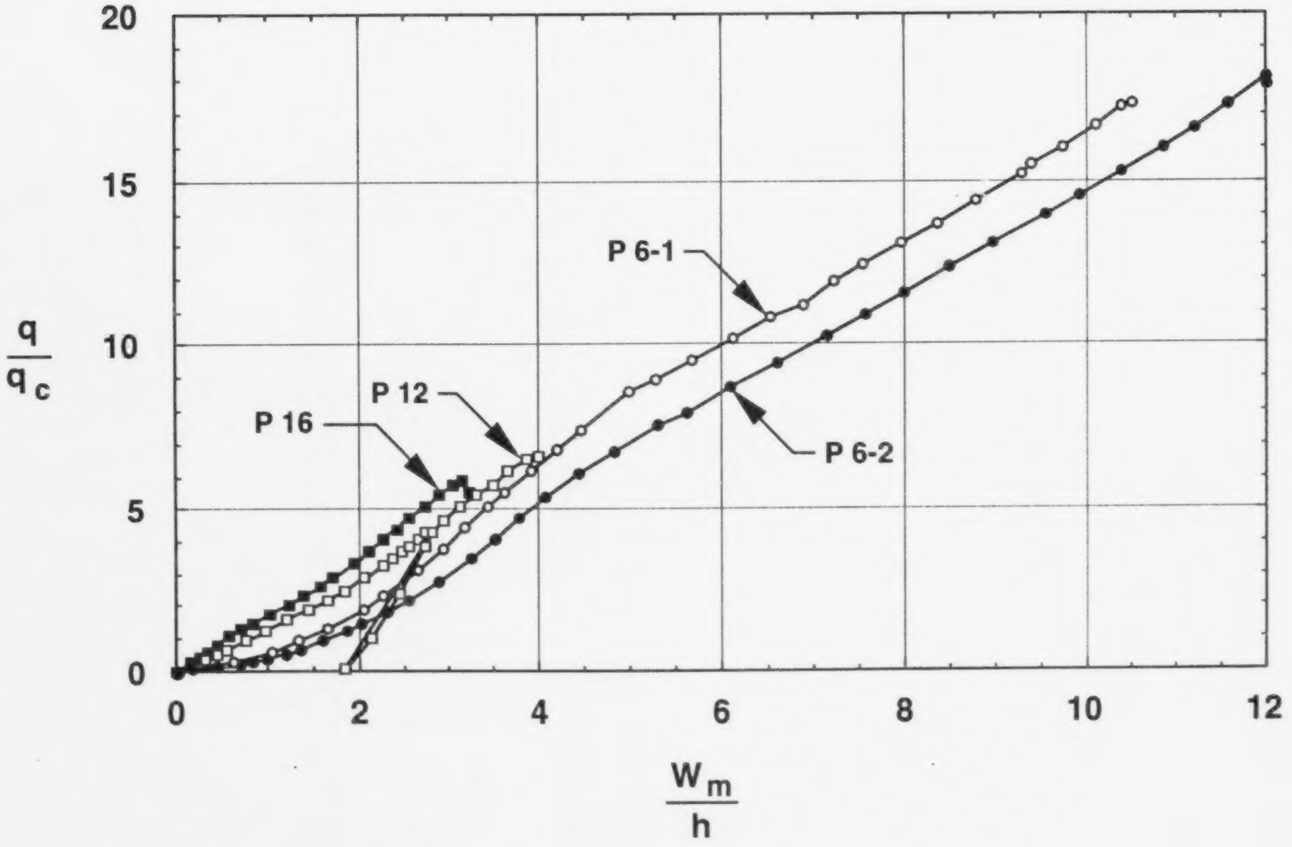

Figure 5.2 Nondimensional load-deflection curves

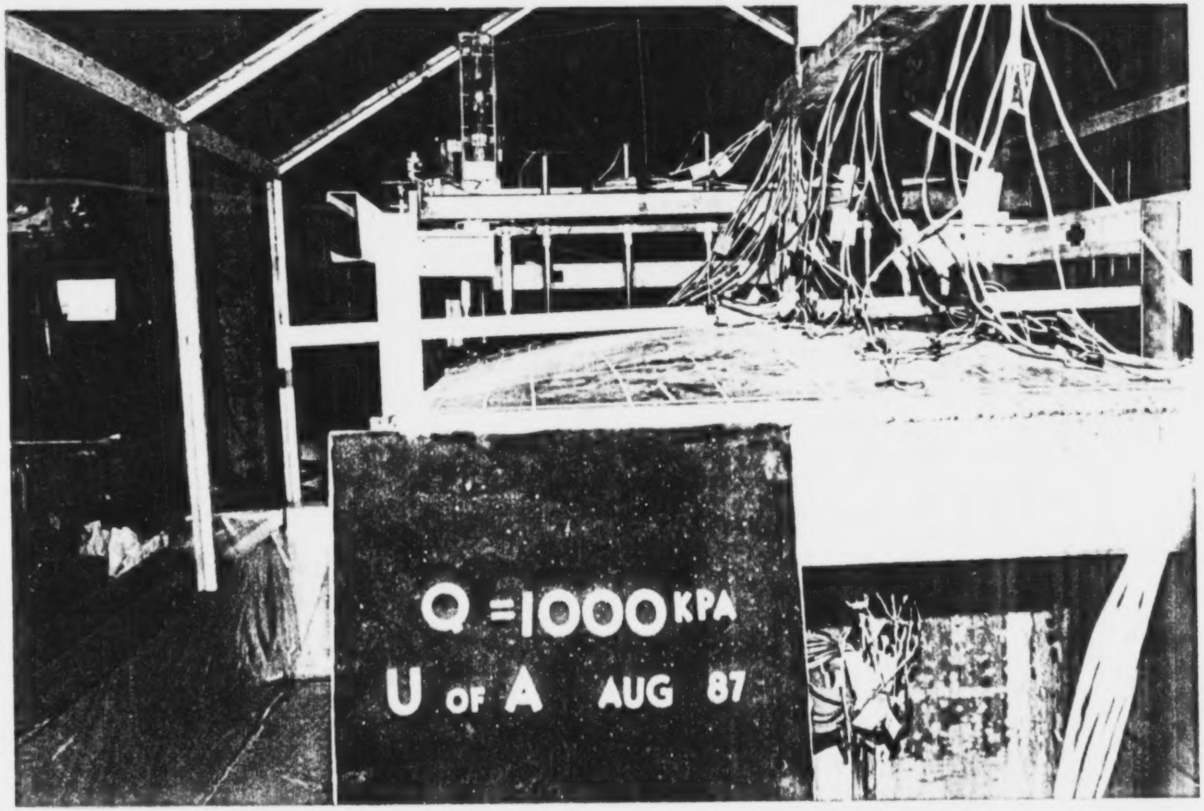
Q =1000 KPA
U OF A AUG 87

Figure 5.3 Specimen P6-1 during testing

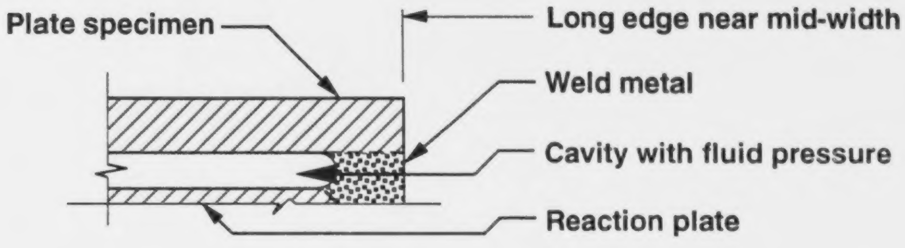
Plate specimen
Long edge near mid-width
Weld metal
Cavity with fluid pressure
Reaction plate

(a) Undeformed plate, prior to testing.

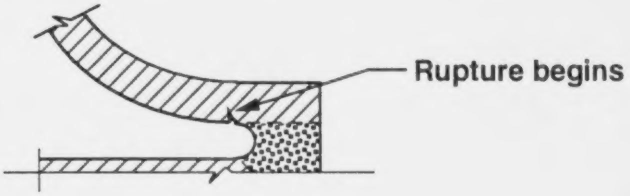
Rupture begins

(b) Rupture initiates at location of fixity near toe of weld.

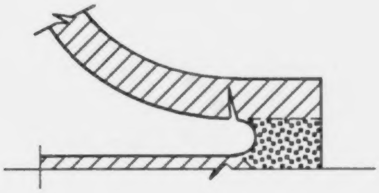

(c) Rupture surface propogates through plate thickness.

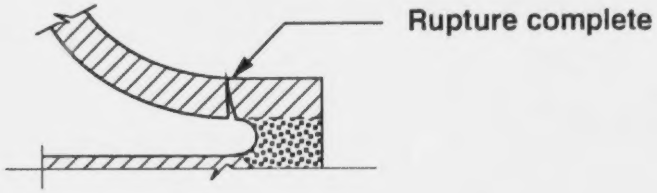
Rupture complete

(d) Rupture is complete. Plate fails by tearing along edge and oil under pressure escapes.

Figure 5.4 Rupture at edge prior to failure of plate specimens

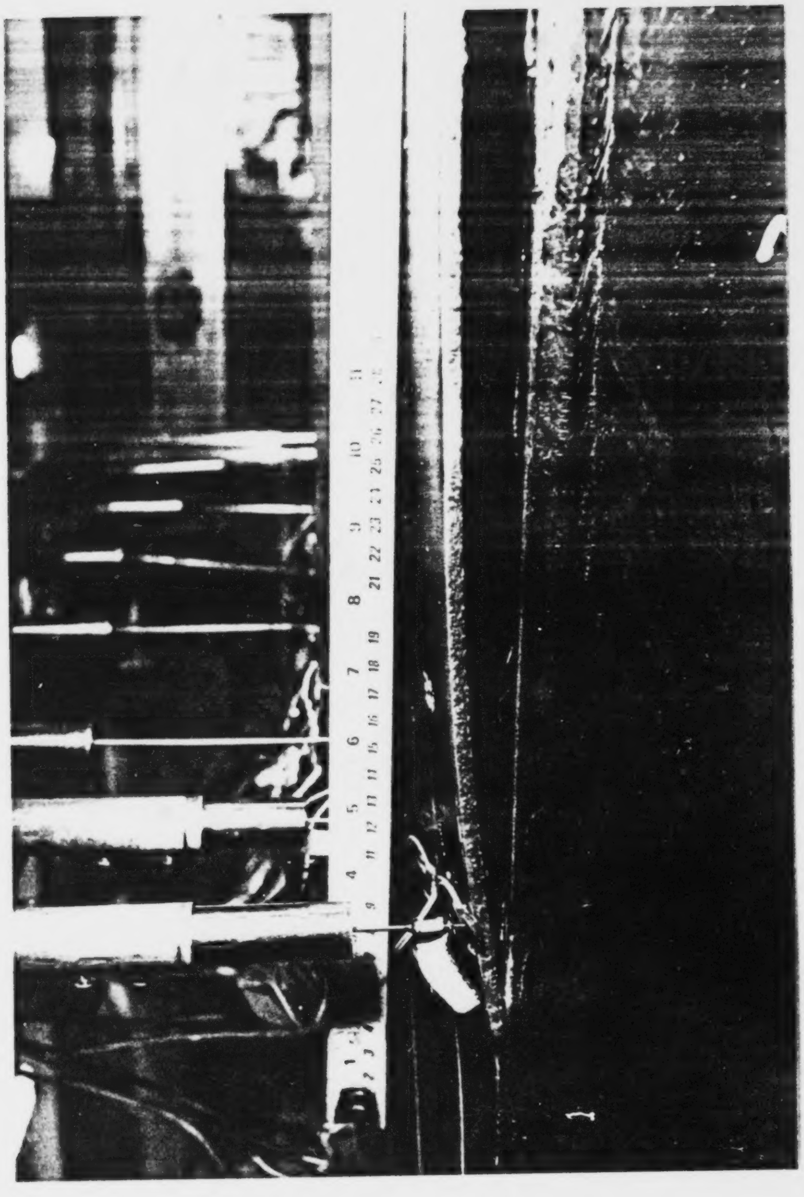

Figure 5.5 Fracture region of specimen P6-1

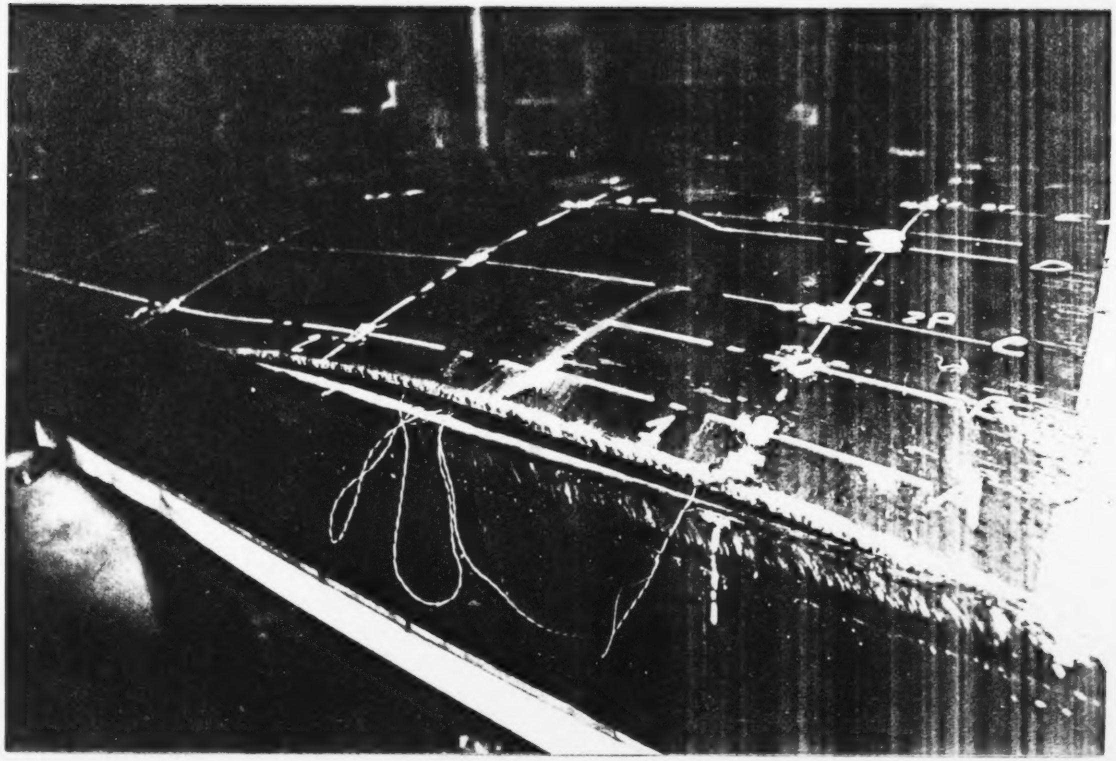

Figure 5.6 Fracture region of specimen P6-2

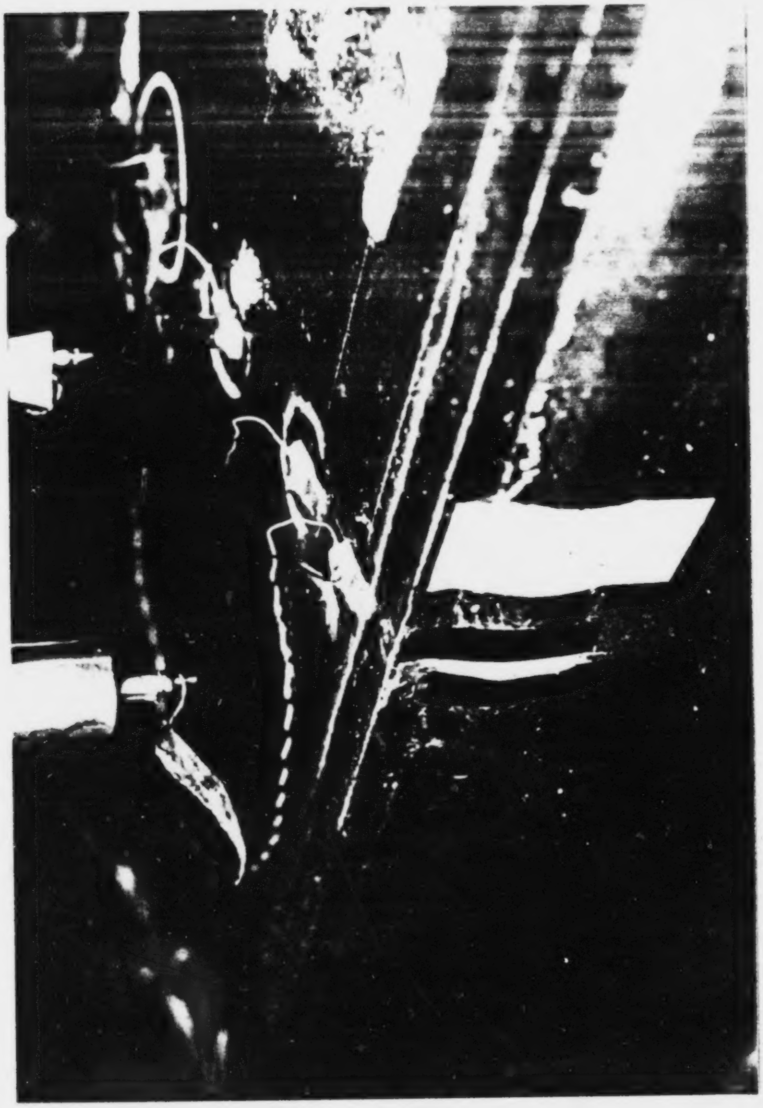

Figure 5.7 Fracture region of specimen P12

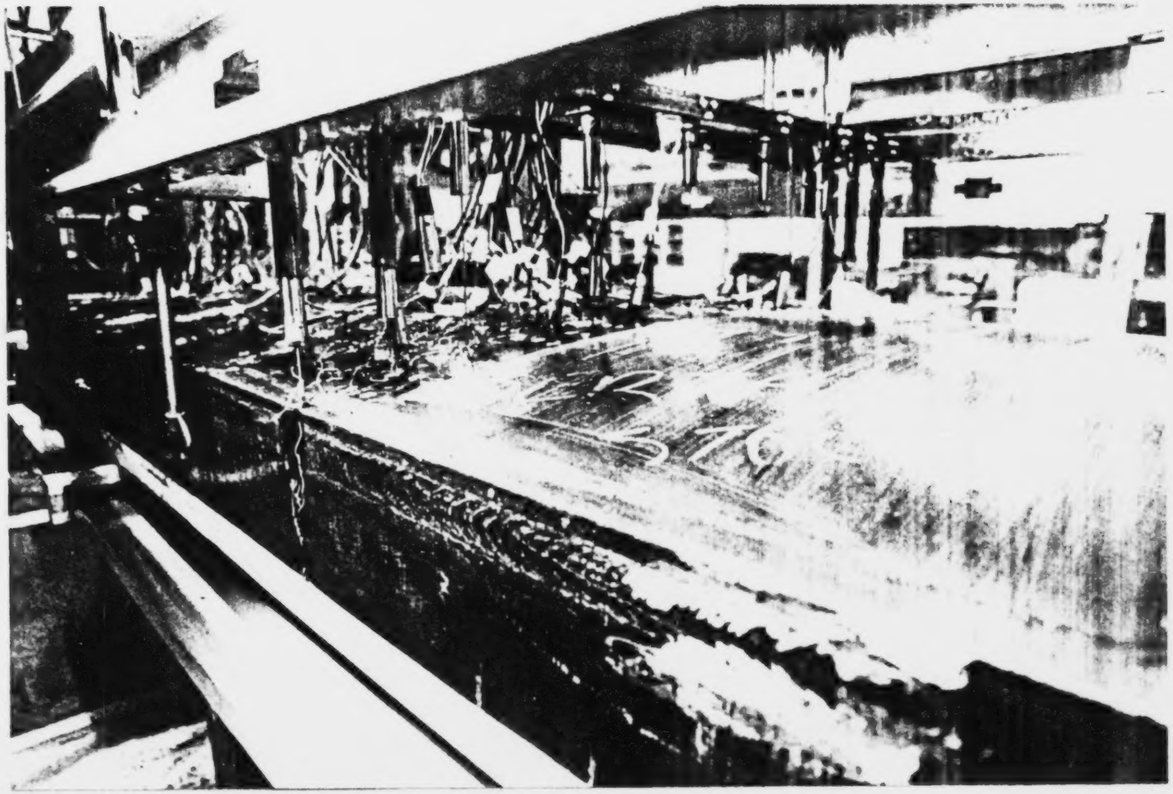

Figure 5.8 Fracture region of specimen P16

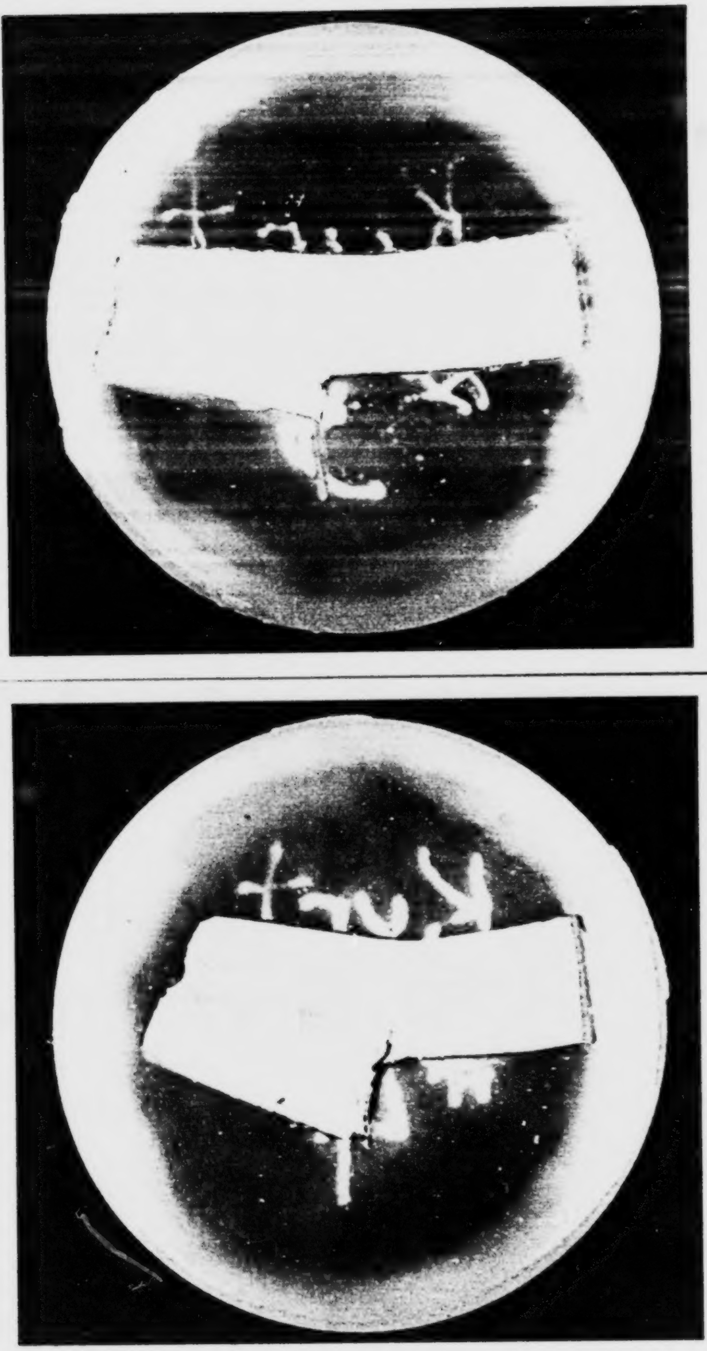

Figure 5.9 Rupture development at plate edge

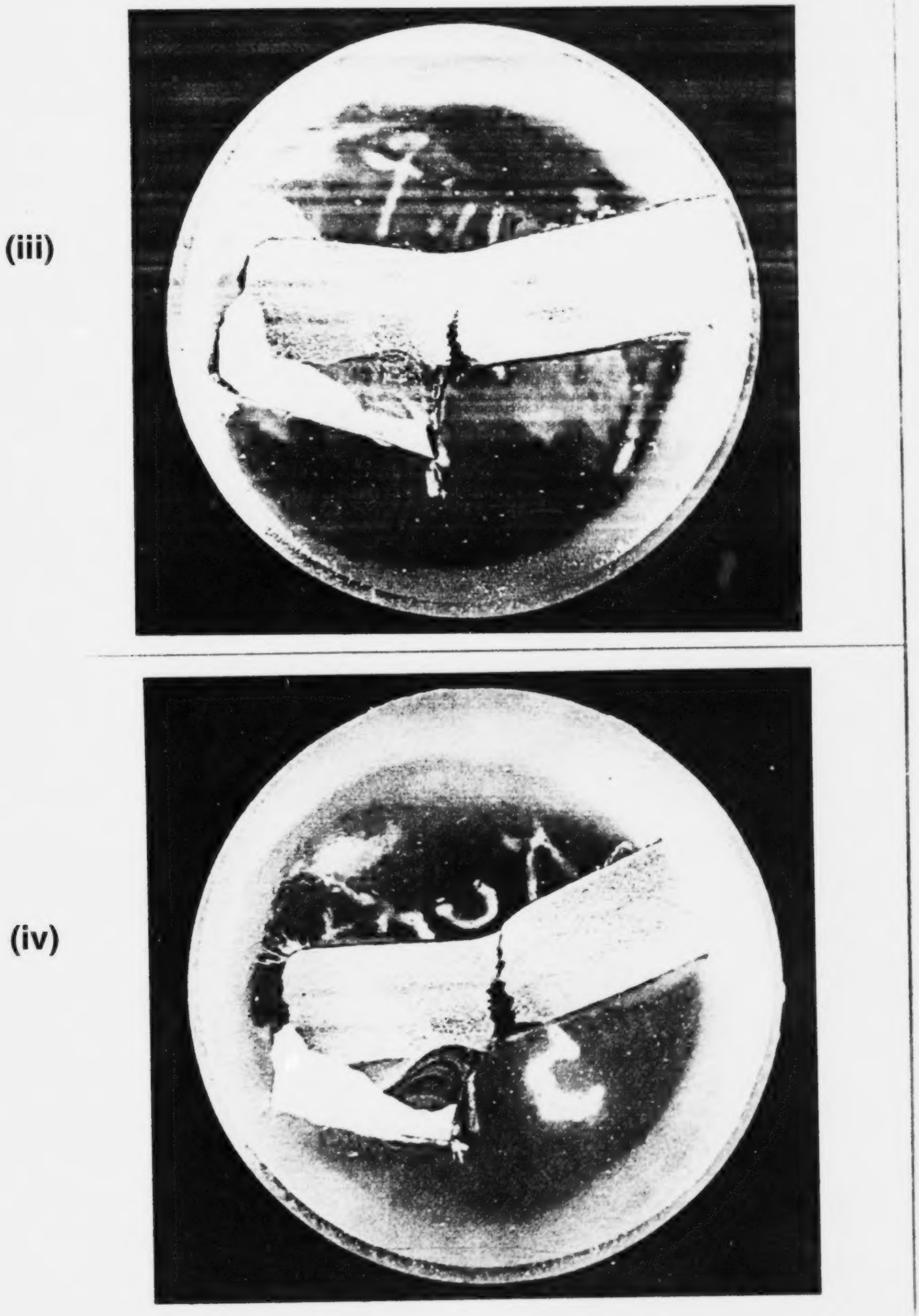

Figure 5.10 Rupture development at plate edge

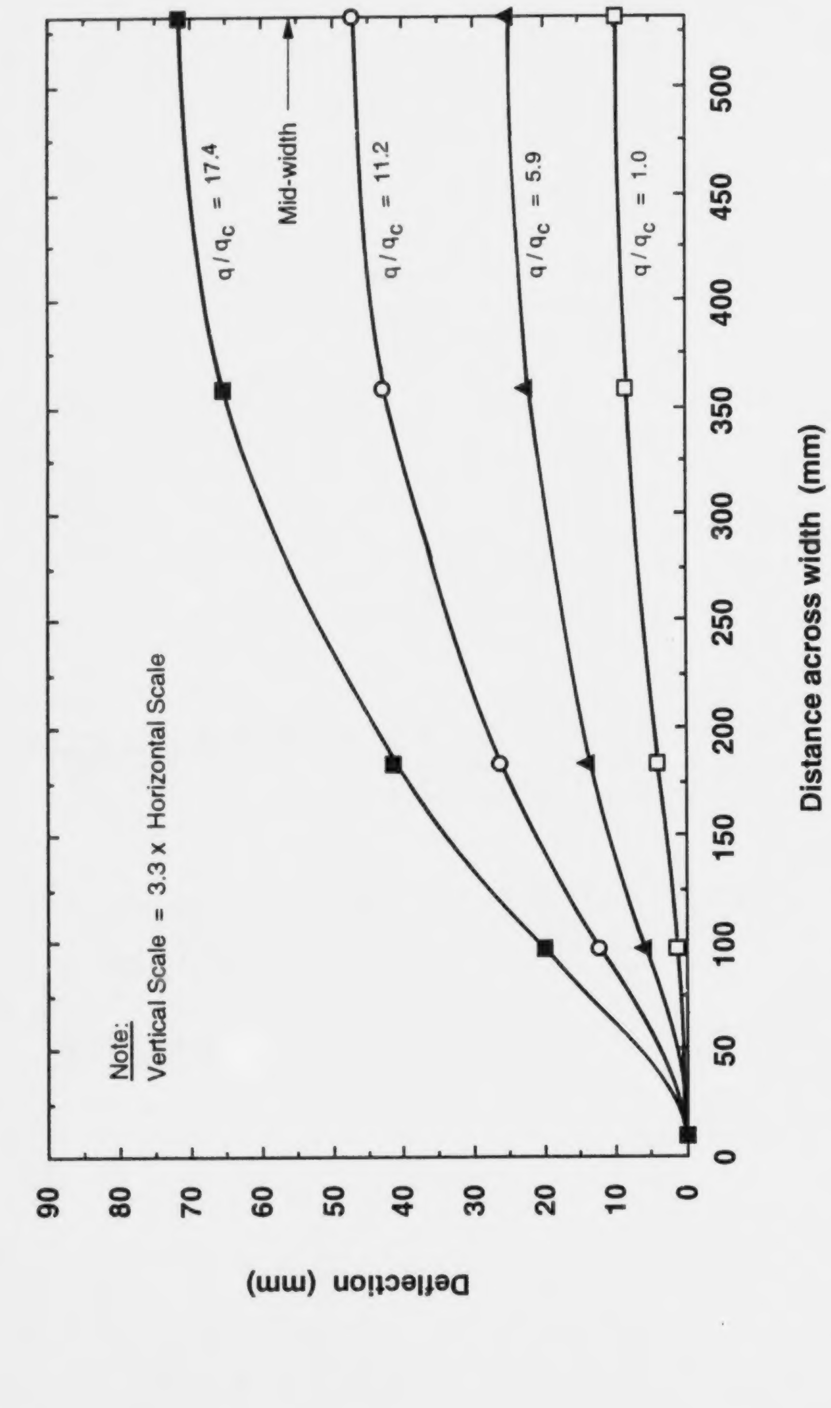

Figure 5.11 Deflections at mid-length, test P6-1

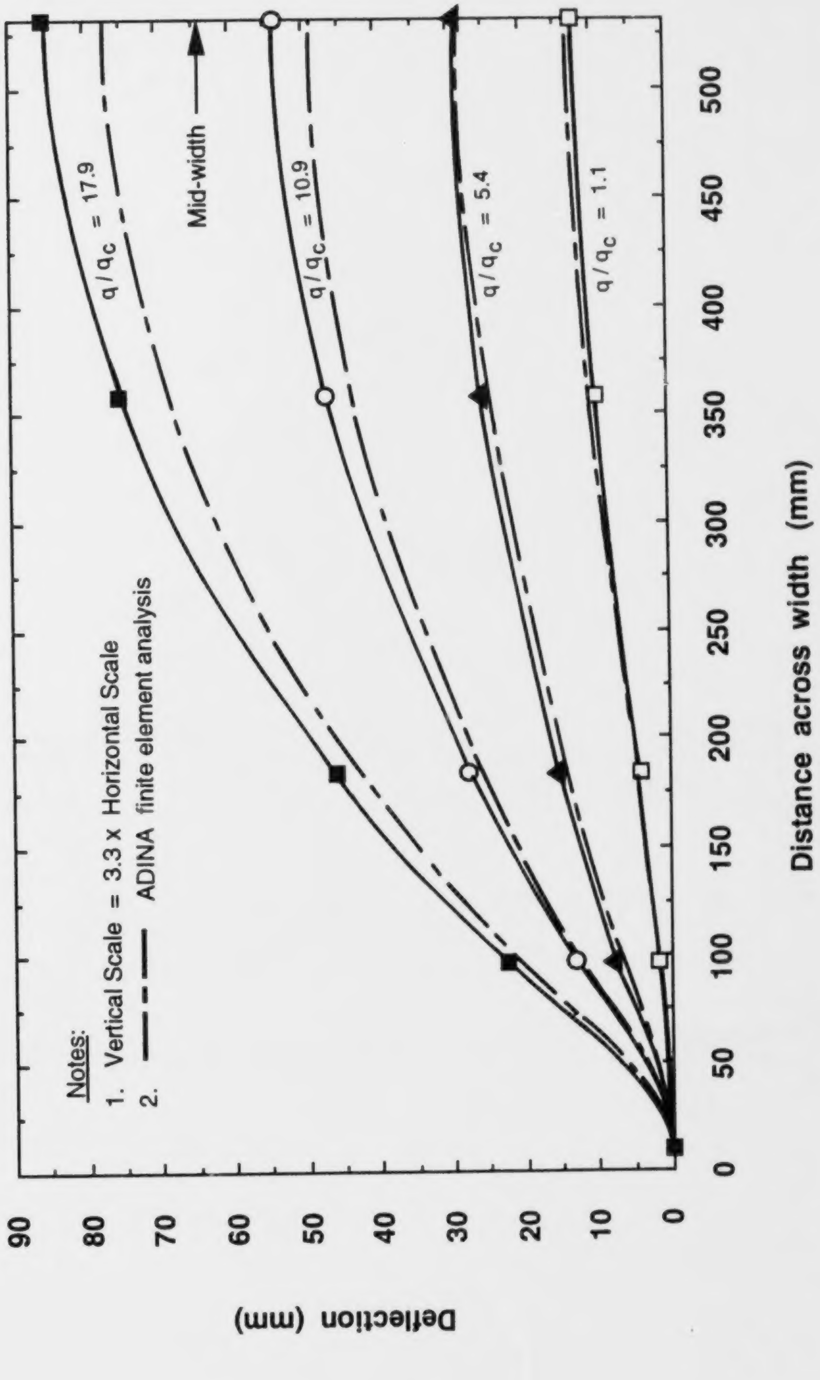

Figure 5.12 Deflections at mid-length, test P6-2

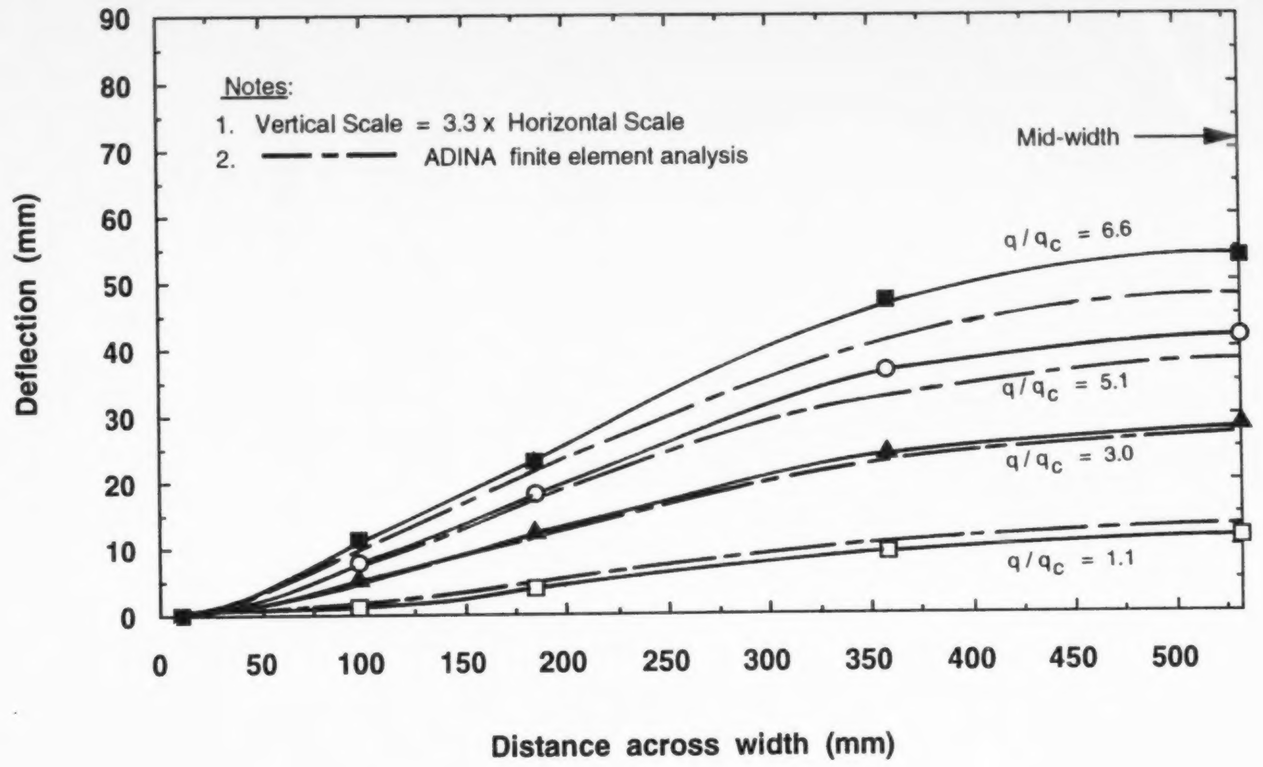

Figure 5.13 Deflections at mid-length, test P12

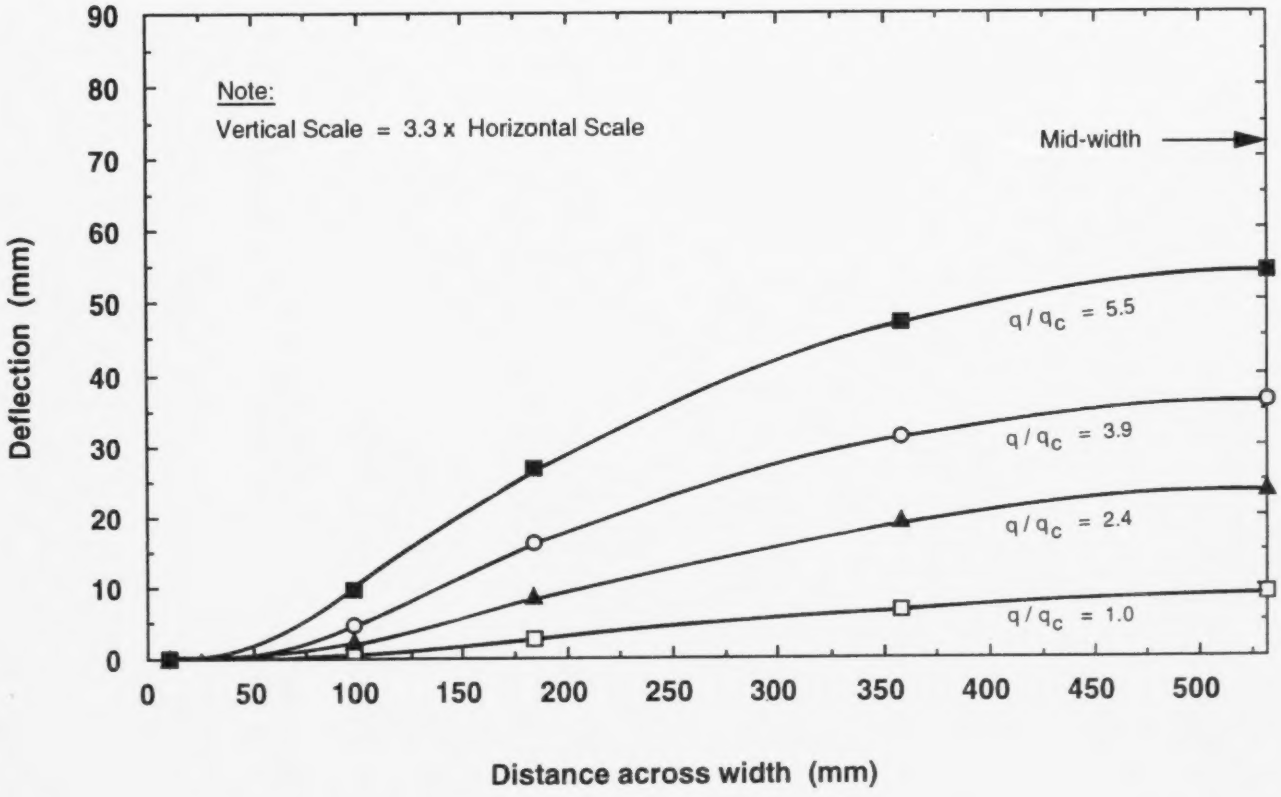

Figure 5.14 Deflections at mid-length, test P16

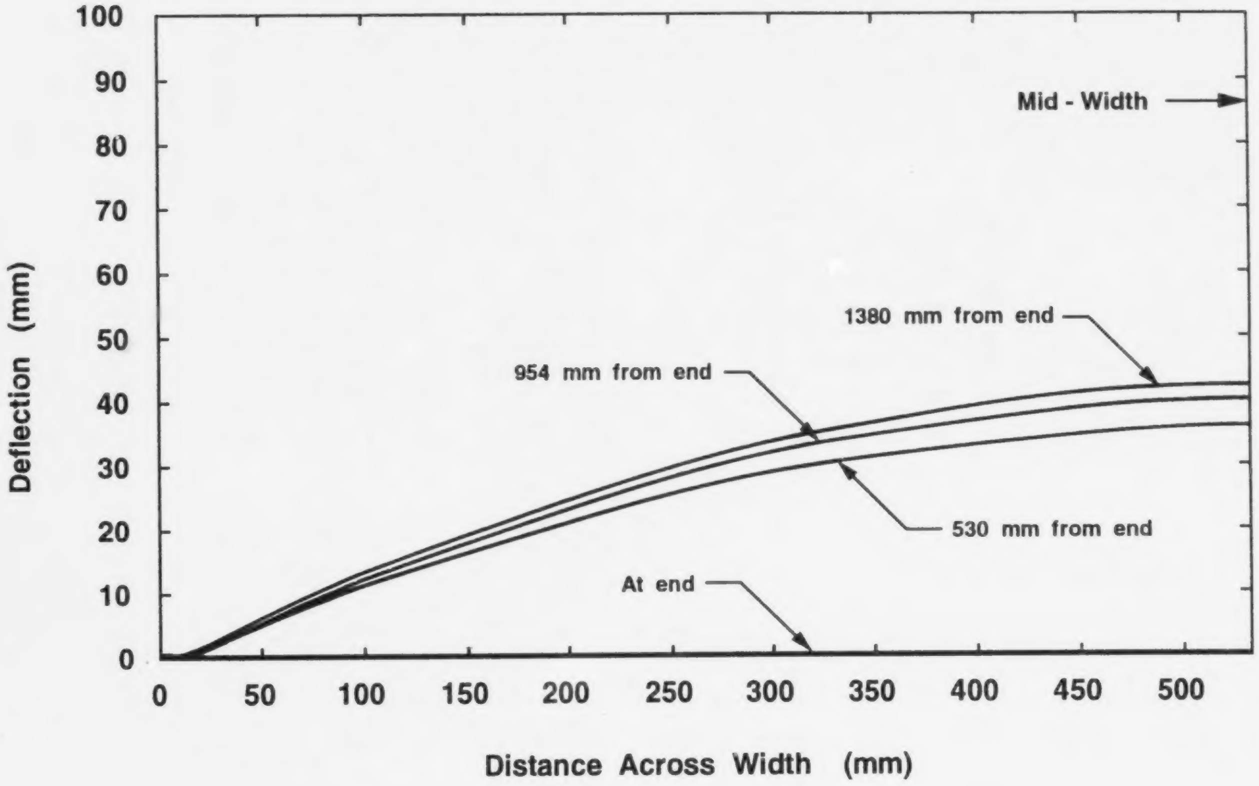

Figure 5.15 SLI deflections for specimen P6-2 at q/qc = 6.0

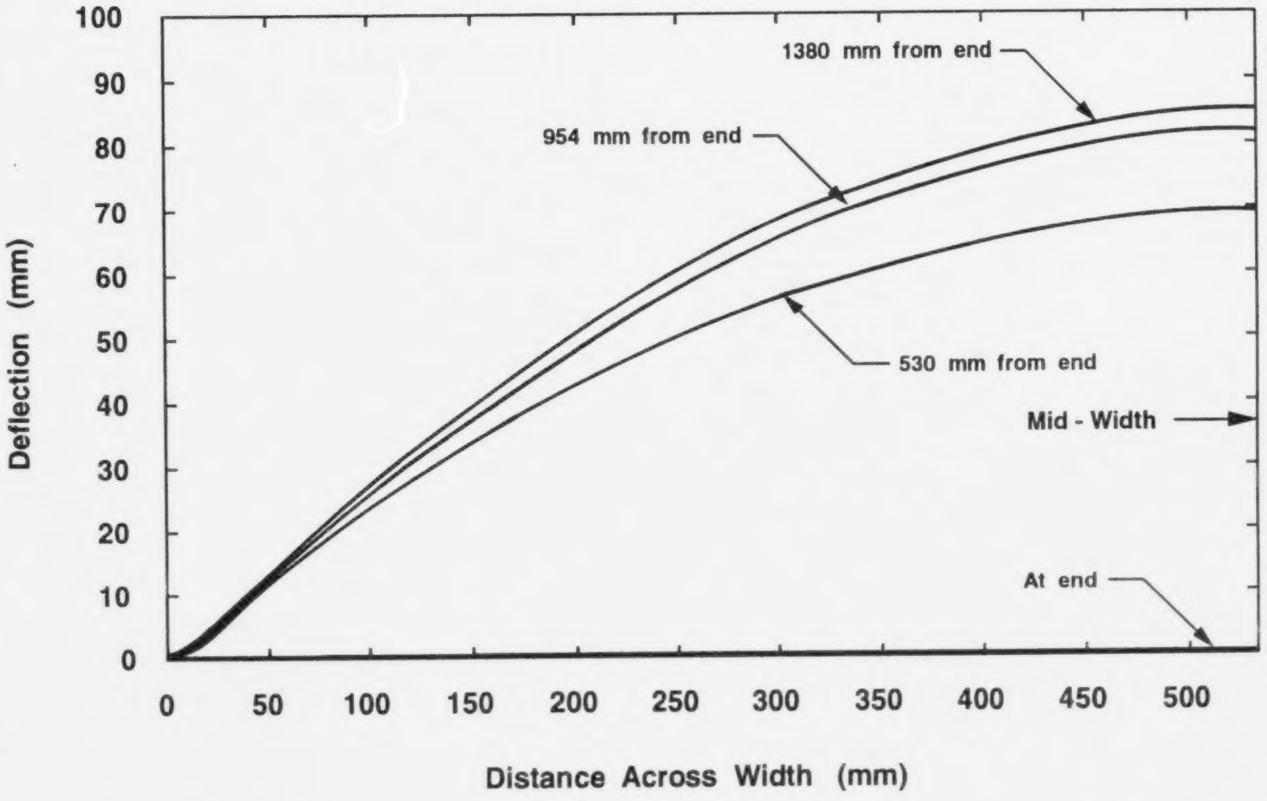

Figure 5.16 SLI deflections for specimen P6-2 after failure

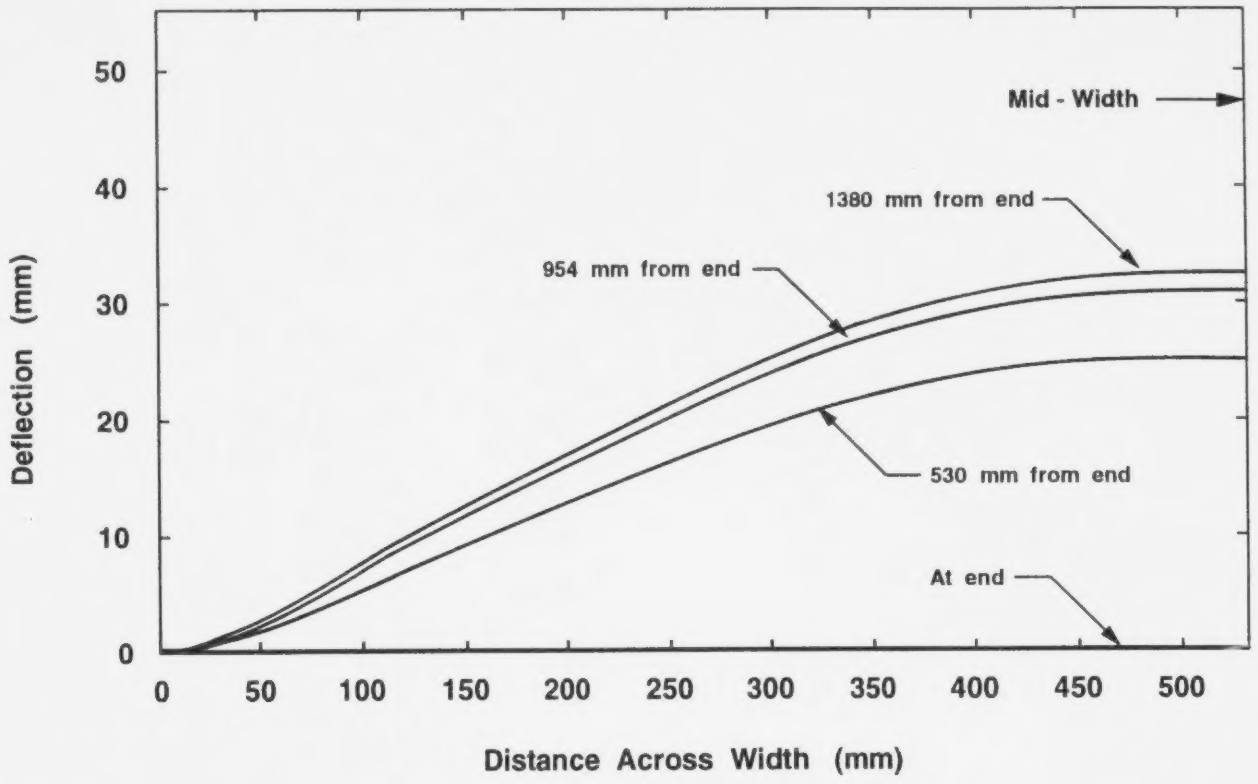

Figure 5.17 SLI deflections for specimen P16 at q/qc = 2.7

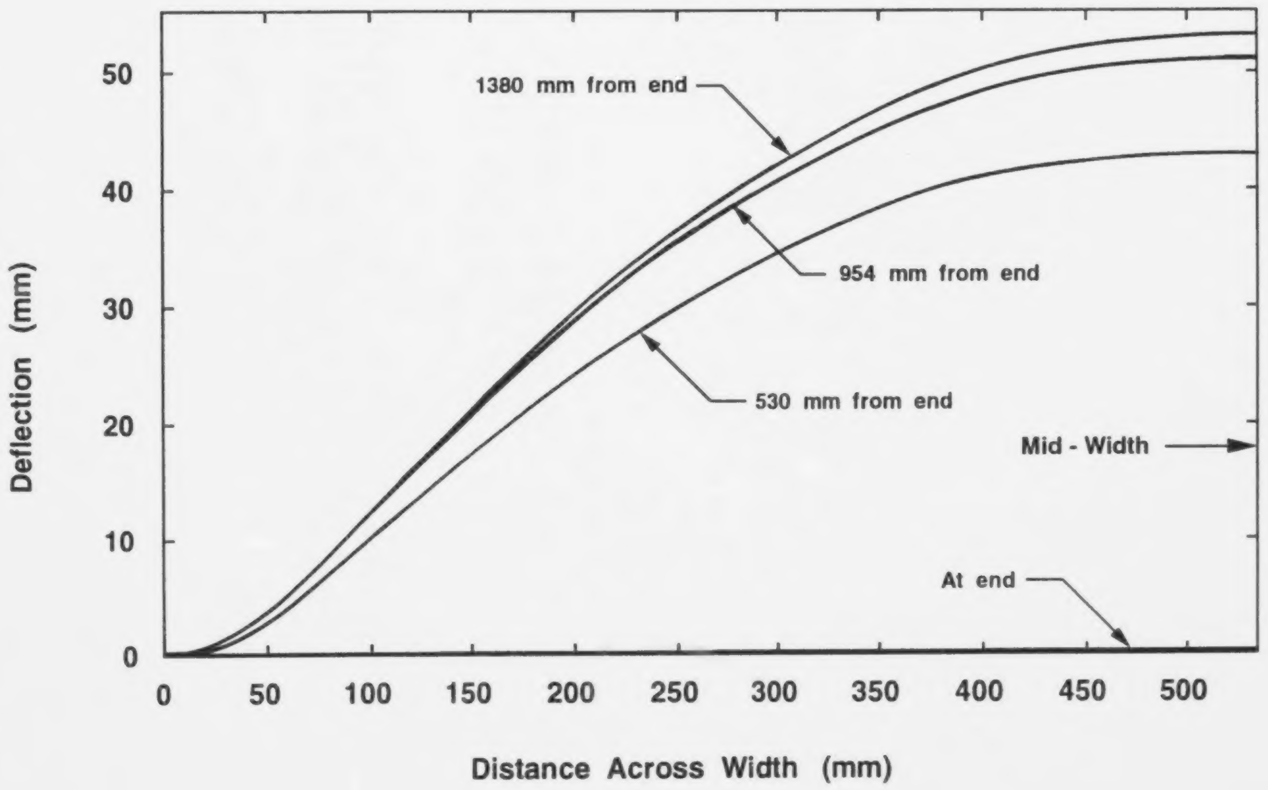

Figure 5.18 SLI deflections for specimen P16 after failure

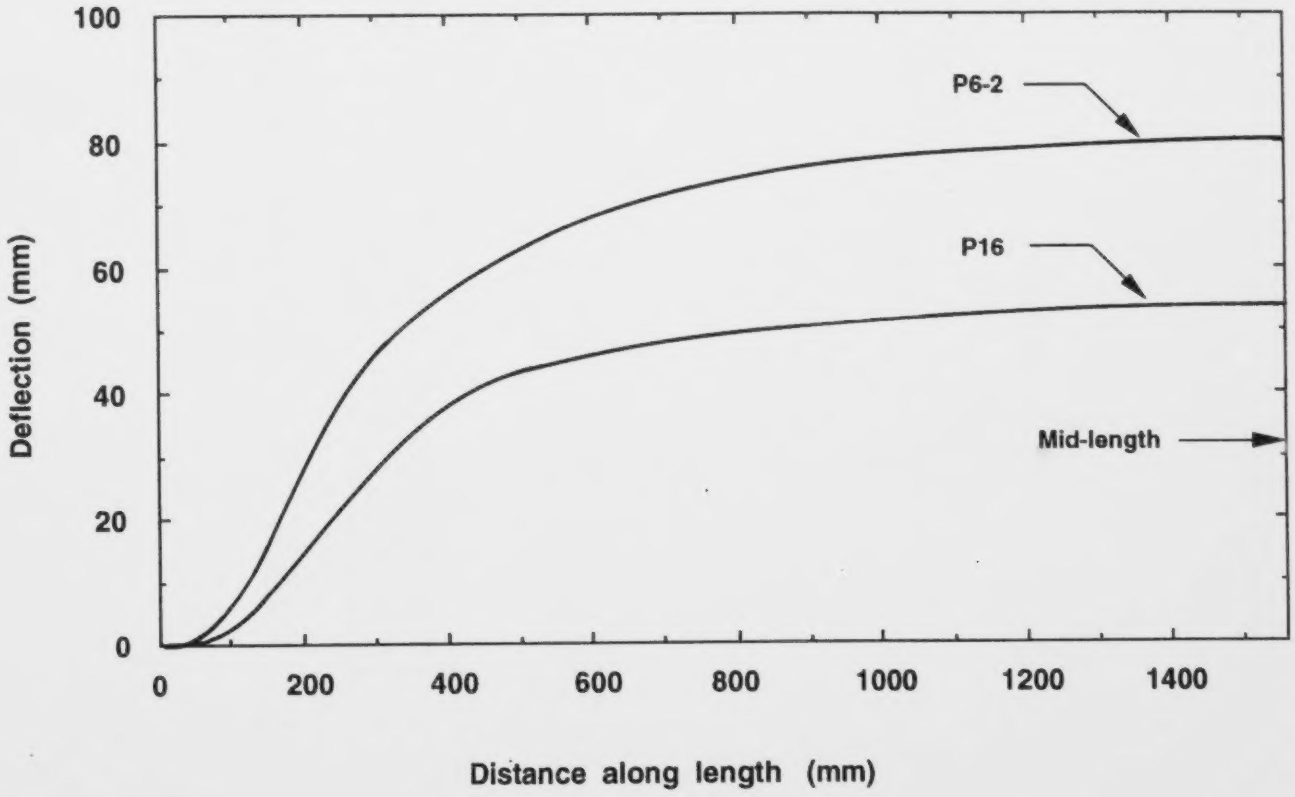

Figure 5.19 SLI deflections at mid-width for specimens P6-2 and P16 after failure

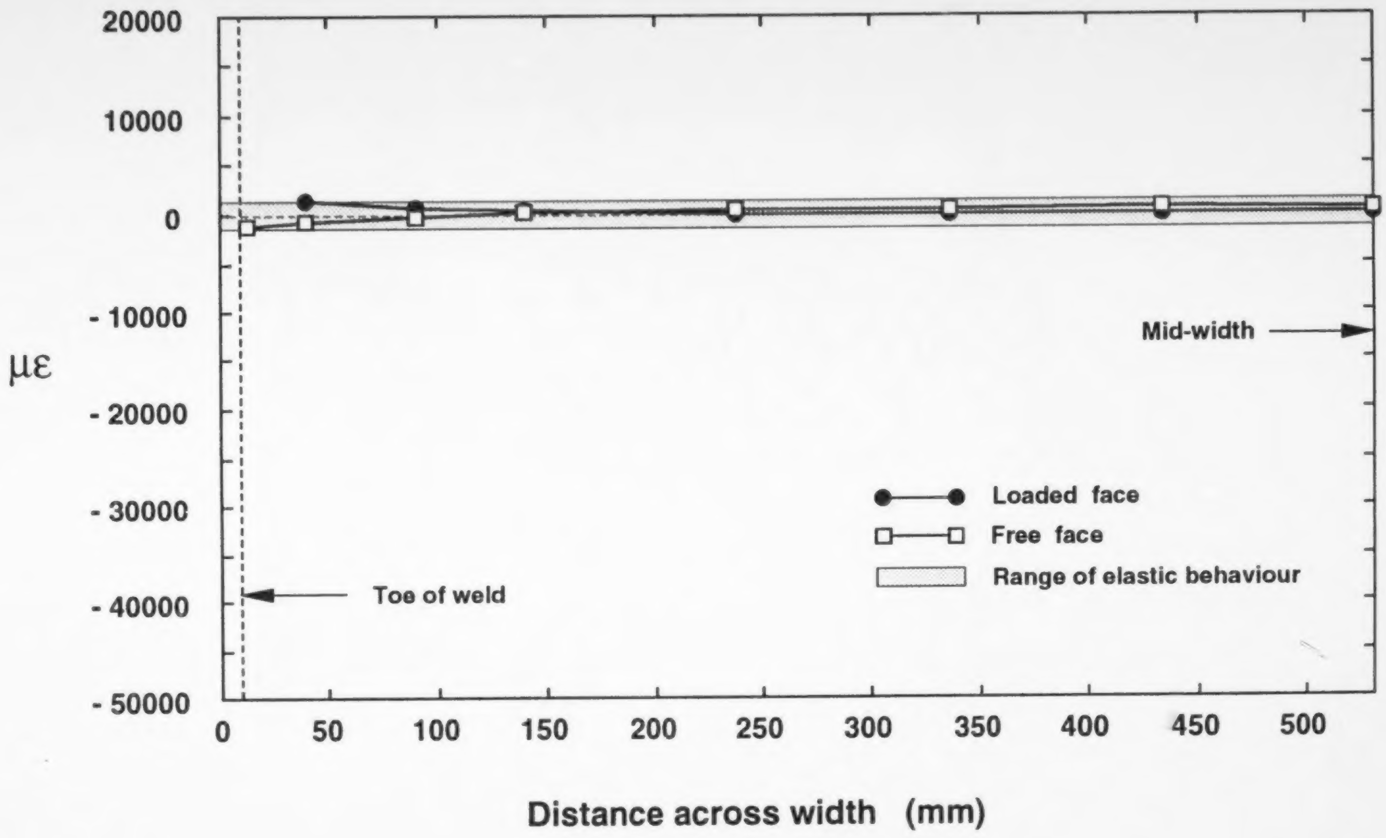

Figure 5.20 Strains across the width at mid-length, q/qc = 1.0, test P6-1

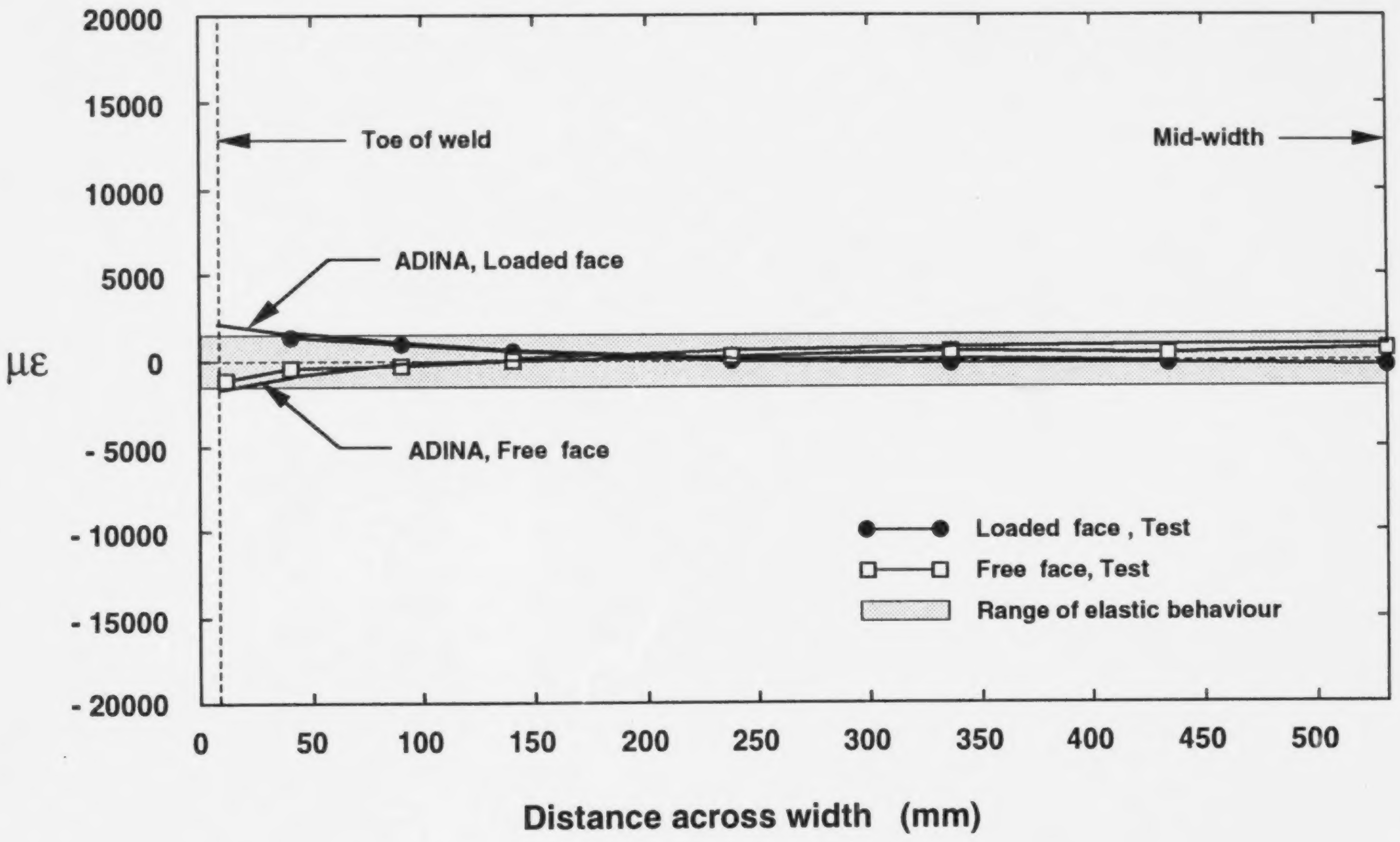

Figure 5.21 Strains across the width at mid-length, q/qc = 1.1, test P6-2

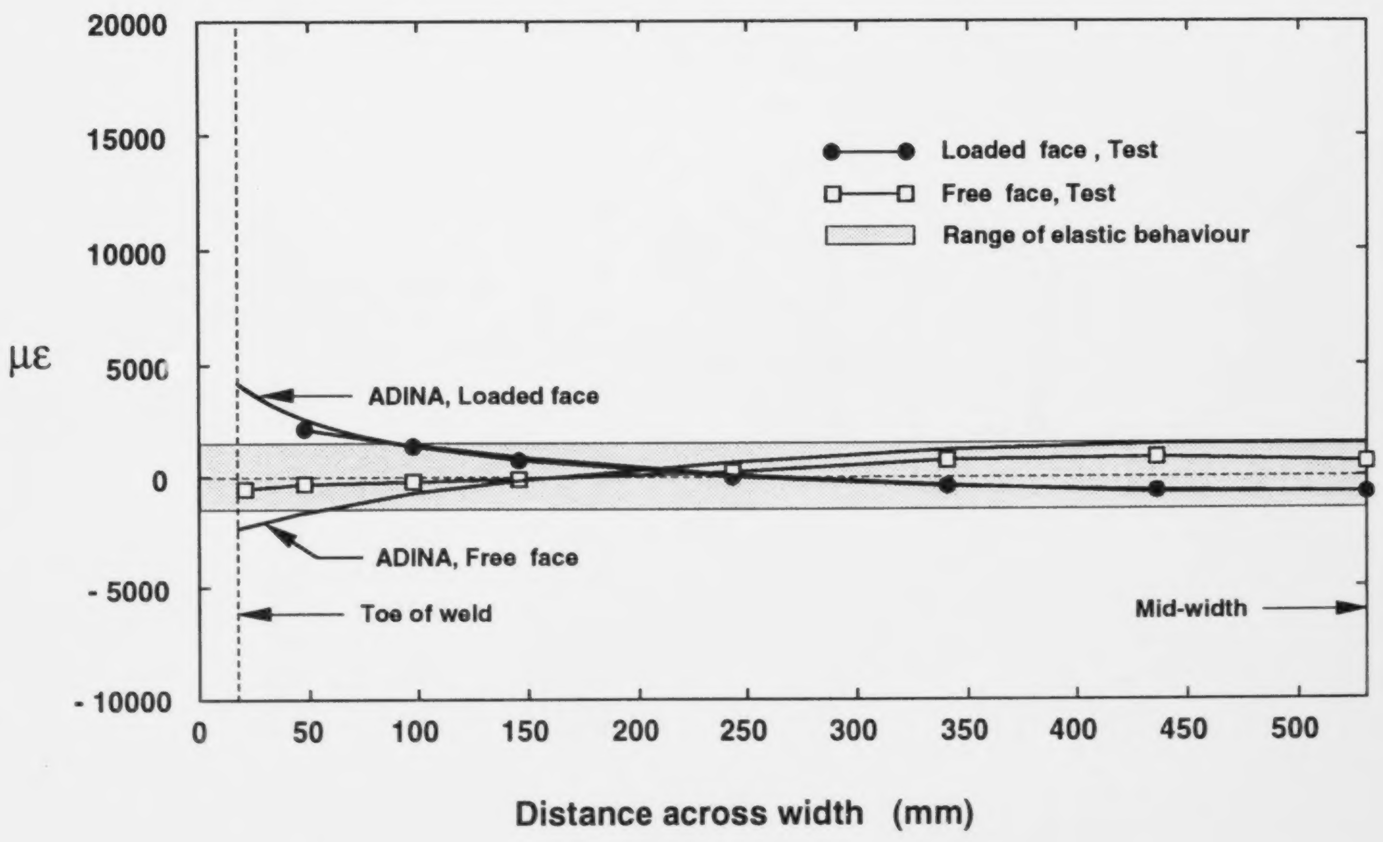

Figure 5.22 Strains across the width at mid-length, q/qc = 1.1, test P12

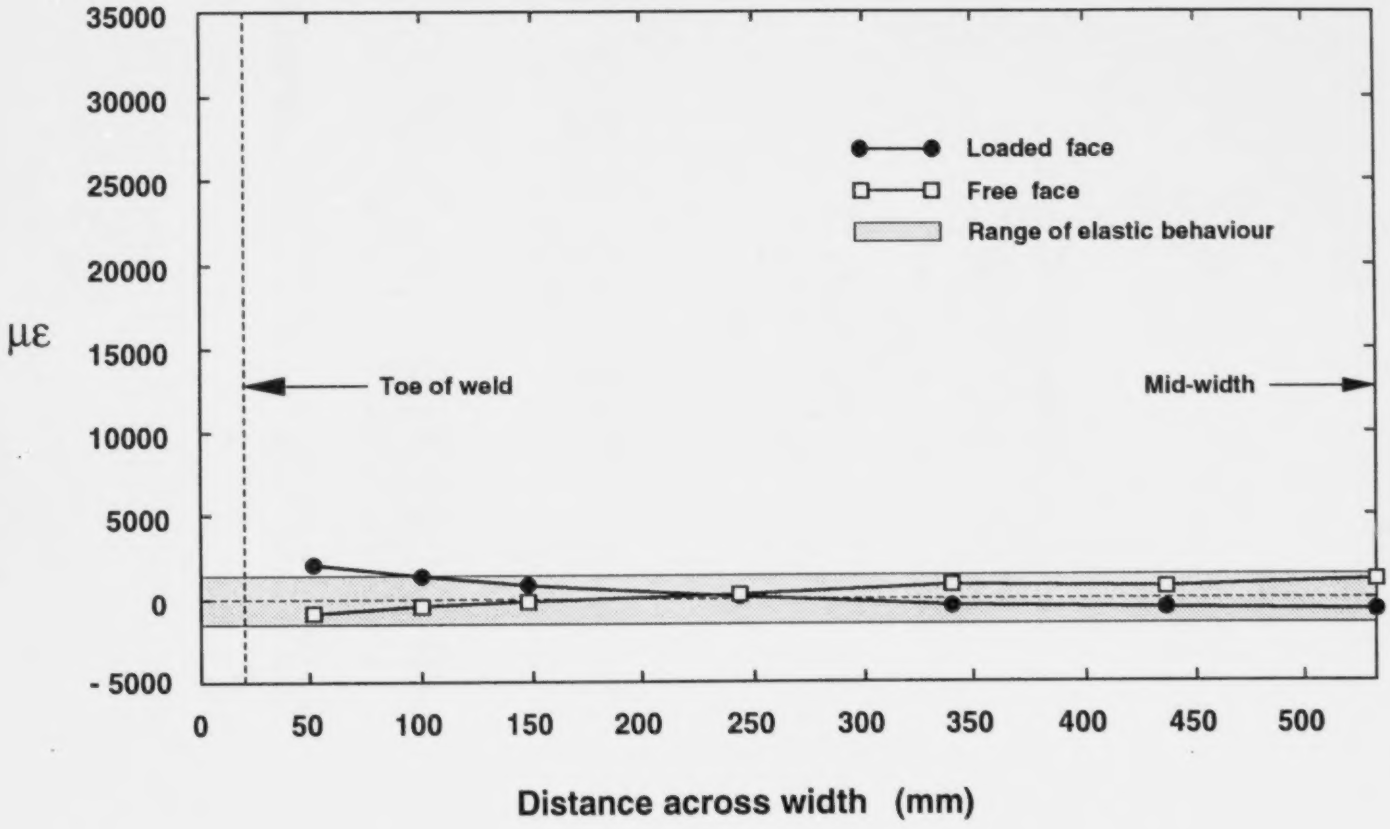

Figure 5.23 Strains across the width at mid-length, q/qc = 1.0, test P16

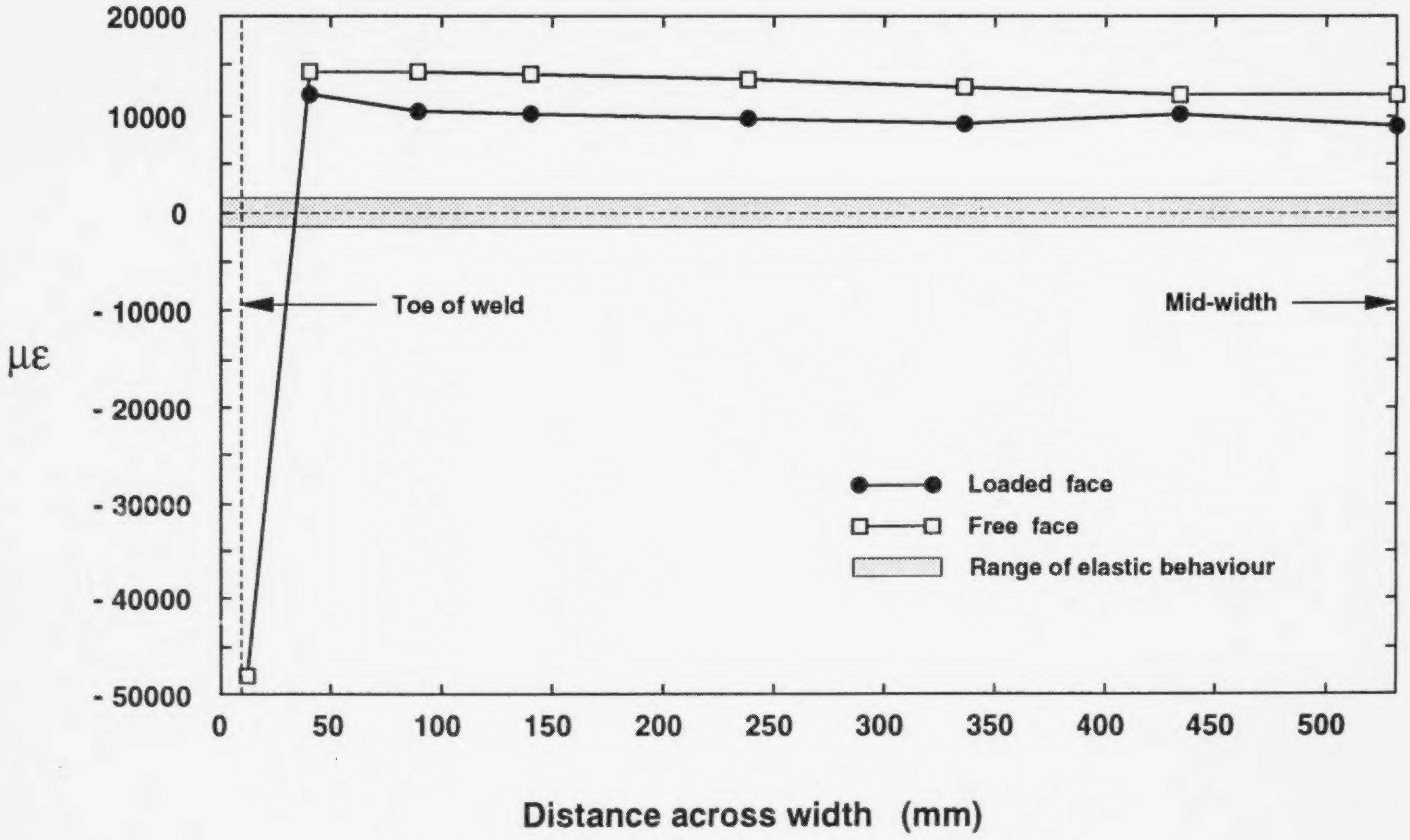

Figure 5.24 Strains across the width at mid-length, q/qc = 17.4, test P6-1

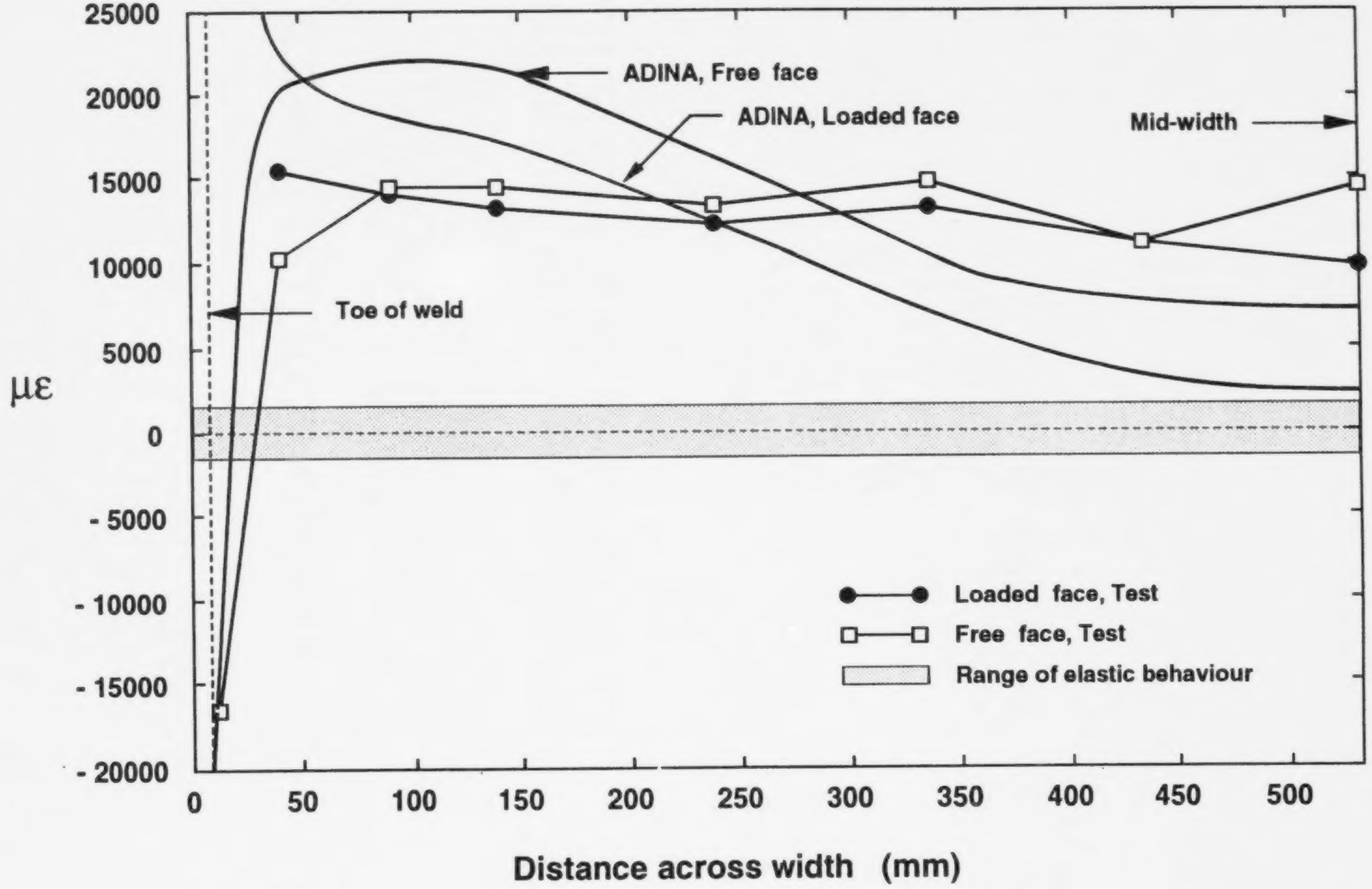

Figure 5.25 Strains across the width at mid-length, q/qc = 17.9, test P6-2

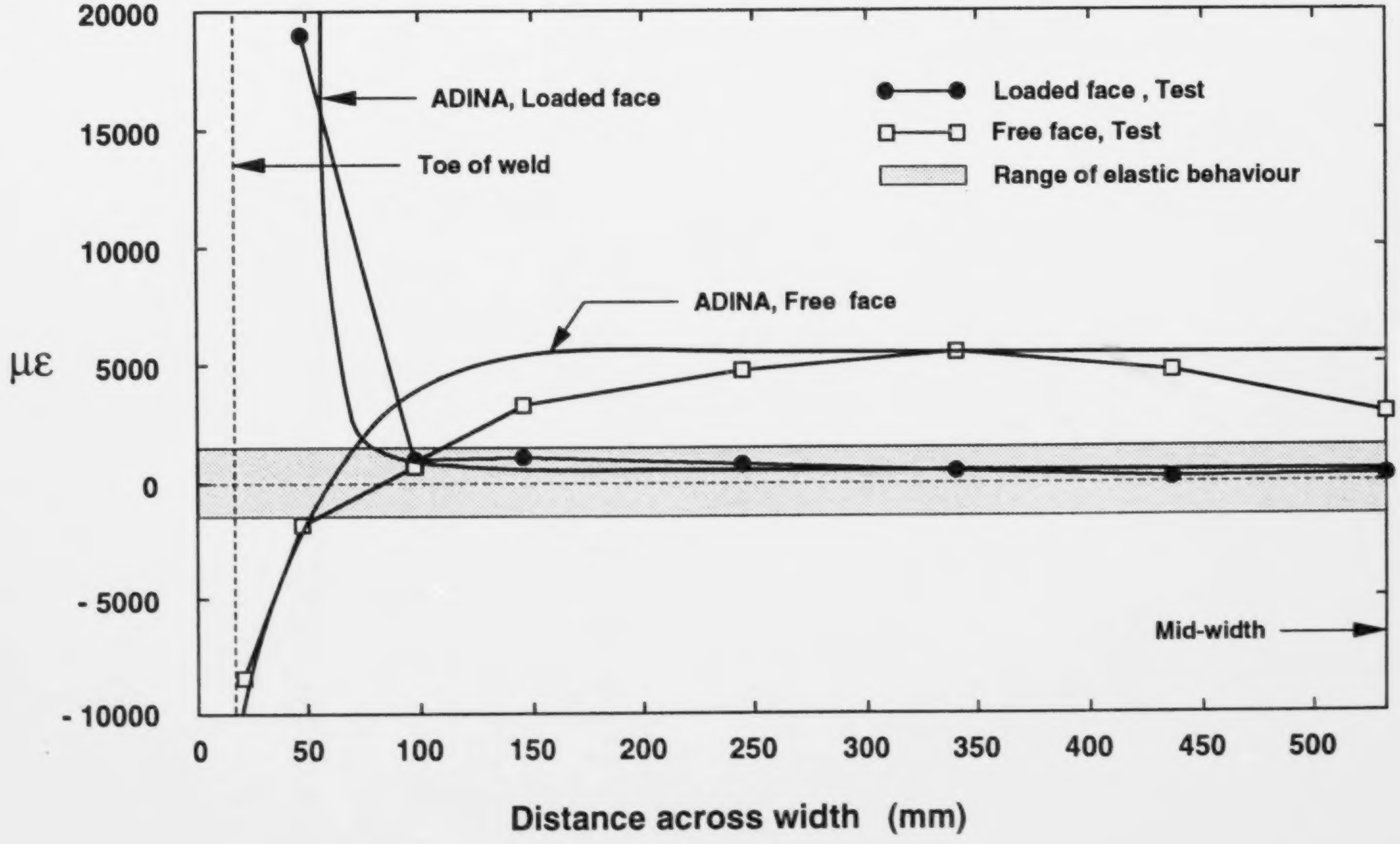

Figure 5.26 Strains across the width at mid-length, q/qc = 6.6, test P12

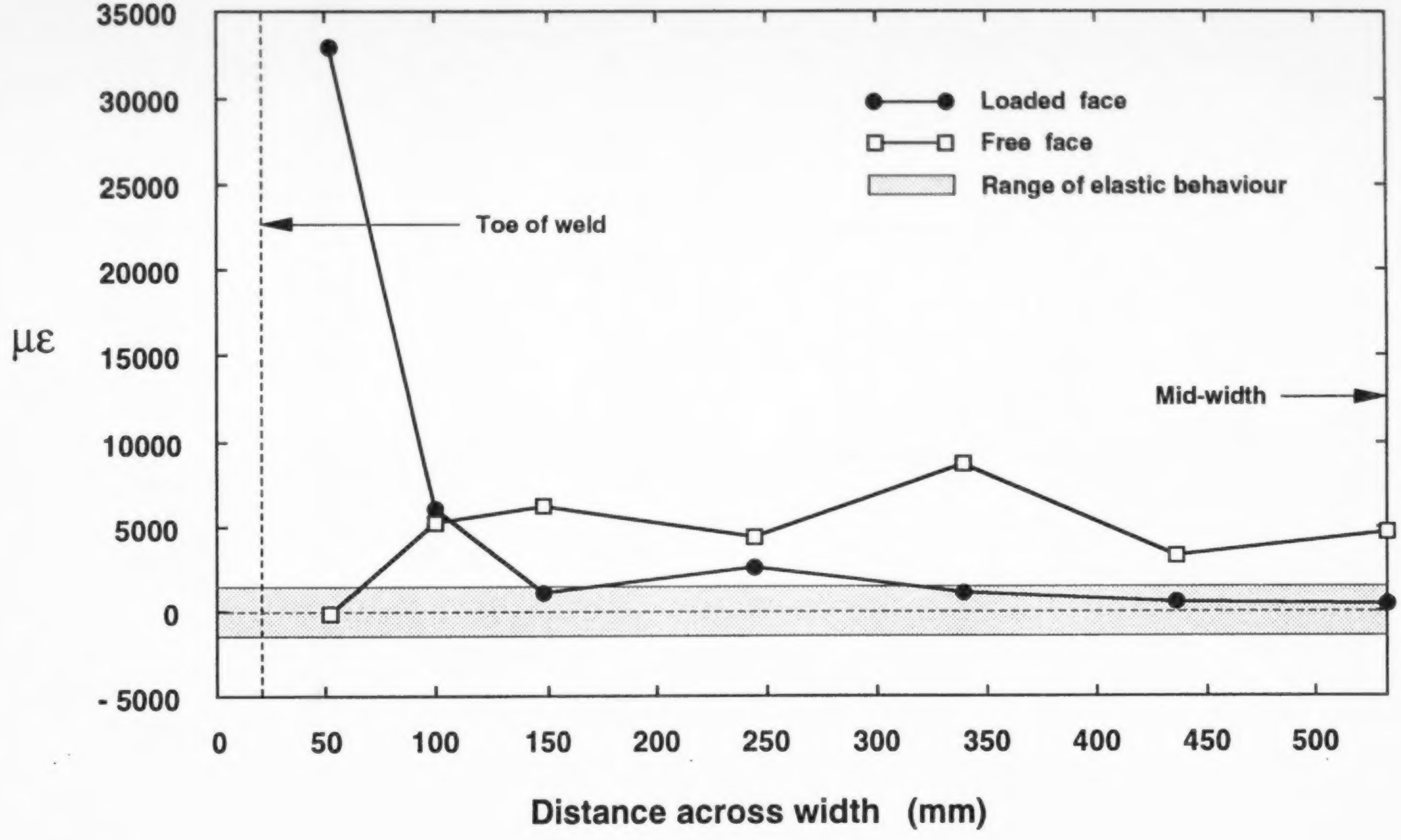

Figure 5.27 Strains across the width at mid-length, q/qc = 5.5, test P16

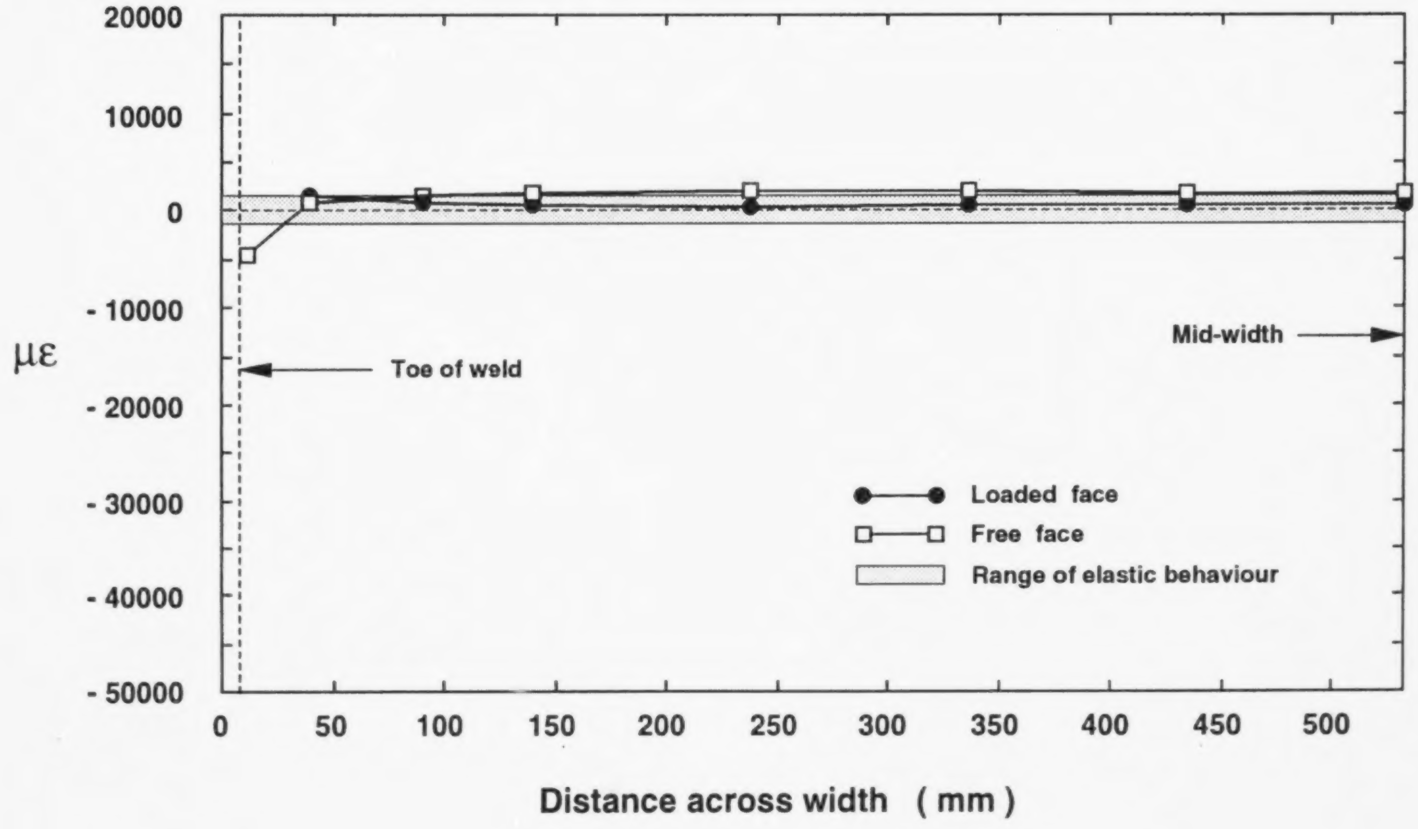

Figure 5.28 Strains across the width at mid-length, q/qc = 5.9, test P6-1

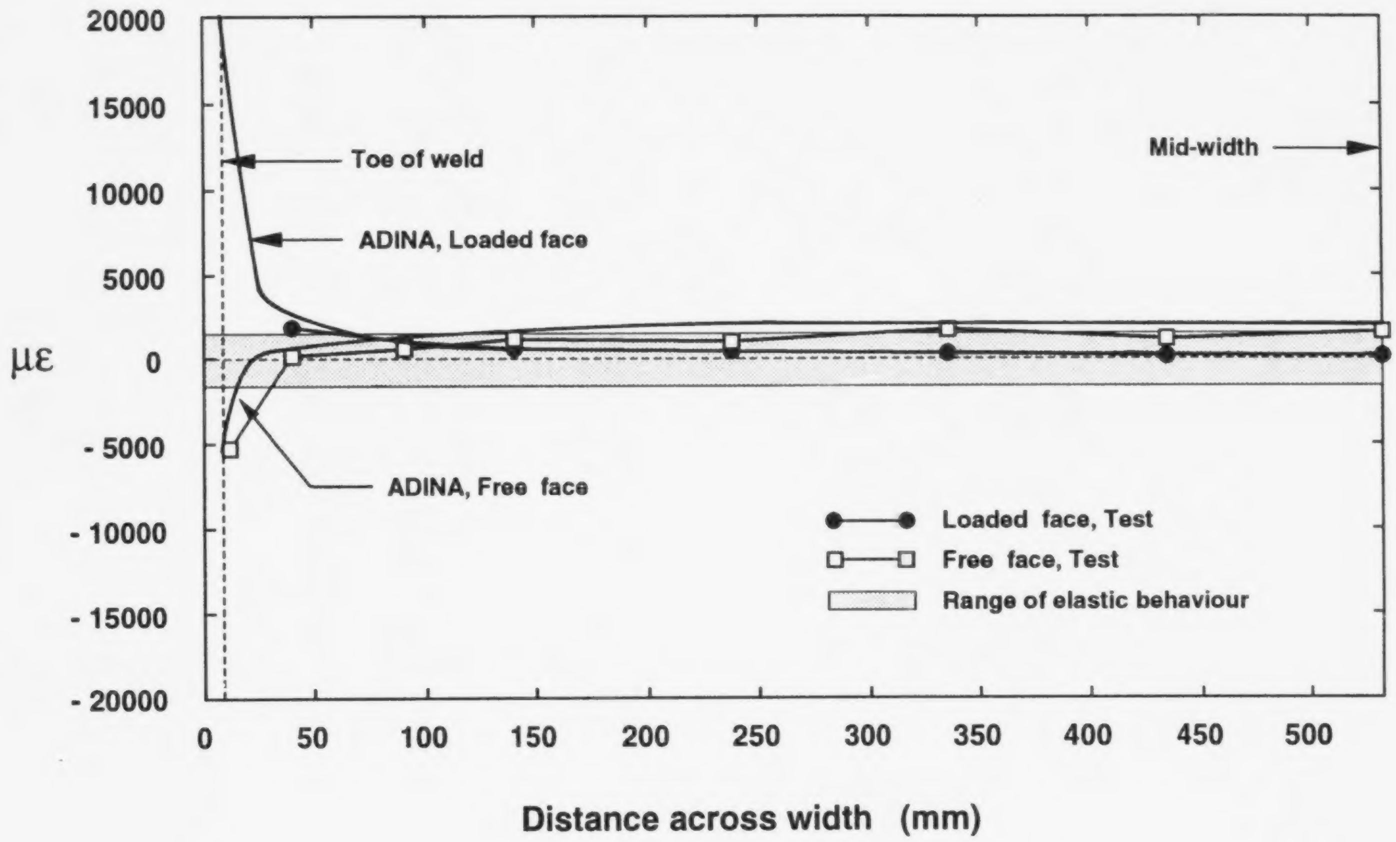

Figure 5.29 Strains across the width at mid-length, q/qc = 5.4, test P6-2

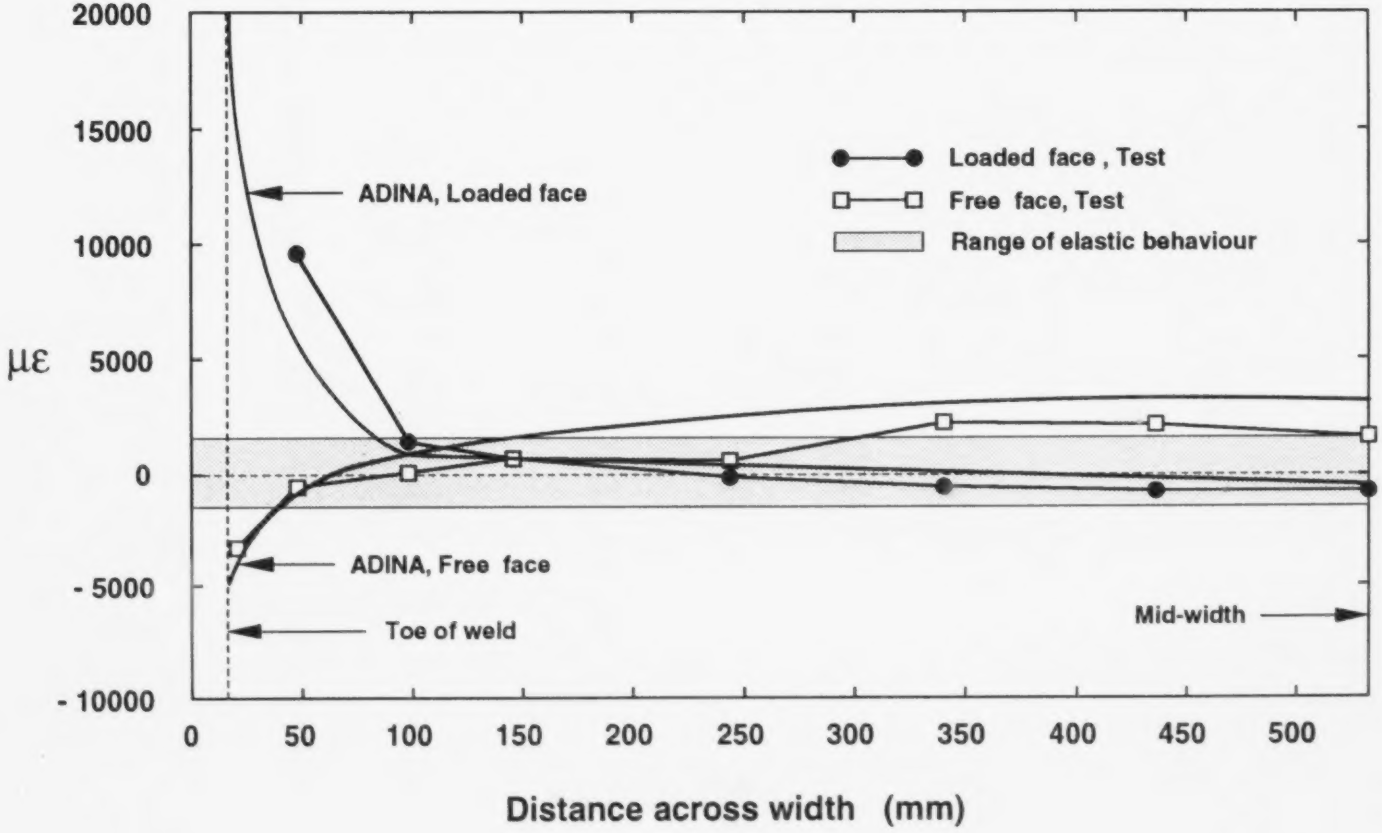

Figure 5.30 Strains across the width at mid-length, q/qc = 3.0, test P12

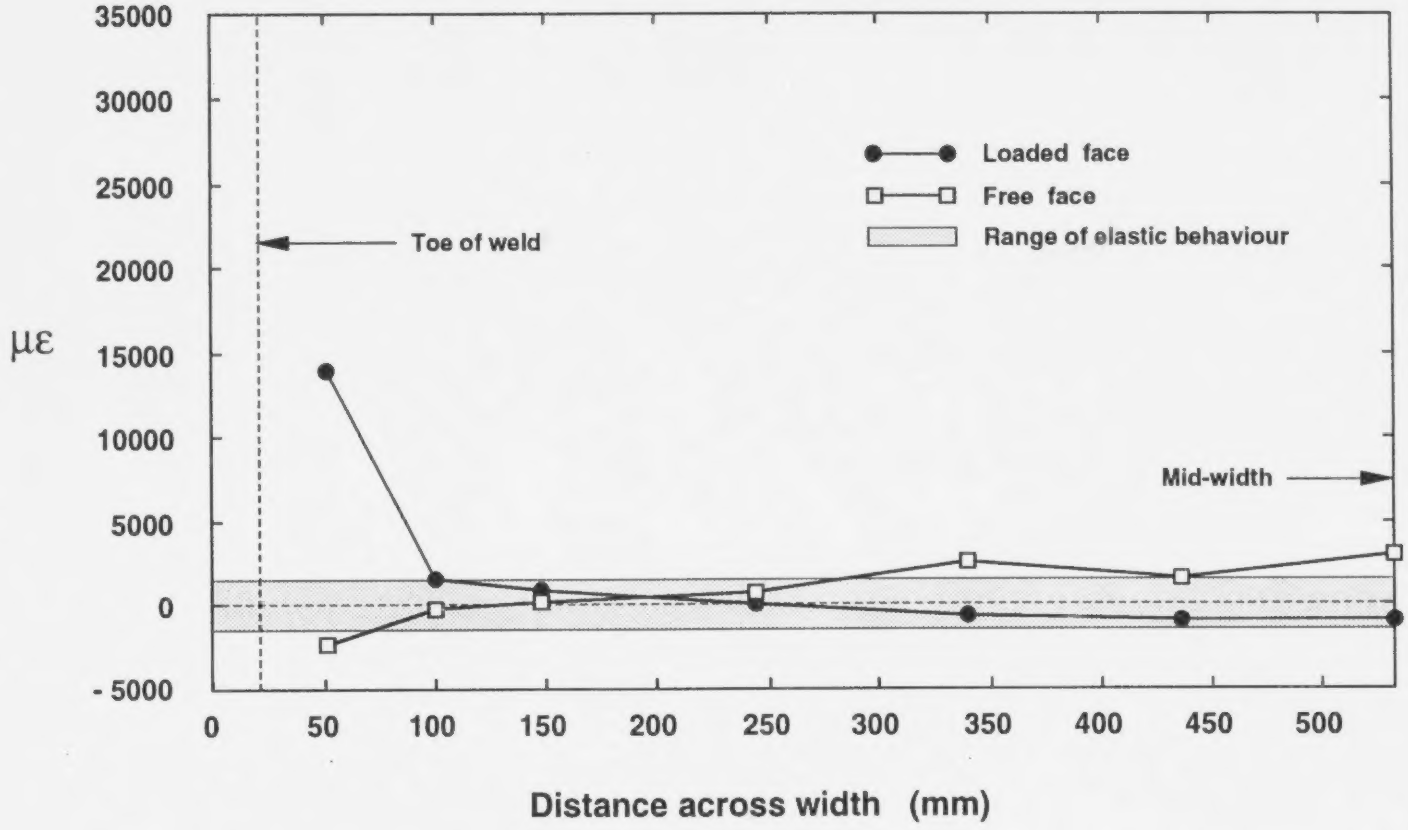

Figure 5.31 Strains across the width at mid-length, q/qc = 2.5, test P16

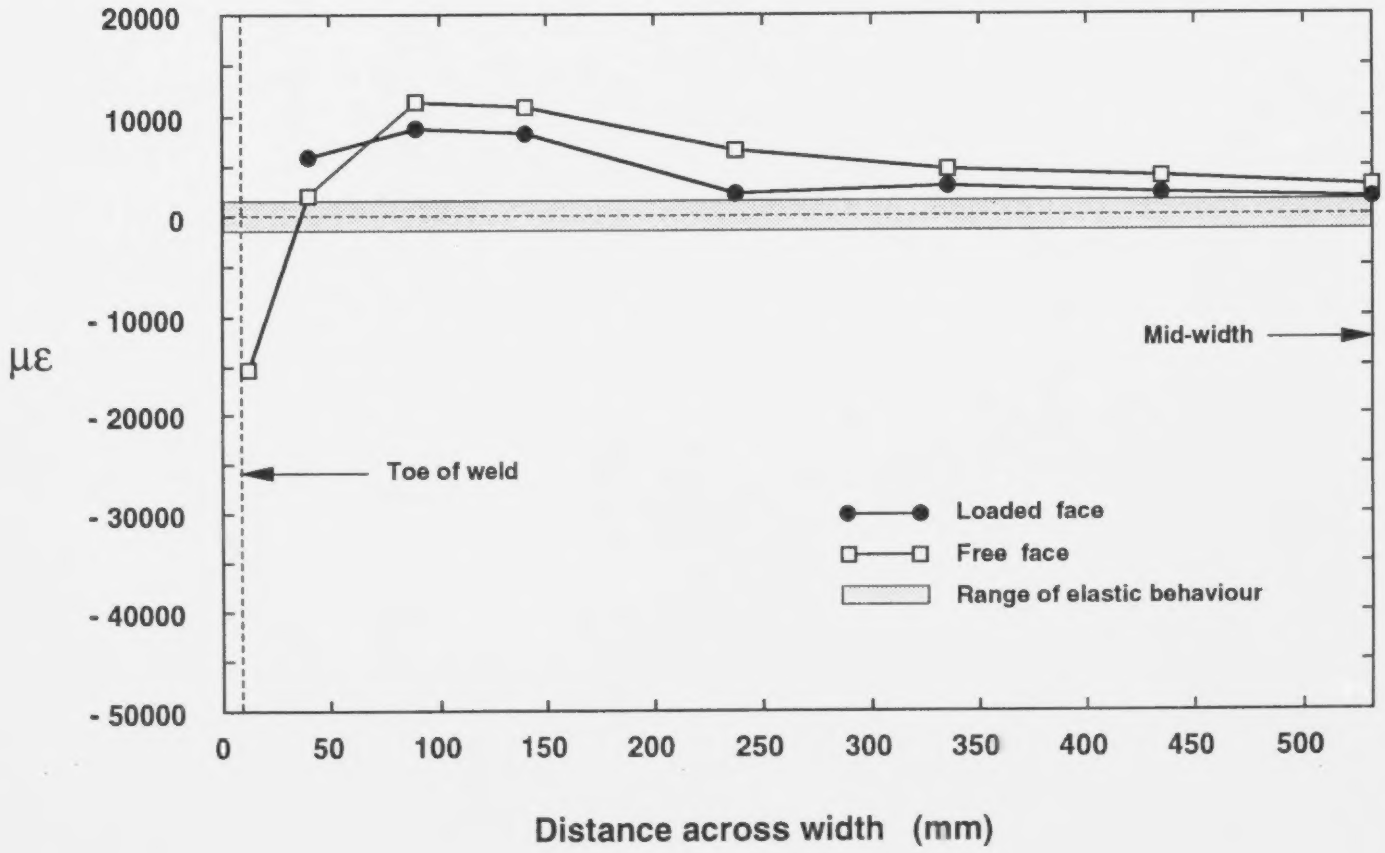

Figure 5.32 Strains across the width at mid-length, q/qc = 11.2, test P6-1

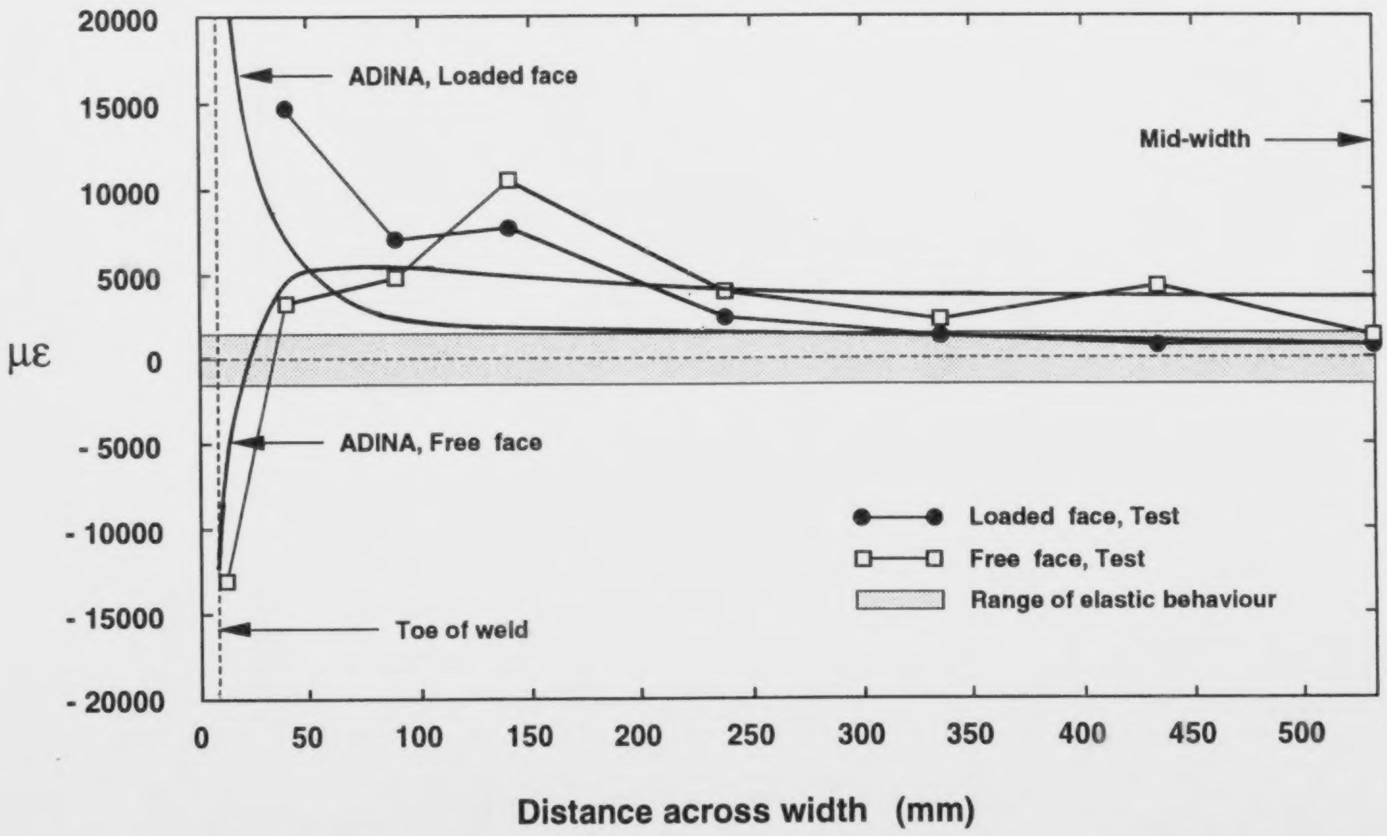

Figure 5.33 Strains across the width at mid-length, q/qc = 10.9, test P6-2

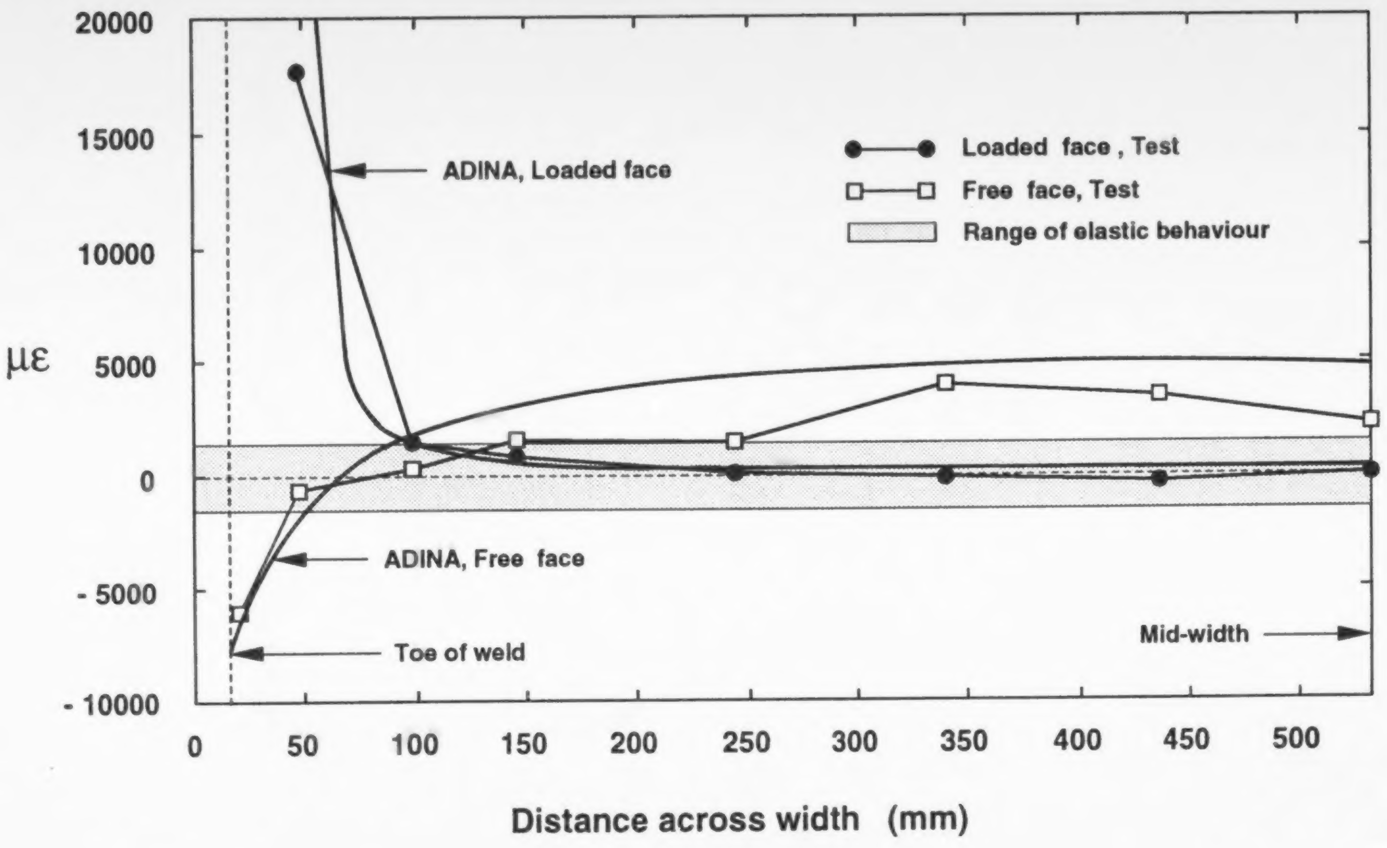

Figure 5.34 Strains across the width at mid-length, q/qc = 5.1, test P12

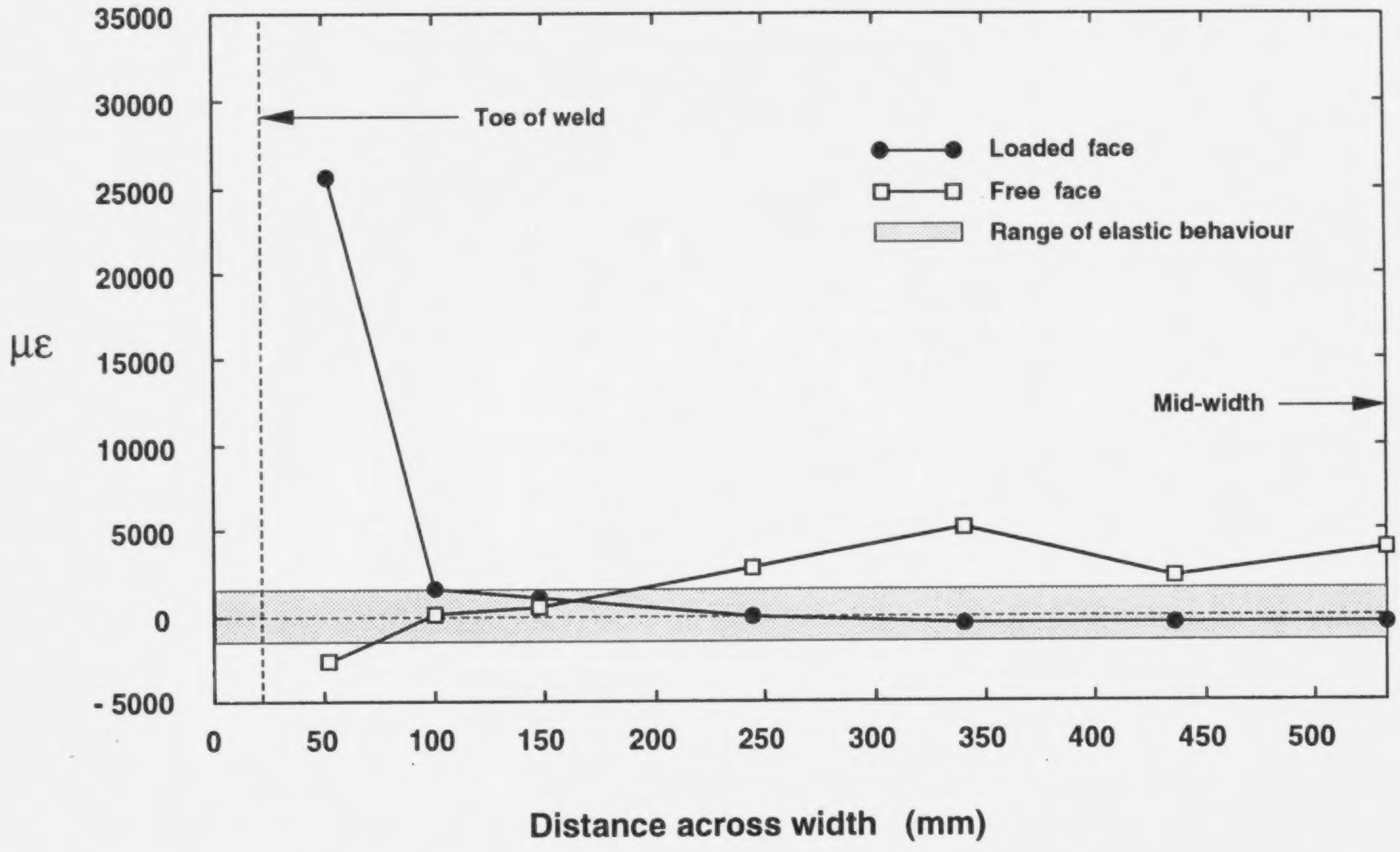

Figure 5.35 Strains across the width at mid-length, q/qc = 3.9, test P16

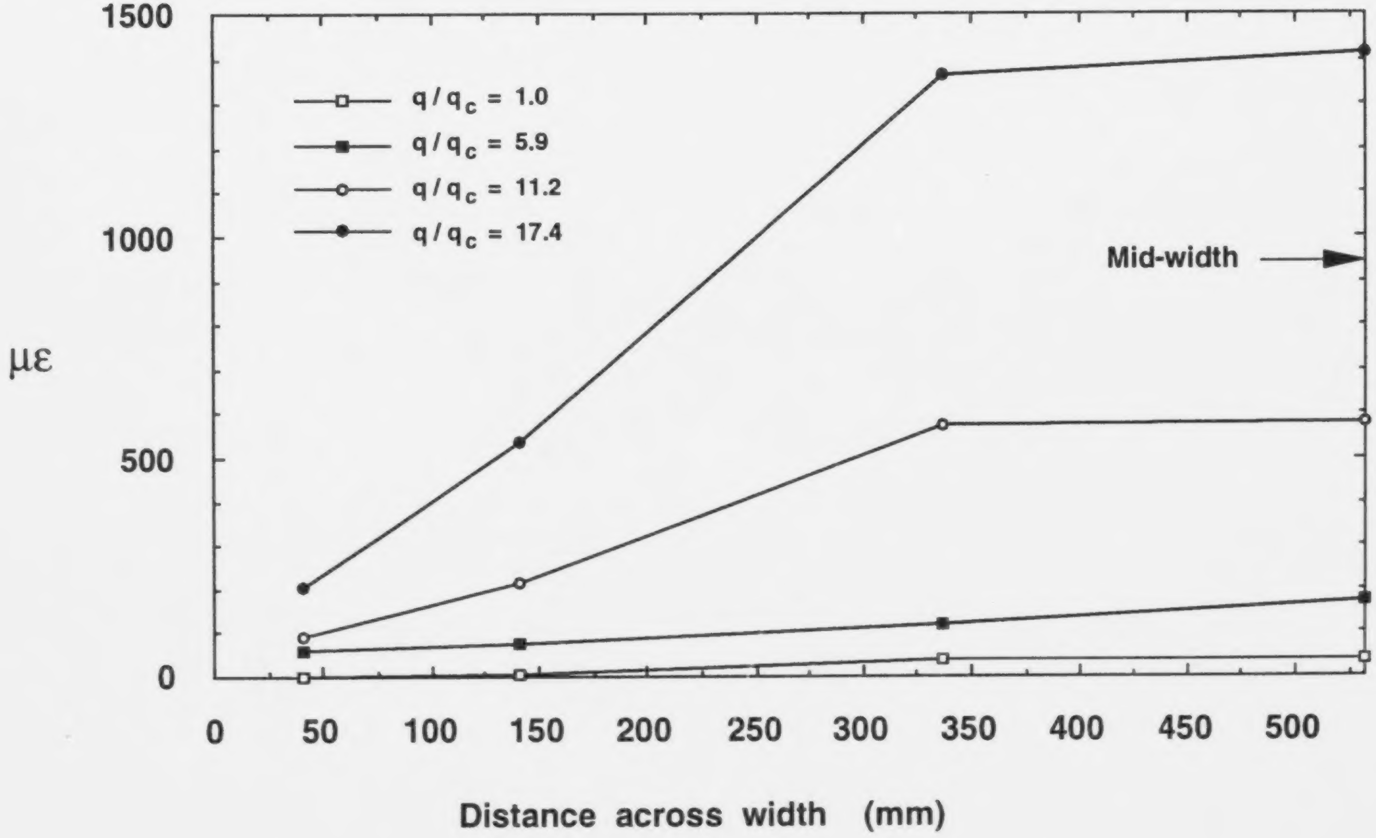

Figure 5.36 Longitudinal strains at mid-length, test P6-1

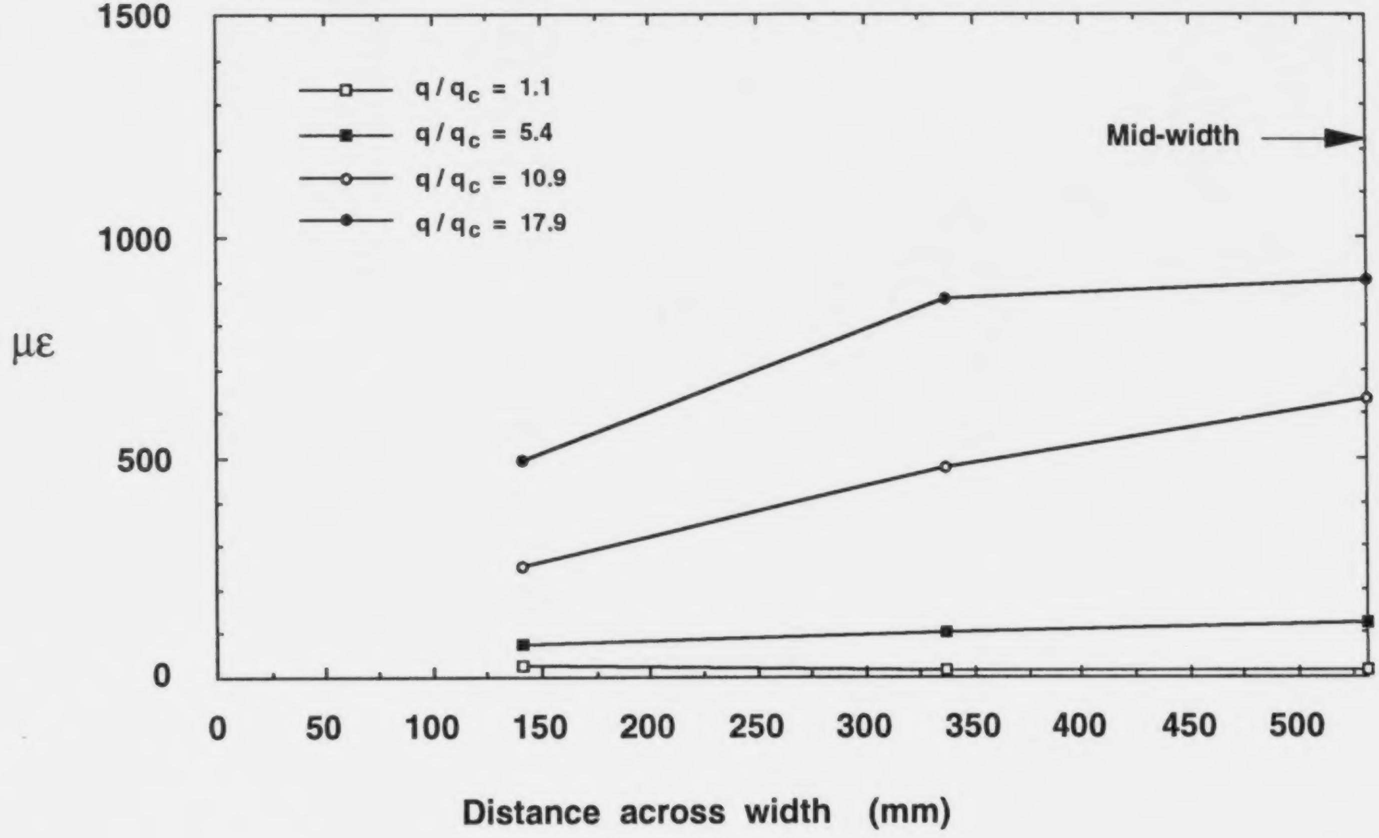

Figure 5.37 Longitudinal strains at mid-length, test P6-2

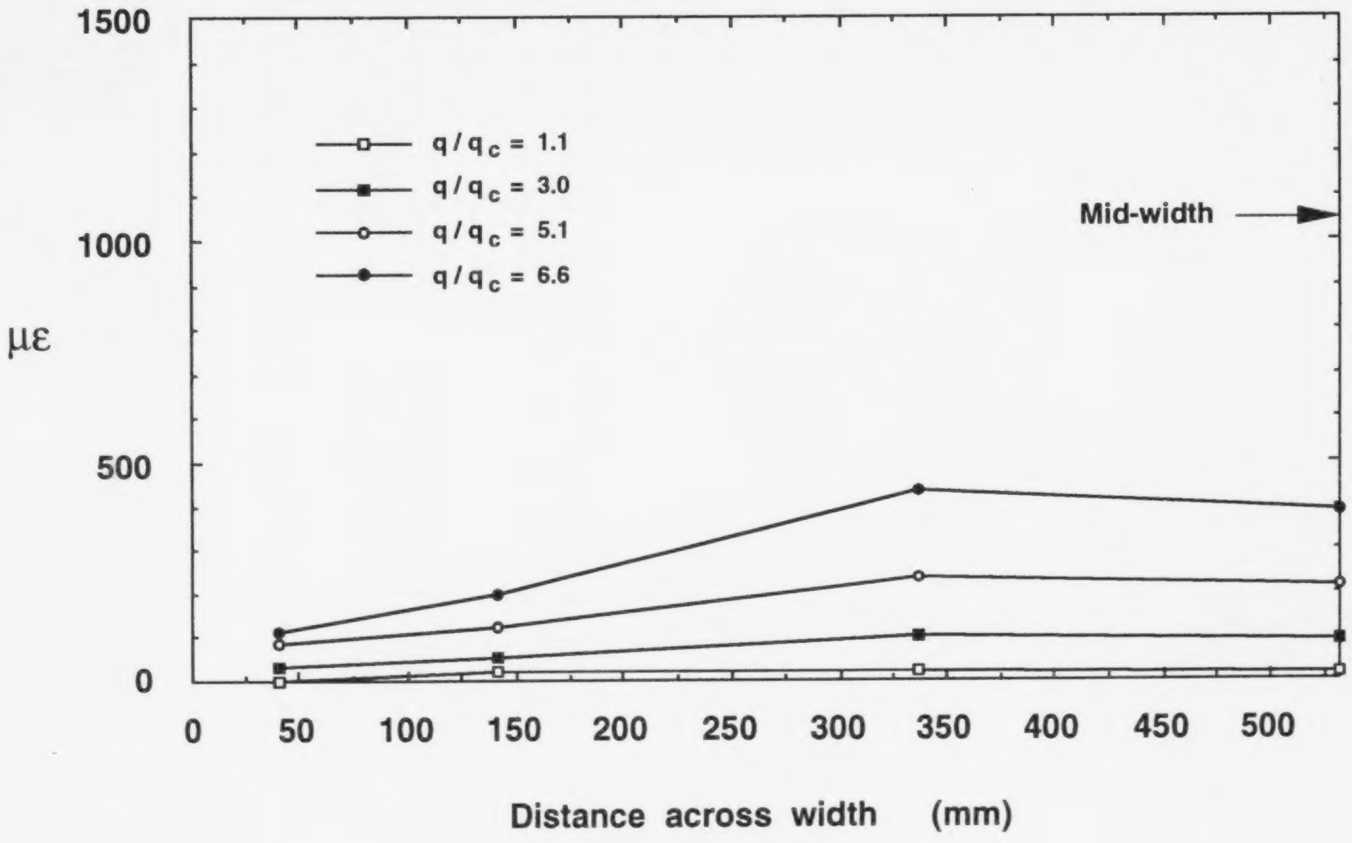

Figure 5.38 Longitudinal strains at mid-length, test P12

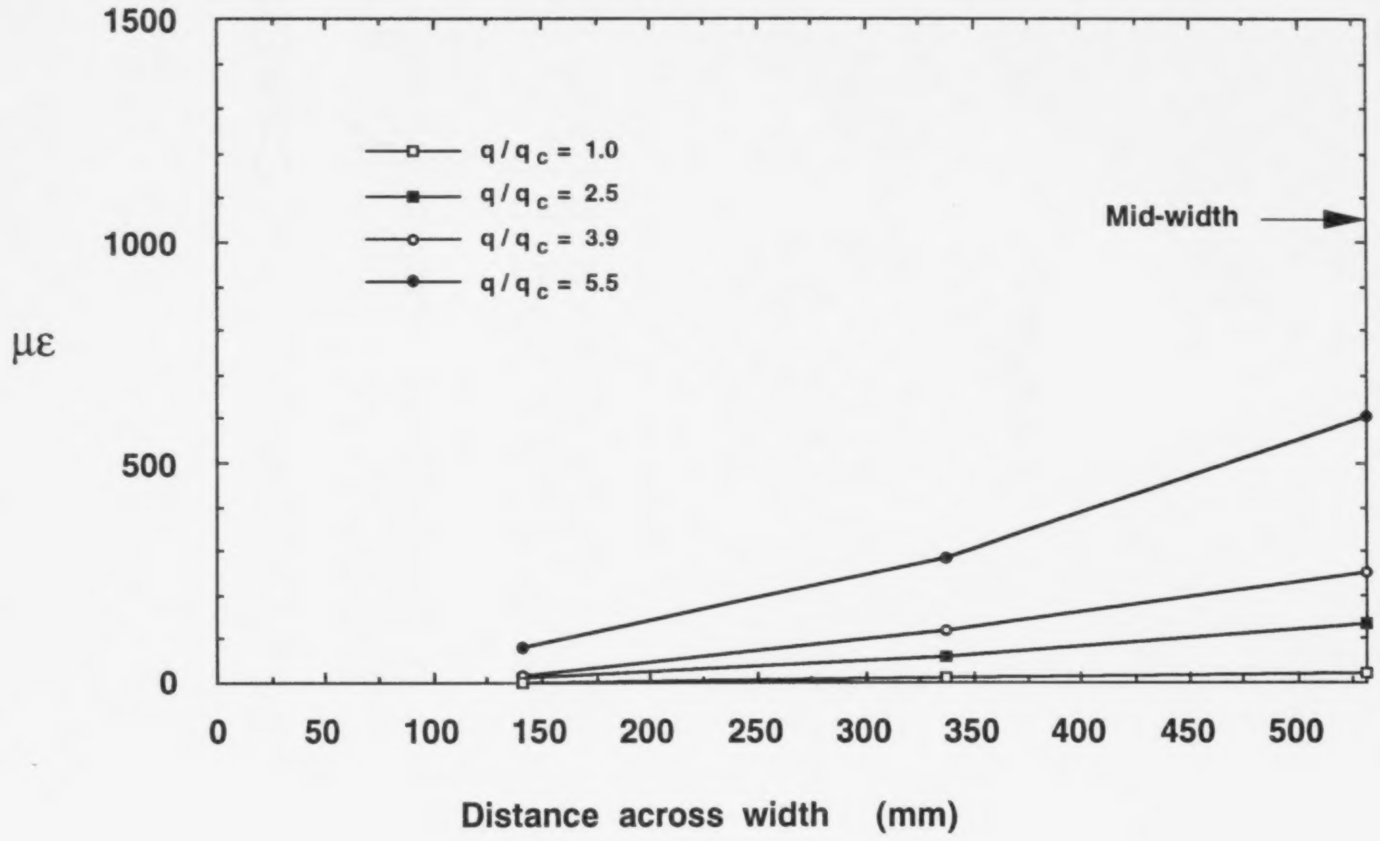

Figure 5.39 Longitudinal strains at mid-length, test P16

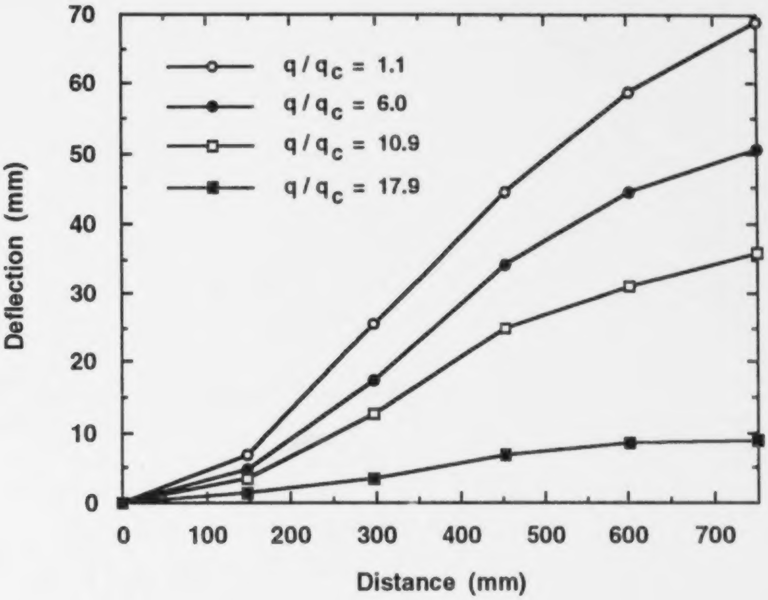

Figure 5.40(a) Deflections along diagonal, test P6-2

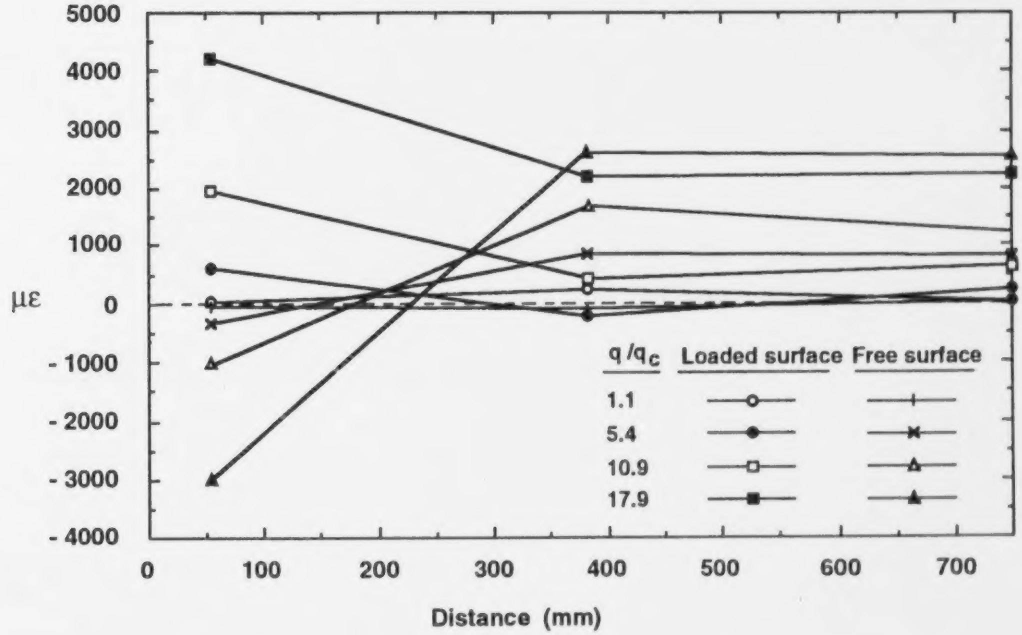

Figure 5.40(b) Strains along diagonal, test P6-2

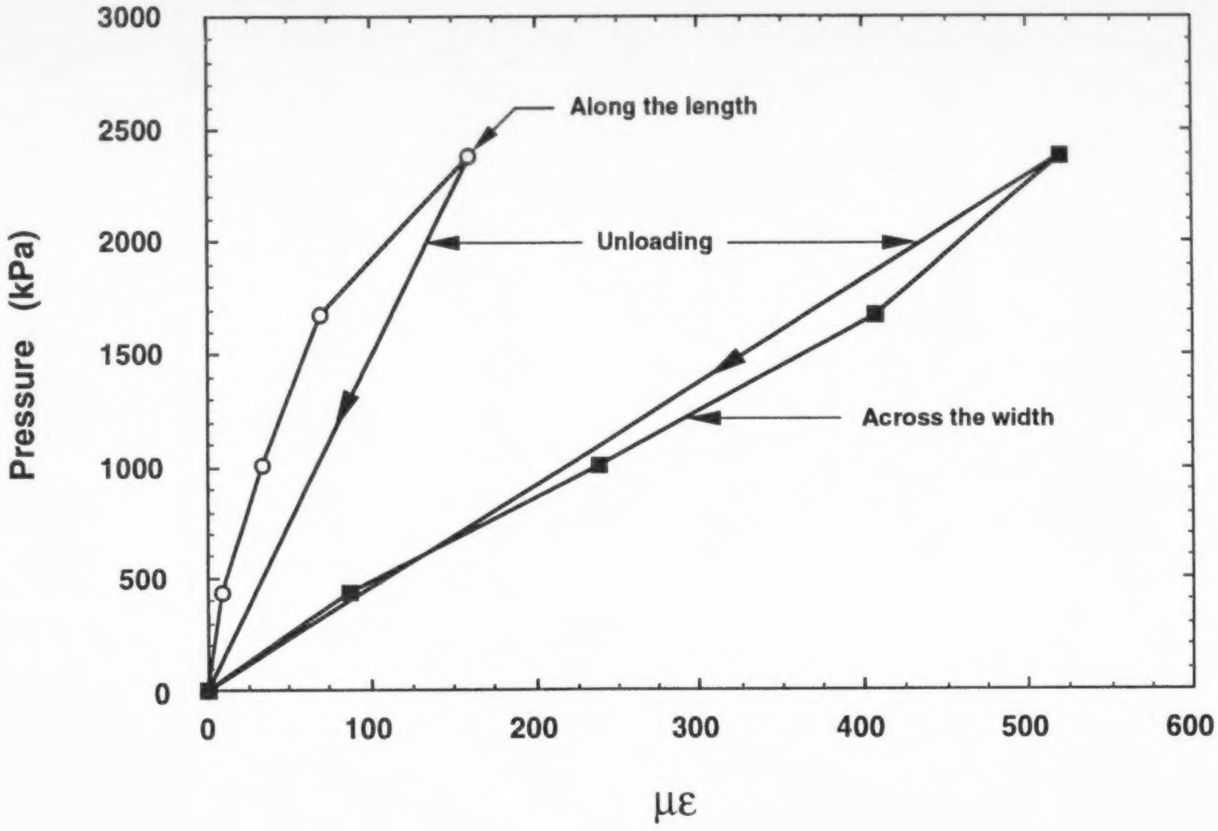

Figure 5.41 Reaction plate strains at mid-width and mid-length, test P16

6. FINITE ELEMENT ANALYSES

6.1 Program

The ADINA (Advanced Dynamic Incremental Nonlinear Analysis) finite element computer program (ADINA, 1984), capable of providing solutions to structural engineering problems that involve both geometric nonlinearities due to large displacements and large strains and as well nonlinear material properties, was used to predict the behaviour of two transversely loaded steel plates. A post-processing program, used in conjunction with it, produced drawings of the deformed shapes. The model plates were assumed to have an aspect ratio (width/length) of zero. The significant features of the ADINA program that were used in the analyses are given in Table 6.1.

The plane strain elements used are consistent with an aspect ratio for the plates of zero. For such plates, no straining can occur in the longitudinal direction and straining is restricted to the transverse and through-thickness directions. In fact, the test plates had an aspect ratio of 0.34 and straining did occur in the longitudinal direction as discussed in Chapter 5. This straining varied from zero at the longitudinal edges (equivalent to a state of plane strain there) to a maximum tensile strain at mid-width. Thus the use of plane strain elements will underestimate the stresses in the longitudinal direction wherever tensile straining in that direction occurs. Furthermore, other things remaining equal, because increased stresses in the longitudinal direction lead to more restraint on the specimen, the ADINA results with lesser stresses would be expected to give greater deflections and therefore portray the plate as being softer than it is.

The same conclusion is reached by comparing the maximum deflections of three plates with aspect ratios of zero, one, and an intermediate value under the same load. The square plate of aspect ratio one has membrane stresses at its centre point of equal value in both directions and deflects the least. The plate with aspect ratio zero deflects the most and has the least longitudinal stresses (in the elastic range these equal Poisson's ratio times the transverse ones). The plate of intermediate aspect ratio has intermediate longitudinal stresses and deflections.

Because in the ADINA program it is assumed that there is zero volume change in the inelastic range the effective value of the inelastic strain ratio is 0.50. As discussed in Chapter 2, elastic and inelastic dilitation leads to a lesser value of Poisson's ratio. A decrease in the inelastic strain means decreased restraint and therefore greater deflections.

6.2 Models

Test P6-2 and test P12 with plate thicknesses of 7.1 mm and 13.4 mm, respectively, were modelled. By using symmetry only one-half of the plate width needed to be modelled.

6.2.1 Discretizations

The complete two-dimensional through-thickness mesh used to model plate specimen P6-2 consisted of 230 elements and 863 nodes. Two hundred elements were used to model the test plate while the remainder were used to describe the weld metal that joined the plate edge to a rigid boundary. Figure 6.1 shows the mesh and nodal boundary conditions, loading, and the smaller elements at the edge of the plate where larger strains were anticipated. None of the nodes joined to the reaction plate displace. Two non-rectangular elements were used to model the contour of the weld against the backing.

Model 2 as shown in Fig. 6.2 and for test plate P12 had 144 elements and 547 nodes. Twelve elements were used for the weld.

The models used in this work, as compared to those analyzed previously by Ratzlaff and Kennedy (1986), in addition to having a greater number of elements, especially near the edges where large strains were expected to occur, also modelled the boundary conditions more realistically.

6.2.2 Material Properties

True stress-strain curves based on 6 uniaxial tension tests for model 1 and 5 tests for model 2 were used to model the material behaviour. Engineering stresses and strains obtained in the tests were transformed to true stresses and strains by (Lay, 1982)

$$[6.1] \qquad \sigma_t = \sigma_e (1 + \varepsilon_e)$$

and

$$\varepsilon_t = \ln(1 + \varepsilon_e) \qquad [6.2]$$

where the subscripts e and t refer to engineering values and true values, respectively. Consistent with the above expressions the fracture stress was obtained, as the average of the number of tension tests performed, as the fracture load divided by the fracture area and the fracture strain as

$$\varepsilon_f = \ln(A_o / A_f) \qquad [6.3]$$

as given by Hosford and Caddell (1983) and verified by tests of MacGregor (1940).

For model 1 of plate P6-2 the mean fracture strain obtained was 660000 $\mu\varepsilon$ and the mean fracture stress was 680 MPa. The true uniaxial stress-strain curve was modelled as 7 linear segments (the maximum permitted as input to the program) as given in Fig. 6.3. The fracture strain and stress determined for model 2 of plate P12 was 580000 $\mu\varepsilon$ and 715 MPa respectively. The true stress-strain curve consisting of 7 linear segments used in this model is also shown in Fig. 6.3. Table 6.2 gives true stress and corresponding true strain values used to describe the steel in the two models.

The stress-strain characteristics of the weld metal were based on uniaxial tension tests of Gagnon and Kennedy (1987) on E48018 electrode weld metal and were transformed into true stresses and strains. As the weld metal never failed in any of the tests performed here the true stress-strain curve was extended to a fracture stress and strain of 820 MPa and 900000 $\mu\varepsilon$ respectively, greater than the values for the plate. The linearized true stress-strain curve used for the weld metal in both models is shown in Fig. 6.4. Because no stress-strain data were available for the very small volume of material in the heat affected zone (HAZ), the stress-strain characteristics of this zone were not modelled in the analysis, i.e., it was assumed to have the same characteristics as the plates themselves. The heat affected zone would be expected however to have a higher strength and reduced ductility as compared to the steel plates. Matic and Jolles (1987) in a finite element model of groove welds used a fracture strain of 0.05 times that of the steel for the HAZ adjacent to the weld metal but did not present a rationale for this choice. Bond (1993) who studied the inelastic membrane behaviour of steel plates used a HAZ fracture strain of 70000 $\mu\varepsilon$ but without substantiation.

A first estimate of the failure strain in the HAZ can be determined from the finite element analysis carried out here. In Figs. 6.5 and 6.6, discussed in more detail later, the true strains across the plate thickness along the line a-a as shown in Figs. 6.7 and 6.8 at the toe of the weld are plotted for various values of the normalized load q/q_c. Point D on Figs. 6.5 and 6.6 gives the maximum true strain at the toe of the weld and therefore in the heat affected zone at the failure loads. These strains of 170000 $\mu\varepsilon$ and

88000 $\mu\varepsilon$ respectively correspond to 0.26 and 0.15 of the mean fracture strains as shown in Fig. 6.3 for the two steels used in the finite element models.

A better estimate, not performed here, could be obtained by inserting additional small elements to model the HAZ, using as a first approximation the failure strain obtained above with some estimate of the higher strength. Several such iterations should lead to convergence of a failure strain and stress consistent with the test observations. It is noted in Figs. 6.5 and 6.6 that the strain distribution through the thickness is decidedly nonlinear. This is attributed to the strain concentration at the toe of the weld where the cross-section suddenly increases in thickness from the test plate thickness to the test plate thickness plus the weld backing and reaction plate thicknesses.

6.2.3 Loading

The initial rate of loading for model 1 (plate P6-2) was 15.8 kPa per load step while that of model 2 (plate P12) was 117.9 kPa. Beyond the early elastic range of behaviour the load increments were decreased to about one-half that used at the outset. Loading was continued until the maximum strain, ε_f , was reached at one or more locations within the models at which the analysis was programmed to stop.

6.3 Results

The load-deflection curves obtained from the finite element analyses of model 1 (plate P6-2) and model 2 (plate P12) are shown in Figs. 6.9 and 6.10, respectively. Failure was considered to have occurred when the maximum true strain of 660000 $\mu\varepsilon$ for model 1 or 580000 $\mu\varepsilon$ for model 2 was reached at one of the integration points. These critical integration points were close to the toe of the weld, the lower end of line a-a in Figs. 6.7 and 6.8 which are drawn for the maximum load the test specimens sustained. The failure strain is reached in the plate where the largest tensile strains due to axial tension and bending occur. The maximum load and deflection for the models are 4066 kPa and 158 mm for model 1 and 11,580 kPa and 178 mm for model 2. These values correspond to a normalized load q/q_c and normalized deflection W_m/h for model 1 of 51.6 and 22.2 respectively and for model 2, 40.0 and 13.3 respectively (The maximum test loads were considerably less than that corresponding to the maximum strains as discussed subsequently in Chapter 7).

Shown in Fig. 6.5 are strain distributions, obtained from the analysis of model 1, through the plate thickness at the plate edge along line a-a of Fig. 6.7. The distributions correspond to five nondimensional load levels between 1.0 and 17.7. Tensile strains are taken to be positive. At a normalized load of 1.0 the strain distribution is essentially linear with zero straining just above the mid-thickness as indicated by point A in the figure and compressive and tensile strains above and below the neutral surface, respectively. For larger loads up to about $q/q_c = 9.6$, the neutral surface location moves upward, reaches a maximum (point B in Fig. 6.5) and then reverses its trend as shown by point C that corresponds to a normalized load of 17.7. The analyses of both models showed that subsequently the neutral surface location moved downward at a decreasing rate for loads up to the postulated failure load. At any significant load levels the strain distribution through the thickness in nonlinear. In each of the analyses and for all load levels the largest tensile straining occurred on the loaded surface at the toe of the weld (at the lower end of the line a-a on Figs. 6.7 and 6.8) as shown in Figs. 6.5 and 6.6. Point D in these figures shows the maximum computed tensile strain at the test failure load. As discussed previously these maximum strains are only a fraction of the fracture strain of the plate and are indicative of reduced ductility in the heat affected zone. Similar behaviour occurred in model 2 as shown in Fig. 6.6 where points A and B are also plotted.

The variation of strains obtained from the ADINA analyses on the top (free) and bottom (loaded) surfaces across the half-width of the plate at mid-length are shown in Figs. 5.21, 5.25, 5.29, and 5.33 for test P6-2 and Figs. 5.22, 5.26, 5.30, and 5.34 for test P12, at a series of load levels.

Table 6.1 Features of the ADINA program

Feature	Type Implemented
Element type	2-D nonlinear serendipidy, plane strain
Maximum number of nodes per element	8
Integration points for stiffness calculations	3 (9 per element), and 2 (4 per element)
Loading	2-D pressure loading
Equilibrium iteration method	Full Newton (no line search)
Convergence criterion	Energy
Energy convergence tolerance	0.001
Stiffness matrix reformation	after each time (load) step
Time function for loading	4 point piecewise-linear curve
Type of analysis	Total Lagrangian formulation
Material model	Elastic-plastic with isotropic hardening
Material characteristics input	7 point piecewise-linear stress-strain curve
Yield criterion	von Mises yield surface

Table 6.2 ADINA program material models

Model	$\mu\varepsilon_t$	σ_t (MPa)
P6-2 (model 1)	1400	292.5
	23000	295.0
	43200	395.9
	63800	437.0
	109800	495.5
	153300	527.8
	660000	680.0
P12 (model 2)	1550	319.4
	19800	325.8
	37300	422.7
	54500	475.2
	104400	563.4
	151900	607.6
	580000	715.0

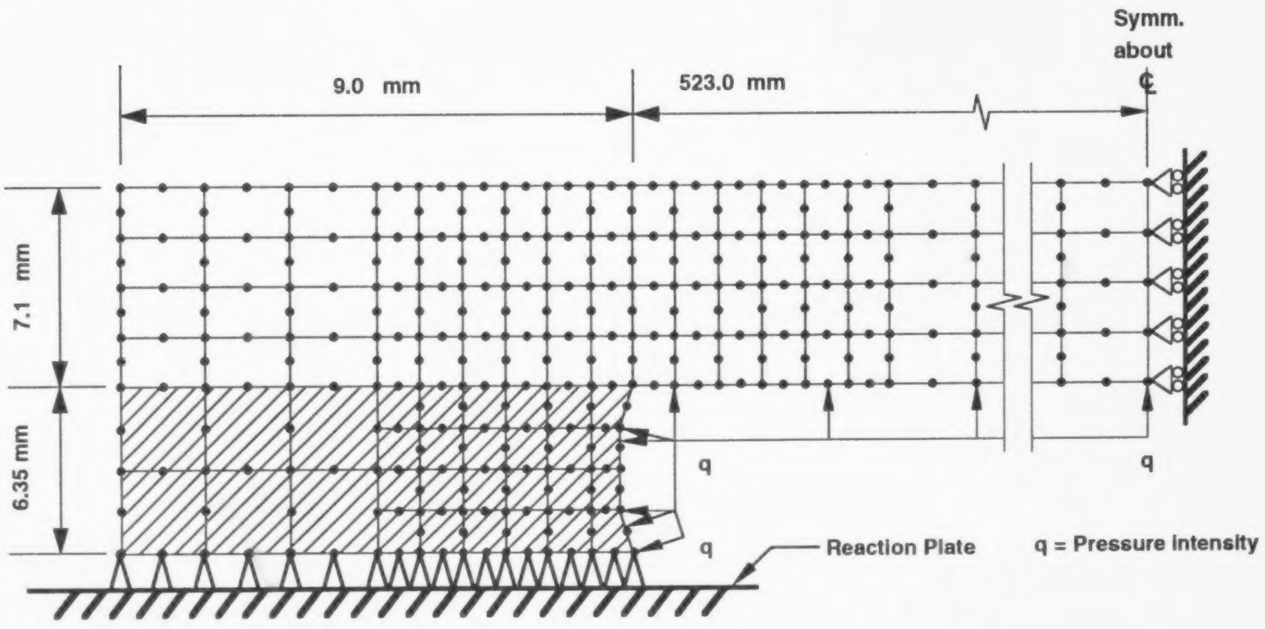
Symm.
about
℄
9.0 mm
523.0 mm
7.1 mm
6.35 mm
q
q
q
Reaction Plate
q = Pressure intensity

Note: hatched area indicates weld metal

Figure 6.1 Finite element model 1

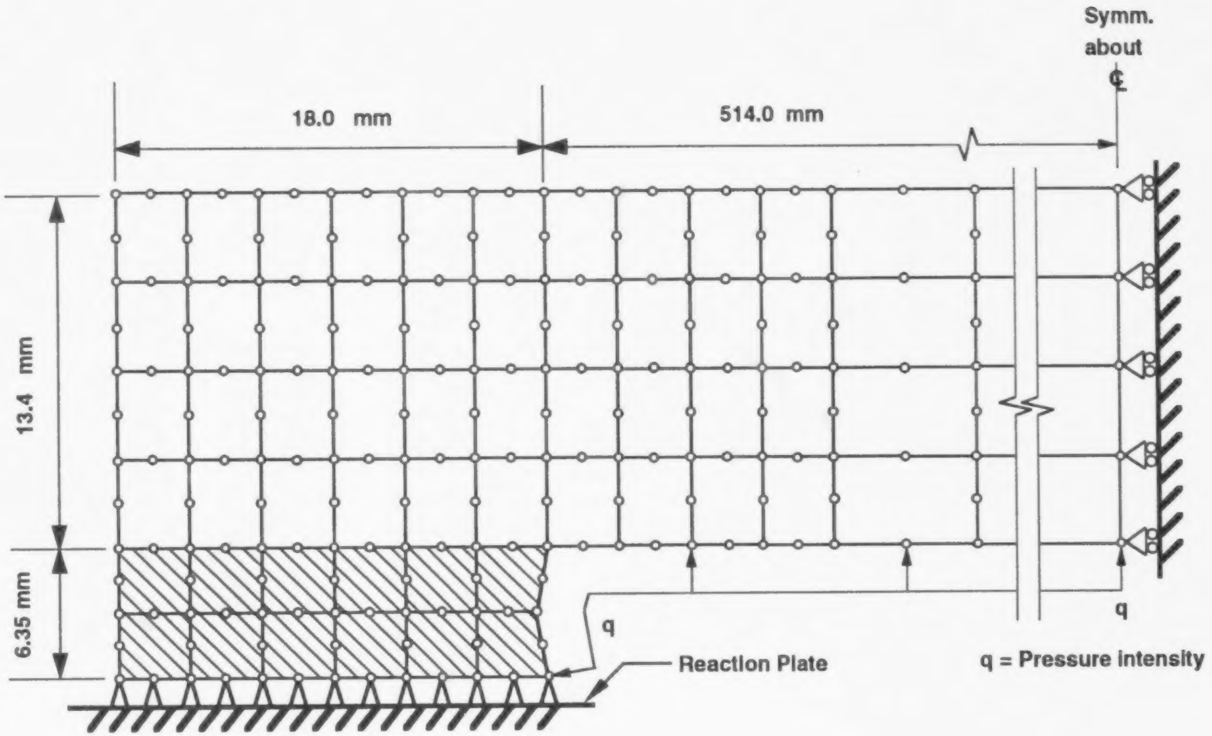
Symm.
about
℄
18.0 mm
514.0 mm
13.4 mm
6.35 mm
q
q
Reaction Plate
q = Pressure intensity

Note: hatched area indicates weld metal

Figure 6.2 Finite element model 2

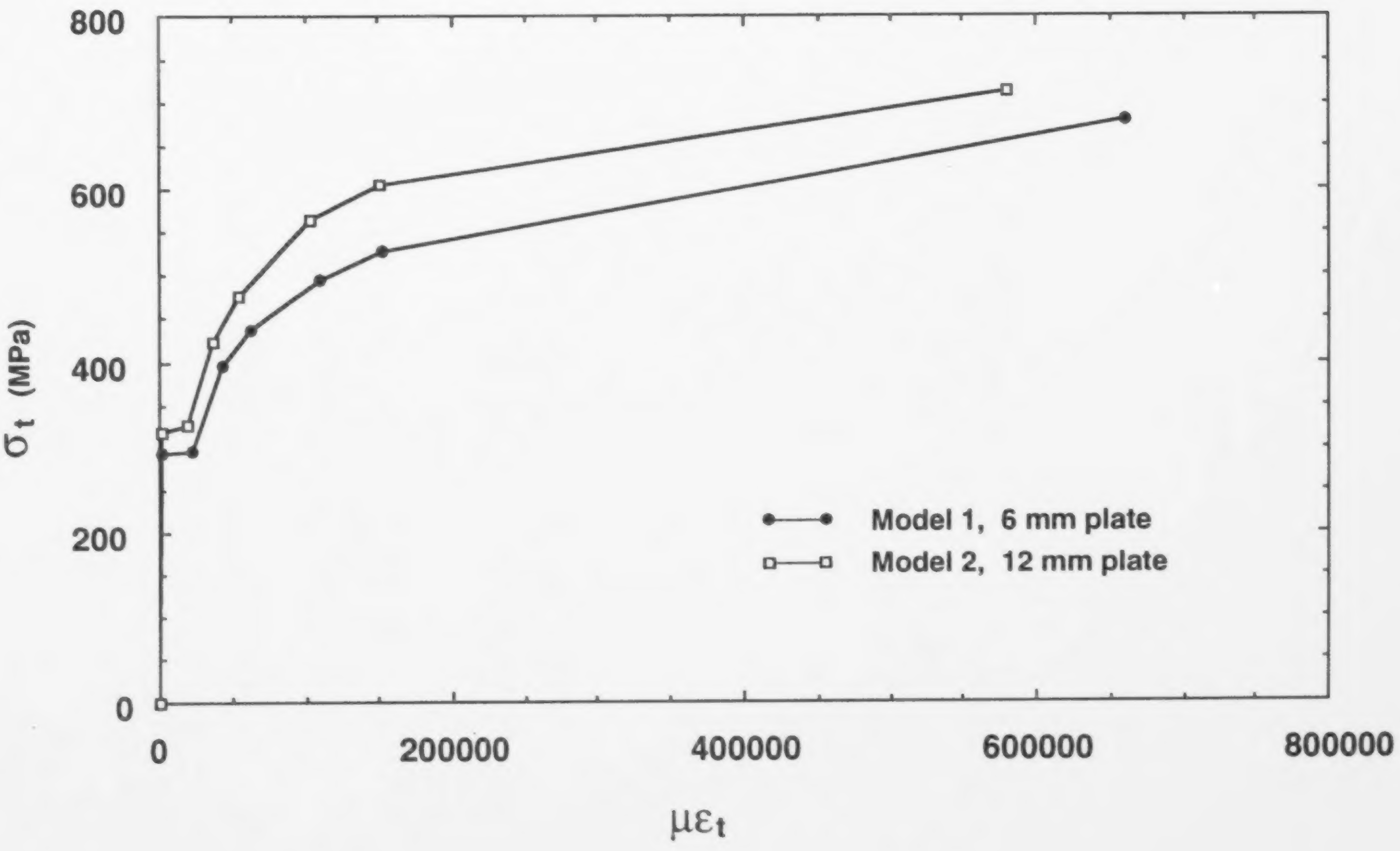

Figure 6.3 True stress-strain curves for steel plates used in the analyses

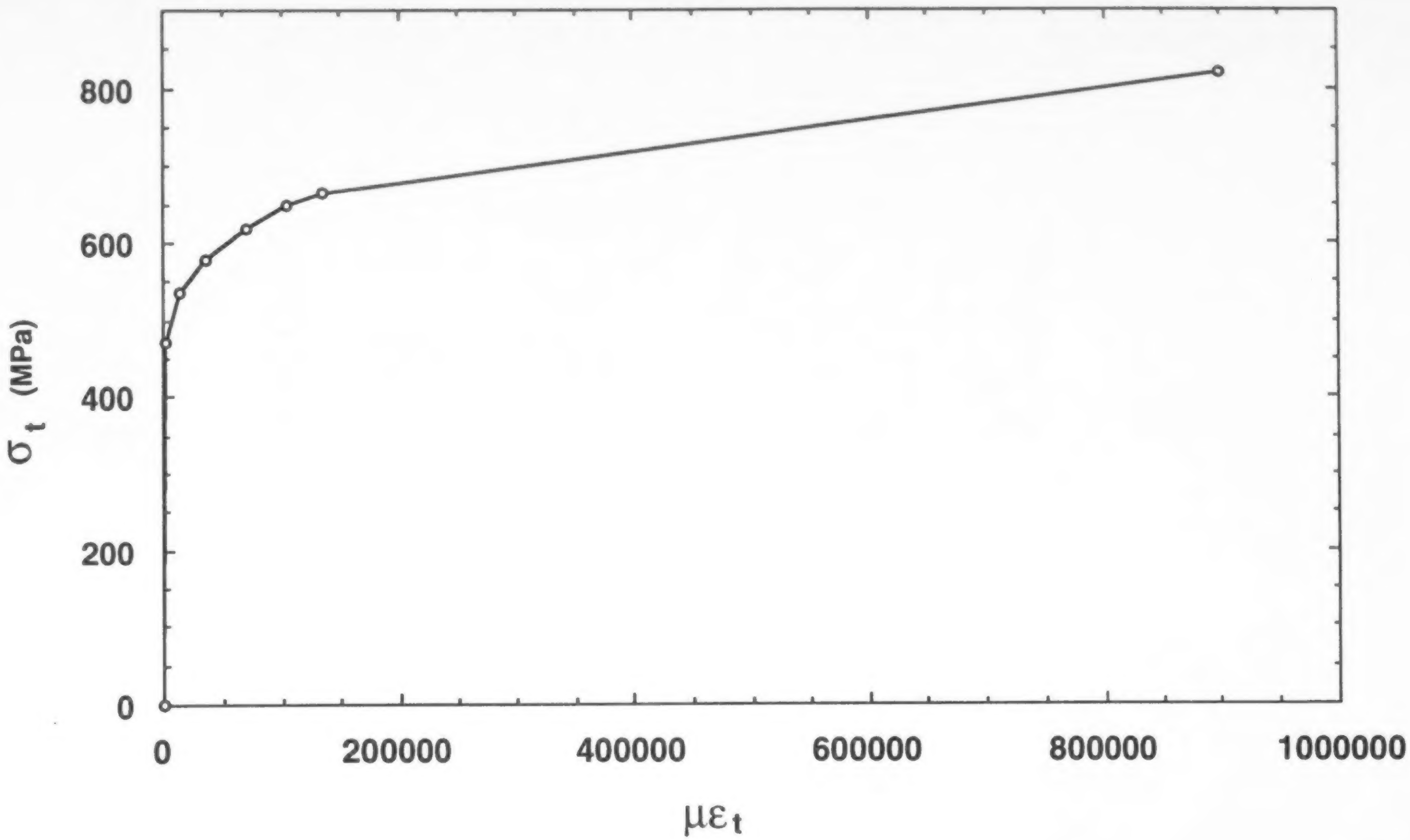

Figure 6.4 True stress-strain curve for weld metal

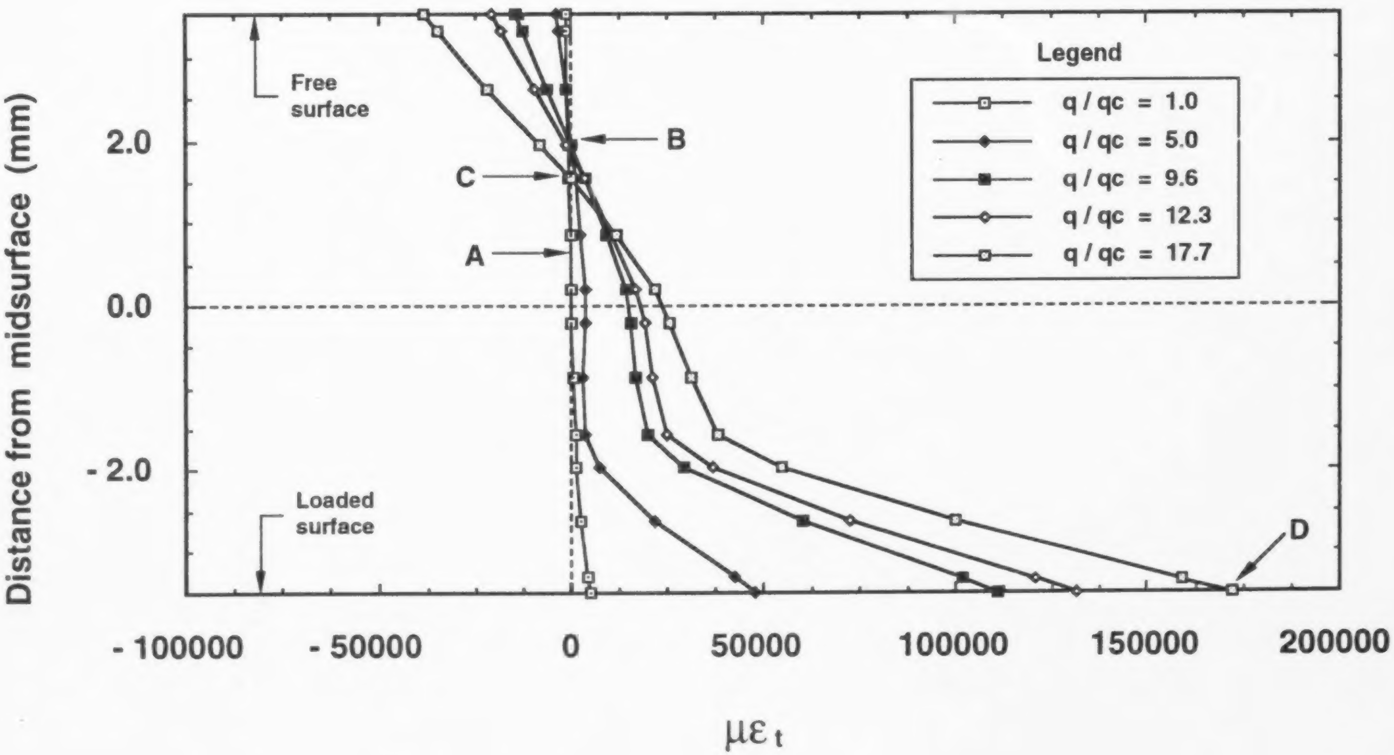

Figure 6.5 Strains at plate edge, model 1, 6 mm plate

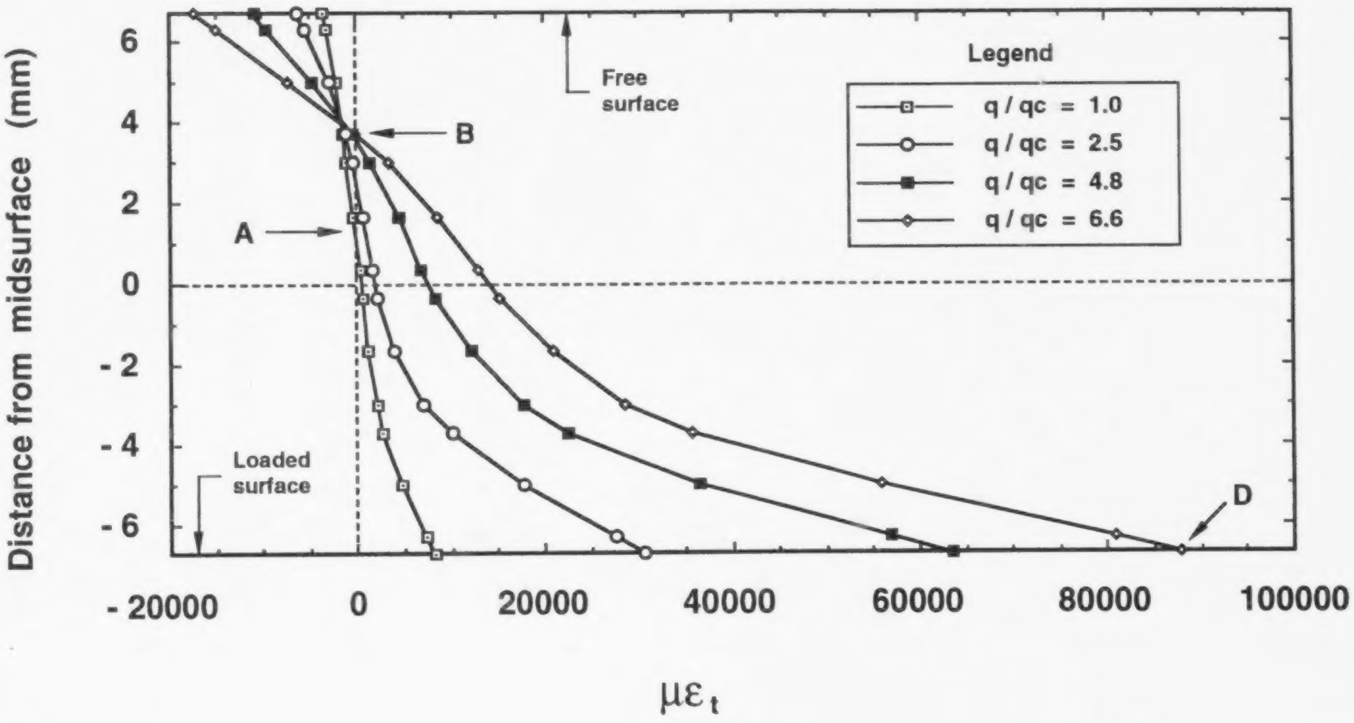

Figure 6.6 Strains at plate edge, model 2, 12 mm plate

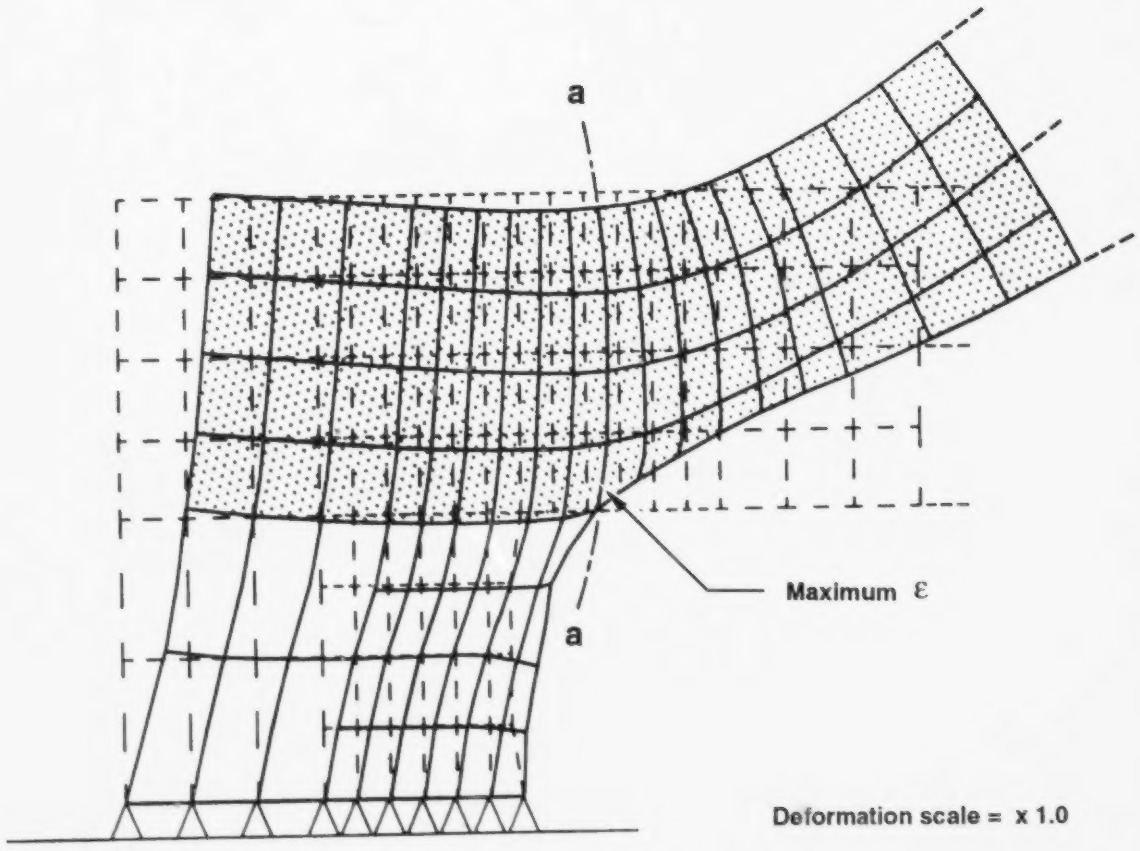
a
Maximum ε
a
Deformation scale = x 1.0

Figure 6.7 Deformed mesh at plate edge, model 1, plate P6-2, q/qc = 51.6

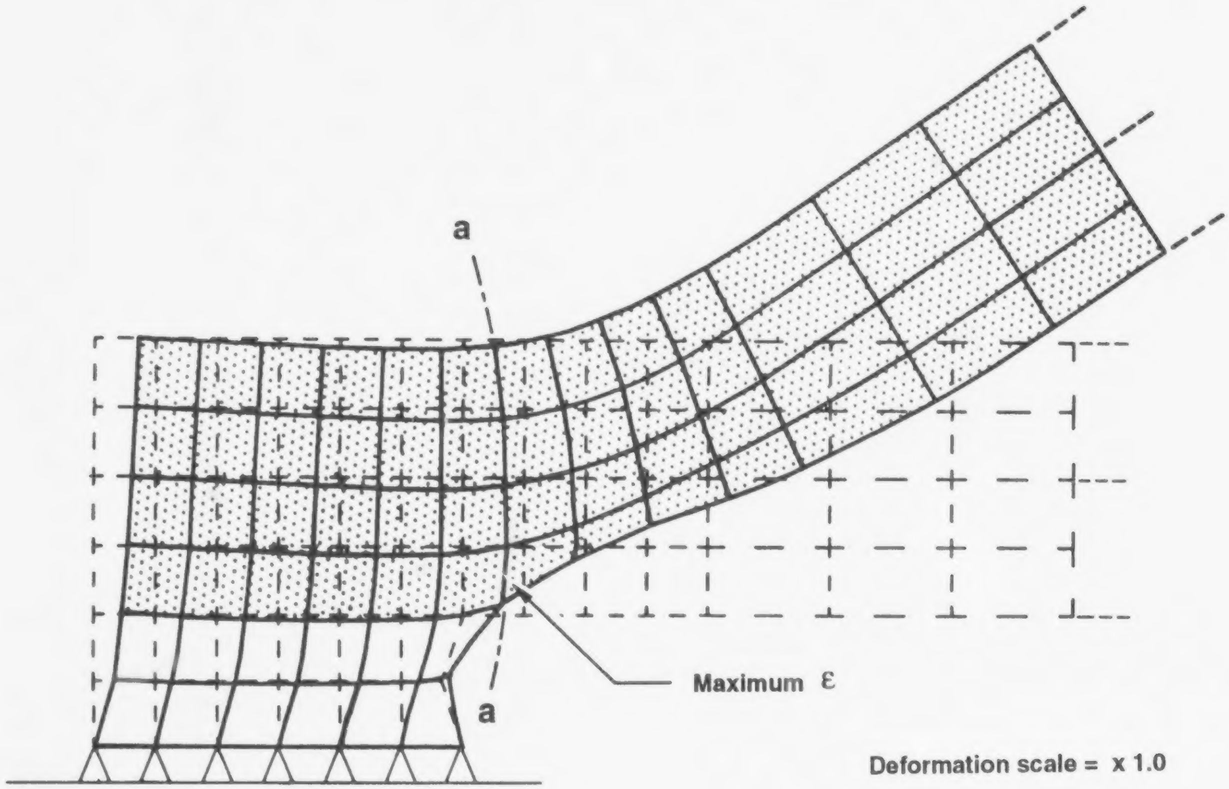
a
a
Maximum ε
Deformation scale = x 1.0

Figure 6.8 Deformed mesh at plate edge, Model 2, plate P12, q/qc = 40.0

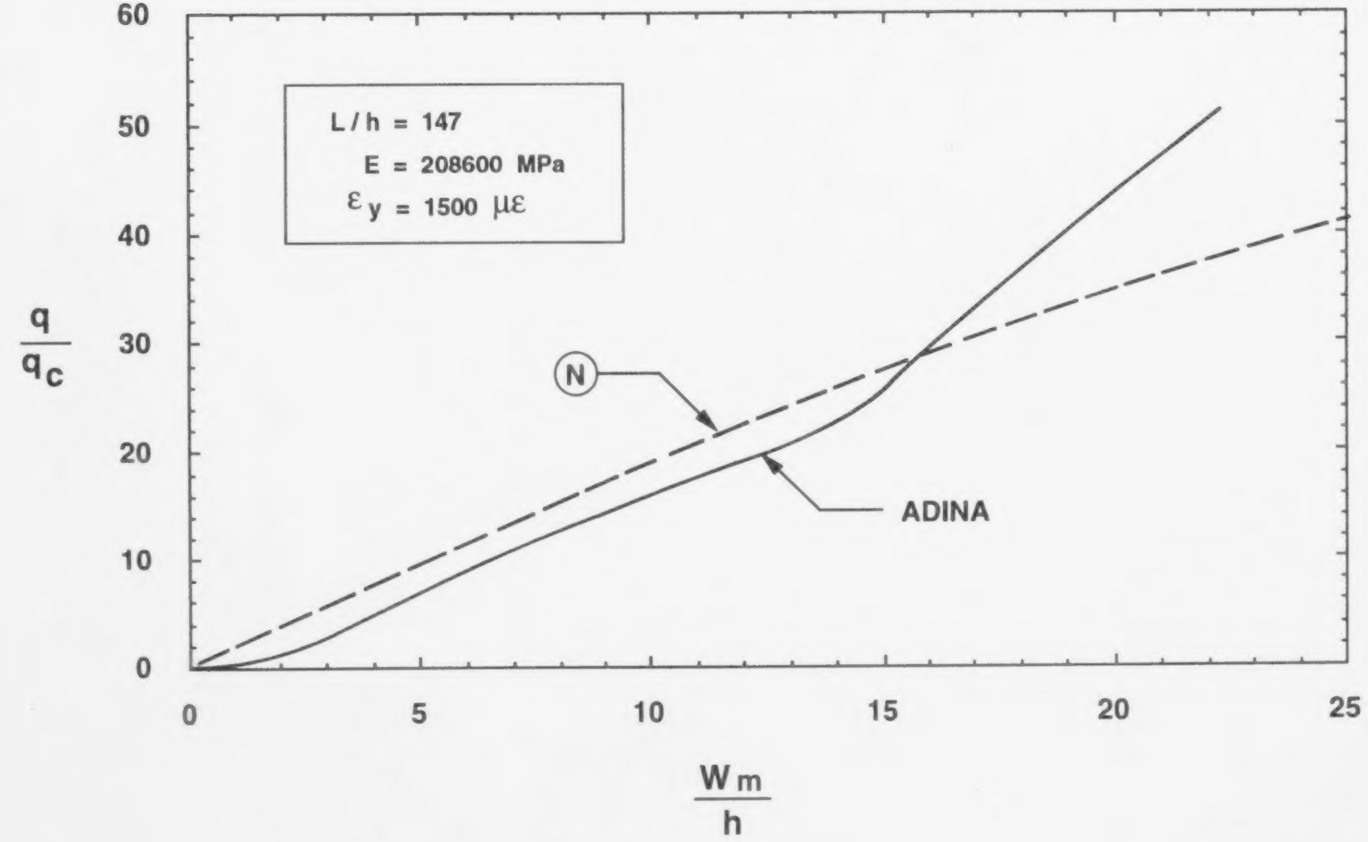

Figure 6.9 Model 1 Load-deflection results

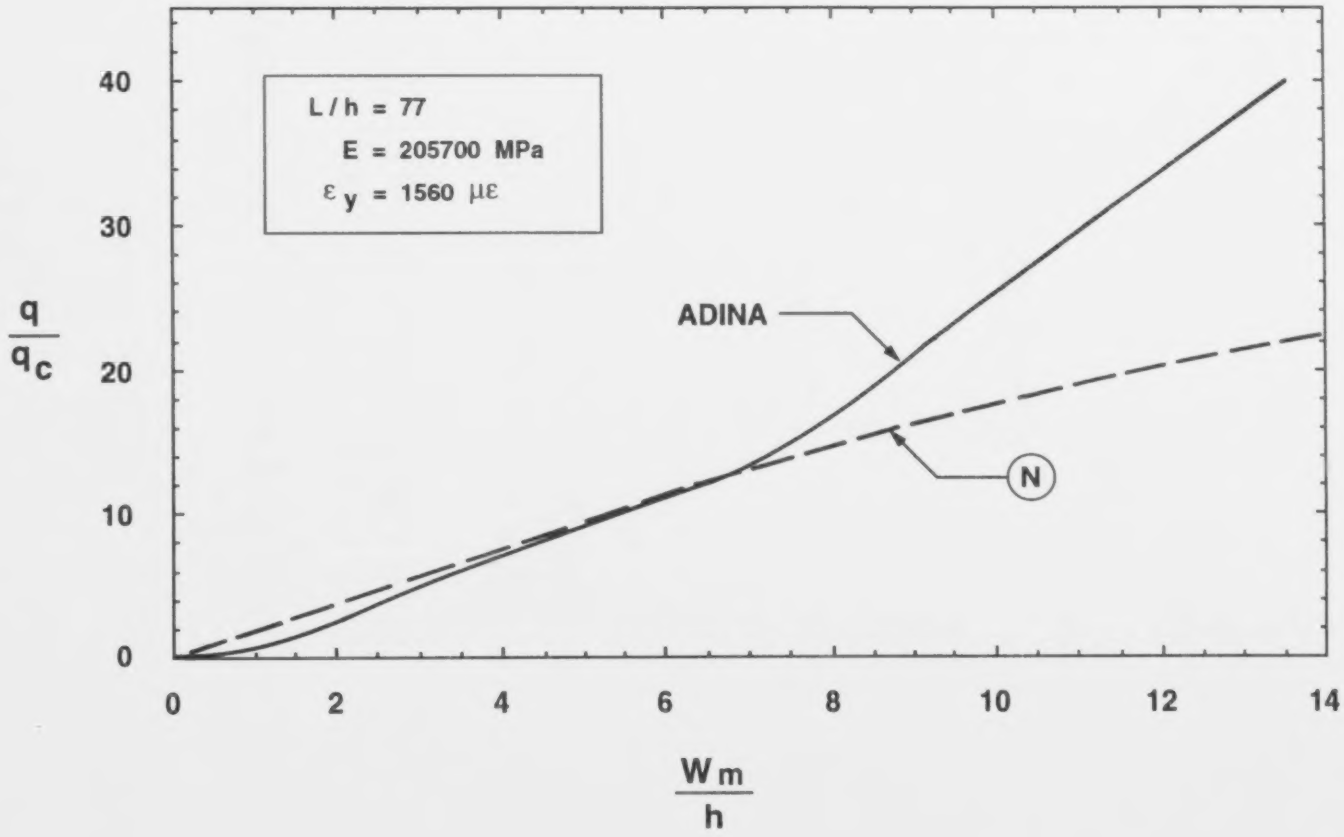

Figure 6.10 Model 2 Load-deflection results

7. ANALYSES OF TEST RESULTS

7.1 Overall Behaviour

The overall behaviour is succinctly described by plotting the transverse load intensity against the maximum deflection at the mid-width of the mid-length. In Figs. 7.1 through 7.4 the nondimensional loads and deflections are plotted for tests P6-1, P6-2, P12 and P16, respectively. For each test the significant portions of the behavioural domains as described in Chapter 2 form the background. These behavioural domains are based on bi-linear stress-strain and moment-curvature relationships, plates of zero aspect ratio and inelastic strain ratios of 0.30 or 0.50.

The assumption that the moment-curvature relationship is bi-linear means that the plastic hinge (which forms at the edges) has no lateral extent and therefore the membrane extends across the entire width, equivalent to assuming that the plate is very thin. This assumption also means that under hydraulic pressure the deflected shape is part of a circular arc from edge to edge. In fact, this shape can only be approached at high loads. Initially, when the plate is acting chiefly in flexure, that is before significant membrane action has developed, the deflected shape will be that of a fixed-ended beam with negative curvature extending over 0.2113 of the width on either side where points of zero curvature exist. With increased pressure the plate tends to form a circular shape and as discussed subsequently the points of zero curvature are forced to migrate towards the edge. At the point of zero curvature, defined as the location where no bending strains exist, tensile membrane straining must be present. Between the points of zero curvature the central portion of the plate, tending to form a circular arc under uniform pressure, must have greater strains on the unloaded or free surface than on the loaded surface. Therefore for all practical load levels for which the hinges have not moved all the way to the edge, the curvature of the plate acting like a membrane will vary from zero at the point of zero curvature to that, in the limit, of a circular arc consistent with the uniform pressure loading. As the domains are based on hinges forming at the edges, the real behaviour may be expected on this basis alone to deviate from them.

Examining Fig. 7.1, the initial portion of the test curve lies to the left of the lower domain, indicating that the test plate was more rigid than assumed. This is attributed to the additional stiffness of the test plate with an aspect ratio of 0.34 as compared to the derived domain curve based on a zero aspect ratio as discussed previously in Section 6.1. The test results fall to the right and below point B indicating more flexible behaviour. This could arise, as discussed in Section 2.2.2, because of the assumption that the moment-curvature relationship is bi-linear when, in fact, significant curvature at the edge, and attendant straining, is required before the hinge forms. Additional deflections beyond the domain values would therefore result. Beyond point

B in the upper domain, the test results climb above the lower boundary based on an inelastic strain ratio of 0.30. The curve N' representing inelastic membrane action and on which one test point lies is based on an inelastic strain ratio of 0.39. The overall behaviour is therefore represented fairly well by the behavioural domain; first with flexural-membrane action, second the flexural action becomes less significant and is restricted to the edge zone with membrane action dominating, and progressing into inelastic membrane action with an inelastic strain ratio of less than 0.50.

From Fig. 7.2 the test behaviour of specimen P6-2 is remarkably similar to that of specimen P6-1, lying to the left of the lower domain initially, falling below and to the right of point B, and then rising to lie in the upper domain. Curve N' drawn in this figure, similarly to that of test P6-1, is based on an inelastic strain ratio of 0.37 as determined from the uniaxial tension tests. The ADINA results (model 1) follow the test results closely with two deviations. In the lower domain the ADINA results initially lie along the line representing elastic flexural membrane behaviour for a plate with zero aspect ratio, as they should, because of the use of plane strain elements. Once significant inelastic membrane action has developed the ADINA results lie significantly above the test results and approach the upper limit of the upper domain, consistent with the fact that both of these predictions are based on an inelastic strain ratio of 0.50.

The overall test behaviour of specimen P12 in Fig. 7.3, plotted to a different scale than Fig. 7.1 and 7.2, agrees with that of specimens P6-1 and P6-2. Curve N' in this figure has been drawn with an assumed inelastic strain ratio of 0.34. The ADINA model 2 results, consistent with those of model 1, also bear the same relationship to specimen P12 as did model 1 results to specimen P6-2. In particular, the results in the lower domain fall initially along the elastic flexural membrane curve before progressing to the right of point B. The model 2 results in the inelastic range rise above the test results and even eventually above the upper limit of the upper domain as can be deduced from Fig. 6.10 where the curve is plotted to higher loads. This also applies to model 1 (see Fig. 6.9). That the model 2 results behave in this manner arises from two sources: (i) the model as described previously takes into account the entire stress-strain curve and therefore considers the increased strength beyond the onset of strain hardening where curve N does not, and (ii) the ADINA model takes into account the reverse curvature at the edge, reducing the portion of the plate that acts in pure membrane action and therefore properly reflects reduced deflections.

The test results of specimen P16 plotted in Fig. 7.4 are in essential conformance with the behavioural domains. Again, the test data lie to the left of the lower domain and where inelastic membrane action exists the data fall within the upper domain. However, when compared with the results of specimen P12 (Fig. 7.3) the test curve in Fig. 7.4 passing through point B is somewhat above that of specimen P12. This is considered to be due to the greater edge effect in the thicker specimen which, as discussed in relation to specimen P12, reduces the deflections (This reduction is estimated to be in the order of 0.25 times the plate thickness). The curve N' in Fig. 7.4 has been plotted with an assumed inelastic strain ratio of 0.46. The larger value of 0.46 compared to a value of about 0.37 for the other three tests is considered also to be manifested in the reduced deflections due to the edge effects.

7.2 Deflections

7.2.1 Deflections Across The Width At Mid-Length

Deflections across the width at mid-length are plotted in Figs. 5.11 to 5.14 for 4 values of nondimensional pressure for tests P6-1, P6-2, P12 and P-16, respectively. The comparisons between the deflections obtained from the ADINA models and from the LVDT's for tests P6-2 and P12 are given in Section 7.2.3.

The deflections at comparable load levels are remarkably similar for the different tests. The extent of reverse curvature near the edge reduces with load and the curvature in this region becomes more pronounced. The curvature at a given load is also more pronounced for the thinner specimens. As the point of zero curvature, marking the end of the reversed curvature near the edge, migrates towards the edge with increasing load, more and more of the plate between the symmetric points of zero curvature acts as a membrane.

7.2.2 Deflections Across The Width At Other Locations

In general, surface level indicator (SLI) deflections given in Figs. 5.15 through 5.19 for tests P6-2 and P16 show:

(i) reversed curvature of the plate surface, concave upwards near the plate edges and concave downwards elsewhere. The point of zero curvature lies closest to the plate edges at locations nearest mid-length. With increasing load, the point of zero curvature moves closer to the plate edges;

(ii) deflections recorded across the width near mid-length (1380 mm from one end) confirm the LVDT readings;

(iii) at about 500 mm (one-sixth of the length) from the ends, the maximum deflection at mid-width is 75% or more of the maximum deflection at mid-length and mid-width;

(iv) little or no vertical displacement occurs along the plate ends.

Figures 5.15 and 5.17 are plotted for loads calculated on the assumption that full yielding in tension along the long edges with no edge moments exists. Because of the finite plate thickness, however, the edge of the plate bends, with the bending strains decreasing to zero at the points of zero curvature. The local bending at the edges extends over about 50 mm and 75 mm for specimens P6-2 and P16, respectively. At failure (see Fig. 5.16 and 5.18), the extent of local bending decreased to about 30 mm and 65 mm for specimens P6-2 and P16, respectively , indicating, that, with increased loading, the extent of local bending decreases and more and more of the plate acts as an inelastic membrane.

From Fig. 5.19 where deflections along the length of the plate are plotted, the deflections within the middle one third of the plate length are relatively constant and show that, insofar as deflections are concerned, the effects of the ends are minimal. However, because the deflections are large, there is significant longitudinal straining in the plate as confirmed by the longitudinal strain measurements discussed subsequently.

In Figs 7.5 and 7.6 are plotted the finite element mid-surface nodal displacements near the edge for model 1 (test P6-2) and model 2 (test P12), respectively, at the test failure load (Figs. 7.7 and 7.8 show the data for the full half width of the respective plates). Also plotted in the figures is a least squares best-fit polynomial. The polynomial fits the data well. Such a curve but with a horizontal tangent and zero displacement at the toe of the weld had been used previously by McDermott et al (1974) and Ratzlaff and Kennedy (1985). These model data corroborate this previous use. Comparing Fig. 7.5 for a 6 mm plate and Fig. 7.6 for a 12 mm plate it is noted that the slope of the deflected curve at the toe of the weld is less for the 12 mm plate suggesting that the bending strain at the toe of the weld would be more for the 12 mm plate than for the 6 mm plate.

7.2.3 Deflections At Mid-Length As A Function Of Load

On Figs. 7.9 to 7.12 are plotted for specimen P6-2 the deflection of the unloaded surface at mid-length at various locations across the width as a function of the applied load. The LVDT deflection plotted for any location is the average of that obtained on the right and left hand side of the specimen. (See Fig. 3.16). The LVDT deflections are compared in these figures with those obtained by ADINA model 1 for this test.

The deflection, or really the distortion, at the toe of the weld in Fig. 7.9 shows that the surface moved downward, that is, in the opposite direction to the deflections in the clear span. This is shown in Fig. 6.7 and is attributed to the Poisson effect as the plate is strained heavily in tension and also to the fact that the end block of the plate rotates slightly clockwise. In Fig. 7.9 the LVDT and model deflection are in reasonable agreement. The LVDT became inoperative when the surface moved away from the spindle.

The LVDT and model deflection at 87 mm away from the toe of the weld, given in Fig. 7.10 are in excellent agreement.

In Fig. 7.11, for deflections at 174 mm from the toe of the weld, the model deflections are greater than those obtained by the LVDT's for lower loads and for higher loads are less. The stiffer behaviour exhibited by the LVDT measurements is attributed to the increased stiffness of the test specimen with an aspect ratio of 0.34 versus zero for the ADINA model. At higher loads this difference is masked by the use in the ADINA model of an inelastic strain ratio of 0.50 as opposed to the measured value of 0.40. Figure 7.12 of deflections at 348 mm from the toe of the weld displays the same relative behaviour as in Fig. 7.11.

Figures 7.13 to 7.16 give the deflections for test P12 at the same locations across the width at mid-length as the respective Figs. 7.9 to 7.12 for test P6-2. Note that the scales used for this set of figures is different from that for Figs. 7.9 to 7.12. These deflections parallel those for the thinner specimen. In Fig. 7.15 the apparent erratic behaviour of the LVDT's at high load levels is due to repositioning of the spindle when the specimen was unloaded.

7.3 Strain Variation With Load

7.3.1 Test P6-2

Figure 7.17 and 7.18 give the locations where transverse strains were measured across the half-width at mid-length for test P6-2 and P12 respectively. These locations are measured from the toe of the weld at location X, i.e., with respect to the net width of the plate. The measured strains are compared with the strains from the ADINA model 1 in Figs. 7.19 through 7.26 throughout the loading history. In examining these figures two strains should be kept in mind, the uniaxial yield strain of 1400 $\mu\varepsilon$ and the strain hardening strain of 23000 $\mu\varepsilon$. Recognizing that yielding is a discontinuous process, a strain gauge with a finite length may indicate any strain between the yield strain and the strain hardening strain when the stress is at the yield level. Therefore all measured (engineering) strains between 1400 $\mu\varepsilon$ and 23000 $\mu\varepsilon$ are indicative of a unique stress level, the yield stress. On the other hand because the yield plateau was given a slight positive slope for the finite element models (See Section 6.2.2) the model (true) strains on the slightly inclined yield plateau would have specific values associated with the appropriate stress level. Differences between the measured and model strains in this region therefore reflect the difference between the actual discontinuous behaviour and the continuous model behaviour and do not signify any difference in stress level. It would be expected that the model strains would increase in a continuous manner with increasing load while the measured strains in all likelihood would exhibit discontinuous behaviour or "jumps" depending on the spread of yielding within the gauge length. The shape of the measured strain versus load curve within this strain range is therefore of little significance.

In Fig. 7.19 strains at location X at the fixed edge at the toe of the weld, and on the free or unloaded side, are plotted. Measured strains (engineering strains) are compared directly to model strains (true strains) as the difference between the two for strains up to the maximum measured of about 39000 με does not exceed about 2% and is generally significantly less. The test and model strains outside of the yield plateau strains are in good agreement and show the development of significant compressive strains as would be expected. There is a delay in the increase in test and modelled compressive strains between loads of about $q/q_C = 2$ and $q/q_C = 6$ (the load increases with little increase in strain). From the load-deflection relationships, this corresponds to a significant portion of the load being carried by elastic membrane action (see Fig. 7.2). With inelastic membrane action and increased deflections, the compressive straining at this location must increase, as both the test and model show, to allow for increased curvature at the edge.

At location A (Fig. 7.17) 31 mm from the edge, where significant bending would have been expected, strains were measured on both the free and loaded sides as given in Fig. 7.20. The difference in both the measured and modelled strains for low loads on the two surfaces indicate that bending occurred. This difference increases up to a nondimensional load of about 1 and then decreases indicating a reduction in bending that persists for the model strains to a nondimensional load of about 8. Beyond this, for the model strains, the bending increases somewhat up to a value of q/q_C of about 10 before finally diminishing to zero at a nondimensional load of about 18, indicating that zero curvature exists at location A at that load. The average strain is always tensile indicative of membrane action. It increases relatively slowly up to a nondimensional load of about 9 when the average model strain equals the yield strain, 1400 $\mu\varepsilon$. Thereafter the average model strains increase rapidly up to a nondimensional load of about 15 where the strains increase less rapidly as discussed subsequently. The model strains increase slowly with load until yielding occurs, then more rapidly. The moderate increases in load over the greater portion of the yield plateau is due to the change in geometry of the membrane as it elongates due to yielding, making it stronger even though the maximum membrane stress has not changed.

The measured strains up to a load of about 6 agree reasonably well with the model strains. The rapid increase of the measured strain on the loaded side beyond this load is indicative of extensive yielding. The measured and model strains within the yield plateau of tensile straining indicate that the membrane is carrying the yield stress. The measured strains reach this value at a load of, q/q_C, of about 8 and the model strains at a load of about 10.

At location B, 81 mm from the fixed edge (Fig. 7.17), in Fig. 7.21 both the model and measured strains show a substantial difference between the strains on the loaded side and free side at a nondimensional load of 1 indicating substantial bending. The free side strains at this load are only slightly in compression and therefore significant tension exists. At a load of about 4 the model strains on the two sides are equal indicating that no bending strains exist and that the section is in tension as the strains are positive. The same tendency for the bending strains to reduce is seen in the measured strains when both strains reach the yield value in tension. Beyond a load of 4 the free side model strains exceed those on the loaded side. This difference is attributed to the strain gradient due to the curvature of the plate. At higher loads, $q/q_C = 16$, the rate of increasing strain decreases with load.

The measured strains at low loads closely follow the model strains and when yielding occurs increase rapidly although not at the same load as the model strains.

Location C (Fig. 7.17) is 131 mm from the edge. At this location, as shown in Fig. 7.20, essentially no negative (compressive) strains exist on the free side indicating that on the average the section is in tension. Whatever bending strains exist in the model disappear at a nondimensional load of about 2.5. Thereafter the free side strains exceed the loaded side strains substantially as is consistent with significant membrane curvature. At low loads the measured strains are in good agreement with the model strains and although they exhibit the same general behaviour as the model strains the break in the curves reflect that yielding occurs at different loads. The free side strains, after the load corresponding to zero curvature at this section is reached, exceed the loaded side strains with the difference representing the membrane curvature.

Locations D, E, F and G (Fig. 7.17), with the latter at the mid-width, are all remote from the edge. The corresponding strains are shown on Figs. 7.23 through 7.26. The free side strains always exceed the loaded side strains consistent with the membrane curvature. In no case is there a cross-over of strains with first one side exhibiting the maximum strain and then the other. The average strain is always a tensile strain. Again, these strains first increase slowly and then more rapidly with yielding. At both locations F and G compressive strains exist on the loaded side at low loads. These are consistent with initial bending of the plate before significant membrane action has developed.

7.3.1.1 Summary

Several distinct trends or patterns can be determined from the strain variation with load. Near the edge (Locations X, A, B and C), very distinct bending strains exist at low loads. At location A specifically, these strains increase up to the plastic collapse load ($q/q_C =$ 1.0). The bending strains gradually reduce and become zero as the point of zero moment migrates towards the edge from point C at a nondimensional load of 2.5 to point B at a load of 4 and to point A at a load of 18.

The model strains increase slowly with load until yielding occurs, then more rapidly and finally, more slowly again as discussed subsequently. The maximum measured strains did not reach the strain hardening region.

At or near mid-width compressive strains existed at low loads on the loaded surface indicating initial bending of the plates here.

The measured strains are in reasonable agreement with the finite element strains up to a nondimensional load of about 6. At the fixed edge on the free side (location X) compressive strains of over 30000 $\mu\varepsilon$ were predicted and observed at the maximum load (results from the finite element model, Fig. 6.9, give tensile strains on the opposite face at this load of 170000 $\mu\varepsilon$).

From the change in strains at the various locations with load the development of elastic and inelastic membrane behaviour can be deduced.

In the inelastic range, because of the discontinuous yielding of the actual plate, the model strains are more useful than the measured strains to examine the extension of yielding, i.e., how yielding progresses from one location to another.

On the loaded surface, tensile yielding progresses from the edge towards the mid-width with increased loading. Yielding occurs on this surface at location A at a load of $q/q_C = 1$ and at location G only when the load has reached a value of 13.3.

On the free surface, tensile yielding progresses in the opposite direction moving from the mid-width, location G, at a load of $q/q_c = 2.9$ to location A at a load of 9.5.

Within the zone acting as a membrane, the strains are greater on the free side than on the loaded side as would be expected because of the curvature of the membrane of finite thickness. Furthermore the difference between the strains on the two sides increases with increasing load as the membrane curvature must increase. Table 7.1 lists for locations A to G, the model strains on the loaded and unloaded surfaces at a load, $q/q_c = 17.7$ and their differences. It is seen that the differences vary by only about 8% from location B to location G. At location A, where the point of zero curvature exists, the strains are about the same. With increasing load the plate, originally deformed in flexure, approaches a portion of a circular arc as indicated by the radii of curvature computed from the strain differences on the two surfaces. At the location of the point of zero curvature the radius is of course infinite.

It is also seen from Table 7.1 that the straining is a maximum near the edges and reduces gradually towards the mid-width. This is consistent with the fact that the portion of the plate near mid-width has to strain less as a membrane to attain a circular shape than the plate at the edge which initially was bent in the opposite direction. Thus, overall, as load is increased the membrane tends to approach a circular shape, first near the mid-width and then progressing towards the edge.

The decrease in the rate of straining with increasing load for the model at high loads at location A and to a lesser extent at locations B and C can be explained by examining a free body of a unit length of the plate extending from the point of zero curvature (point A when $q/q_C = 17.7$) to its mid-width as shown in Fig. 7.27 where the corresponding strain diagram is also shown. For the model with an aspect ratio of zero, a strip of unit length must be in equilibrium without forces in the longitudinal direction. Therefore, the strains are consistent with the forces required to hold the free body, subject to uniform pressure, in equilibrium. At higher loads, with increasing pressure, the rate of straining at the edges is less than at mid-width because, at the edge, the increase in the horizontal component is less than at the mid-width and the increase in the vertical component is obtained by the changing angle of inclination, while at the mid-width the increase in the force can only be obtained with increased straining.

7.3.2 Test P12

The variation of strain with load for test P12 at locations X, A, B, C, D, E, F and G, as shown on Fig. 7.18, are given on Figs. 7.28 through 7.35, respectively. The behaviour, in general, is similar to that of plate P6-2 with quantitative differences due to the increased plate thickness.

At location X at the toe of the weld where the plate is severely bent, the strains on the free side reach large compressive values. Significant bending strains exist for considerable distance near the edges and reach a maximum value at location B at a nondimensional load of 1.0. The bending strains at location A, closer to the edge, continue to increase, as does the average (membrane) strain, throughout the test. Away from the edge the bending strains diminish with load and eventually become zero for the model strains at a load of less than 2 at location C and at a load of 4 at location B. Thus, as for plate P6-2 the point of zero curvature migrates towards the edge with increasing load, moving from point C, for the model, at a load of 2 to point B at a load of 4 but never reaching point A.

In the central portion of the plate, away from the edges, the difference in strains between the free and loaded sides due to curvature is again evident. At lower loads, however, because of bending of the thicker plate, compressive strains exist on the loaded side near mid-width. The average strain is always tensile and increases with increasing load as would be expected in this region for membrane behaviour. The maximum tensile strains reach about 26000 $\mu\varepsilon$ for model 2 and 21000 $\mu\varepsilon$ for the test at location A. Therefore, the plate was loaded beyond the yield plateau region and strain hardening had begun. The reduction in measured strain on the loaded side at location A just prior to failure may be indicative of the rupture of the plate at the toe of the weld.

The measured and finite element strains are generally in remarkably good agreement in the elastic region with some divergences in the yield plateau region as would be expected because of the discontinuous yielding of the test specimen. The strain variation in plate P12 is consistent with significant bending at the edges, a point of zero curvature that migrates towards the edges as the load is increased, and membrane behaviour extending over 90% of the width of the plate at maximum load.

As for specimen P6-2, from the change in model strains at the various locations with load, the development of the membrane behaviour can be deduced. On the loaded surface, yielding in tension progresses from location A near the edges at a load of $q/q_C = 1.0$ to location B at a load of $q/q_C = 4.0$ but never reaches location C or those beyond. On the free surface, yielding in tension progresses from location G at a load of $q/q_C = 1.0$ to location B at a load of q/q_C of 4.0 but never reaches location A where the free surface is always in compression.

Within the zone acting as a membrane the strains are greater on the free side than on the loaded side and the difference between them increases with increasing load as would be expected. Table 7.2 lists for locations A to G the model strains on the loaded and unloaded (free) surfaces at a load $q/q_C = 6.6$ and the differences between these strains (the specimen failed at about this load). As for model 1, it is seen that the differences vary only by 3% in the central region from location C to G. At location A the plate is still bent in the opposite direction whereas for model 1 at the maximum load no curvature existed at this point. Location B exhibits a relatively large curvature as would be expected in this transition zone between the plate acting as a pure membrane and at the edges where bending in the opposite direction exists. Again the plate is tending to form a circular arc which develops from the mid-width towards the edges where bending exists and where as noted previously the tensile strains are the highest.

The strain variation through the thickness at any location can be considered to consist of two parts: that due to the curvature of the plate acting as an inelastic membrane subject to fluid pressure and, because of its stiffness, that due to bending. At any location where the radius of curvature approaches the minimum value the bending strains are relatively small. At location B where the radius of curvature is considerably larger than in the central near-circular portion the plate in fact is partially straightened-out because of bending in the reverse direction and, of course, at A the bending is very pronounced. Thus, a point of zero curvature, which in this case would lie between locations X and A (and which for model 1 was at location A) represents the case where curvature due to membrane action is balanced by bending curvature in the opposite direction. The total strain at this location must be such that the force developed in tension here is sufficient to keep the portion of the plate between the points of zero curvature near the edges in equilibrium.

7.3.3 Test P6-1

The variation of measured strain with load for test P6-1 at locations X,A,B,C,D,E,F and G, as shown on Fig. 7.36, are given on Figs. 7.38 through 7.45, respectively. The behaviour resembles closely that of plate P6-2 which has the same nominal thickness. Near the edge (locations X, A and B in particular) very distinct bending strains exist at low loads. At location A, these strains increase up to a load, q/q_c of about 1. The net bending strains gradually reduce and become zero as the point of zero curvature migrates towards the edges from point C at a load of about 1.8 to point B at a load of 3 and to point A, apparently approached at a load of about 7. Keeping in mind that the plotted strains are measured strains and that yielding is discontinuous and therefore that strains beyond yielding are more difficult to assess, on the loaded surface yielding is seen to progress as in the previous tests, from location A at a load of about 1 to location F at a load of about 10. No measurement was made at location G. On the free surface the progressive yielding is again in the opposite direction moving from location G at a load of about 3.5 to location A at a load of 8. In both cases at the intermediate locations, the yielding progresses rapidly across the half width. As before, the strains, within the zone acting as a membrane, are greater on the free side than on the loaded side though a quantitative assessment of these differences is not appropriate because of the discontinuous yielding phenomenon. In so far as the strain may be assessed qualitatively it appears that the membrane action spreads from the mid-width to the edges and, at the maximum load, inelastic membrane behaviour extends over 90% of the width of the plate.

7.3.4 Test P16

The variation of strain with load for test P16 at locations X,A,B,C,D,E,F and G, as shown on Fig. 7.37, are given on Figs. 7.46 through 7.53, respectively. Except for quantitative differences resulting due to the increased plate thickness the behaviour, in general, is similar to that of plates P6-1, P6-2 and P12.

The strain variation in plate P16 is consistent with significant bending at the edges, a point of zero curvature that migrates towards the edges as the load is increased and inelastic membrane behaviour extending over 75% of the width of the plate at maximum load.

As would be expected, bending is much more significant than for the thinner plates. The point of zero curvature moves from a point between locations D and C to location C at a load of 4.2 to location B at a load greater than 5 and never arrives at location A. On the loaded surface yielding occurs at location A at a nondimensional load, $q/q_C = 0.6$ and moves to location E at a load of about 5.5 and never gets to locations F or G. On the free side, yielding occurs at mid-width, location G, at a load of about 1.1 and progresses to location B at a load of about 5.2 but never reaches A. In the central portion where inelastic membrane action occurs, although at some locations not through the entire thickness, the strains on the free surface are greater than those on the loaded surface. The variation in the difference in strains between the two surfaces at different locations suggest that significant bending still exists, all the while recognizing the discontinuous yielding process.

7.4 Strains Across The Width At Mid-Length

In this section the strain distribution across the half width at mid-length at four different load levels is presented. Some information presented previously is reiterated.

The measured strain distribution is plotted for the four tests at four different load levels in Figs. 5.20 to 5.35. Strains, as deduced using the ADINA finite element model, are plotted in the figures for tests P6-2 and P12. In examining these strains, it is again emphasized that measured strains in the yield plateau because of discontinuous yielding may vary between the yield strain and the strain hardening strain and still represent the same stress level. Because the ADINA model requires a finite slope in the region between yielding and strain hardening, model strains vary continuously.

In Fig. 5.21 for test P6-2 at a nondimensional load of about 1.0 the behaviour is essentially elastic with bending strains at the fixed edges and a point of zero curvature at about 190 mm from the toe of the weld. The model strains are in good agreement with the measured strains. Close scrutiny reveals that the average strain is tensile, indicative of a limited amount of membrane behaviour. Figure 5.22 for test P12 at the same load level exhibits very similar behaviour with bending at the edge and a point of zero curvature again 190 mm from the toe of the weld. The experimental results are in good agreement with the model values and show on the average a small tensile strain. Some inelastic bending, as would be expected, occurs near the edge of the plate.

Figures 5.25 and 5.26 compare the ADINA model results to the measured strains at loads approaching failure, q/q_C = 17.9 for test P6-2 and q/q_C = 6.6 for test P12. The strains in the former case are of course considerably larger.

From Fig. 5.25, both the measured and model strains indicate significant bending at the edge of the plate. ADINA predicts the point of zero curvature to be at 40 mm from the edge. The point of zero curvature has therefore migrated substantially towards the edge from its position of 190 mm at a normalized load of 1.0. Beyond the point of zero curvature where the plate acts as a membrane both the model and measured strains are on the tensile yield plateau. The model strains are higher near the hinge and reduce towards the mid-width. As discussed previously, this variation is attributed to the fact that significant bending is required at the edges to develop membrane action there but not at the mid-width.

For test P12 bending again is found to exist at the edge of the plate and the point of zero curvature at q/q_C = 6.6 is only about 80 mm from the edge as compared to 190 mm at q/q_C = 1.0. Both the test results and the ADINA values show that the vast central portion of the plate is acting as a membrane with the strains on the free surface in the inelastic region and strains on the loaded surface in the elastic region. The difference in strains on the two surfaces is a measure of the membrane curvature.

Figures 5.29 and 5.30 for test P6-2 at q/q_C = 5.36 and test P12 at q/q_C = 3.03 respectively were drawn for the case when the average membrane strain at the point of zero curvature was about equal to the yield strain. It is noted that points of zero curvature at 70 mm and 100 mm from the edge for tests P6-2 and P12, respectively, are intermediate to their previous positions for higher and lower load levels. In the elastic region the test results (associated with the loaded surface) are in good agreement with the ADINA model strains. On the free surface the model strains are just within the inelastic range with measured strains above and below these values.

Figures 5.33 and 5.34, for tests P6-2 at q/q_C = 10.9 and test P12 at q/q_C = 5.1 respectively, both represent the case when significant inelastic membrane action exists. Bending still exists at the edges and the points of zero curvature are found at intermediate points to those for higher and lower loads, as should be the case. With some scatter, the experimental values are in reasonable agreement with the model results. In the central portion inelastic straining exists. For tests P6-2 this extends through the thickness of the plate except for a limited elastic zone on the loaded surface near the mid-width. For test specimen P12, Fig. 5.34, the free surface has inelastic strains while the loaded surface, where the model and measured strains are in good agreement, remains elastic.

The average (membrane) strains of the 6 mm plate are greater than those of the 12 mm plate. But on the other hand because of its greater thickness, the strain variation through the thickness of the 12 mm plate is greater than that for the 6 mm plate.

For both specimens, bending strains at the edge increase with increasing loads. The point of zero curvature migrates towards the edge with increasing loads. Tensile membrane strains, tending to be higher near the hinge than at mid-width are first relatively small, reach the yield strain and then progress into inelastic strain hardening. The free surface membrane strains are greater than the loaded surface membrane strains to accommodate the curvature of the membrane as discussed previously.

7.5 Membrane Behaviour

Figures 5.20 to 5.35 give strains across the width at four different load levels for the four tests. The strains obtained from the ADINA models are shown on figures drawn for tests P6-2 and P12. At lower load levels (see Figs. 5.20 to 5.23) the strains away from the edges and between points of zero curvature on both the loaded and free surfaces are in the elastic range of behaviour. Figures 5.24 to 5.35 that are drawn for higher load levels show that the points of zero curvature move toward the edges as the load is increased. Between points of zero curvature and with higher load levels the strains on both surfaces of the plate become tensile, increase in magnitude, and eventually become inelastic. The free surface strains increase at a higher rate than do the strains on the loaded surface as the curvature of the membrane increases with increasing load.

A plate acting as an inelastic membrane and subject to fluid pressure loading, has a mean tensile strain that, for any given load, is the same at all locations across its width. Hence, the average tensile stress and curvature of such a plate is constant from edge to edge and the deformed shape is circular. The load-deflection behaviour of a plate subjected to fluid pressure loading and acting as an inelastic membrane from edge to edge is given by Ratzlaff and Kennedy (1985, 1986), hereafter referred to as the Ratzlaff-Kennedy model. Curves Mi, N and N' in Figs. 7.1 to 7.4 are derived from their analysis. In these figures the test results follow curve N' closely as discussed previously in Section 7.2 and indicate that, at the higher loads, the plates act predominantly as inelastic membranes. The basic reason for the slight differences between the load-deflection behaviour of the test plates and that given by Ratzlaff-Kennedy model is that the test plates with significant thickness do not form line hinges at the edge (i.e. hinges of no lateral extent). As discussed in Section 7.3 the plates first of all, at very small deflections, behave as flexural members. With increasing deflections elastic membrane action asserts itself and eventually becomes inelastic in nature. The initial deflected shape is dissimilar to the final deflected shape which gradually approaches that of a circular arc with divergences from this shape representing bending at the edges. More straining is required to approach the circular shape near the edges where the initial curvature is in the opposite direction. The result, therefore, is that the final membrane shape approaches closely that of a circle over the central portion where inelastic straining occurs, but at the so-called points of zero curvature, which will be subject to significant straining and bending to maintain equilibrium, the resulting curvature is zero. From the edges to the point of zero curvature the plate acts primarily flexurally. It follows therefore that while in most of this central portion the curvature is sensibly constant, within a short distance of the point of zero curvature the curvature changes rapidly to zero. The deflected membrane shape is therefore not exactly circular.

Figures 5.24 for test P6-1 and 5.25 for test P6-2 show that the measured and model strains across the width from a point within about 40 mm of the edge are in the inelastic region. The model strains show a variation from a maximum value near the point of zero curvature to the mid-width, as discussed previously, and show a strain gradient consistent with a membrane approaching constant curvature in this region. All of these strains therefore reflect stresses in the yield plateau. It follows that within this strain range any increase in load carrying ability of the membrane must arise simply from increased curvature, increased deflections, and increased inclination of the member near its edges.

Figure 5.26 gives the measured and model strains for test P12 and Fig. 5.27 the measured strains for test P16, at their failure loads. For both tests the free surface strains are inelastic while the loaded surface strains tend to lie in the elastic region. Therefore for these thicker plates full inelastic membrane behaviour had not developed at failure. The ADINA strains for test P12 show a constant difference between the free and loaded surface strains over most of the width where membrane action is occurring indicating that the deflected shape of the plate is circular.

7.6 Longitudinal Strains

For a plate acting as a membrane in a state of plane strain, the longitudinal strains at any location would be expected to be zero. Figures 5.36 through 5.39 that give measured longitudinal strains across the width at mid-length for tests P6-1, P6-2, P12, and P16 respectively, at four different load levels, show that these strains approach zero along the long sides. However, the strains, at loads near failure, approach yield levels (about 1500 $\mu\varepsilon$) near mid-width for the two thinner plates and about one-third of the yield strain values for the two thicker plates. The greater longitudinal strains at mid-width for the thinner plates are attributed to the relatively larger deflections of the thinner plates as compared to the thicker plates as shown in Fig. 5.19 for plates P6-2 and P16.

The near-zero longitudinal strains along the long edges for all plates is simply due to the restraint provided by the stiff reaction plate to which the test plates were welded. The condition of straining therefore deviates from that approaching plane strain along the long sides to a triaxial strain condition that increased to a maximum at mid-width.

7.7 Behaviour At Edges

Sections through the thickness and across the width at mid-length of the plate specimens taken after failure indicated that considerable bending had occurred at edge locations. The geometry at the edges was similar to that obtained from the ADINA analysis as shown in Figs. 6.7 and 6.8 for Model 1 and Model 2 (specimens P6-2 and P12), respectively. A considerable amount of inelastic deformation occurred within the region along the edges as was evident from small samples taken there that retained their deformed geometry after being isolated from the remainder of the specimen.

As discussed in Chapter 5, failure for all four specimens was observed to initiate within the HAZ near the toe of the weld and along the edges at mid-length. After initiation, separation or rupture of the steel plate progressed through the plate thickness to the unloaded surface as shown in Figs. 5.9 and 5.10. In some cases, rupture was observed to have began but not propagated through the plate thickness at locations along the long edge opposite to the actual failure.

7.8 Failure Loads And Deflected Shapes

Ratzlaff and Kennedy (1986) proposed relationships for a membrane subject to fluid pressure, relating the membrane deflection, the maximum membrane stress and strain, and the membrane edge inclination to the fluid pressure and the material properties as follows.

$$[7.1] \qquad \frac{\sin\theta}{\theta} = \frac{\pi}{180(1+\varepsilon_s)}$$

$$[7.2] \qquad q = \frac{\sigma_s h \sin\theta}{(L/2 - d\sin\theta)(1-\nu_s^2)}$$

$$[7.3] \qquad Wm = (L/2 - d\sin\theta)\frac{\sqrt{1-\cos\theta}}{\sqrt{1+\cos\theta}}$$

where d $\sin\theta$ is the distance from the edge of the plate to the point of zero curvature. These equations are derived in Appendix A. Also derived in Appendix A is the relationship relating the maximum membrane stress, the fluid pressure, and the membrane edge inclination, based on the material properties and also based on full plastification of the cross-section in tension and bending at the support. This relationship is

$$[7.4] \qquad \left[\frac{\sigma_s}{\sigma_u}\right]\left[\frac{4\ \sin^2\theta\ (1 + \varepsilon_p)\left(1 - \nu_p^2\right)}{3\ \cos\theta\ (\varepsilon_u - \varepsilon_p)\left(1 - \nu_s^2\right)}\right] + \left[\frac{\sigma_s}{\sigma_u}\right]^2 \frac{\left(1 - \nu_p^2\right)^2}{\left(1 - \nu_s^2\right)^2} \cos^2\theta = 1$$

In the latter derivation (See Appendix A) it is assumed that the strain distribution at the edge is linear with the maximum tensile strain on the concave side set equal to σ_u.

From the test (measured) geometry at failure (W_m and d $\sin\theta$) and the stress-strain curves for the tensile coupons, the loads corresponding to failure were predicted from the Ratzlaff-Kennedy equations [7.3], [7.1], and [7.2] (in this order) and are given in Table 7.3 together with the test failure loads. The test/predicted values are in excellent agreement ranging from 0.965 to 1.002. The maximum strain on the loaded side at the very edge of the plate, ε_u, predicted from [7.4] is also given in the table.

At the test failure loads, the maximum deflection and other quantities were determined from the ADINA models 1 and 2 for tests P6-2 and P12, respectively, as given in Table 7.4. Equations [7.1] through [7.4] can again be used together with the stress-strain curves as modelled by ADINA and the ADINA geometry,to predict the failure loads (This parallels the calculations given in Table 7.3 based on the measured geometry). In making these predictions the test values for the inelastic strain ratio were used. These calculations lead to test/predicted ratios of 1.022 and 0.954, respectively, as shown in Table 7.4. Had the inelastic strain ratio been taken equal to 0.50 (no volume change as used in the ADINA models) the predicted failure loads from equations [7.1] to [7.3] would have increased substantially resulting in test/predicted ratios of 0.86 and 0.78, respectively. These data therefore establish that the simple model for the circular deflected shape between points of zero curvature is consistent with the loads required to deform the membrane into that shape. Implicit in this is the fact that inelastic strain ratio is significantly different from 0.50.

In Figs. 7.54 to 7.57 are plotted deflected shapes of the plate at mid-length across the half width for the failure load. Each figure has 3 curves: (i) the deflected (test) shape as measured using the surface level indicator, (ii) the shape as deduced from the Ratzlaff-Kennedy equations based on measured values of W_m, the maximum deflection, and of d $\sin\theta$, the distance measured from the edge to the point of zero curvature (i.e.,the geometry at failure) and the stress-strain curves, by matching membrane deflections at mid-width to the test deflections, and (iii) the shape as deduced from the Ratzlaff-Kennedy equations based on the test (measured) failure loads and the stress-strain curves (matching failure loads). The data for these latter calculations are summarized in Table 7.5. In this table, using the stress-strain curves to determine coincident values of σ_s, ε_s, and v_s, as determined from the stress-strain data, values of W_m, d sinθ, θ, ε_s, and ε_u are computed iteratively from [7.1] through [7.4] for the test failure loads. The maximum strains at the edge based on the ADINA models and the ratio of these strains to those predicted using equations [7.1] through [7.4], as discussed subsequently, are also given in Table 7.5.

Curves (ii), based on measured values of the maximum deflection of the membrane portion of the plate (W_m) at mid-width and the distance to the point of zero curvature (d sinθ) have been plotted through these two points and extended backward towards the edge based on the Ratzlaff-Kennedy relationships. In the membrane region these curves and the test curves are in reasonable agreement. The difference between the two curves arises from the edge behaviour and the fact that the membrane is not circular over the entire range between points of contraflexure.

Curves (iii) have been computed from the Ratzlaff-Kennedy relationships for the test failure load and have been drawn with zero deflection at the edge. Again the behaviour of the plate at the edge and the non-circular shape between the points of contraflexure accounts for the difference in the deflections between curve (iii) and the test curve. The point of zero curvature is closer to the edge than for the measured (test) curve.

It is concluded that both sets of predicted curves, one matched in terms of deflections and the other in terms of failure load, are in substantial agreement with the observed (test) deflections.

7.9 Failure Mechanisms

Four failure mechanisms have been suggested by various researchers with the first three of these based on previous work as discussed in Section 2.4.

Ratzlaff and Kennedy (1986) put forward the hypothesis of a maximum tensile strain criterion which was used in the ADINA analysis here as an upper bound. Failure is postulated to occur when the tensile strain at the edge (on the loaded surface in these tests) due to combined tension and bending reaches the true fracture strain.

Ratzlaff and Kennedy, as discussed in Section 2.3, also postulated a maximum shear stress criterion, based on failure observations, that failure occurs at the edge when the average shear stress reaches $0.577\sigma_u$. This criterion applied to the one test they did that failed in shear gave a test/predicted ratio of 0.97.

Kennedy and Cheng (1992) proposed the criterion that failure occurs when, under a state of plane strain, by extending the von Mises-Huber-Hencky yield criterion to ultimate the relationship

$$[7.5] \qquad 0.75 \left(\frac{P}{\sigma_u A} \right)^2 + 3 \left(\frac{V}{\sigma_u A} \right)^2 = 1.0 ,$$

where P and V are the tension and shear acting on a unit length of the plate cross-section through its thickness at the toe of the weld, A is the cross-sectional area (1xh) and σ_u is the uniaxial ultimate tensile stress. As the equation shows, no stresses due to bending are considered. Because of the significant bending at the edge where failure occurred in these tests this criterion is not further considered.

The fourth criterion developed as a result of these tests, applicable only when a heat affected zone exists in an area of large tensile strains, such as existed here at the edge of the plate, is that failure occurs when the maximum strain reaches that which causes rupture in the HAZ. The data obtained in these tests are limited but the results of the two tests for which ADINA analyses were performed (see Section 6.2) suggest that failure occurs when the true strain, under conditions of plane strain that exist at the edge of the plate, reaches the range of 88000 $\mu\varepsilon$ to 170000 $\mu\varepsilon$. Even the least of these values exceeds that proposed by Matic and Jolles (1987) very considerably. The least value even exceeds that used by Bond (1993) by 1.26 times. For this criterion of maximum strain in the HAZ the ADINA strain of 170000 $\mu\varepsilon$ at the failure load in test P6-2 was used to predict the failure load for both tests P6-2 and P6-1 because the stress-strain curves for the two 6 mm plates are quite similar, as given in Table 7.6. Of course the individual stress-strain data for the respective test plates were used. Similarly the ADINA strain of 88000 $\mu\varepsilon$ at the toe of the weld for test P12 was also used for test P16, again because of the similarity of the stress-strain curves for these two steels (see Table 7.6). The Ratzlaff-Kennedy (1986) model was used to predict the failure load based on the maximum strain at the toe of the weld, taken to be 170000 $\mu\varepsilon$ for the 6 mm plates and 88000 $\mu\varepsilon$ for the 12 and 16 mm plates. The results of these calculations are summarized in Table 7.6 and discussed subsequently.

Table 7.7 summarizes the non-dimensional failure loads, q/q_C, for the four tests and the predicted failure loads based on the three criteria considered to be valid as discussed previously. The smallest predicted failure loads are those due to the straining in the HAZ. These loads were used to determine the test/predicted ratios which vary from 0.69 to 0.80 indicating that the predicted failure loads even using the HAZ strain limits were too high. This is attributed to the fact that the strains at the toe of the weld as shown by the ADINA model (Figs. 6.5 and 6.6) are very much non-linear and a basic simplifying assumption of the Ratzlaff-Kennedy model is that the strains vary linearly. Non-linear straining means that less load can be carried for the same maximum strain. In particular, examining Table 7.6, based on linear straining it is seen that the maximum deflections are greater than those observed as given in Table 7.3 and those predicted by ADINA as given in Table 7.4.

These tables also show that the distances from the edge to the point of zero curvature, as observed (Table 7.3) and calculated by ADINA (Table 7.4), are in good agreement but are much greater than when the maximum strain in the HAZ is used with the assumption that the strain distribution is linear (Table 7.6).

As discussed in Section 7.8 the failure loads in tables 7.3 and 7.4 were determined from measured or computed (ADINA) deflected shapes of the central portion that acted as a membrane and gave predicted failure loads in good correspondence with the test values (test/predicted ratios range from 0.954 to 1.022). The question still remains, however, what maximum strains does the Ratzlaff-Kennedy model predict based on the failure load and how do these compare with the strains determined from ADINA? Table 7.5 summarizes the calculations for determining these strains and compares them to the ADINA strains. The ADINA strains range from 1.4 to 1.8 times the linear strains, suggesting that, within the bounds of all the assumptions made, that the strain concentration factor at the toe of the weld was about 1.5 on the average. It is emphasized again that in this comparison the contributions from the various assumptions both in the ADINA program and in the Ratzlaff-Kennedy model (particularly the deformation and straining at the edge) contributed to this number. It is possible that the strain concentration factor may even be higher.

Taking the strain concentration factor to be 1.5 and using the maximum linear strain for the 6 mm plates as that determined by ADINA divided by this factor, i.e. 170000 $\mu\varepsilon$ /1.5 = 113000 $\mu\varepsilon$ and for the 12 mm and 16 mm plates, 88000 $\mu\varepsilon$ /1.5 = 58700 $\mu\varepsilon$, the Ratzlaff-Kennedy model can be used to determine the failure loads. The resulting failure loads, given in Table 7.8, give a mean test/predicted value of 1.00 and a coefficient of variation of 0.09. The lowest of these values was determined for test P6-1 for which it is recalled a copper backing bar was used that resulted in contamination of the weld metal with copper in the area where fracture initiated.

In the four major tests conducted here it is pointed out that two factors contributed to the failure at loads less than expected based on the shear limit which otherwise would likely have governed. These are of course the reduced ductility in the HAZ and the strain concentration due to the abrupt change in cross-section at this location. Neither of these factors need be present in a real structure as discussed subsequently.

Table 7.1 ADINA strain differences, model 1, q/qc = 17.7

Location	Free surface strain (με)	Loaded surface strain (με)	Difference in strain (με)	ρ (mm)
G	6600	2475	4125	1721
F	7303	3185	4116	1725
E	10439	6363	4076	1742
D	16097	12086	4011	1770
C	21433	17525	3908	1817
B	22193	18386	3807	1865
A	20845	20861	- 16	***

*** Approximate point of zero curvature

Table 7.2 ADINA strain differences, model 2, q/qc = 6.6

Location	Free surface strain (με)	Loaded surface strain (με)	Difference in strain (με)	ρ (mm)
G	6221	883	5338	2510
F	6214	889	5325	2516
E	6214	905	5309	2524
D	6204	932	5272	2542
C	6158	975	5183	2585
B	4830	1229	3601	3721
A	- 1156	26761	- 27917	- 480

Table 7.3 Failure loads based on Ratzlaff-Kennedy model and test (measured) geometry

	Measured		Predicted (equations [7.1] to [7.4])							
Test	W_m (mm)	d $\sin\theta$ (mm)	θ	ε_s ($\mu\varepsilon$)	σ_s (Mpa)	ν_s	ε_u ($\mu\varepsilon$)	$q_{pred.}$ (kPa)	q_{test} (kPa)	$\frac{q_{test}}{q_{pred.}}$
P6-1	60.8	44.3	14.5	10700	294.5	0.33	41000	1174	1152	0.981
P6-2	71.8	40.6	16.9	14700	292.5	0.33	55000	1407	1411	1.002
P12	39.5	84.1	10.5	5620	318.9	0.29	31100	1978	1909	0.965
P16	37.1	94.0	10.2	5340	307.9	0.31	34000	2456	2383	0.970

Table 7.4 Failure loads based on Ratzlaff-Kennedy model and ADINA geometry

	ADINA			Predicted (equations [7.1] to [7.4])							
Test	W_m (mm)	d sinθ (mm)	ε_u ($\mu\varepsilon$)	θ	ε_s ($\mu\varepsilon$)	σ_s (Mpa)	v_s	ε_u ($\mu\varepsilon$)	$q_{pred.}$ (kPa)	q_{test} (kPa)	$\frac{q_{test}}{q_{pred.}}$
P6-1	-	-	-	-	-	-	-	-	-	-	-
P6-2	71.9	34.3	170000	16.7	14400	294.0	0.33	64000	1381	1411	1.022
P12	38.1	93.1	88000	10.3	5450	320.8	0.29	28000	2001	1909	0.954
P16	-	-	-	-	-	-	-	-	-	-	-

Table 7.5 Comparison of maximum strains based on Ratzlaff-Kennedy model using test load and geometry, with ADINA strains

		Predicted (equations [7.1] to [7.4])							ADINA	
Test	q_{test} (kPa)	σ_s (Mpa)	ν_s	W_m (mm)	d $\sin\theta$ (mm)	θ	ε_s ($\mu\varepsilon$)	ε_u ($\mu\varepsilon$)	ε_u ($\mu\varepsilon$)	$\frac{\varepsilon_{u(ADINA)}}{\varepsilon_{u(pred.)}}$
P6-1	1152	293.7	0.33	66.3	19.5	15.0	11500	94900	170000	1.79
P6-2	1411	294.4	0.34	78.1	18.5	17.6	15900	123100	170000	1.38
P12	1909	321.0	0.32	45.1	41.0	10.9	6100	64600	88000	1.36
P16	2383	307.4	0.35	42.0	55.5	10.6	5820	58200	88000	1.51

Table 7.6 Failure loads based on Ratzlaff-Kennedy model and ADINA strains in HAZ at test failure load

	ADINA	Predicted (equations [7.1] to [7.4])									
Test	ε_u ($\mu\varepsilon$)	ε_s ($\mu\varepsilon$)	σ_s (Mpa)	v_s	ε_u ($\mu\varepsilon$)	W_m (mm)	d sinθ (mm)	θ	$q_{pred.}$ (kPa)	q_{test} (kPa)	$\frac{q_{test}}{q_{pred.}}$
P6-1	170000	23500	296.0	0.38	170000	95.4	15.7	21.3	1685	1152	0.80
P6-2	170000	25000	296.5	0.34	170000	98.4	17.0	22.0	1762	1411	0.69
P12	88000	10600	322.6	0.31	88000	60.3	40.1	14.5	2518	1909	0.76
P16	88000	8100	321.6	0.44	88000	50.7	43.0	12.4	3107	2383	0.77

Table 7.7 Actual and predicted failure loads

Specimen	Nondimensional Loads at Failure (q/q_c)				Test/Predicted Ratio
		Predicted			
	Test	Shear Limit	Strain Limit	Strain in HAZ	
P6-1	17.4	53.8	68.7	25.4	0.69
P6-2	17.9	45.1	62.0	22.4	0.80
P12	6.6	27.1	37.3	8.68	0.76
P16	5.5	22.7	37.2	7.22	0.77

Table 7.8 Failure loads based on Ratzlaff-Kennedy model and linear strains in HAZ

Specimen	Strain in HAZ ($\mu\varepsilon$)	q (test) (kPa)	q (pred.) (kPa)	$\frac{q\ (test)}{q\ (pred.)}$
P6-1	113000	1152	1340	0.86
P6-2	113000	1411	1344	1.05
P12	58700	1909	1821	1.05
P16	58700	2383	2285	1.04

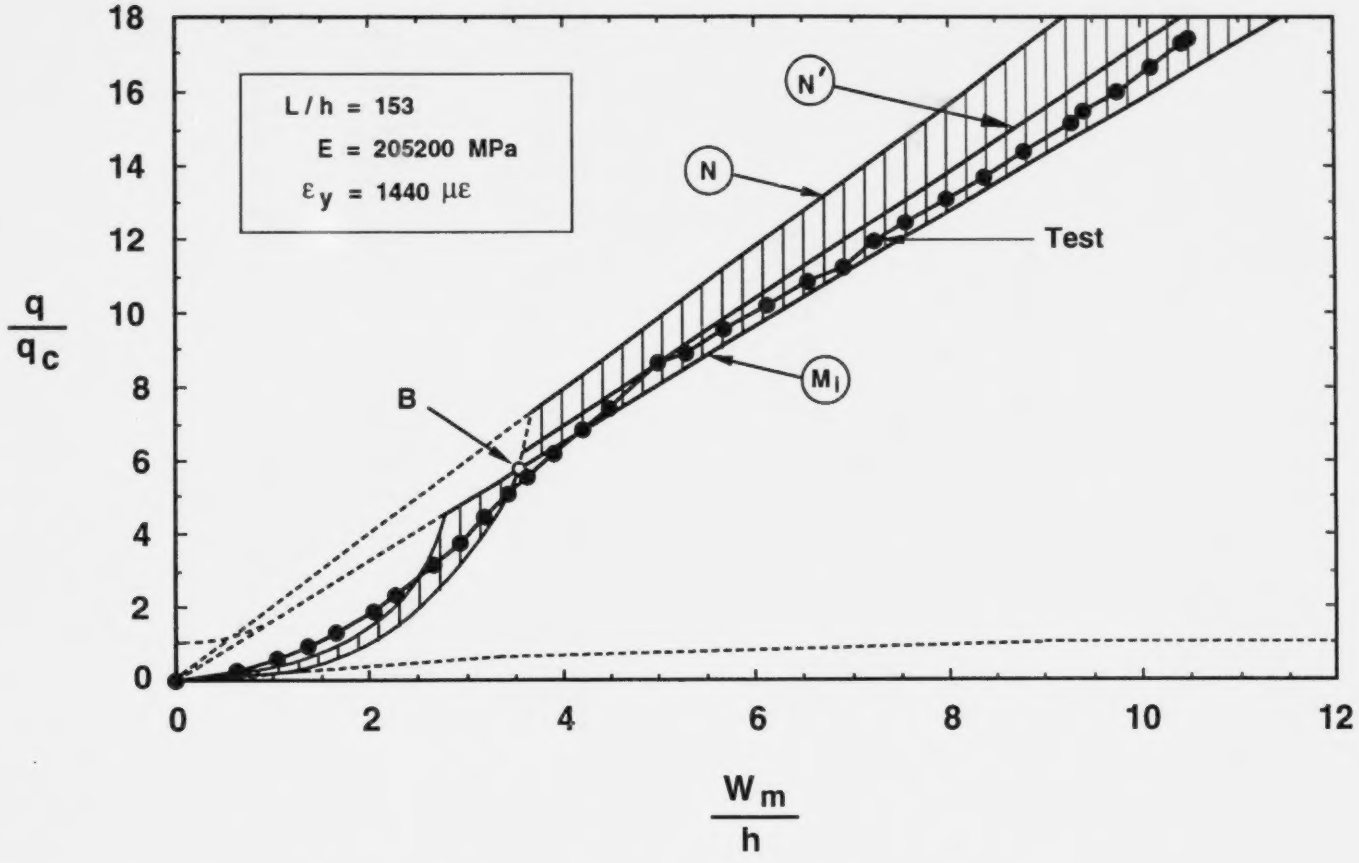

Figure 7.1 Load-deflection relationships, plate P6-1

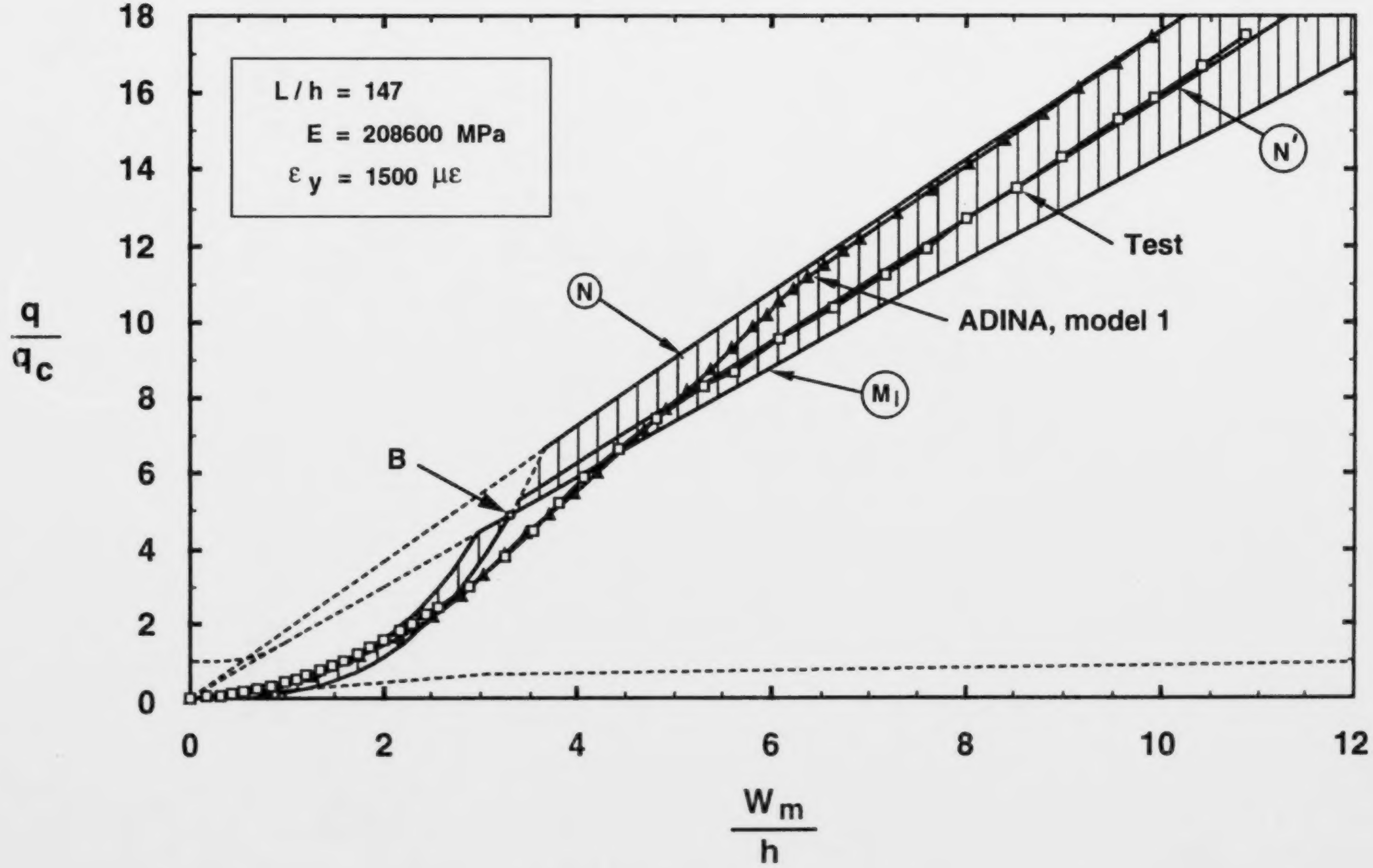

Figure 7.2 Load-deflection relationships, plate P6-2

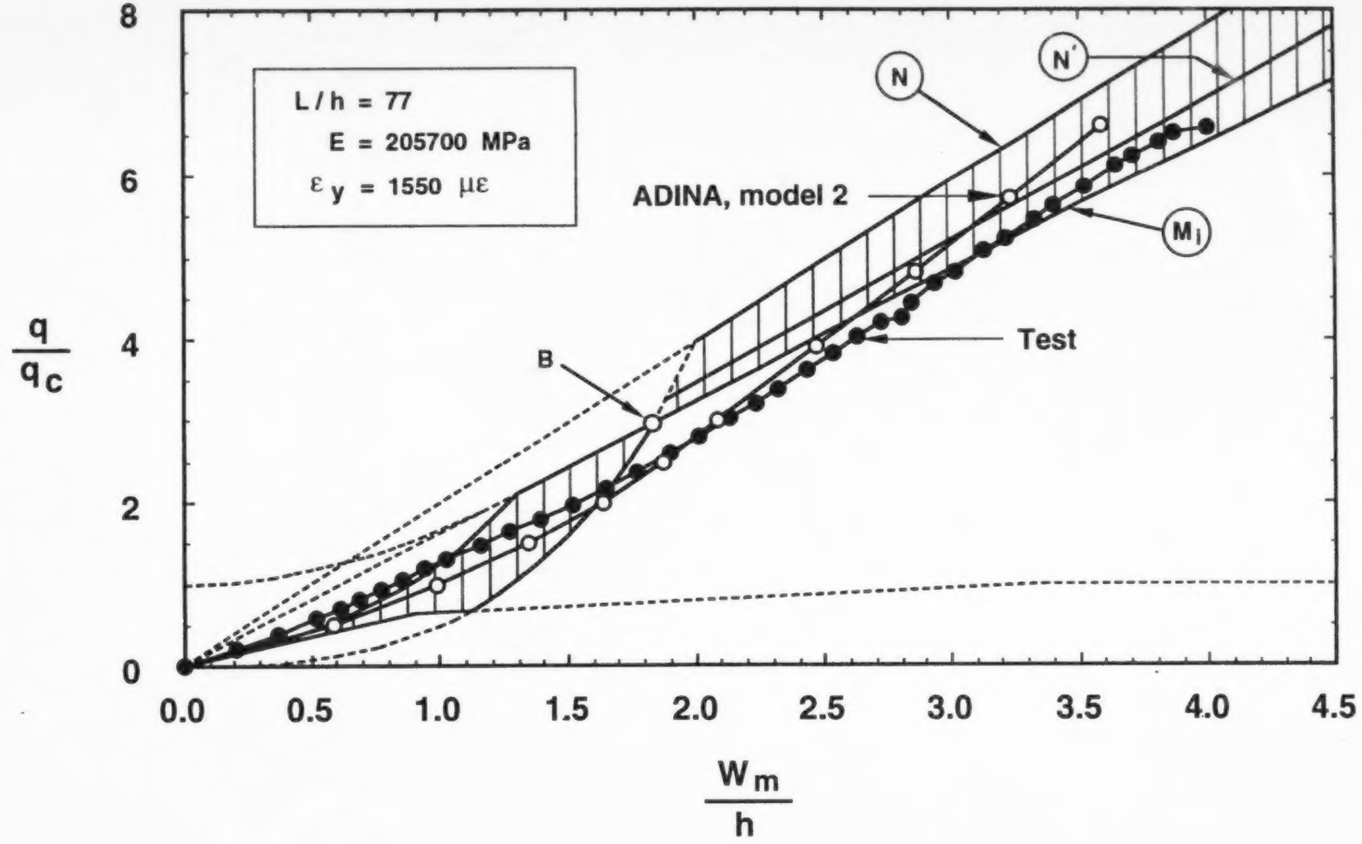

Figure 7.3 Load-deflection relationships, plate P12

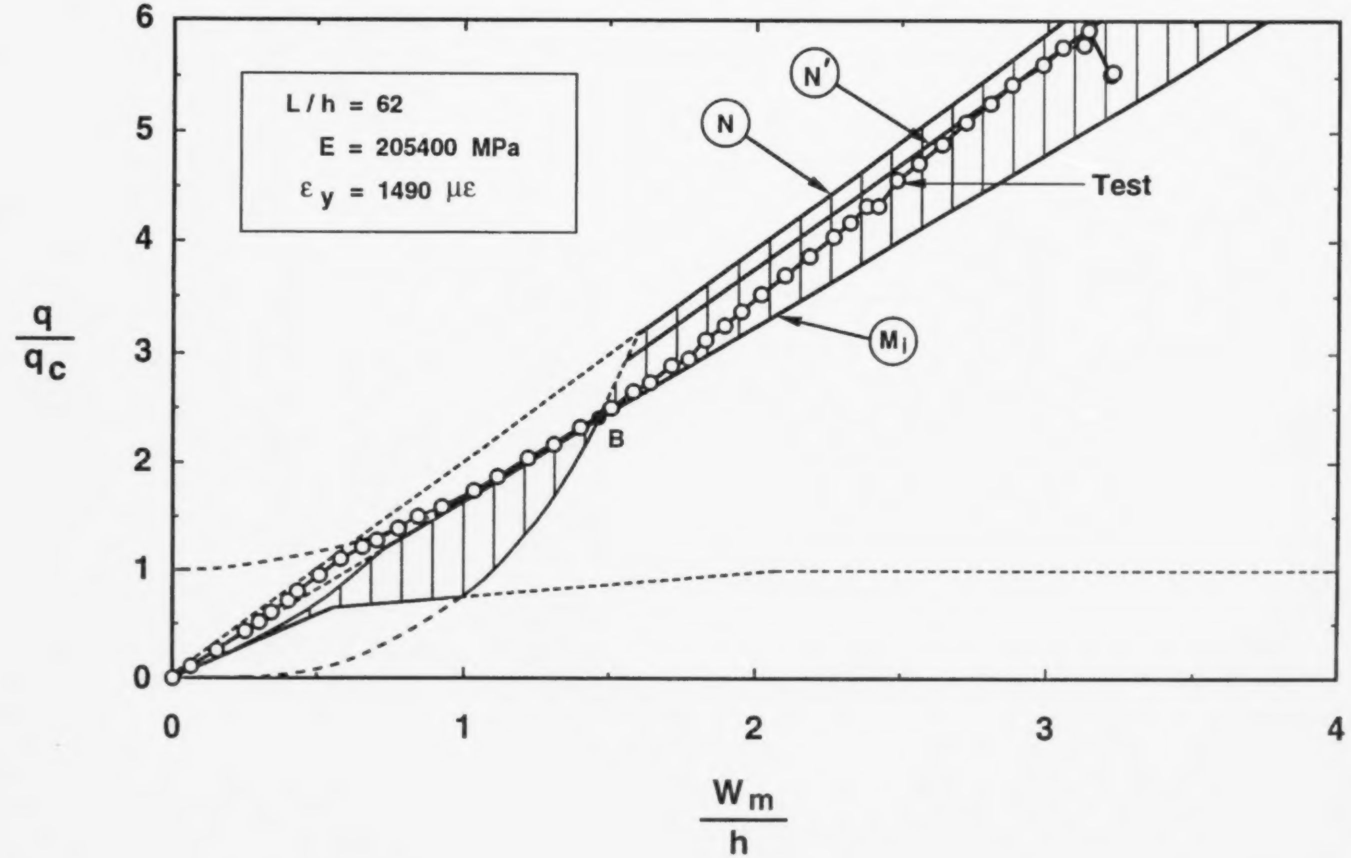

Figure 7.4 Load-deflection relationships, plate P16

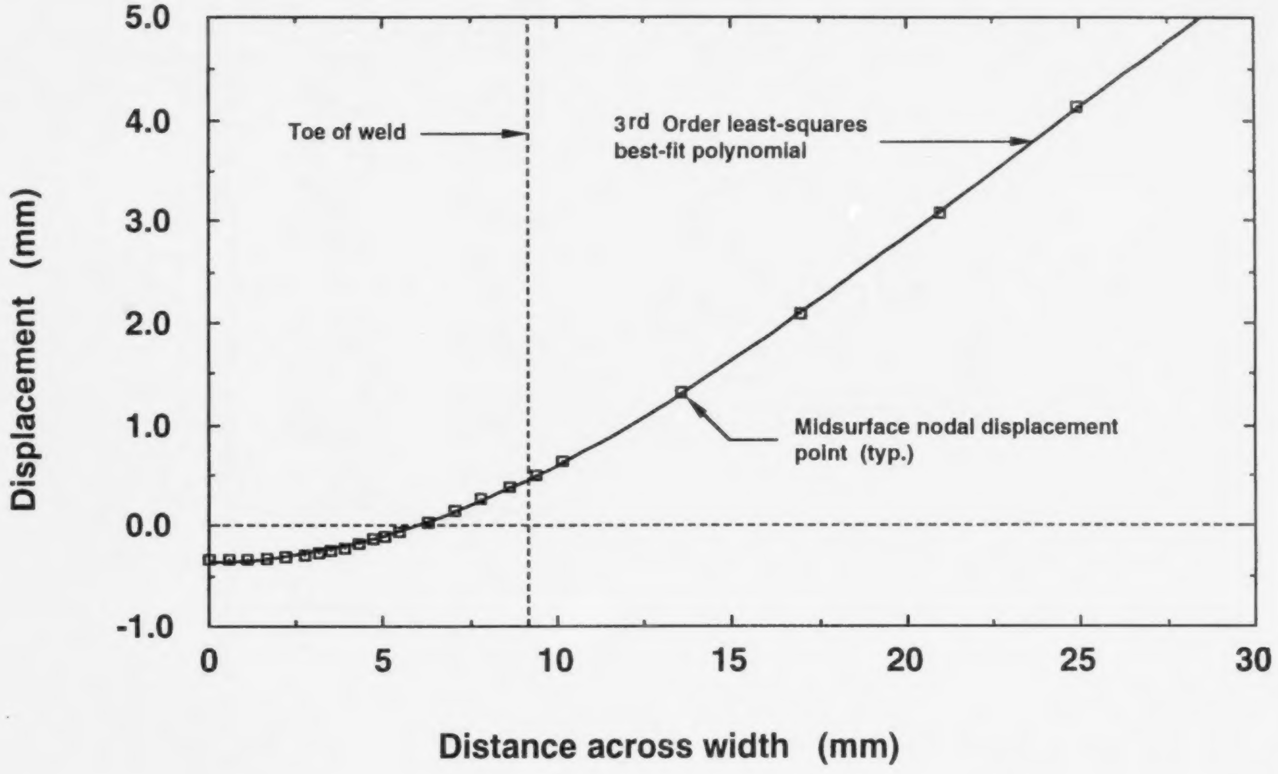

Figure 7.5 Model 1(test P6-2) midsurface nodal displacements, q/qc = 17.7

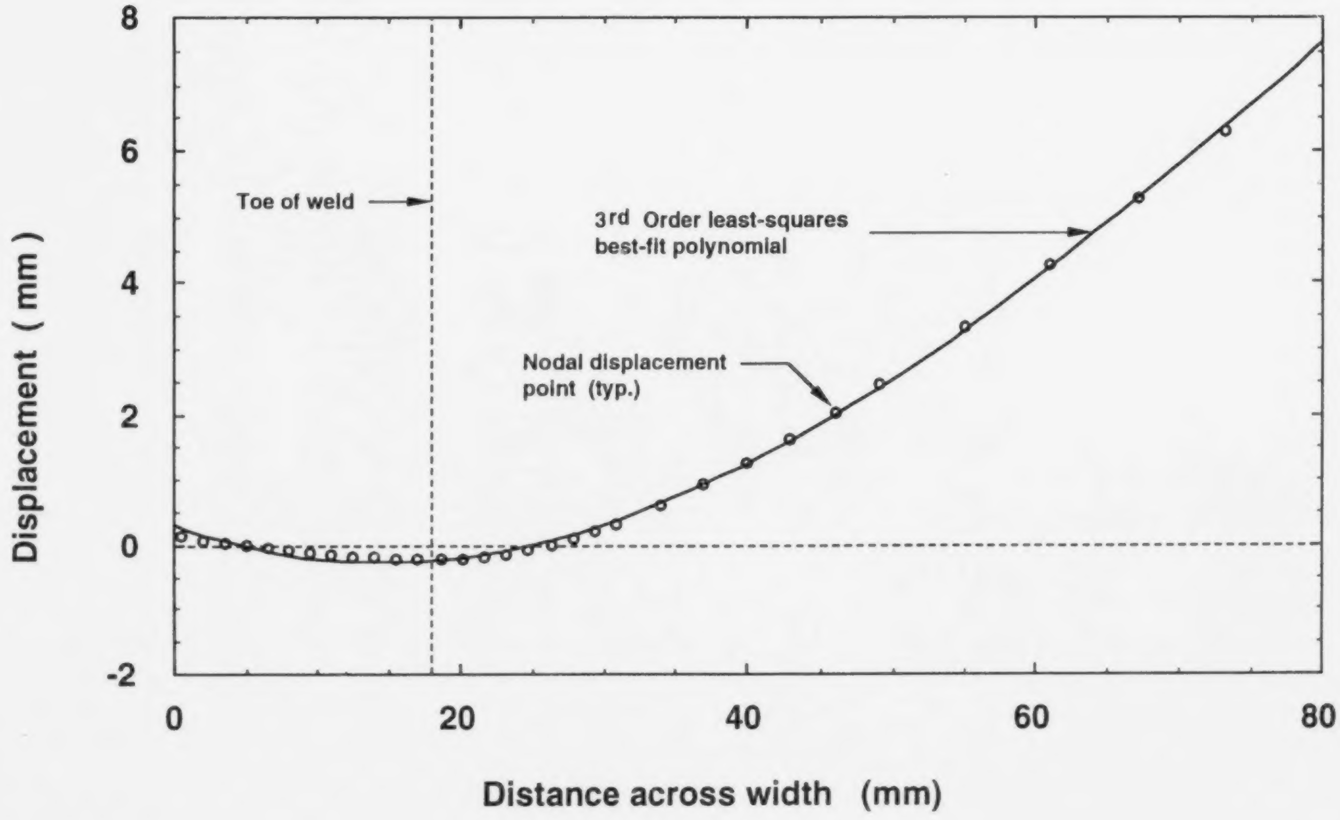

Figure 7.6 Model 2(test P12) midsurface nodal displacements, q/qc = 6.6

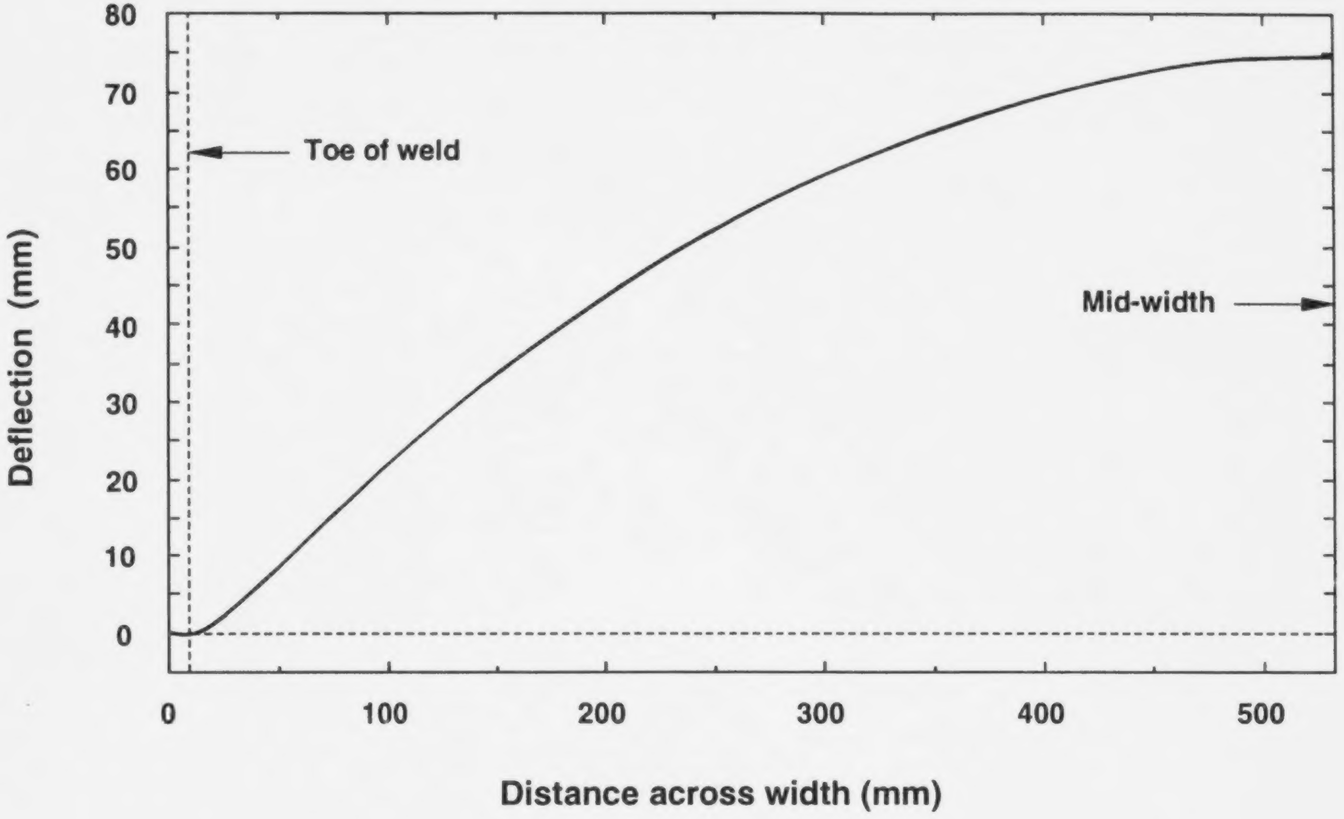

Figure 7.7 Model 1 (test P6-2) mid-surface deflections at test failure load

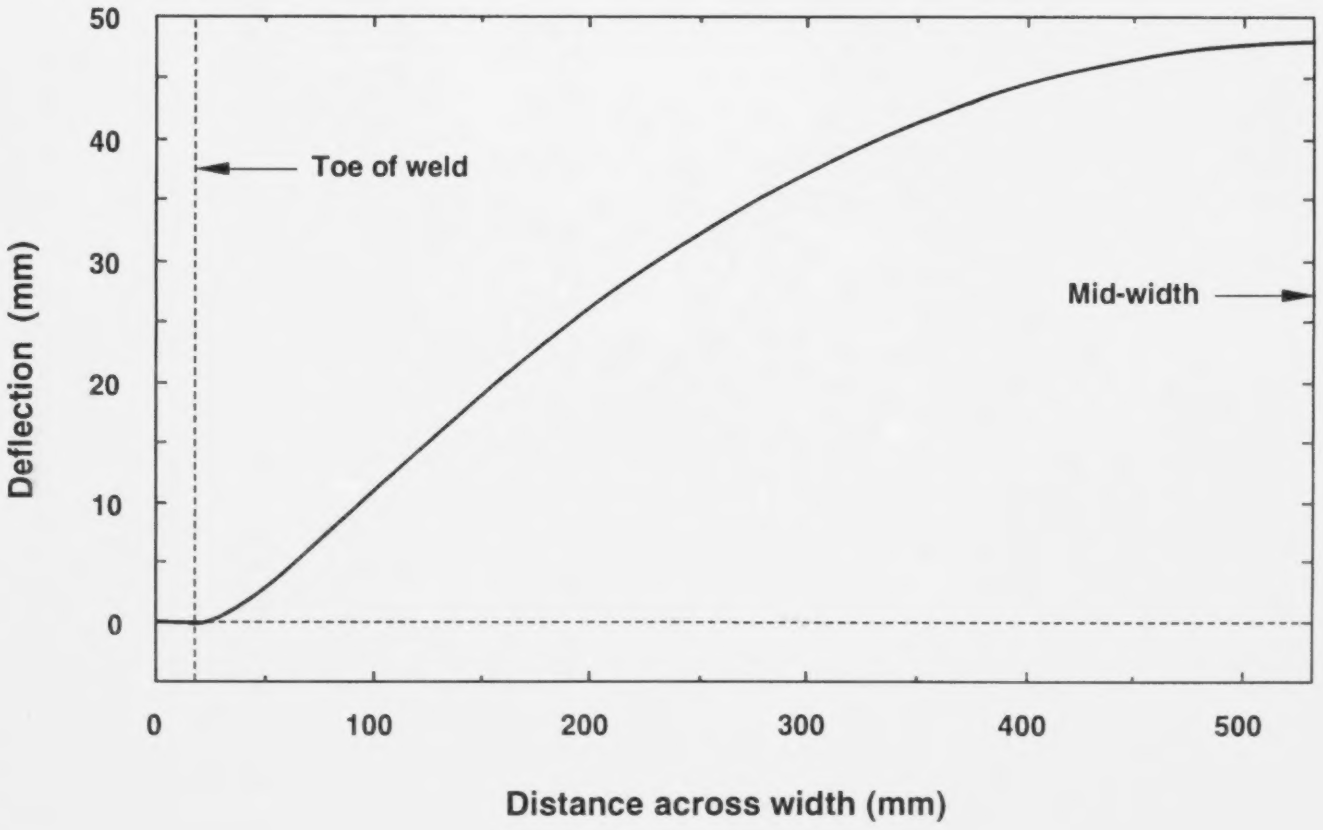

Figure 7.8 Model 2 (test P12) mid-surface deflections at test failure load

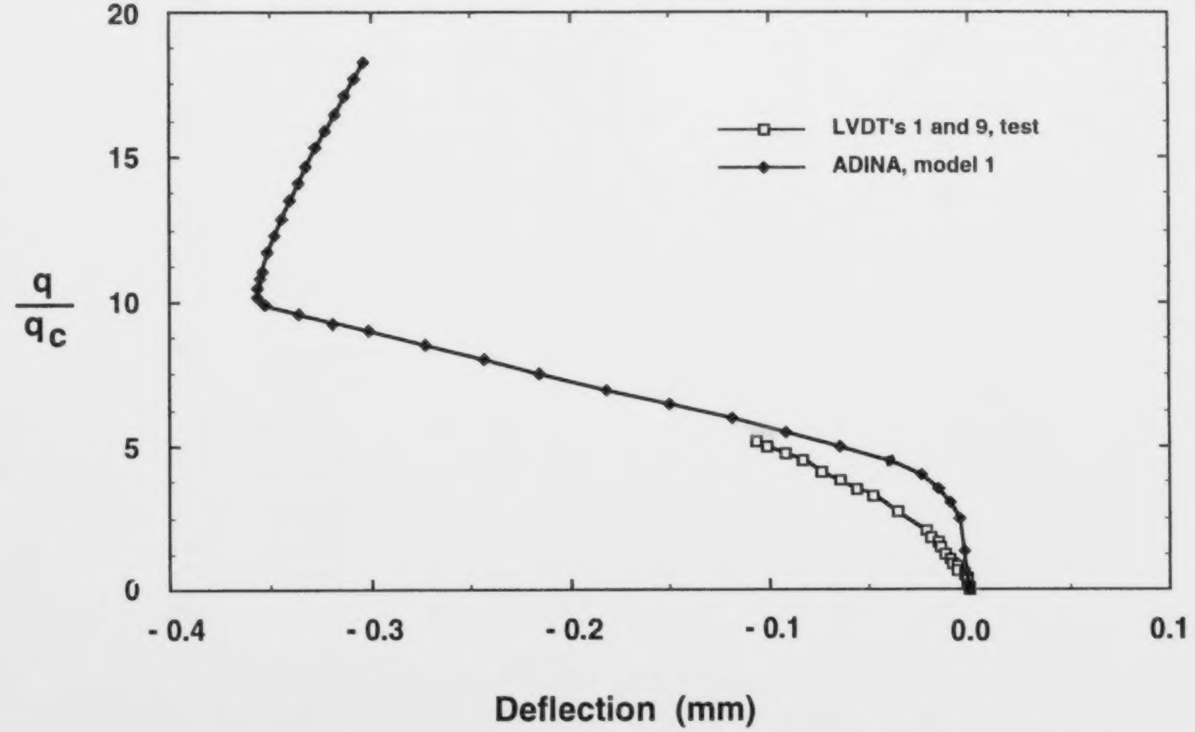

Figure 7.9 Deflection at toe of weld by LVDT's and ADINA model 1, test P6-2

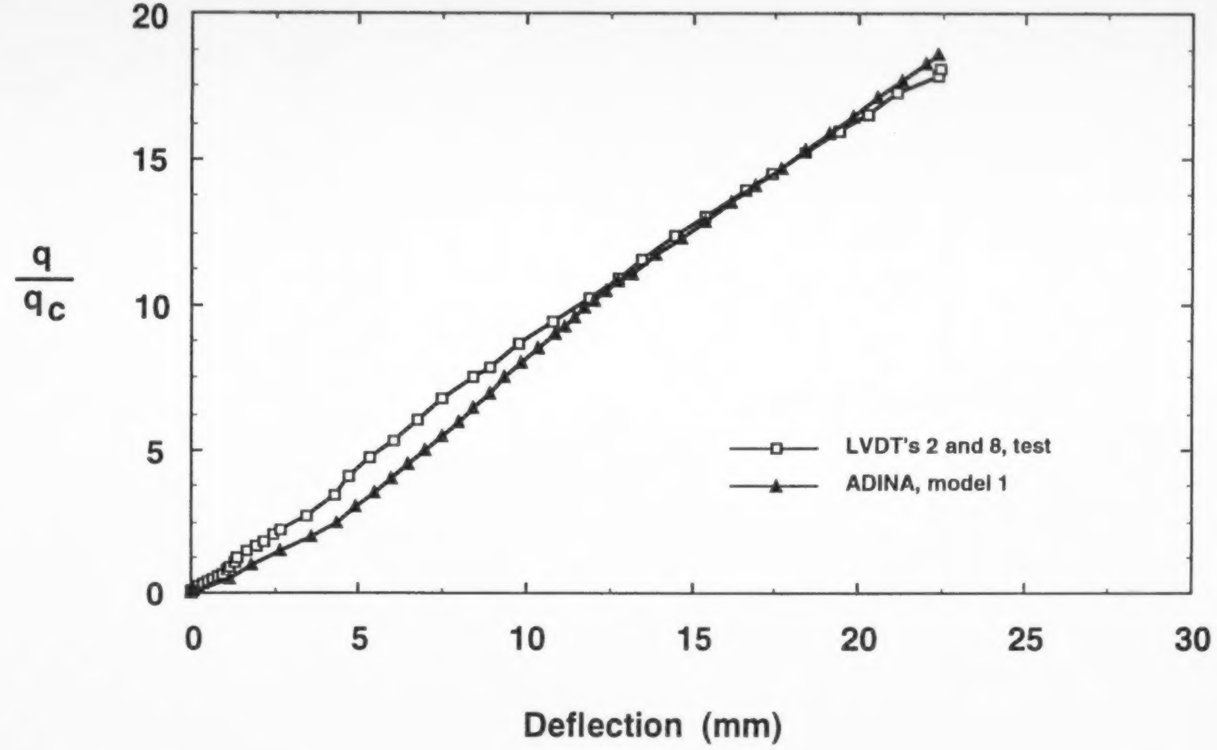

Figure 7.10 Deflection at 87 mm from toe of weld by LVDT's and ADINA model 1, test P6-2

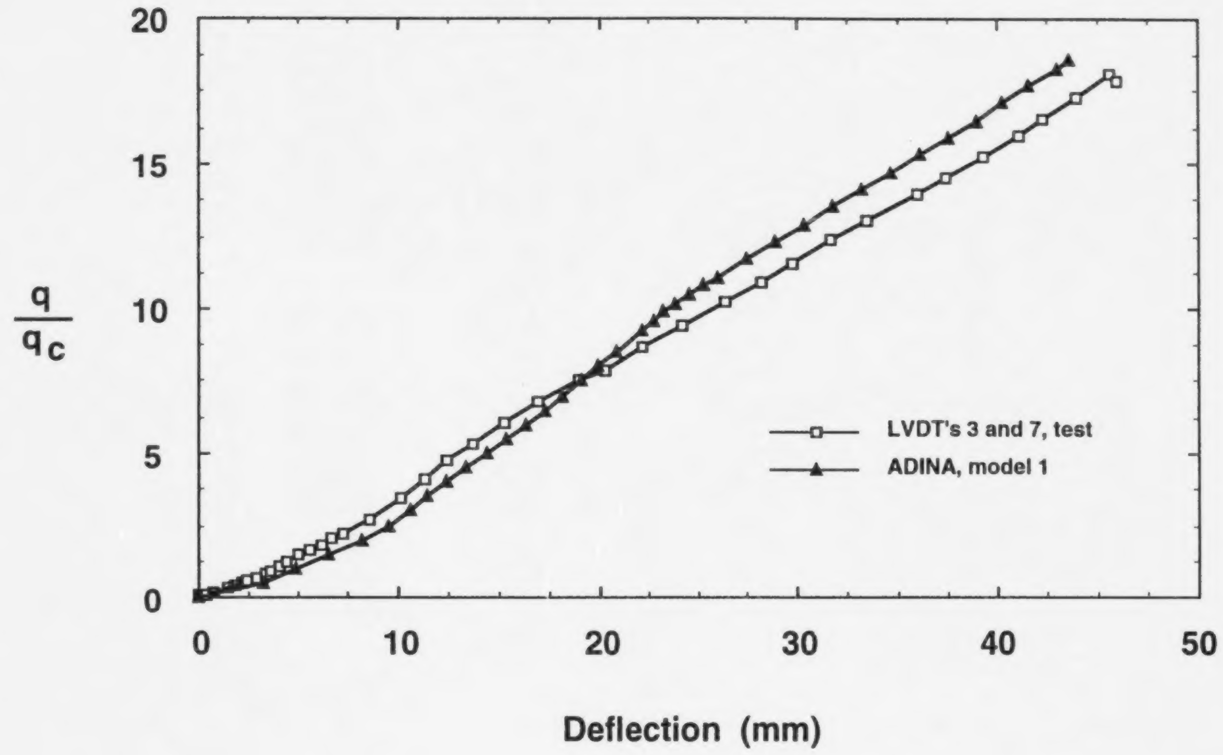

Figure 7.11 Deflection at 174 mm from toe of weld by LVDT's and ADINA model 1, test P6-2

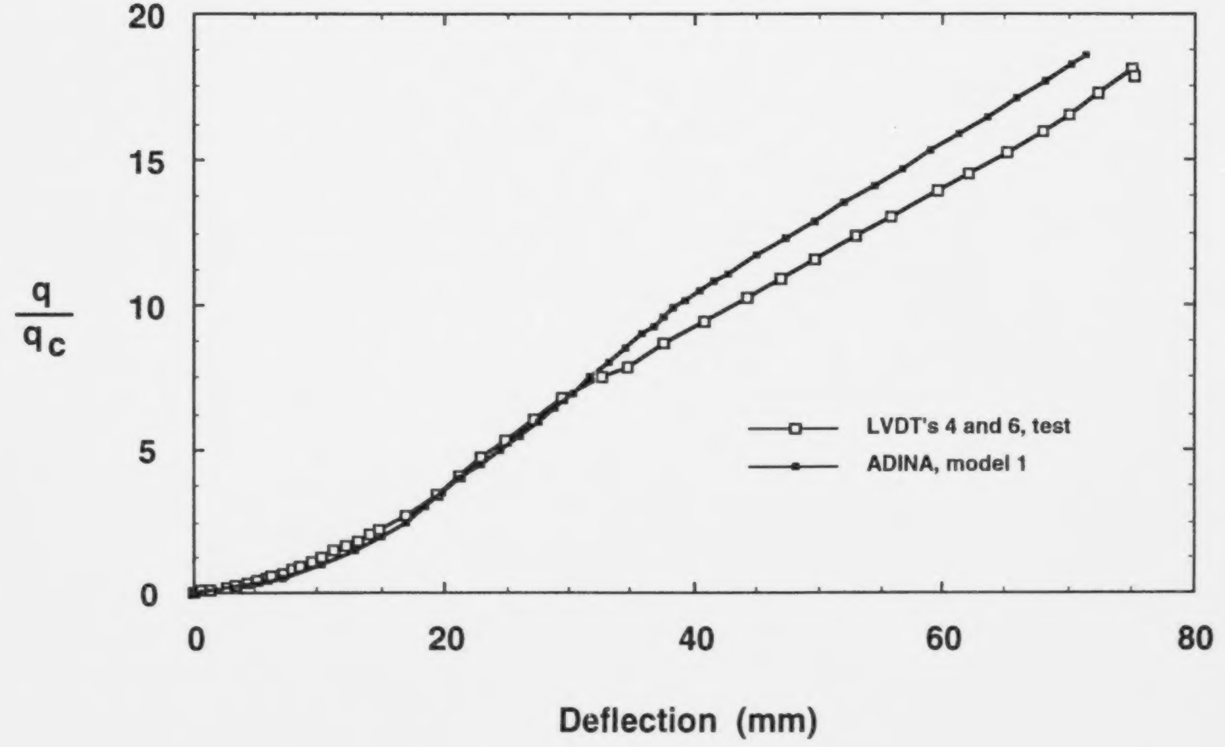

Figure 7.12 Deflection at 348 mm from toe of weld by LVDT's and ADINA model 1, test P6-2

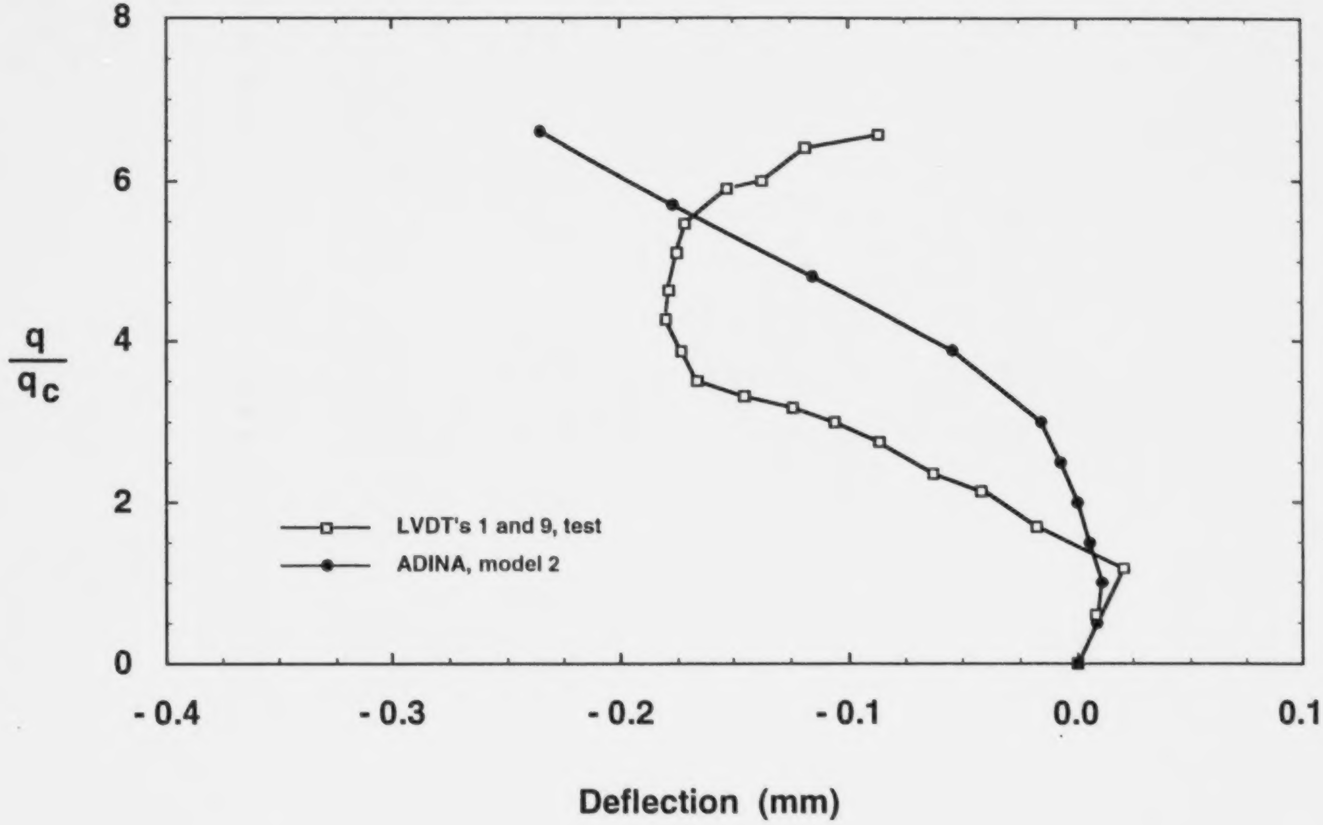

Figure 7.13 Deflection at toe of weld by LVDT's and ADINA model 2, test P12

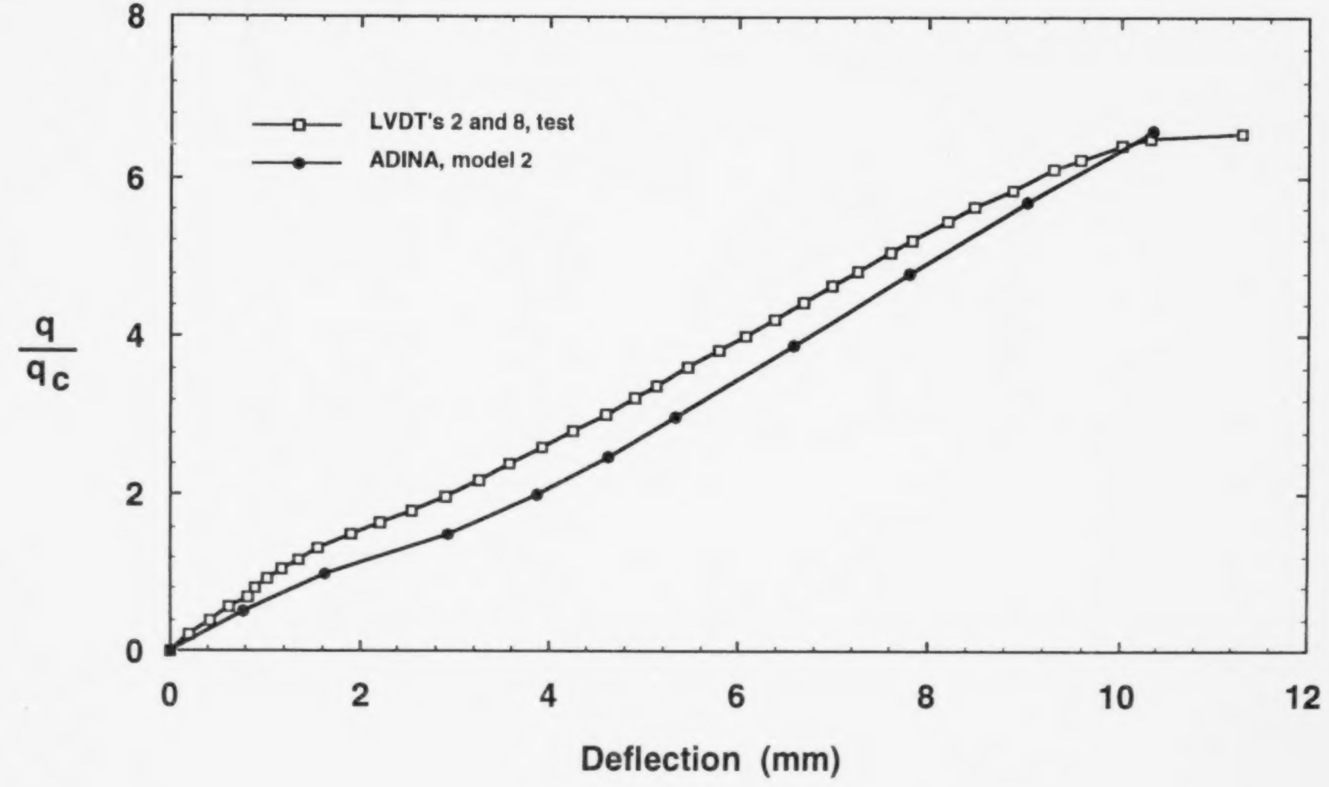

Figure 7.14 Deflection at 87 mm from toe of weld by LVDT's and ADINA model 2, test P12

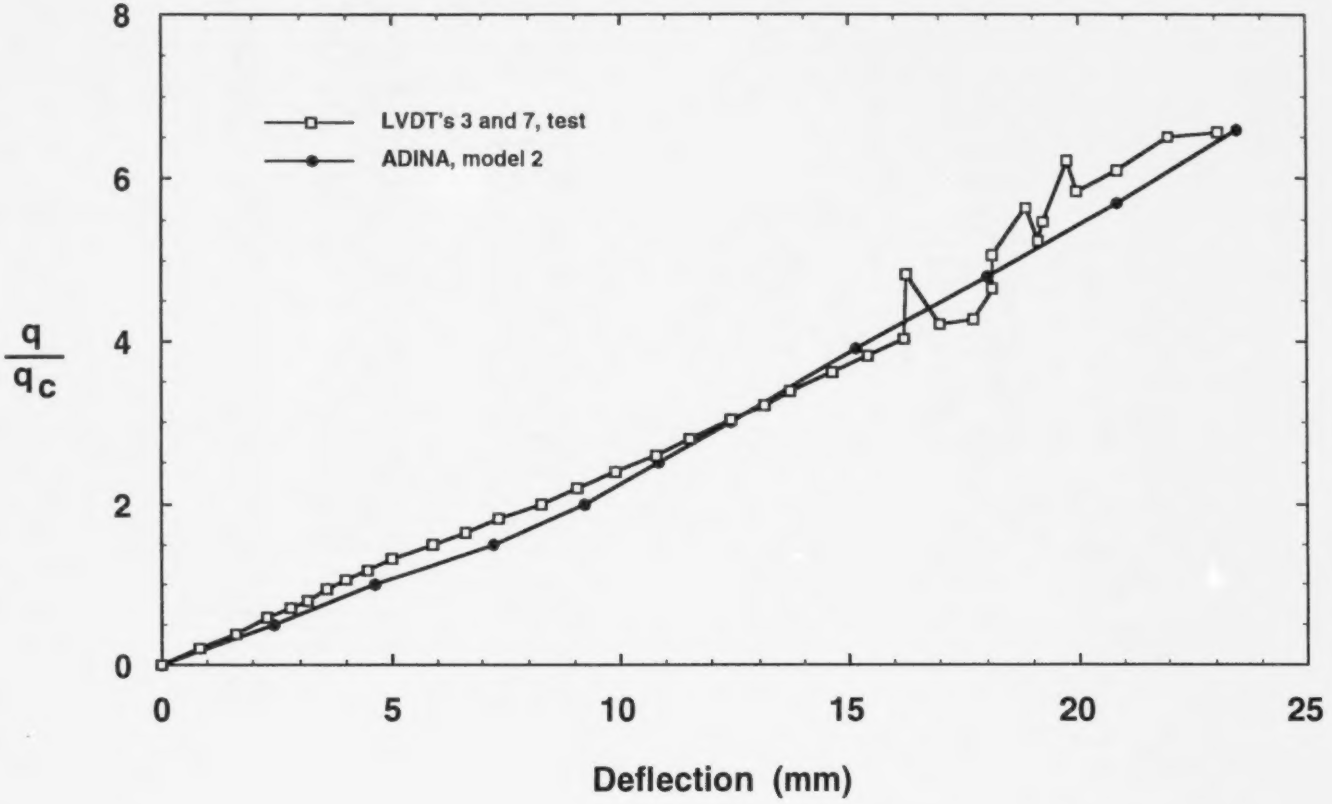

Figure 7.15 Deflection at 174 mm from toe of weld by LVDT's and ADINA model 2, test P12

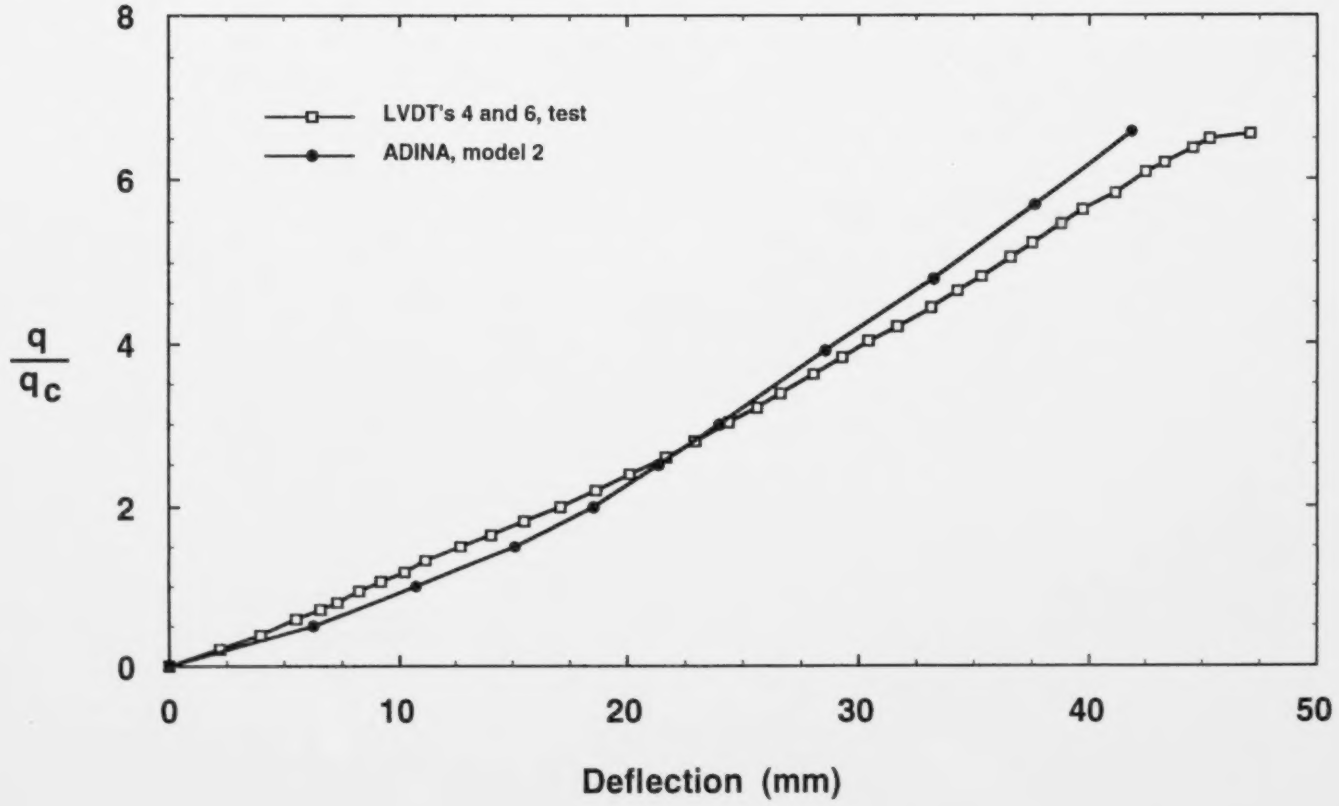

Figure 7.16 Deflection at 348 mm from toe of weld by LVDT's and ADINA model 2, test P12

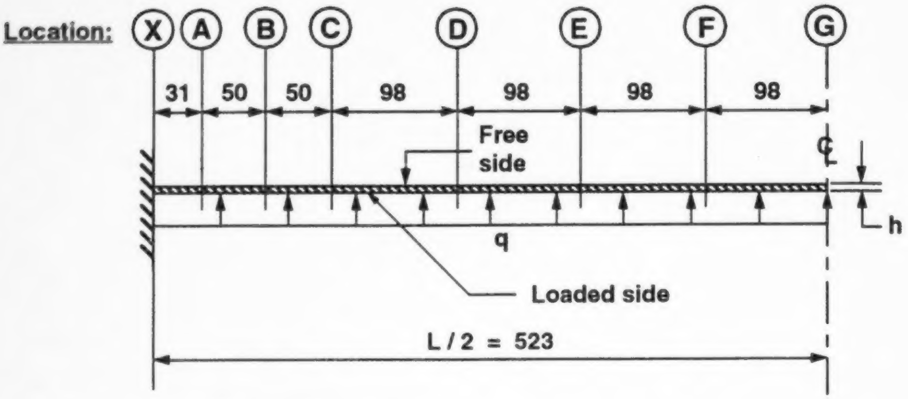
Location:
X
A
B
C
D
E
F
G
31
50
50
98
98
98
98
Free side
℄
h
q
Loaded side
L / 2 = 523

Note: All dimensions in mm

Figure 7.17 Locations for strain comparisons at mid-length between ADINA and test P6-2

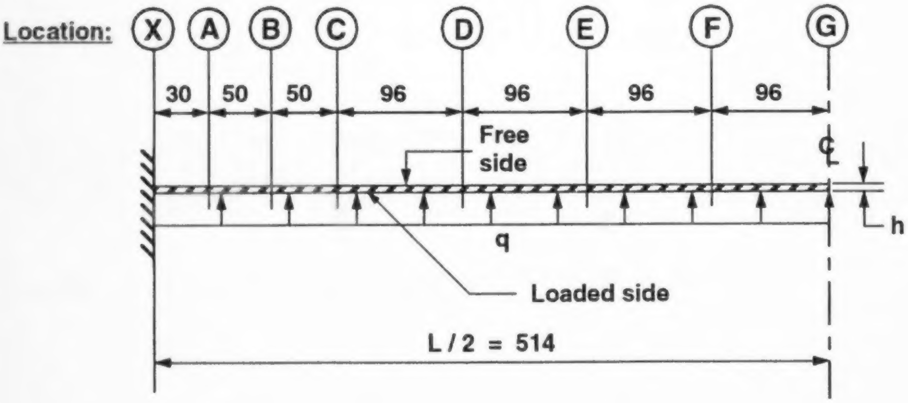
Location:
X
A
B
C
D
E
F
G
30
50
50
96
96
96
96
Free side
℄
h
q
Loaded side
L / 2 = 514

Note: All dimensions in mm

Figure 7.18 Locations for strain comparisons at mid-length between ADINA and test P12

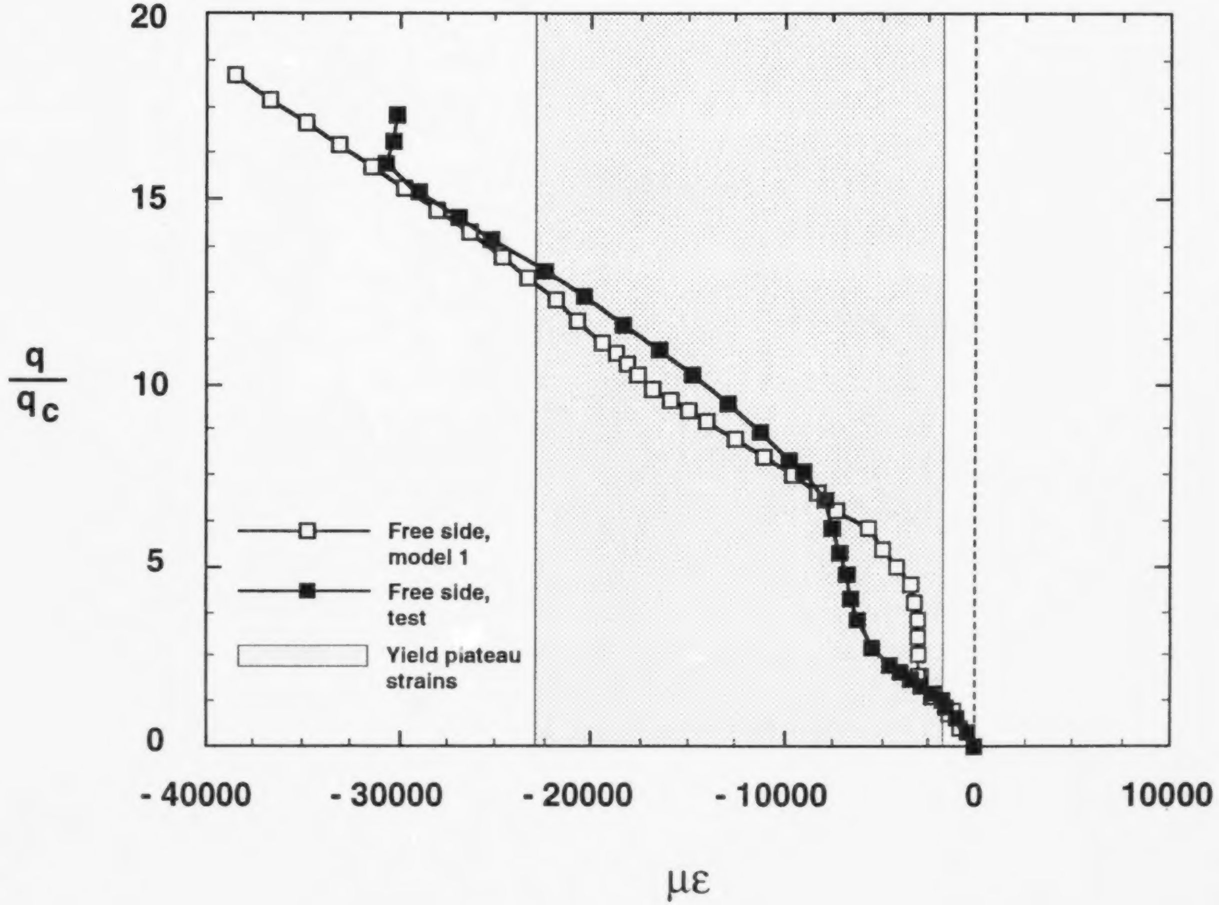

Figure 7.19 Strains at location **X** given by ADINA and gauges on plate P6-2

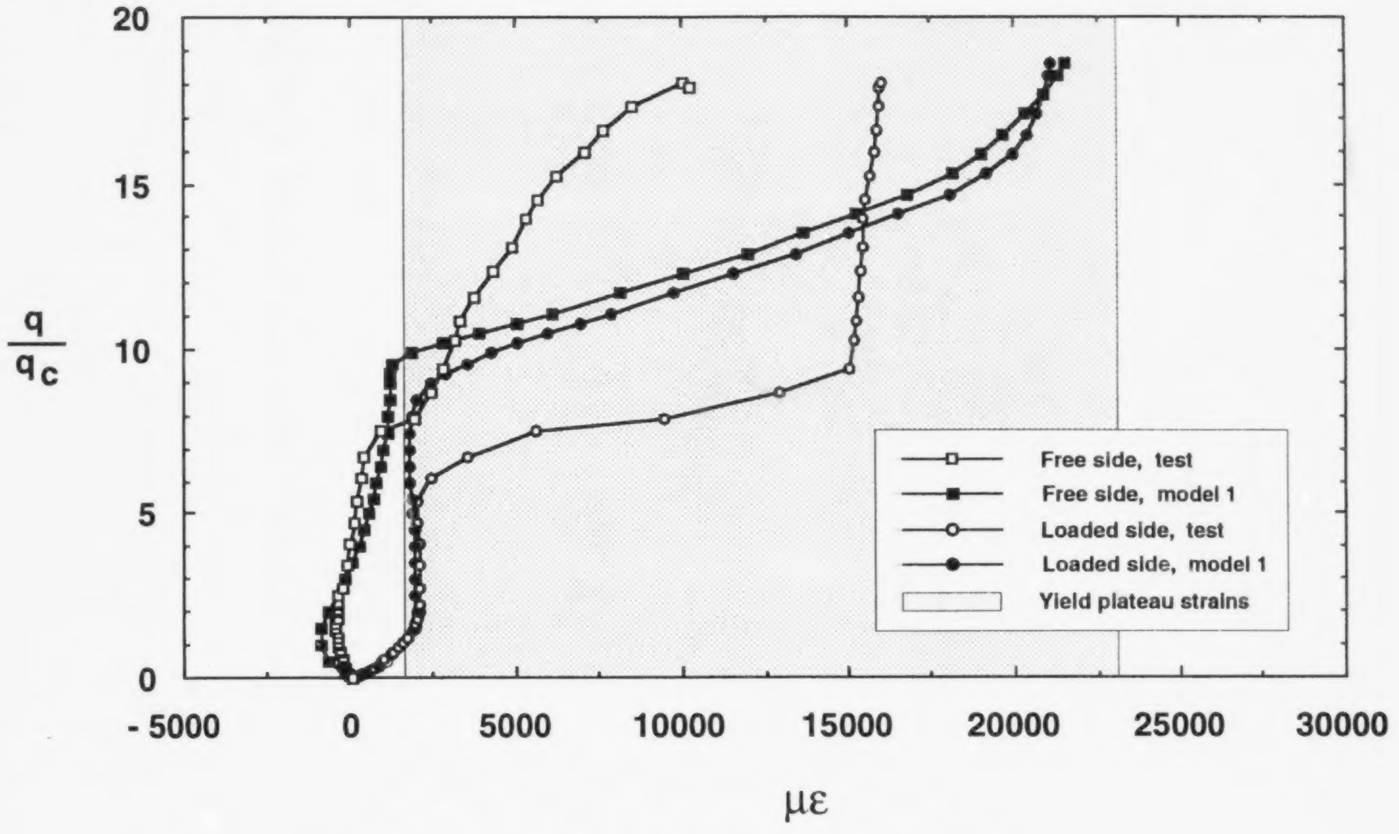

Figure 7.20 Strains at location **A** given by ADINA and gauges on plate P6-2

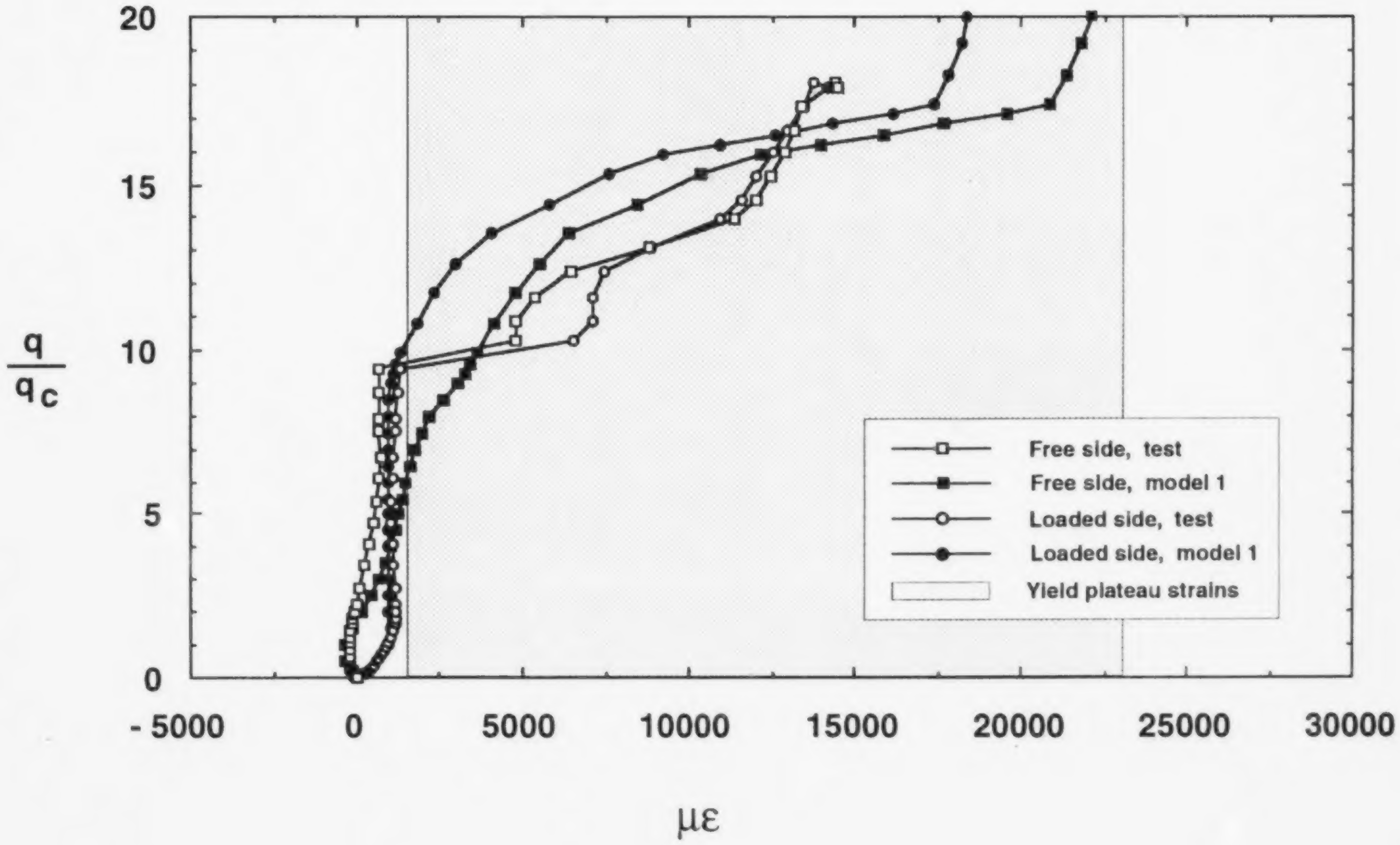

Figure 7.21 Strains at location **B** given by ADINA and gauges on plate P6-2

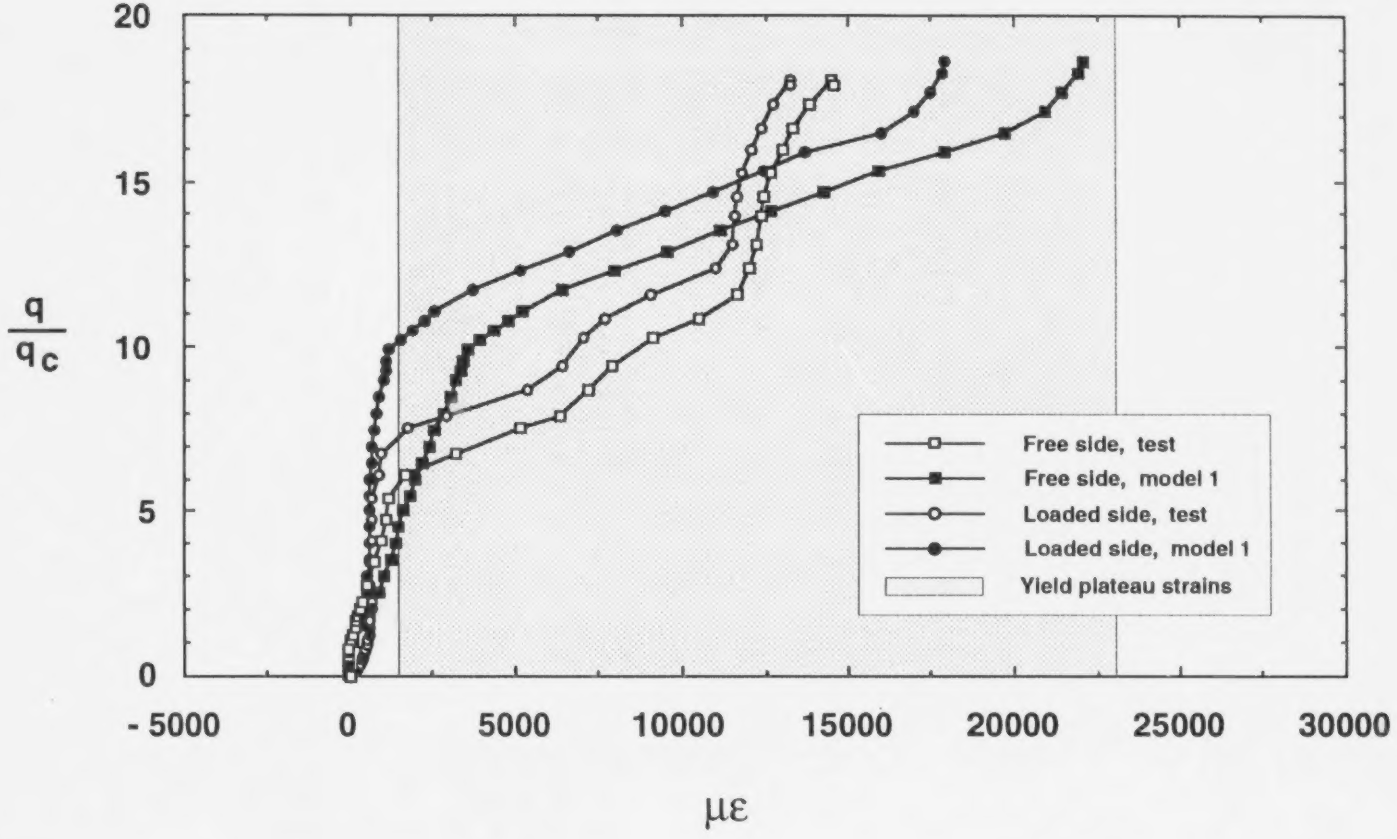

Figure 7.22 Strains at location **C** given by ADINA and gauges on plate P6-2

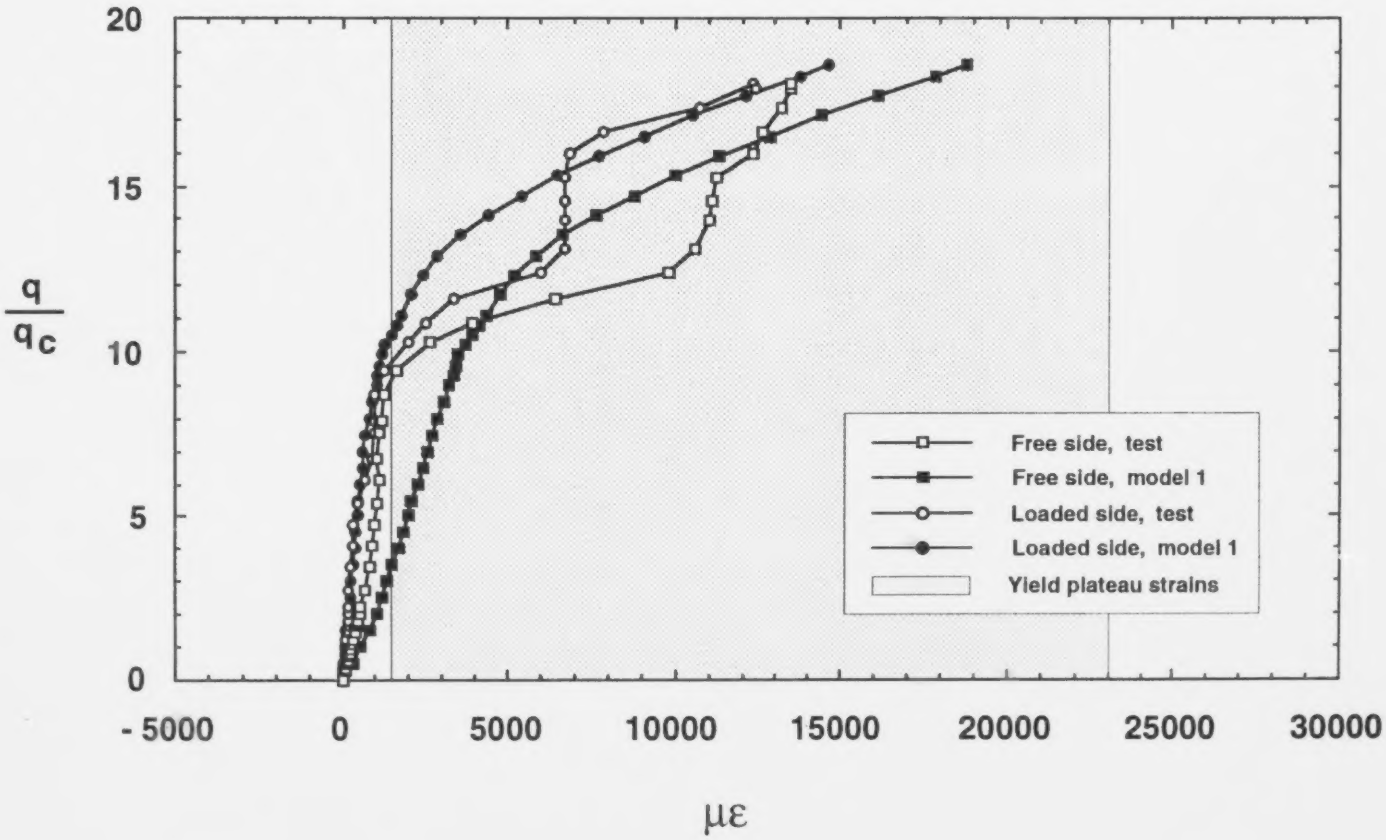

Figure 7.23 Strains at location **D** given by ADINA and gauges on plate P6-2

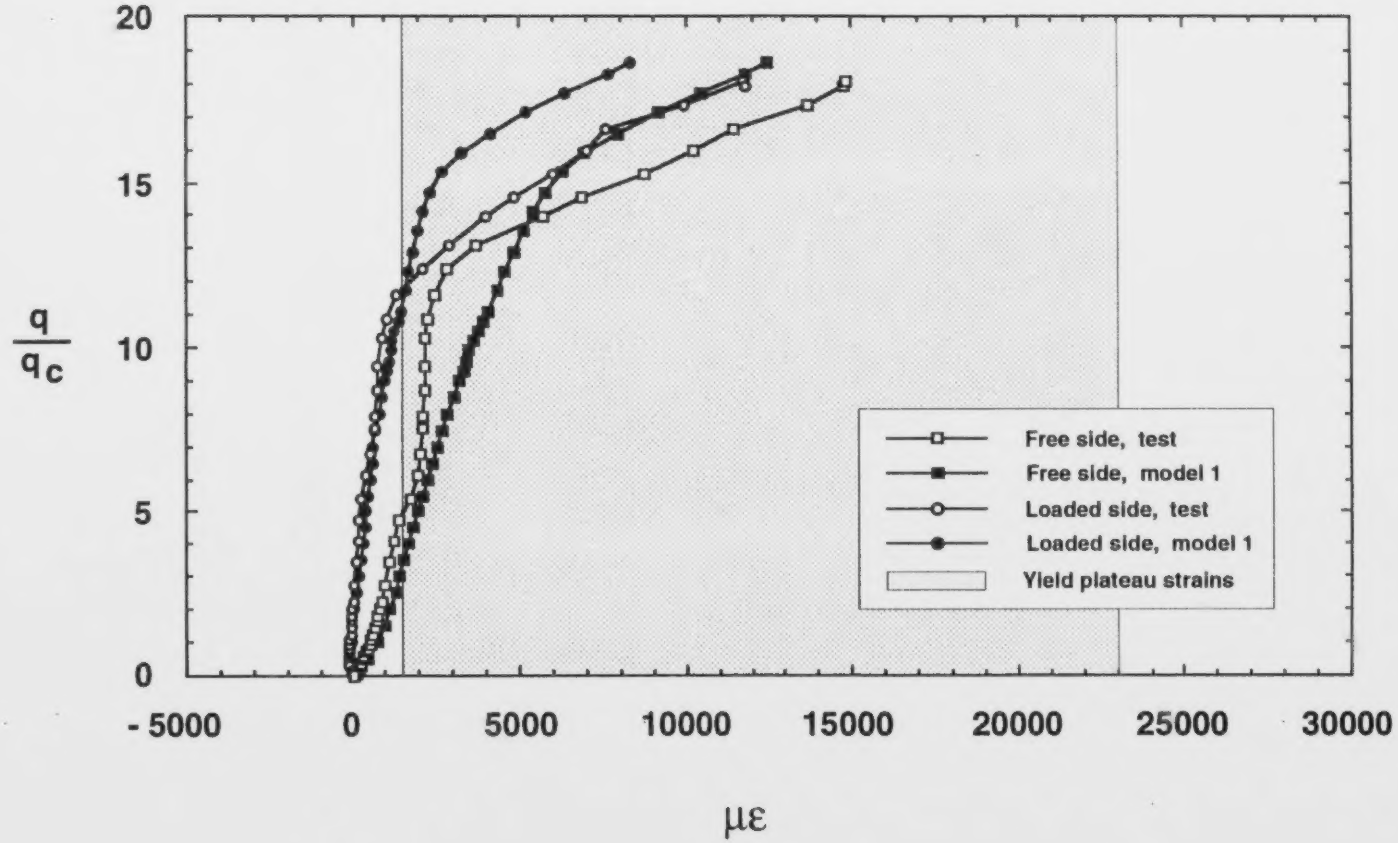

Figure 7.24 Strains at location **E** given by ADINA and gauges on plate P6-2

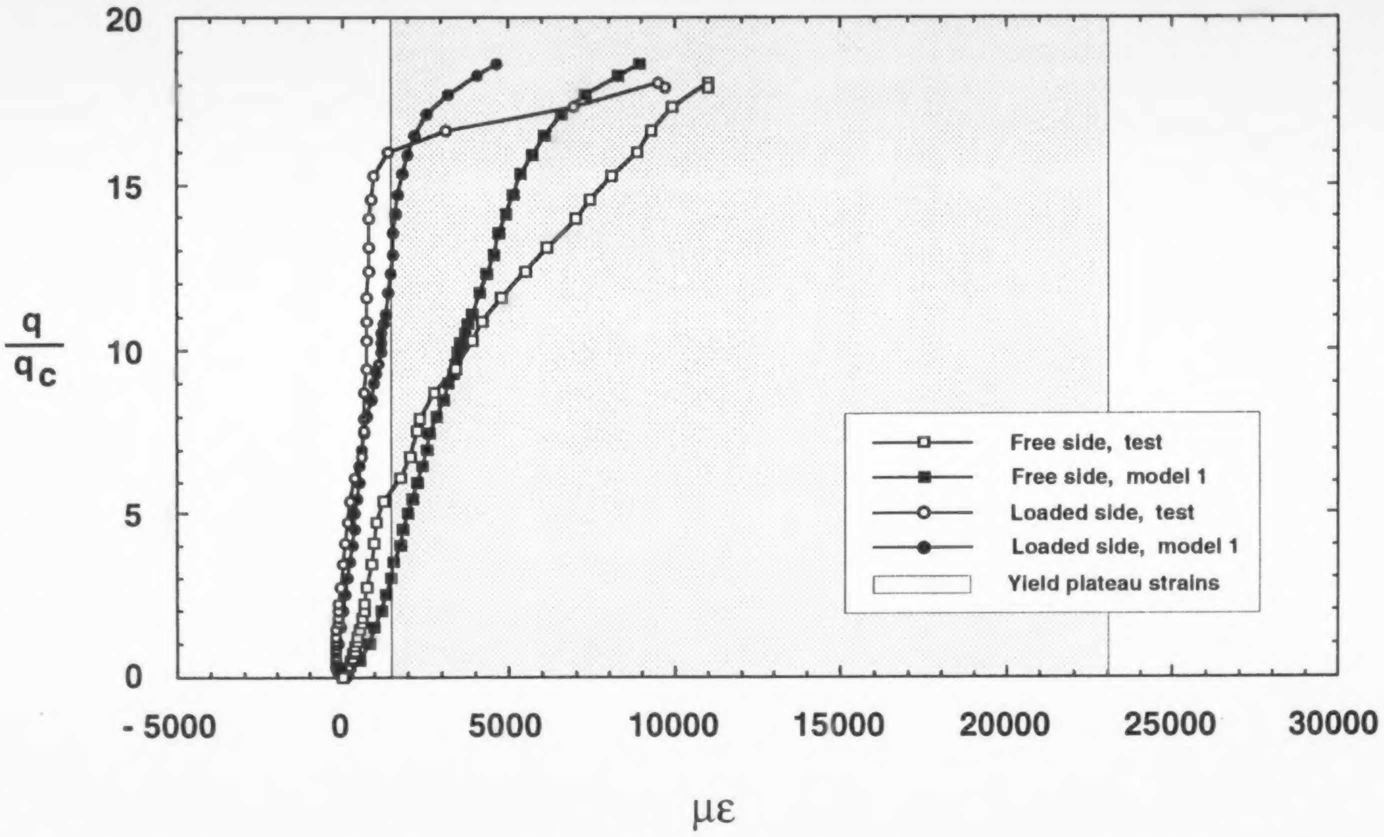

Figure 7.25 Strains at location **F** given by ADINA and gauges on plate P6-2

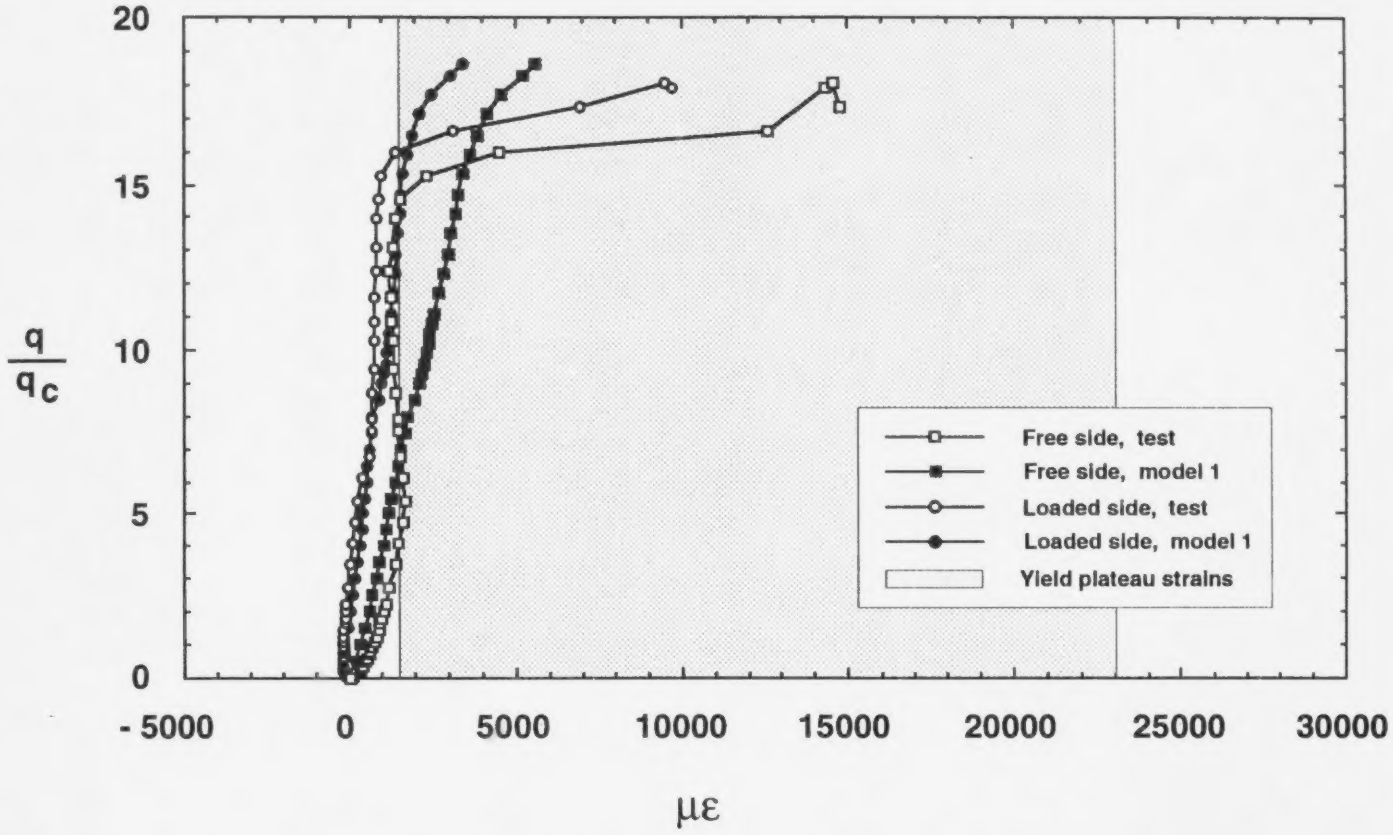

Figure 7.26 Strains at location **G** given by ADINA and gauges on plate P6-2

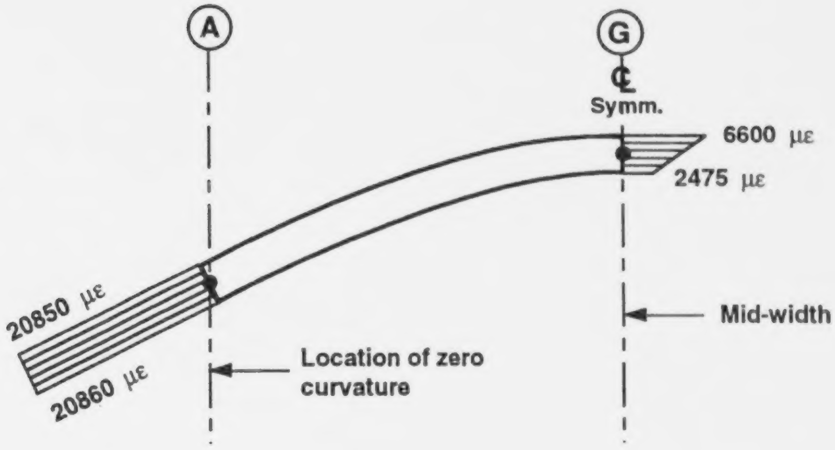
A
G
℄
Symm.
6600 με
2475 με
20850 με
20860 με
Location of zero curvature
Mid-width

(a) Strains

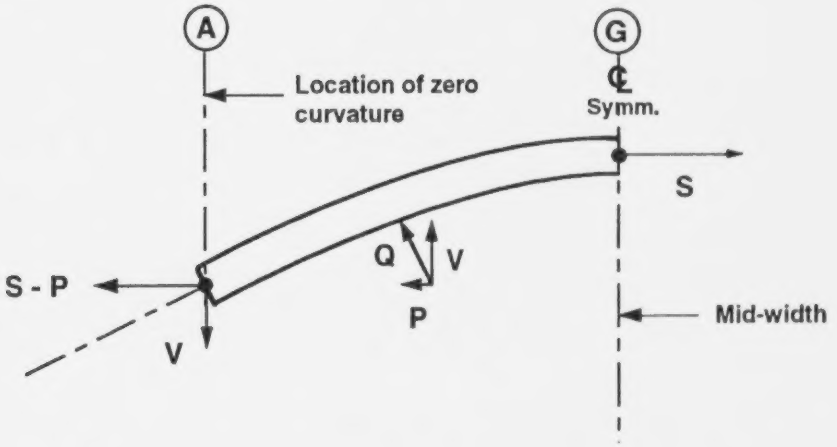
A
G
Location of zero curvature
℄
Symm.
S
S - P
Q
V
P
V
Mid-width

(b) Free body diagram

Figure 7.27 Strain and free body diagrams from location **A** to location **G**, model 1, q/qc = 17.7

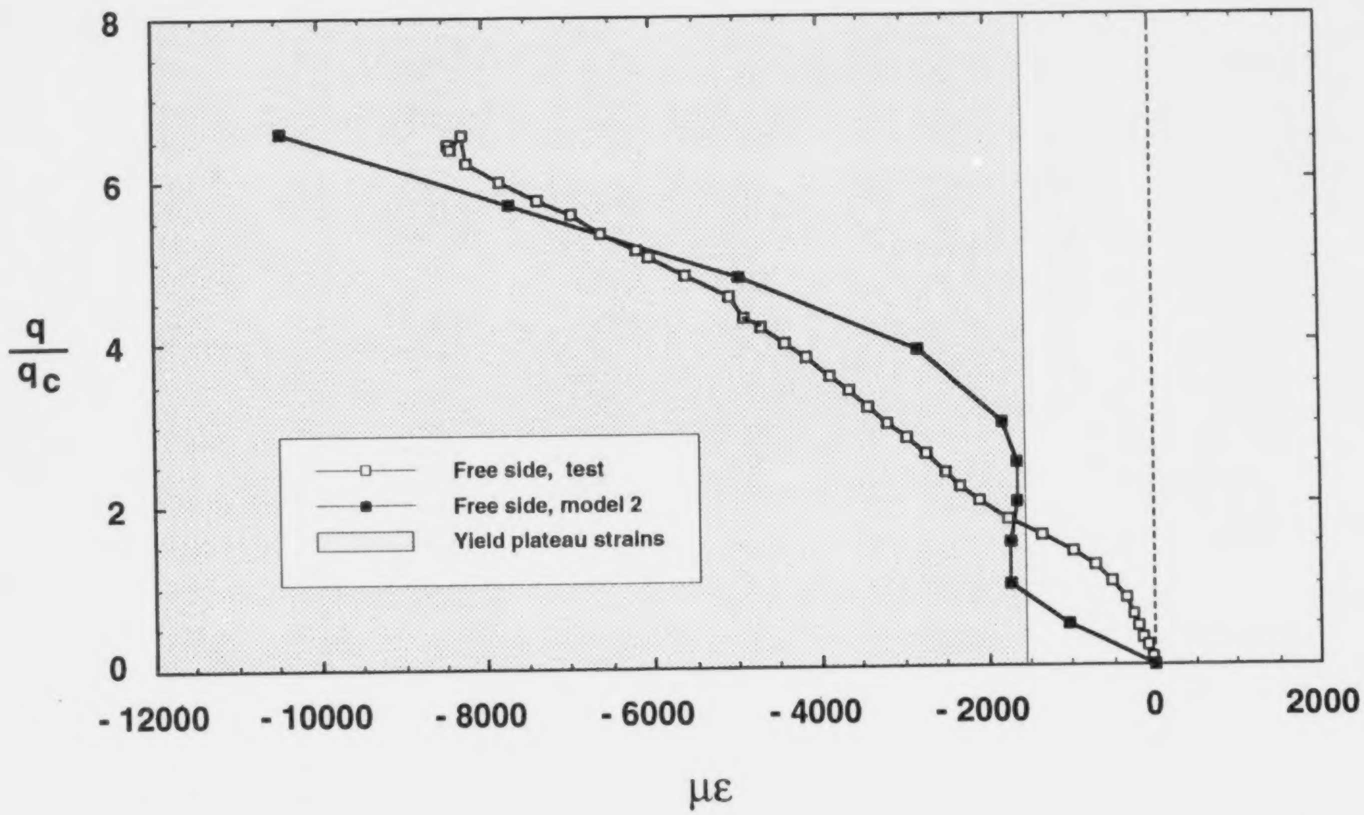

Figure 7.28 Strains at location **X** given by ADINA and gauges on plate P12

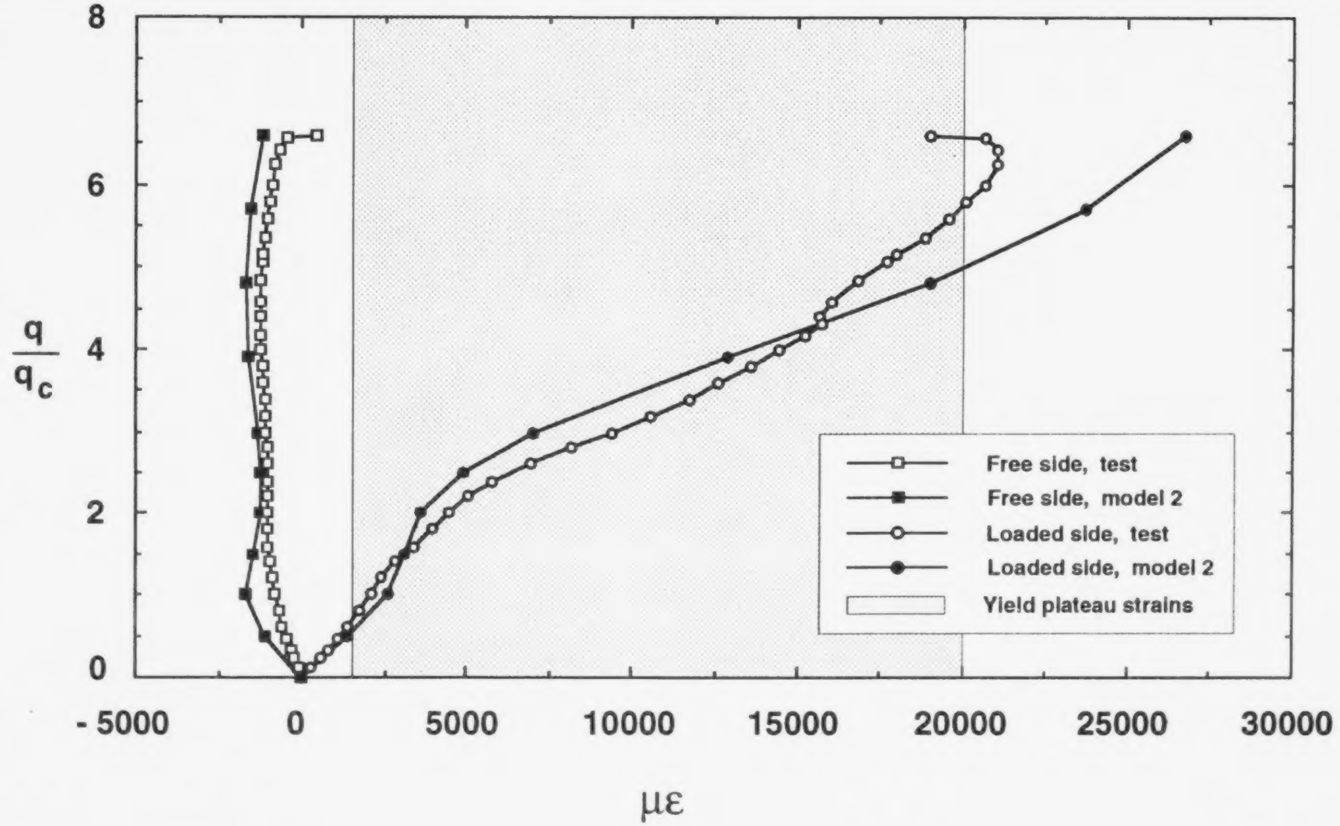

Figure 7.29 Strains at location **A** given by ADINA and gauges on plate P12

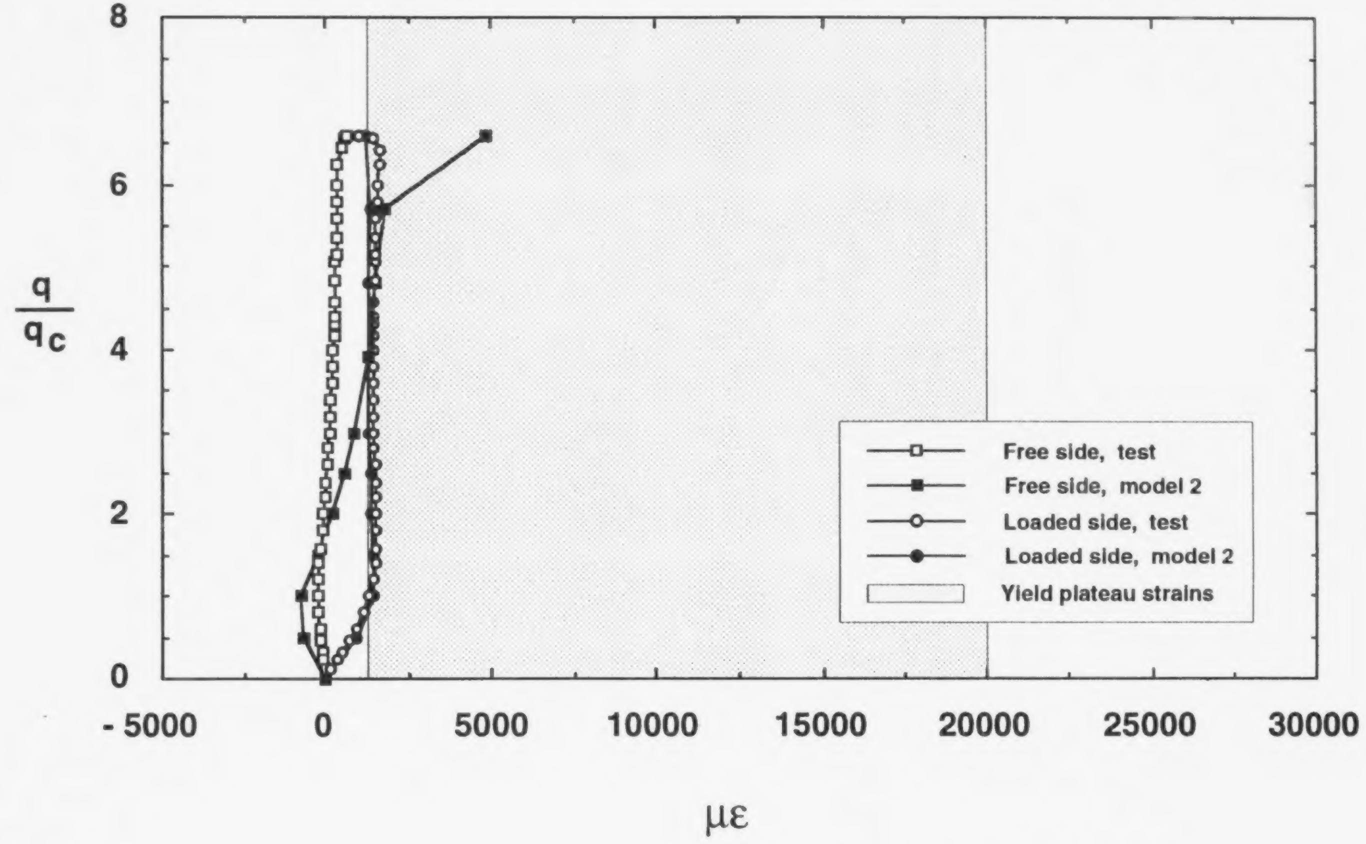

Figure 7.30 Strains at location **B** given by ADINA and gauges on plate P12

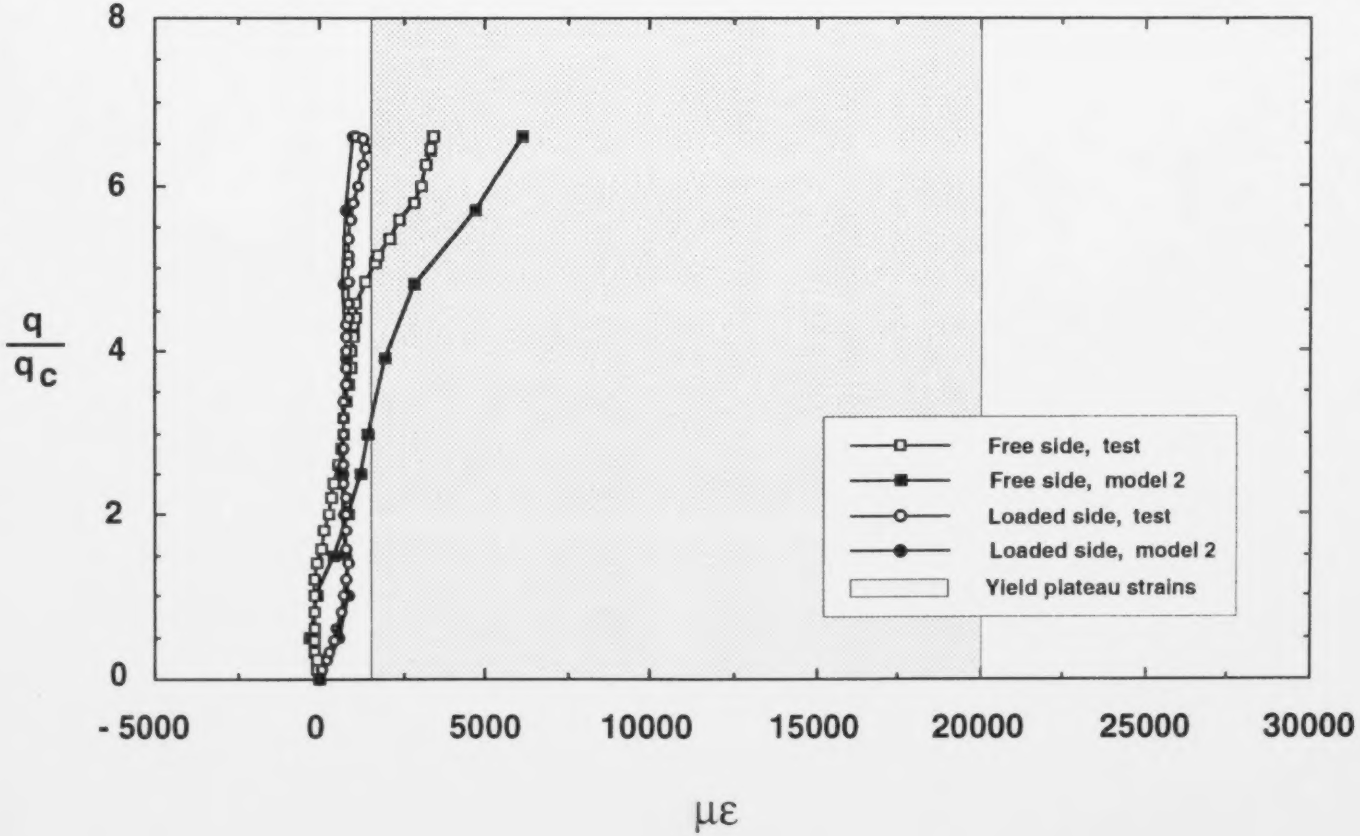

Figure 7.31 Strains at location **C** given by ADINA and gauges on platge P12

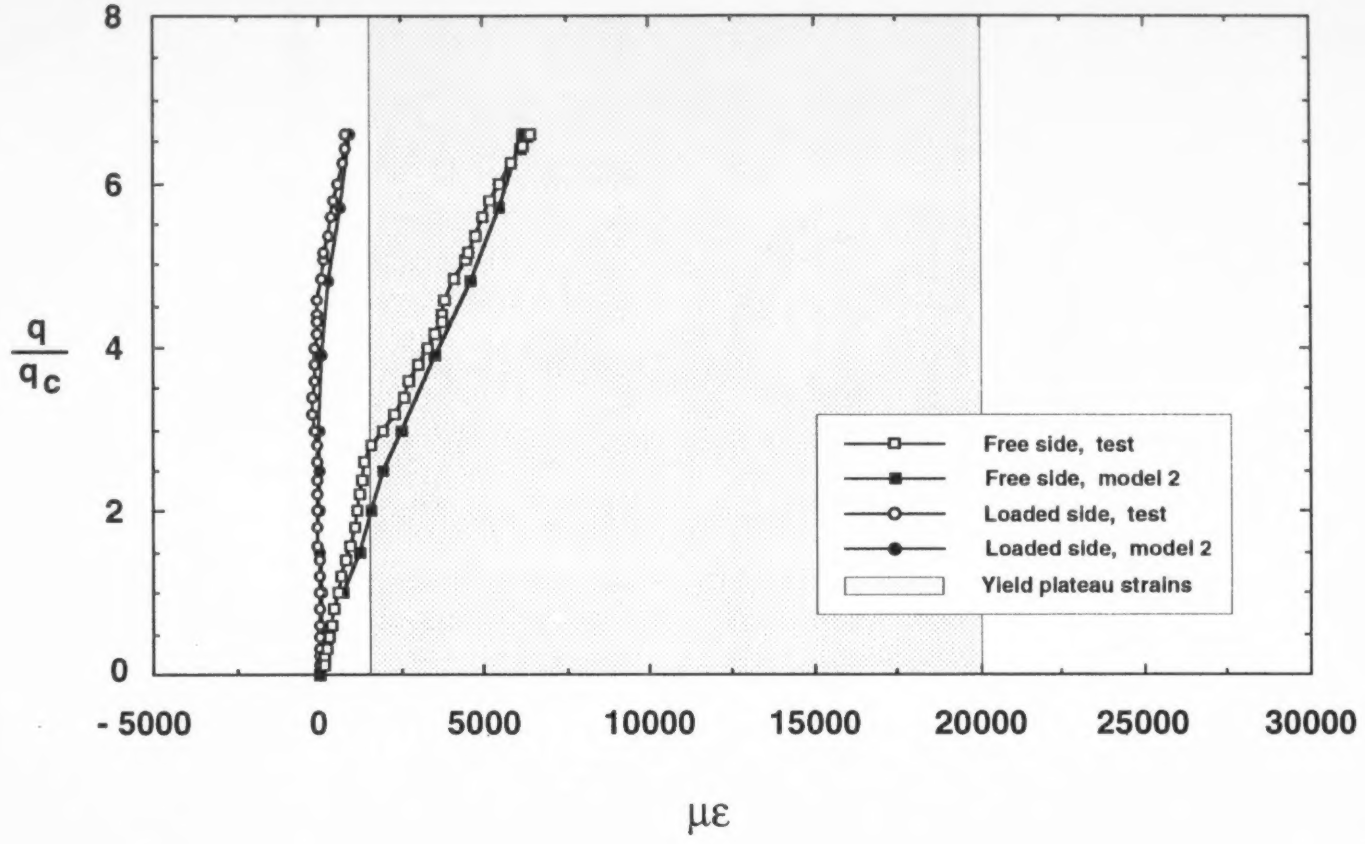

Figure 7.32 Strains at location **D** given by ADINA and gauges on plate P12

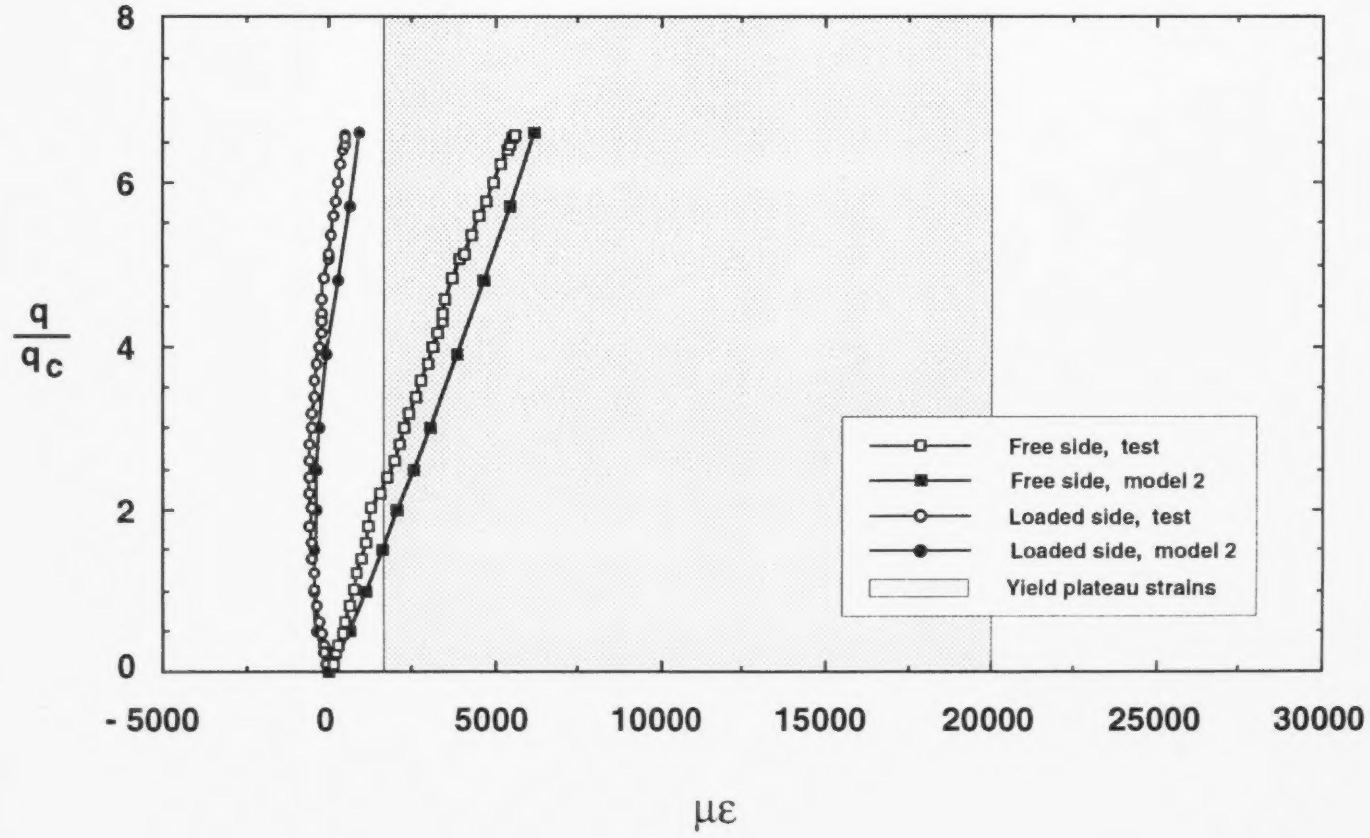

Figure 7.33 Strains at location **E** given by ADINA and gauges on plate P12

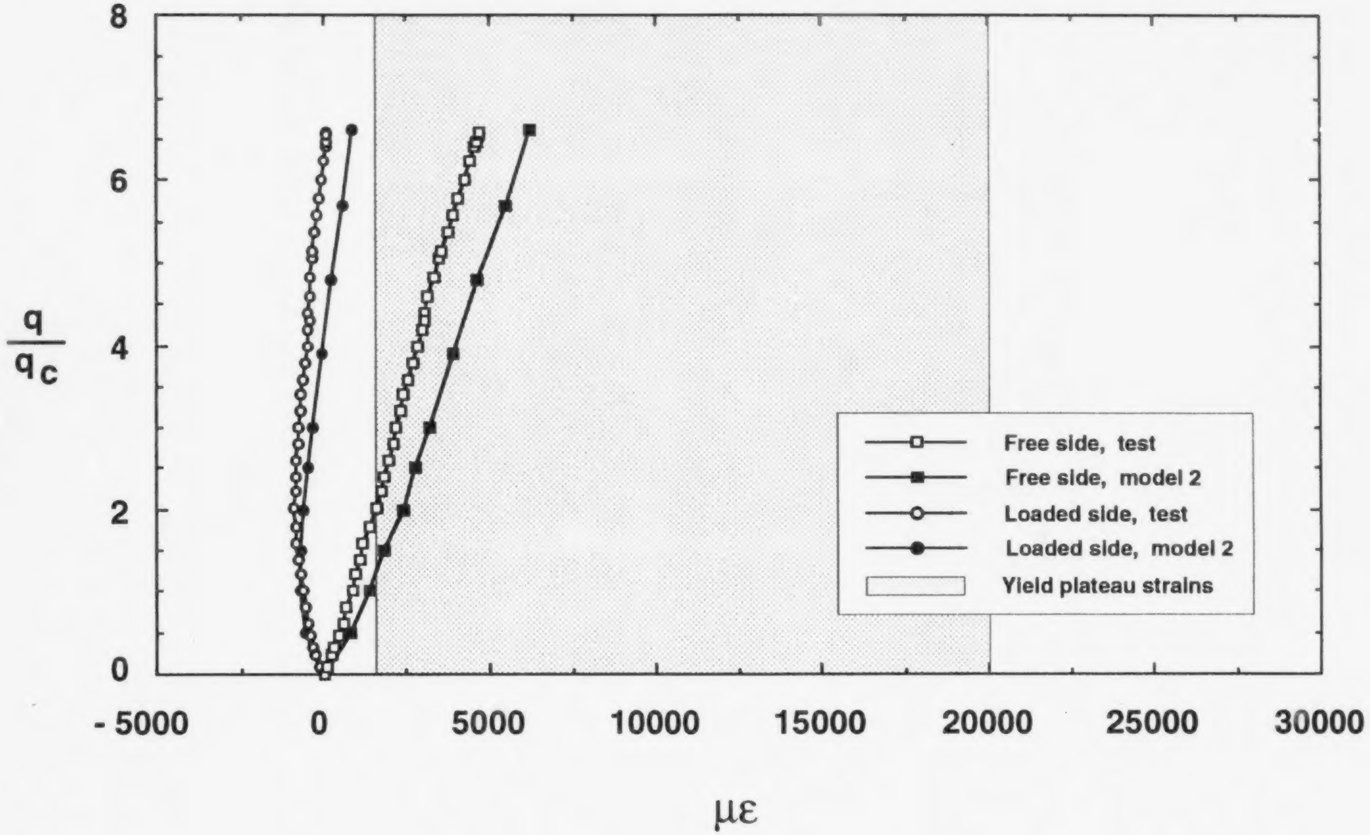

Figure 7.34 Strains at location **F** given by ADINA and gauges on plate P12

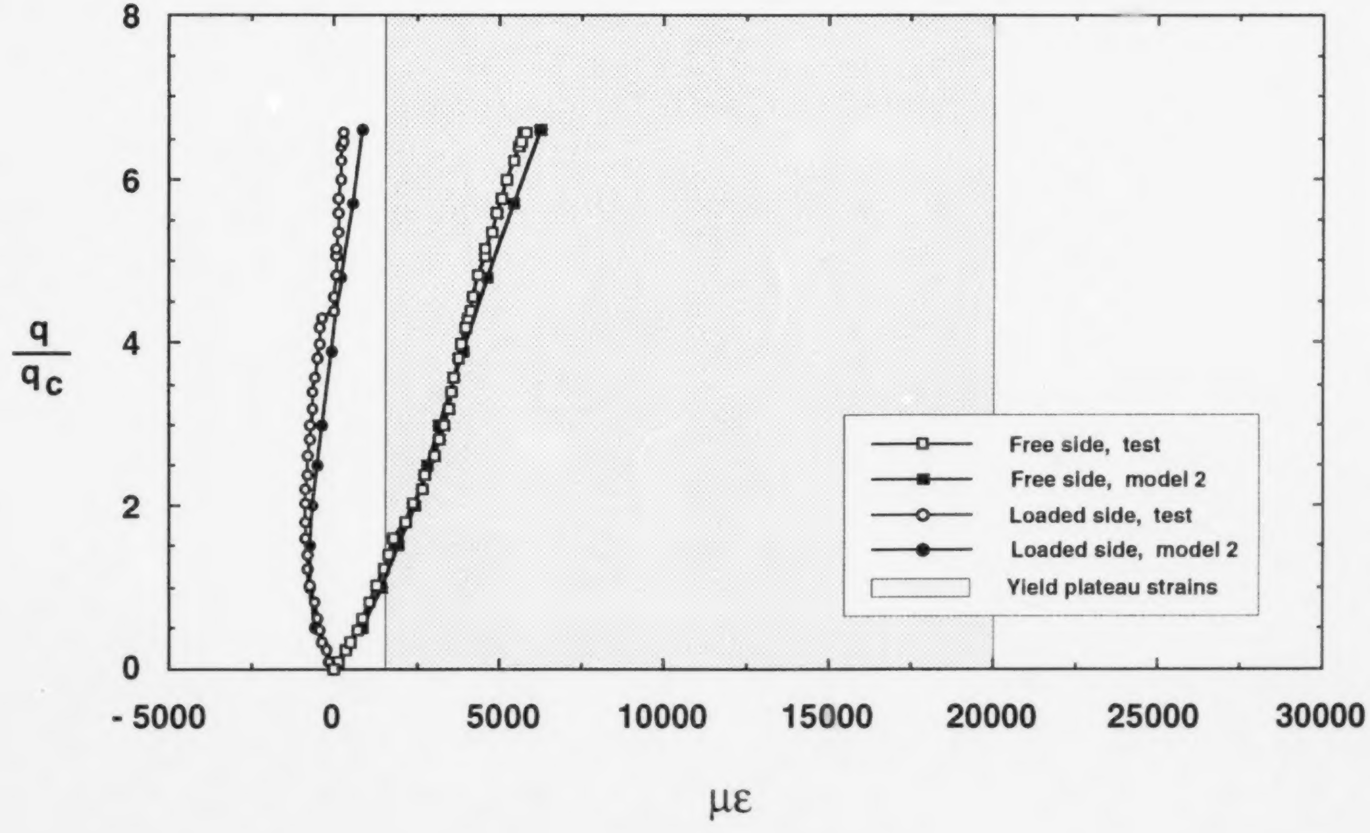

Figure 7.35 Strains at location **G** given by ADINA and gauges on plate P12

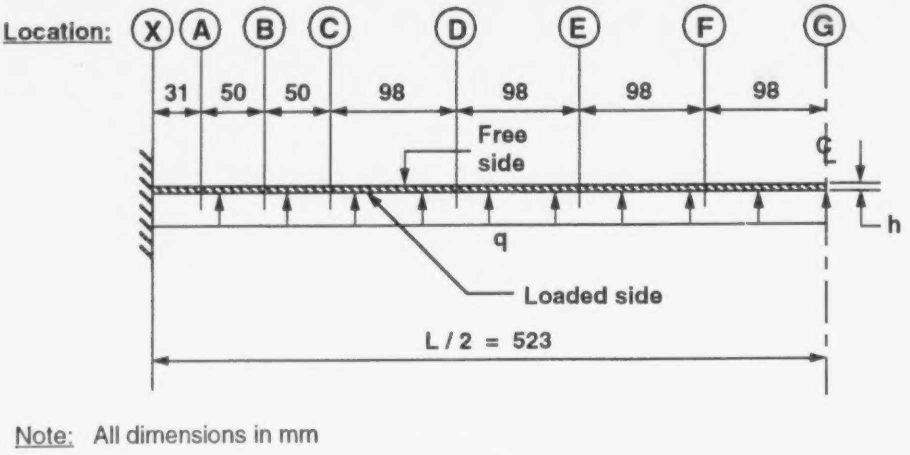
Location:
X
A
B
C
D
E
F
G
31
50
50
98
98
98
98
Free side
℄
h
q
Loaded side
L / 2 = 523
Note: All dimensions in mm

Figure 7.36 Locations of strain measurements, test P6-1

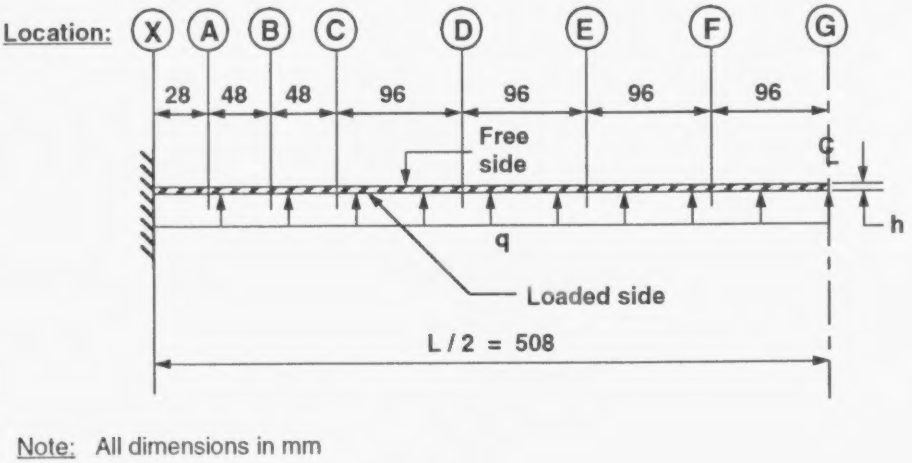
Location:
X
A
B
C
D
E
F
G
28
48
48
96
96
96
96
Free side
℄
h
q
Loaded side
L / 2 = 508
Note: All dimensions in mm

Figure 7.37 Locations of strain measurements, test P16

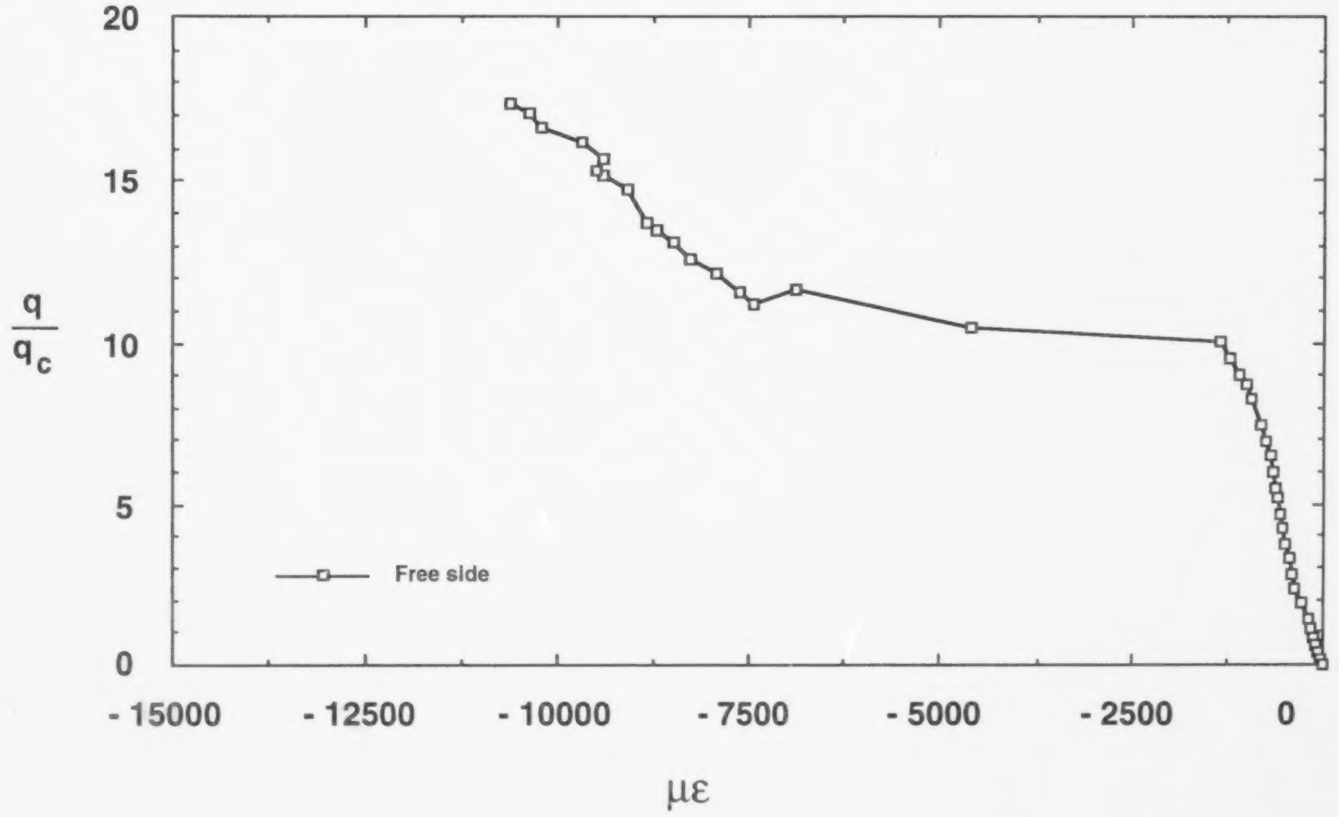

Figure 7.38 Strains at location **X**, test P6-1

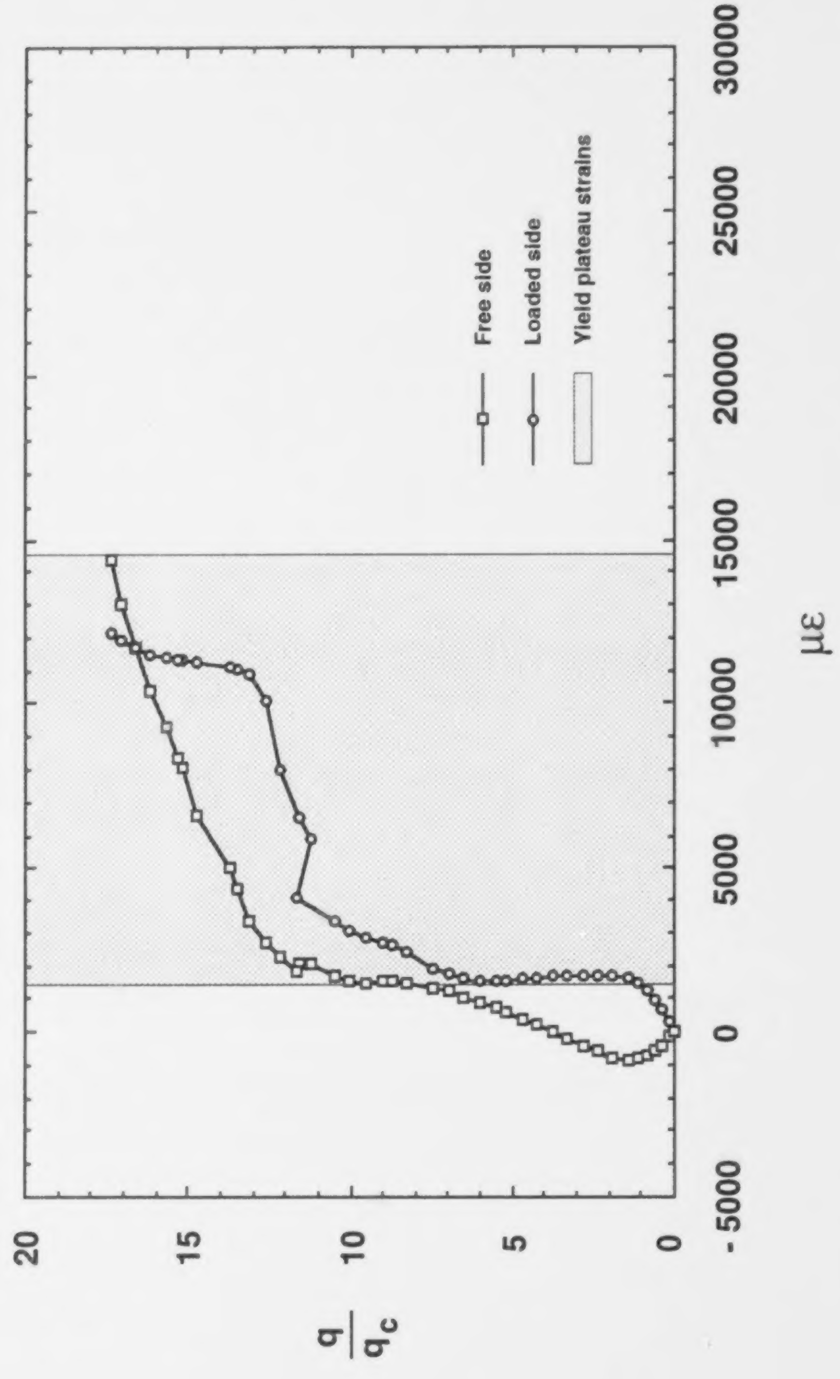

Figure 7.39 Strains at location **A**, test P6-1

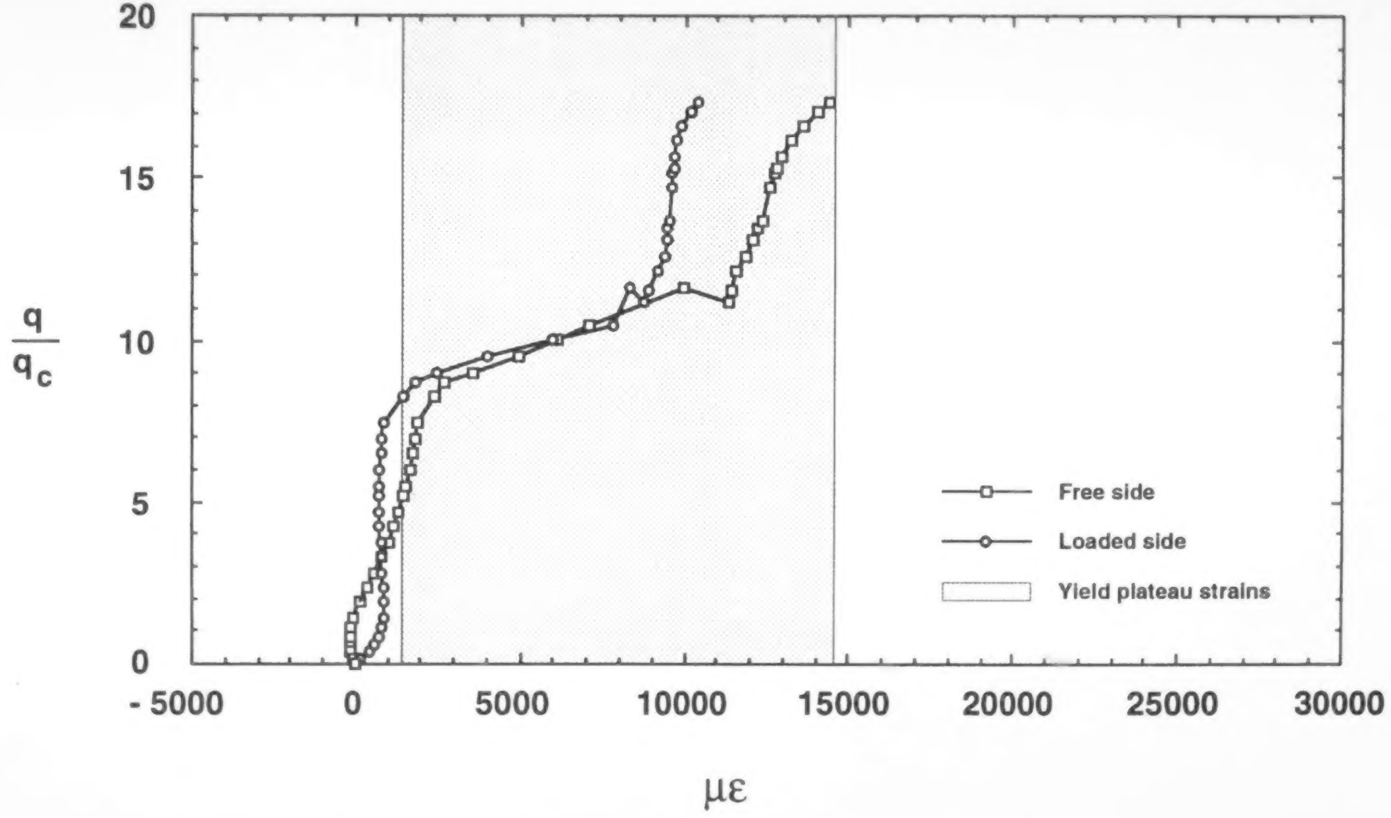

Figure 7.40 Strains at location **B**, test P6-1

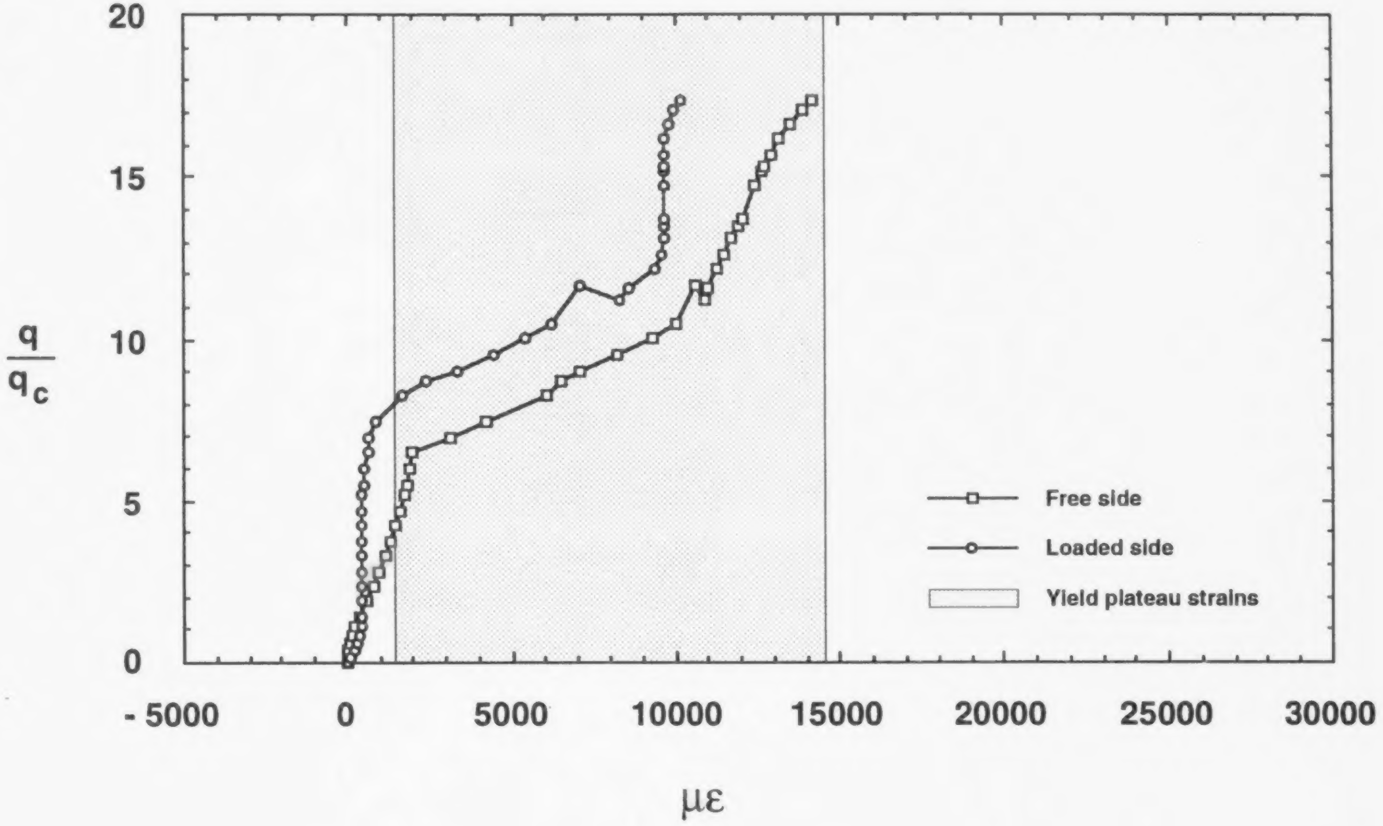

Figure 7.41 Strains at location **C**, test P6-1

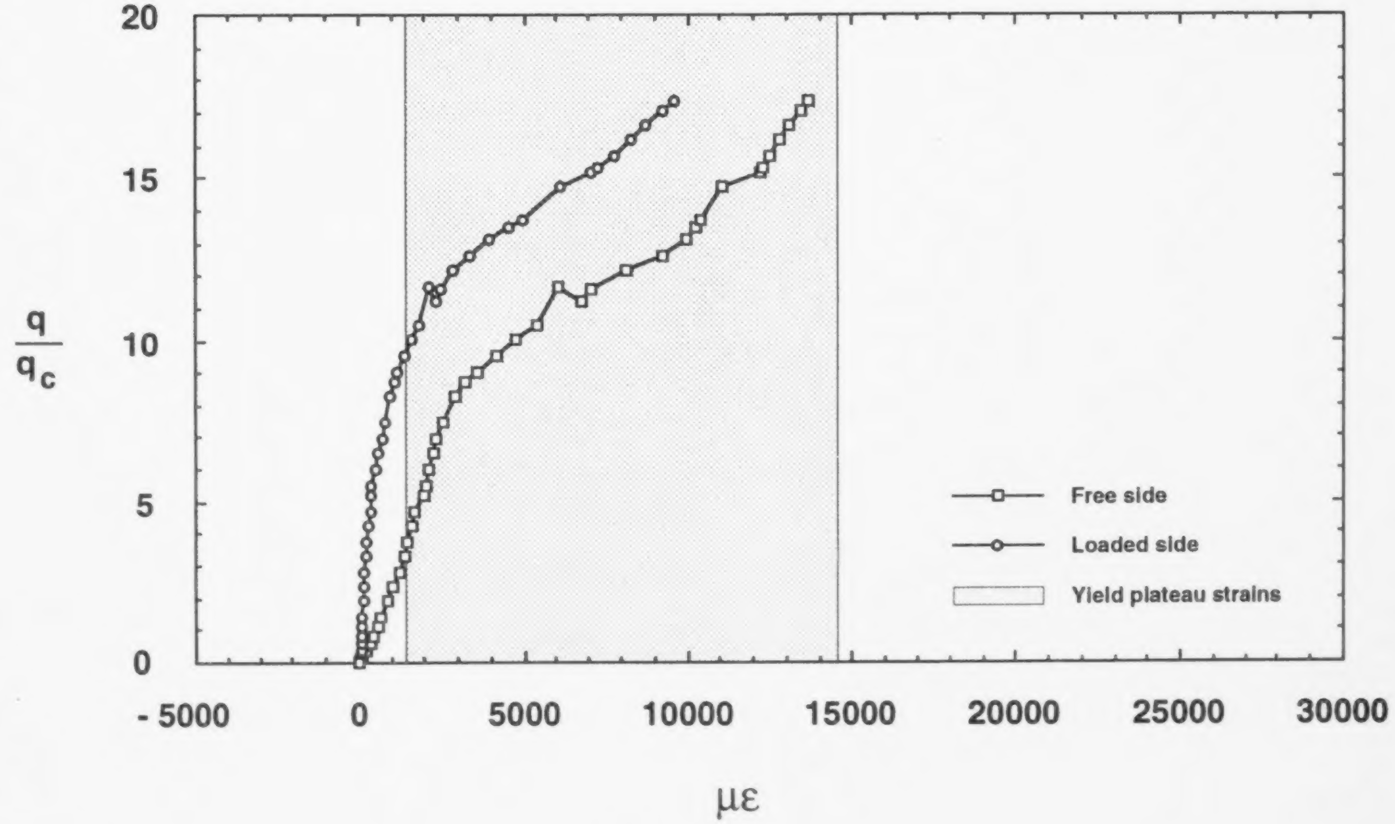

Figure 7.42 Strains at location **D**, test P6-1

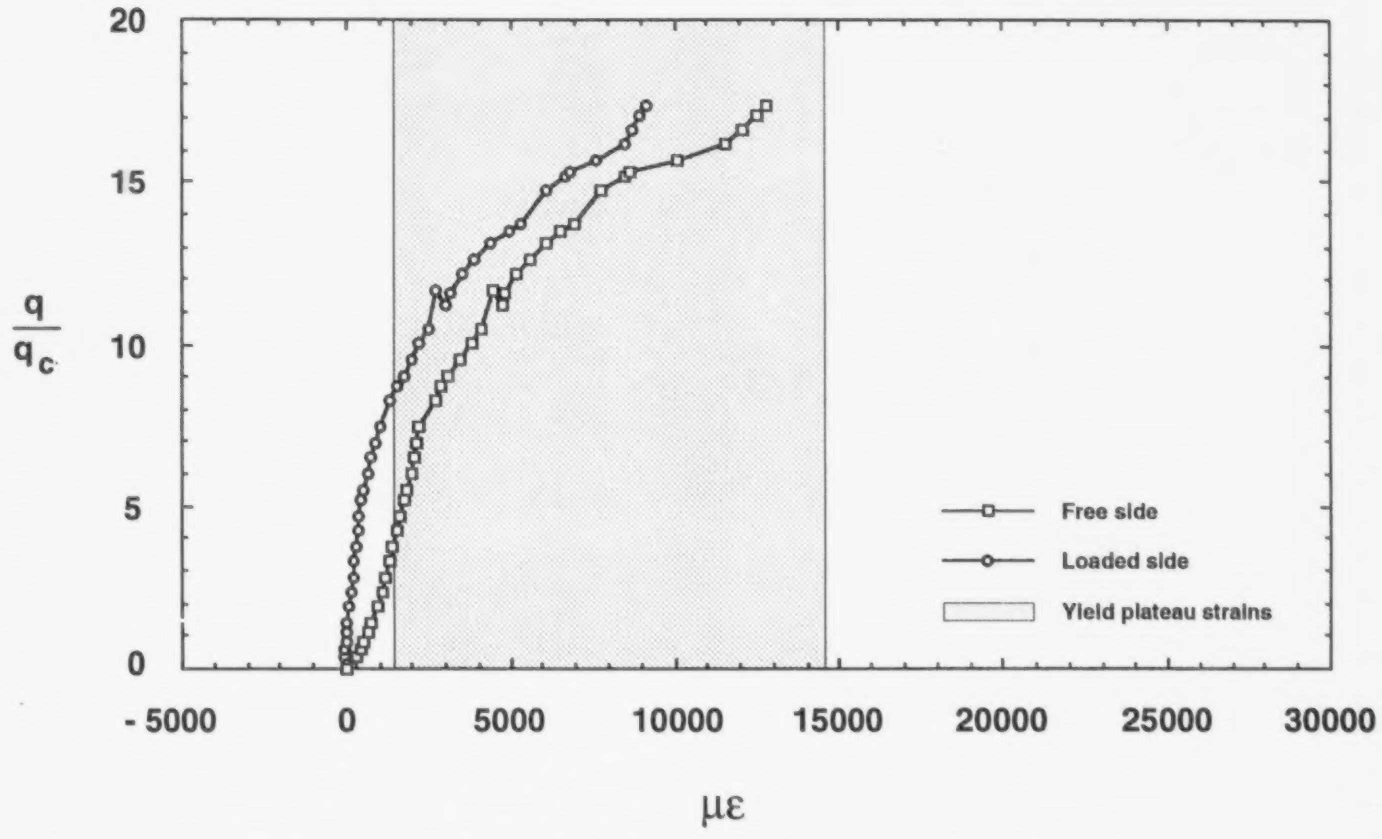

Figure 7.43 Strains at location **E**, test P6-1

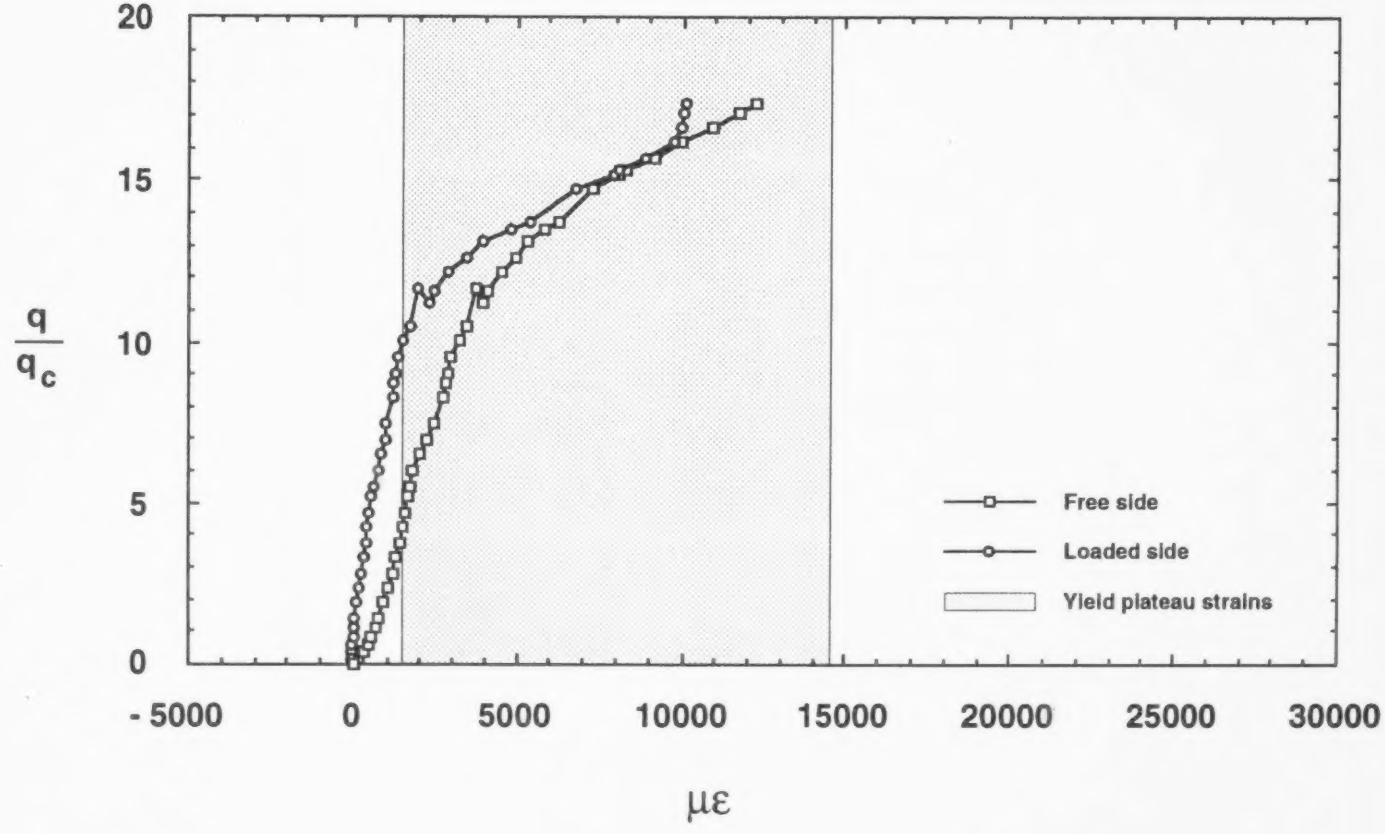

Figure 7.44 Strains at location **F**, test P6-1

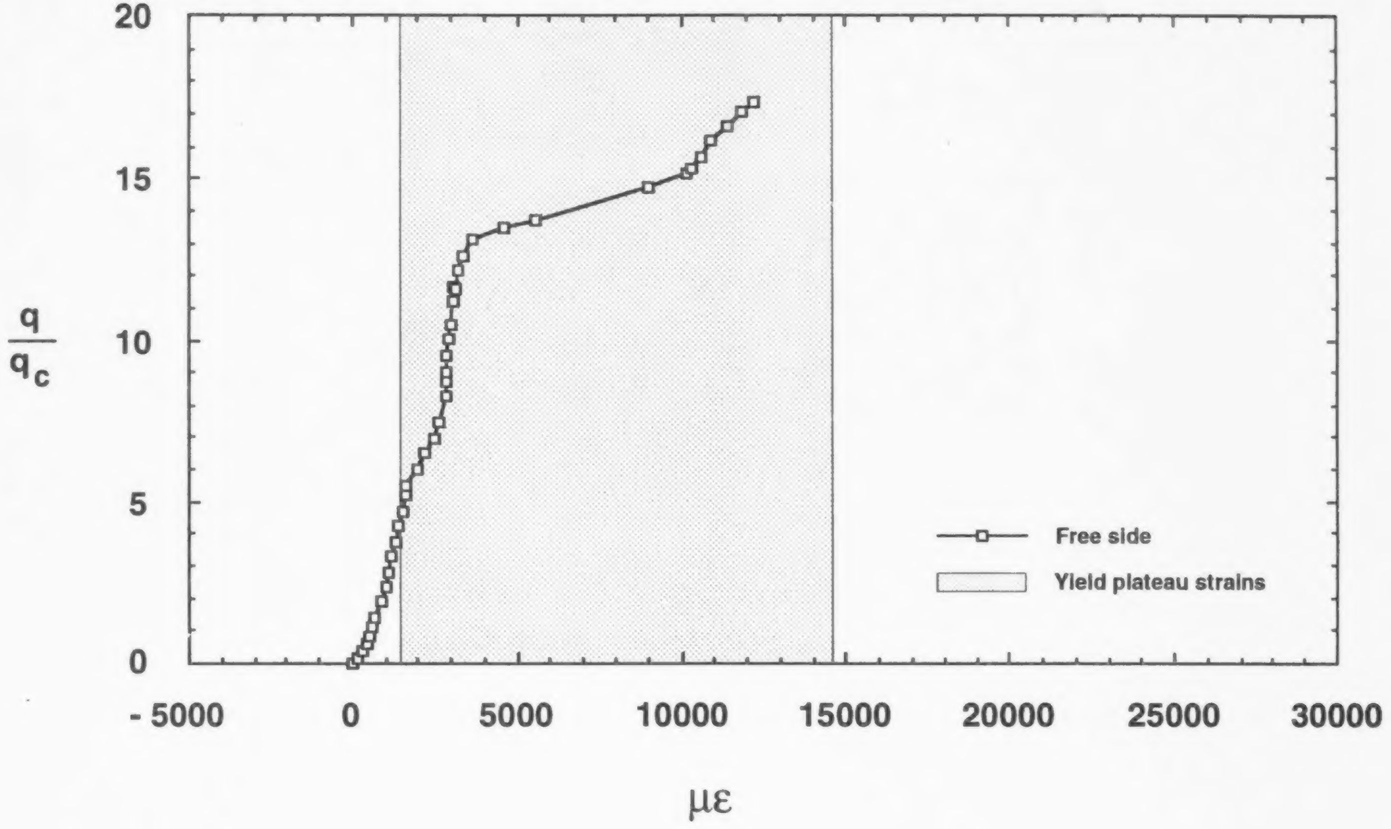

Figure 7.45 Strains at location **G**, test P6-1

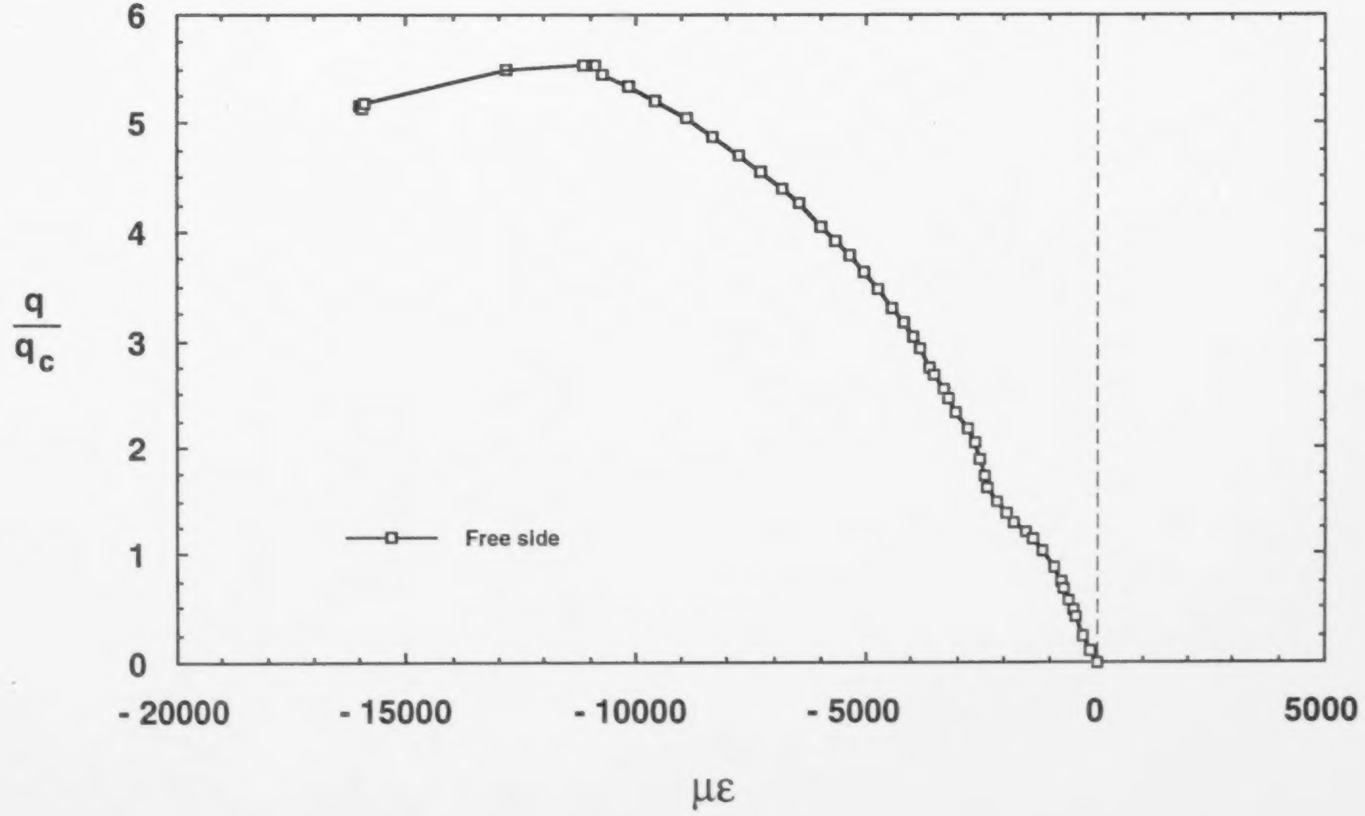

Figure 7.46 Strains at location **X**, test P16

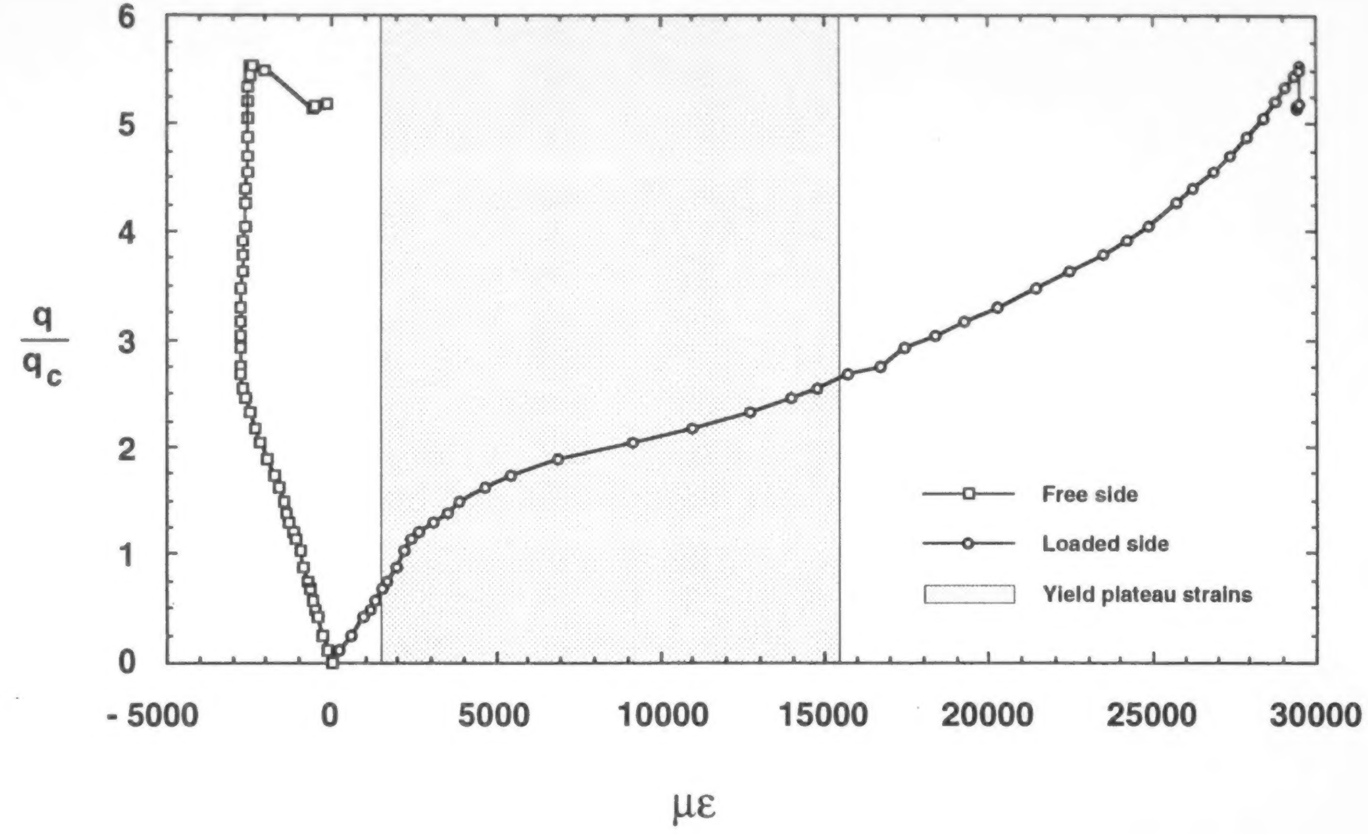

Figure 7.47 Strains at location **A**, test P16

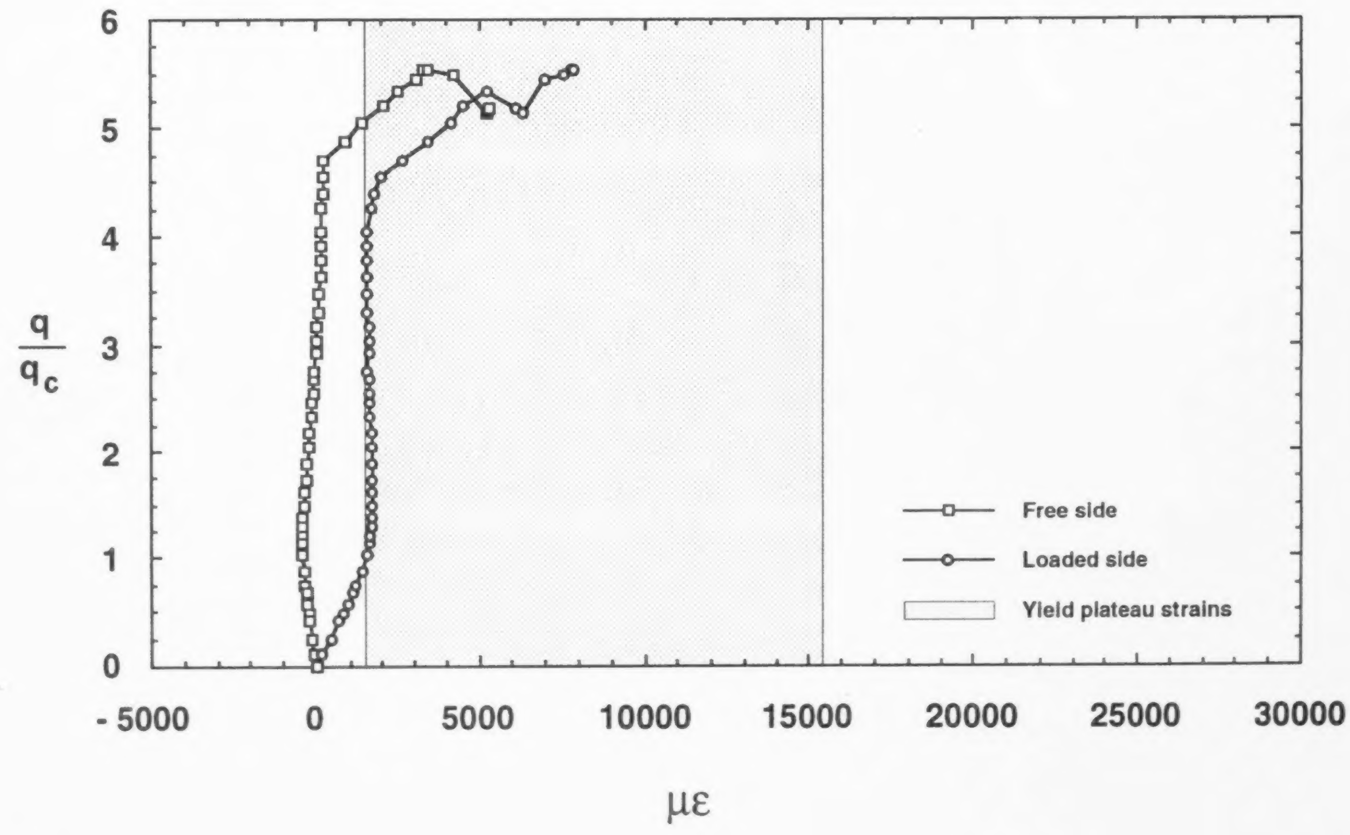

Figure 7.48 Strains at location **B**, test P16

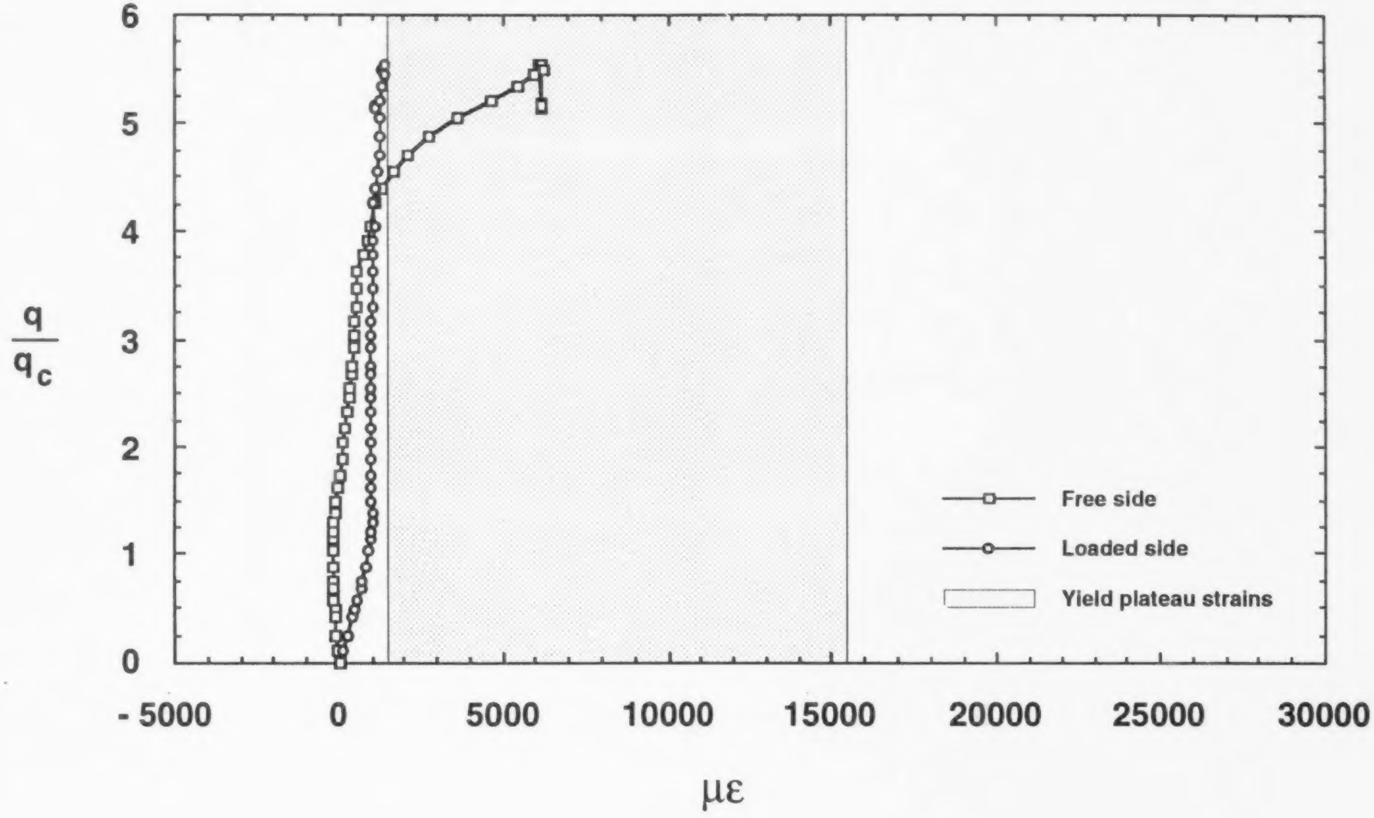

Figure 7.49 Strains at location **C**, test P16

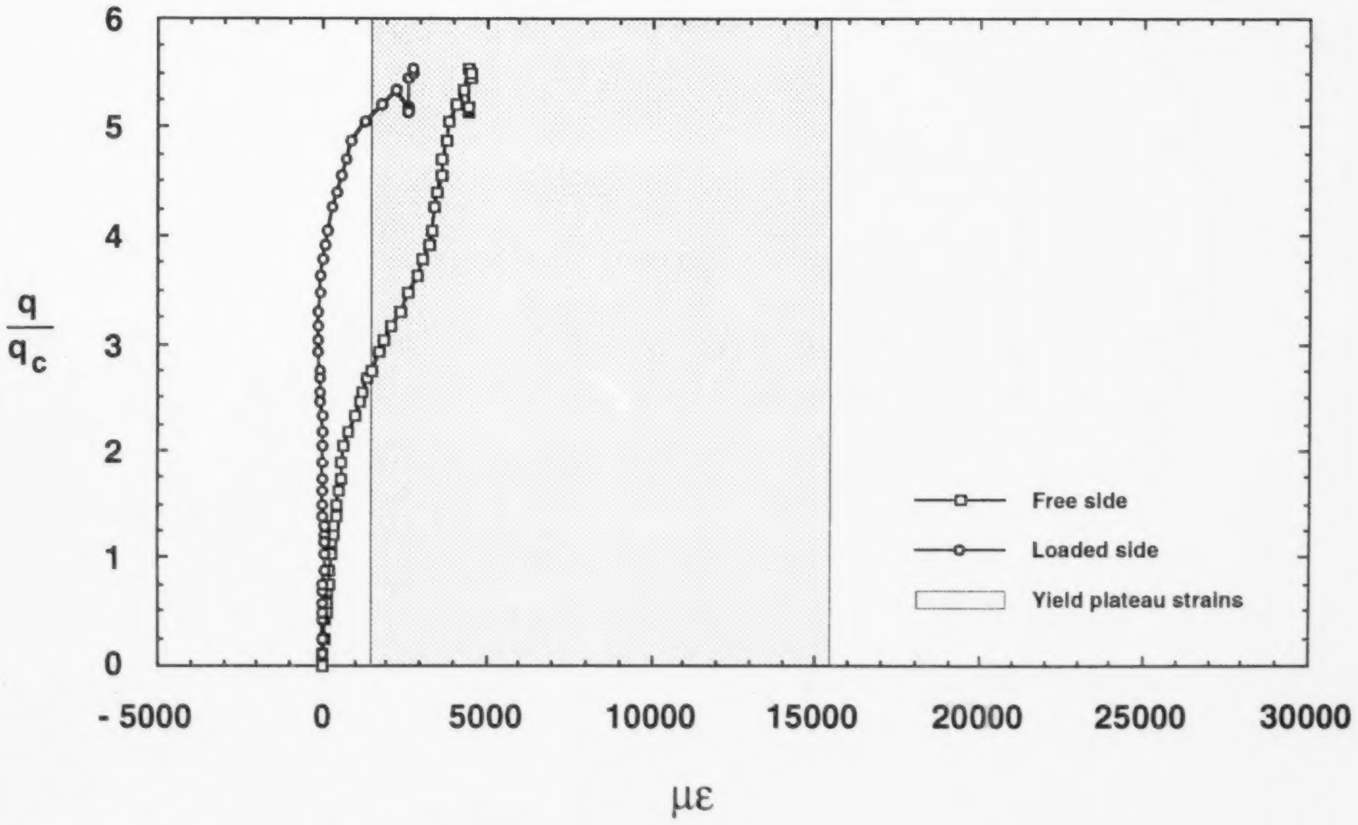

Figure 7.50 Strains at location **D**, test P16

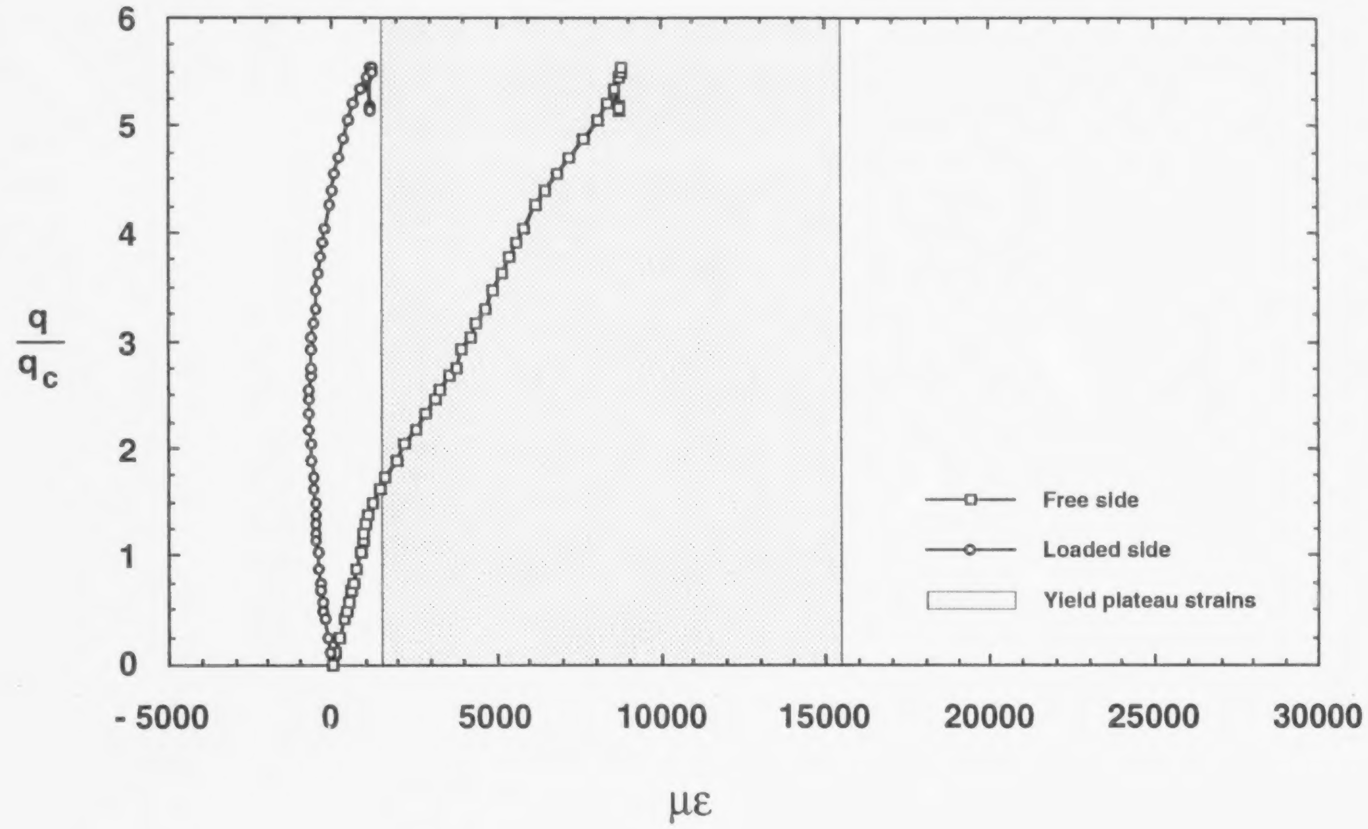

Figure 7.51 Strains at location **E**, test P16

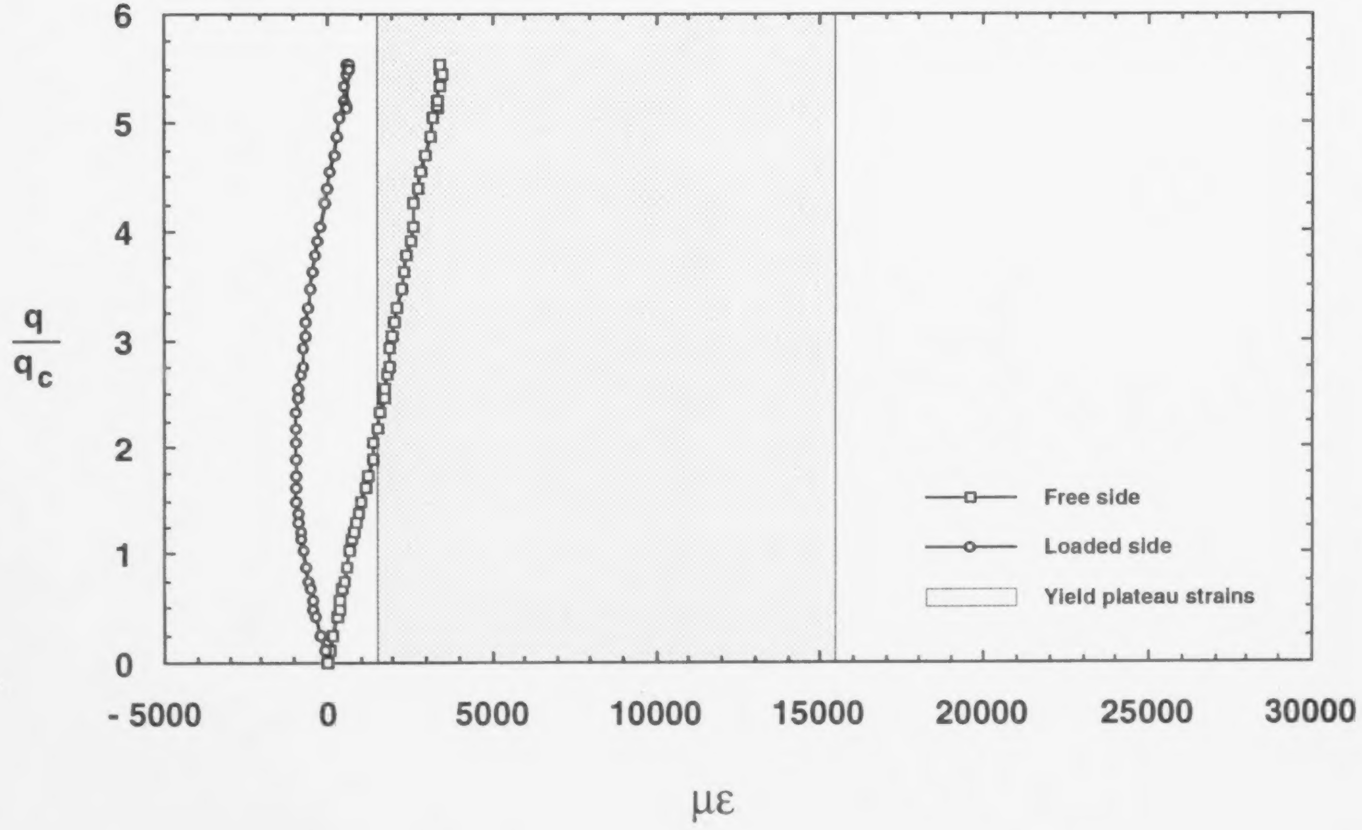

Figure 7.52 Strains at location **F**, test P16

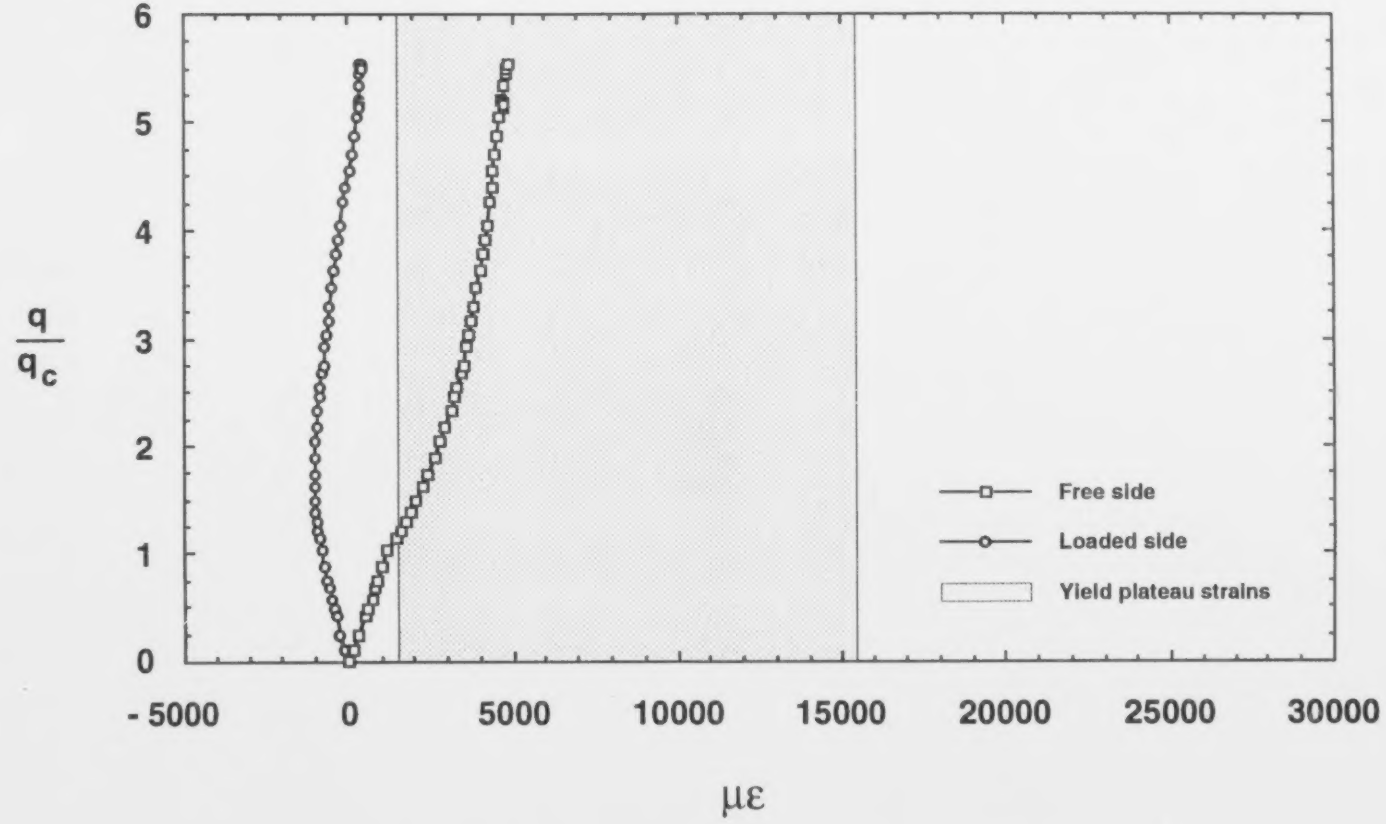

Figure 7.53 Strains at location **G**, test P16

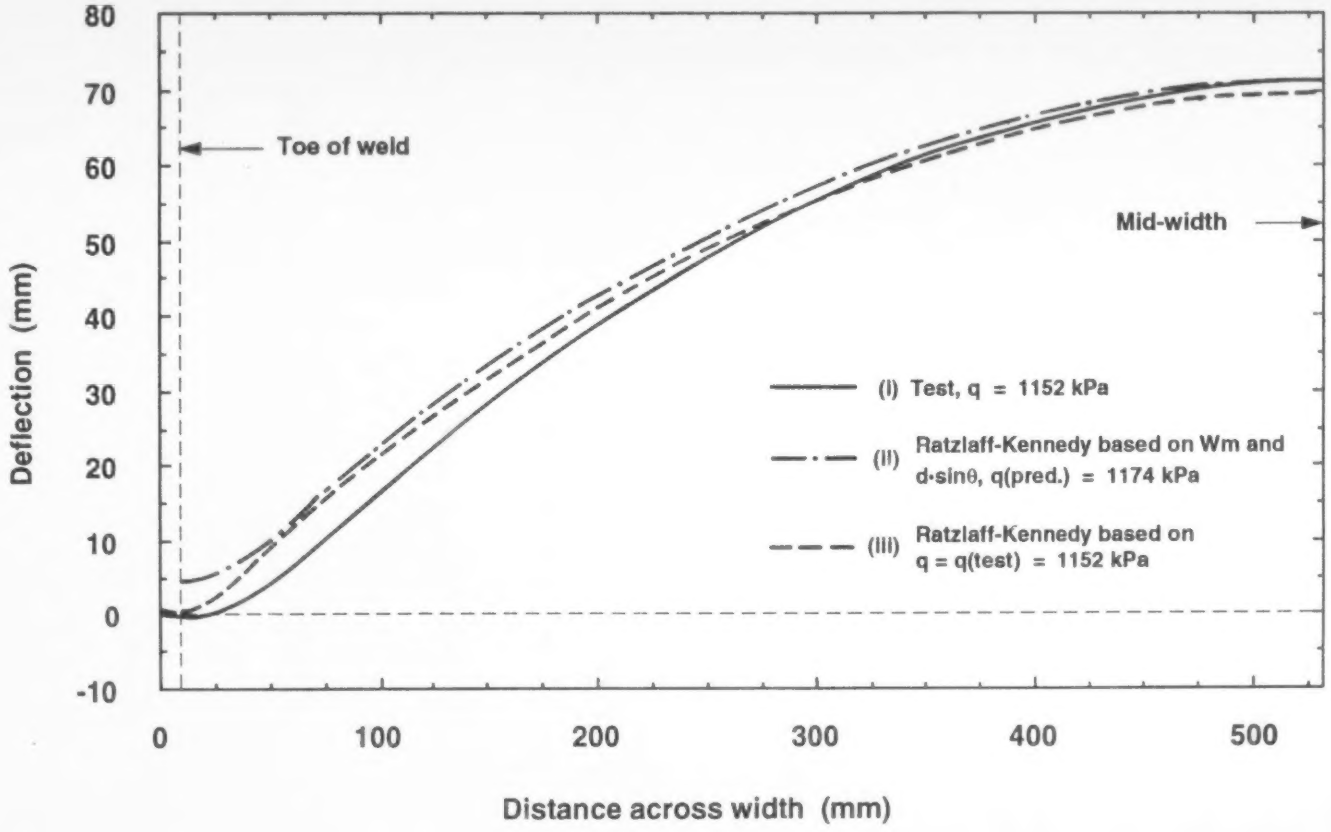

Figure 7.54 Deflected shapes, plate P6-1

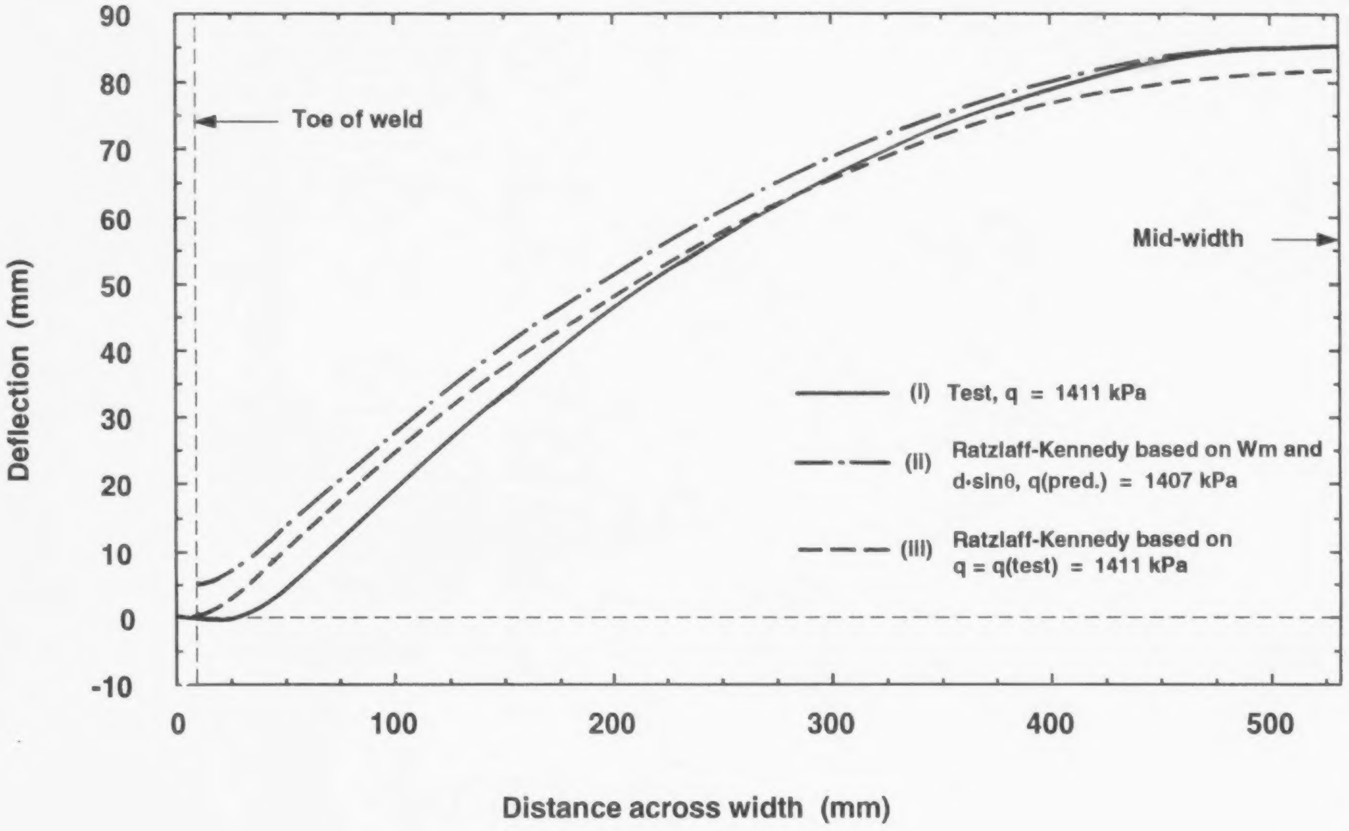

Figure 7.55 Deflected shapes, plate P6-2

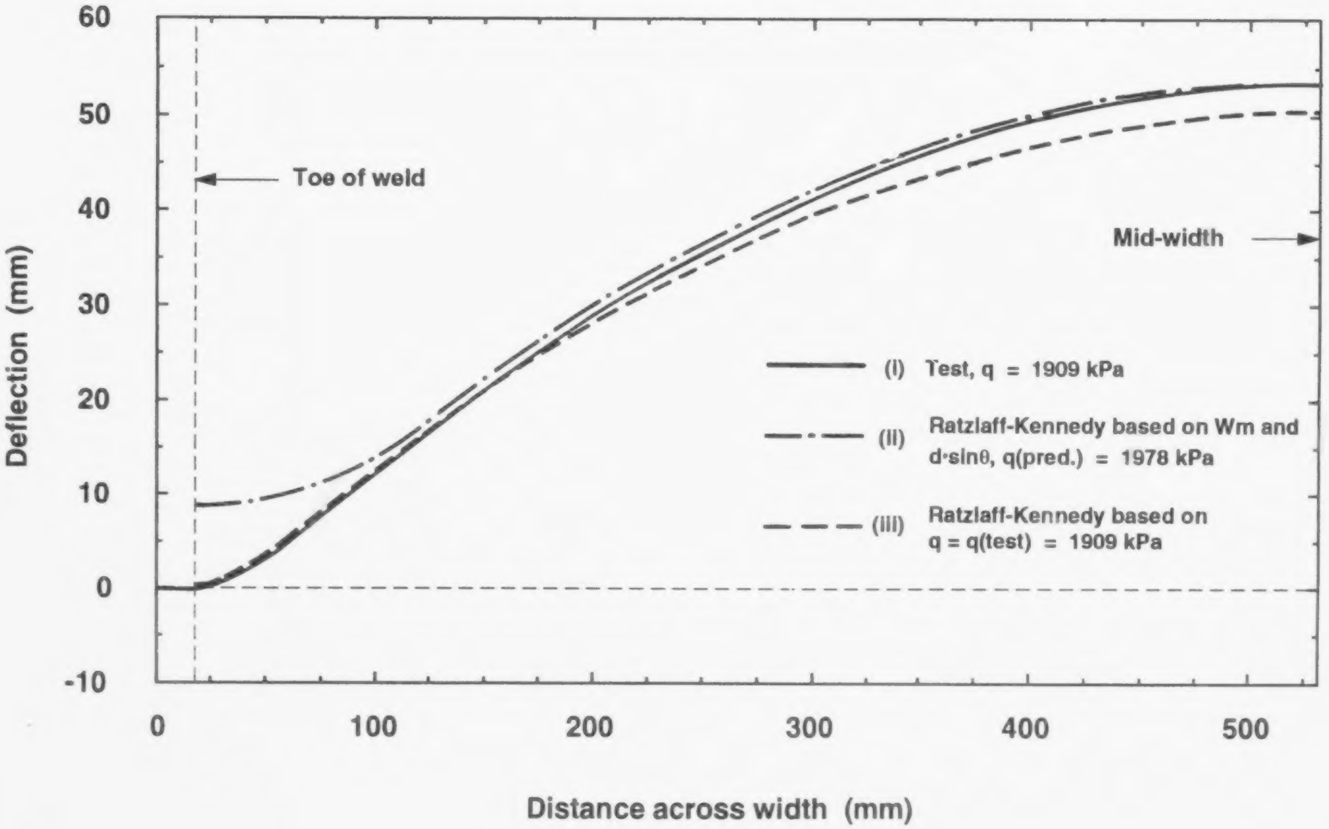

Figure 7.56 Deflected shapes, plate P12

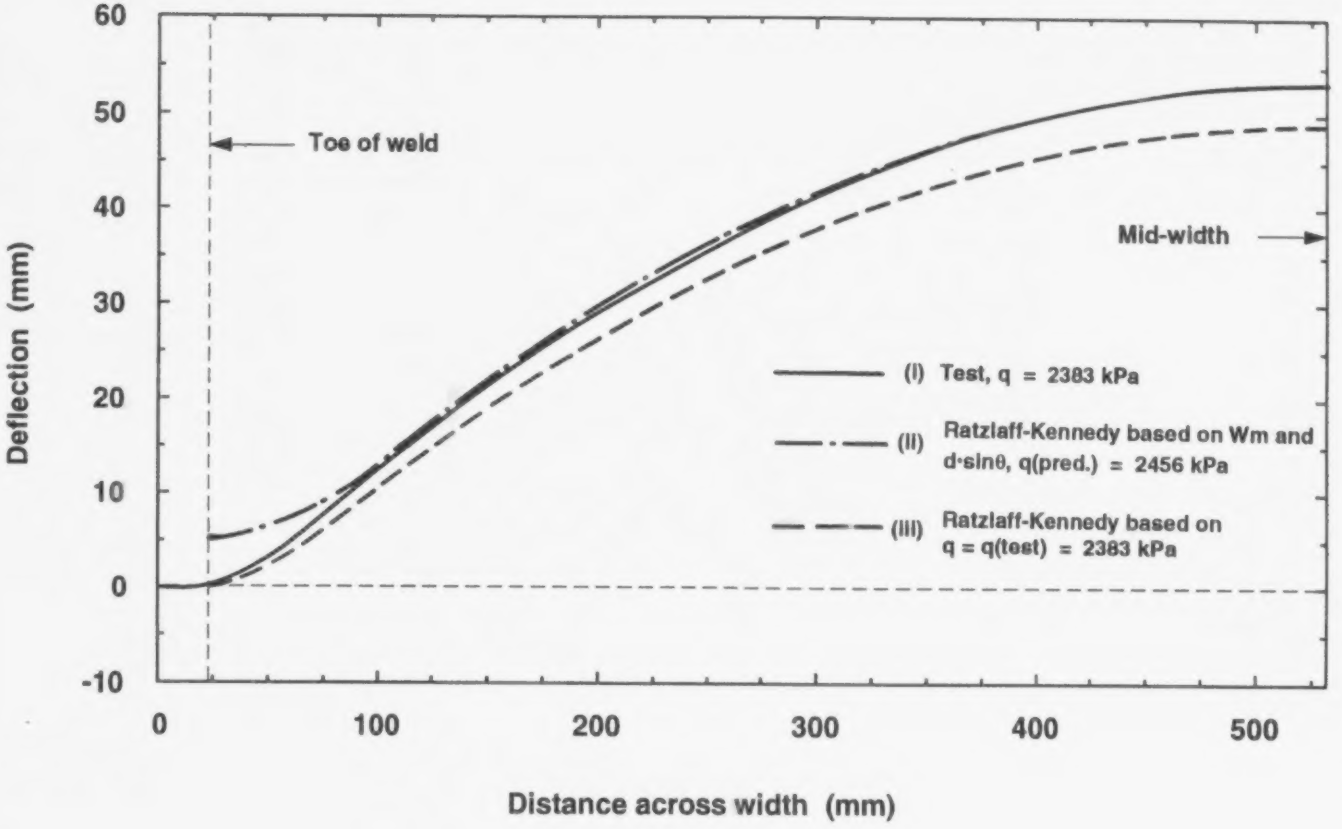

Figure 7.57 Deflected shapes, plate P16

8. SUMMARY, OBSERVATIONS, CONCLUSIONS AND APPLICATIONS

8.1 Summary

A series of four tests were conducted on transversely loaded rectangular mild steel plates, about 1000 mm wide by 3000 mm long, with thicknesses of 6 mm to 16 mm, fixed against rotation and translation on all four edges. Therefore, the plates had an aspect ratio of the width divided by the length of about 0.34.and an effective width/thickness ratio of between 64 and 154.

The plates were subjected to fluid pressure loading until failure occurred. Deflection and strain measurements were taken at numerous locations across the width and along the length throughout the loading.

Two models (both based on an aspect ratio of zero, implying plane strain conditions) were used to predict the behaviour of the test plates. The Ratzlaff-Kennedy (1986) model taking into account elastic and inelastic material behaviour and large deformations and hence flexural action and elastic and inelastic membrane behaviour including bending at the edges, describes behavioural domains in which the response would be expected to lie. Three failure modes of excessive straining in the steel, excessive straining in the HAZ, or shear, all at the edge of the plate, have been identified.

The ADINA finite element model, used to predict the behaviour of two of the test plates, takes into account geometric nonlinearities due to large displacements and large strains and, as well, nonlinear material properties.

Strain measurements from uniaxial tensile coupon tests gave values of Poisson's ratio of about 0.28. Just beyond the yield plateau the inelastic strain ratio reaches about 0.43 and then decrease almost linearly to about 0.35 at an axial strain of 200000 $\mu\varepsilon$.

8.2 Observations

In general, the load-deflection responses were consistent with analyses that describe a domain of behaviour. Initially, the plates exhibit elastic flexural membrane action, then elastic membrane behaviour with inelastic hinges near the supports and mid-width and finally, inelastic flexural membrane action was observed.

Significant bending of the plate exists in a relatively narrow region at the edges. With increased loading the curvature at the edge increases and the width of the region decreases, the curvature decreasing from a maximum at the edge to zero at the limit of this region. Between the bending regions at the edges and between the points of zero curvature, the plates under the action of fluid pressure nearly formed the circular arc that would be expected.

For the same load levels, the measured deflections are in excellent agreement with those predicted by the Ratzlaff-Kennedy (1986) model and those of the ADINA finite element model.

The pressures at failure for the 16 mm, 12 mm, and two 6 mm plates were 2383 kPa, 1909 kPa, 1411 kPa, and 1152 kPa with corresponding deflections of about 53, 54, 85, and 71 mm, respectively. The pressures at failure are 5.5, 6.6, 17.9 and 17.6 times the pressure required to develop a three-hinge collapse mechanism assuming flexural action only. The maximum deflections, in the same order, are 3.2, 4.0, 12.0 and 10.5 times the respective plate thicknesses.

Failure of all four plates occurred along one edge near mid-length. Rupture, initiated in the HAZ at the toe of the restraining weld, and cracks propagated through the thickness and along the length of the plate.

Recognizing the discontinuous nature of yielding, the strains from the ADINA model are in reasonable agreement with the measured strains.

At the failure loads and within the membrane portion of the plate, i.e., between the points of zero curvature, the thinner plates were fully yielded throughout with larger tensile strains occurring on the convex (free) surface than on the concave (loaded) surface. Even at failure loads, the thicker 12 mm and 16 mm plates were strained only elastically on the loaded surface.

8.3 Conclusions

Because of the inelastic membrane action that develops as inelastic straining occurs, transversely loaded steel plates can carry many times the fully plastic flexural collapse mechanism load. The ratio of the inelastic membrane failure load to the collapse mechanism load increases with increasing width/thickness ratios or with thinner plates. Both the maximum deflection at ultimate failure and the deflection normalized by dividing by the plate thickness increase with decreasing plate thickness.

Three failure mechanisms associated with rupture at the edge of the plate have been identified that are considered to be valid when significant bending exists at that location or when the transverse shears are large. These are: (i) a maximum tensile strain criterion where the tensile strains arising from the tensile forces and bending moments reach the true ultimate tensile strain of the steel, (ii) a maximum tensile strain criterion where the tensile strains occurring from the tensile forces and bending moments at the edges reach the ultimate tensile strain of the HAZ (This condition may be further exacerbated by introducing a strain concentration at this same location), (iii) a maximum shear stress criterion when the average shear stress at the edge reaches $0.577\sigma_u$, The criterion giving the lowest failure load in a given set of circumstances will govern. Real structures can be designed to eliminate or at least minimize the third criterion. With failure in the HAZ precluded because of good design it is likely that the shear criterion would govern.

All four plates achieved at least partial inelastic flexural membrane behaviour but are considered to have failed prematurely due to rupture of the steel in the HAZ.

Test/predicted ratios for the 4 tests ranging from 0.69 to 0.80 were obtained based on the failure criterion of rupture in the HAZ when the Ratzlaff-Kennedy model was used to predict the strains and the test strains were taken as the maximum strains computed from the ADINA models (strains could not be measured on the loaded surface at the toe of the weld). These test/predicted ratios are considered to be low because the ADINA model shows that the strains vary non-linearly through the thickness while the Ratzlaff-Kennedy model assumes a linear distribution of strain there.

A comparison of the ADINA strains at the failure loads with those computed from the Ratzlaff-Kennedy model suggests that the strain concentration factor at the toe of the weld was in the order of 1.5. When this factor is applied to the maximum tensile strains in the Ratzlaff-Kennedy model the test/predicted ratios range from 0.86 to 1.05 with a mean value of 1.00.

8.4 Applications

The highly predictable inelastic membrane behaviour, demonstrated by these large-scale tests, that results in transverse load carrying resistances of steel plates many times that based on fully plastic flexural collapse mechanisms, suggests a completely different limit states design approach for those structures in which the deformations associated with inelastic membrane action are of little consequence. Obviously, for membrane action to develop, the remote edges of the plate must be anchored against translation. For any postulated loading condition, whether distributed over the entire plate or a portion thereof, the inelastic membrane behaviour at the factored load level can be established either using the Ratzlaff-Kennedy model or an inelastic finite element analysis using a program such as ADINA. Points of maximum tensile straining and maximum shear, whether at supports or under load points, are identified. The values of the tensile strain and shear at these locations are compared to the limiting values to satisfy the ultimate limit states criteria. It is suggested that the nominal shear resistance for the plate material is $0.577\sigma_u$ and the nominal maximum strain is the ultimate true strain (this presumes that the failure mode associated with high tensile straining in the HAZ has been obviated by good detailing). Resistance factors and load factors are established consistent with the desired reliability of the structure.

Based on analyses to date it is expected that the shear criterion would govern and that the postulated failure loads would be in the order of 25 to 50 times the fully plastic flexural collapse mechanism loads and increase with decreasing plate thickness. The membrane deflections also, of course, increase as the thickness is decreased.

Two classes of structures for which it is suggested that local deformations, so long as fracture does not occur, cause little more than cosmetic damage, are arctic caisson-type structures used for petroleum exploration and production and the hulls of ice-breakers. Both of these structures are likely to be subject to large ice loads and deformations are not a serviceability issue. Therefore such structures can be designed utilizing the membrane action to the fullest.

Figure 8.1 shows that the deflected shape of an individual plate panel is directly related to the distribution of loads to which it has been subjected. Ratzlaff and Kennedy (1986) state, therefore, that if a panel is subjected to a loading pattern different from that which first occurred, then a new inelastic deflected shape would be developed as shown by McDermott et al. (1974) provided the second load becomes sufficiently large. The panel simply adapts to the new loading conditions. The variation in loading on a panel is therefore seen not to be a problem. As a matter of fact, the permanent deformations that have occurred can be used directly to determine the intensity of the forces to which plate panels of the structure have been subjected. The structure itself becomes a conglomeration of virtually indestructable load measuring devices. The deflected shapes could be recorded and would thereby provide a significant clue to the distribution of load. Yearly observations would enable the operator to catalogue the forces to which the structure has been subjected, thus accumulating a body of statistical data.

Consider the load-deformation response of plate P12 of Fig. 5.1. On unloading and reloading, the path is retraced. If a certain load has been reached and then removed, further cycles of loading to the same or a lesser level would simply cause elastic cycling. If on the other hand the maximum load on a subsequent cycle is greater, cycling would occur through this point on another line, elastically. It is anticipated that a significant number of cycles of loading displaying this essentially elastic behaviour could be withstood before fatigue cracking would ensue.

For design, to minimize overall costs, parametric studies should be carried out to determine the best distribution of steel between the face plate subject to the heavy loads and the supporting members. It is envisaged that the optimum structure for a given plate thickness would have a minimum number of supporting bulkheads. In no case should a large number of intermediate stiffeners be used. These are unlikely to be able to accommodate the deformations associated with the development of inelastic membrane action without failing themselves. They therefore are ineffective. The volume of steel in such stiffeners, it is suggested, based on the behaviour observed here, is better placed in the membrane plate or its major supporting members. It is further suggested that satisfactory performance can be obtained when one-way membrane action is developed. There is no real need for two-way action. The design concept is fundamentally to reduce the number of pieces incorporated in the structure. Of course, at the ends of the structure, provision must be made to anchor the membrane force in the original plane of the membrane.

A double-hulled approach appears to be desirable, with a second membrane behind the surface membrane at such a distance to allow full membrane action of the surface membrane to be developed without impinging on it. Should rupture of the surface membrane occur, fluids would be retained within the ruptured cell. Of course, once the surface membrane is deformed and unloaded, on reloading it deforms elastically until the previous maximum load is approached. Figure 8.1 shows a possible cross-section of the geometry for a structure designed in accordance with these principles.

The use of the full strength of continuous steel plates developed with inelastic membrane action has further applications in any circumstance where deformations that develop are of little consequence. Other applications could include structures for storing materials such as tanks, bins, and hoppers.

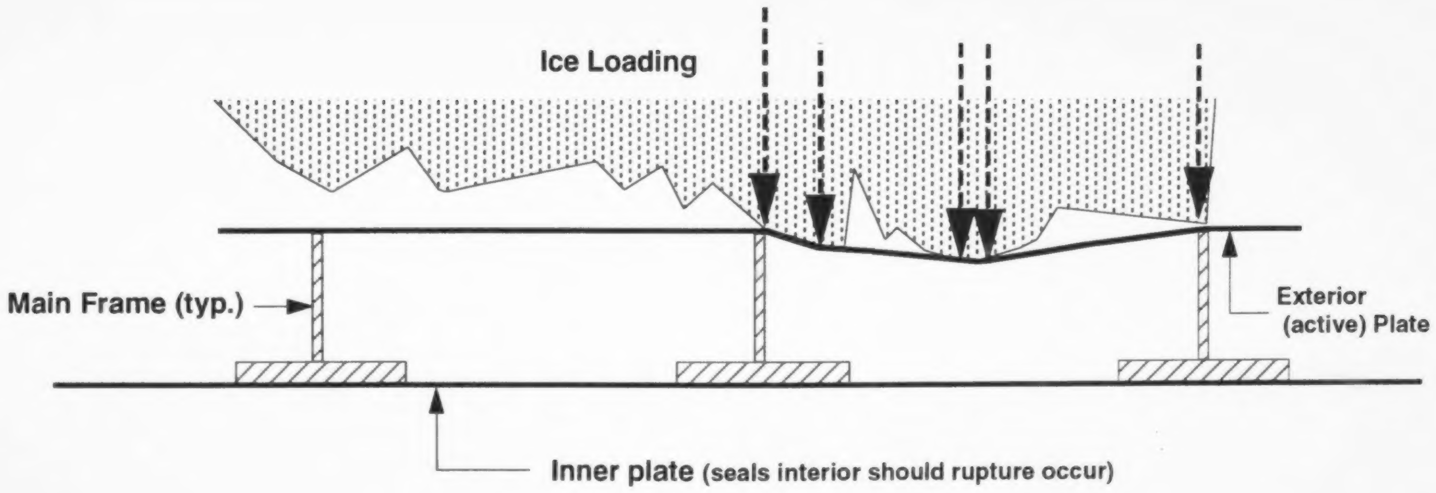
Ice Loading
Main Frame (typ.)
Exterior (active) Plate
Inner plate (seals interior should rupture occur)

Figure 8.1 Partial section through ice-resisting wall

REFERENCES

ADINA Engineering Inc. 1984. ADINA Engineering Report AE 84-1, Users Manual, Watertown, Massachusetts.

American Welding Society (AWS). 1979. "Specification for Carbon Steel Covered Arc Welding Electrodes", AWS A5.20-79. American Welding Society, 550 N.W. LeJeune Rd., Miami, Florida.

American Welding Society (AWS). 1981. "Specification for Carbon Steel Electrodes for Flux Cored Arc Welding", AWS A5.1-81. American Welding Society, 550 N.W. LeJeune Rd., Miami, Florida.

Bond, J., 1993. Inelastic Membrane Analysis on Continuous Steel Plates (IMASP). Master of Engineering Thesis, Carleton University, Ottawa.

Boobnoff, I.G., 1902. On the Stresses in Ship's Bottom Plating Due to Water Pressure. Transactions of the Institution of Naval Architecture, 44, p.15.

Canadian Standards Association (CSA). 1984. "Steel Structures for Buildings - Limit States Design", National Standard of Canada CAN3-S16.1-M84. Canadian Standards Association, Rexdale, Ontario.

Canadian Standards Association (CSA). 1981. "Structural Quality Steels", National Standard of Canada CAN3-G40.21-M81. Canadian Standards Association, Rexdale, Ontario.

Chien, W.Z. and Yeh, K.Y., 1957. On the Large Deflection of Rectangular Plate. Proceedings of the 9th. Congress of Applied Mechanics, Brussels, pp. 403-412.

Clarkson, J., 1956. A New Approach to the Design of Plates to Withstand Lateral Pressure. Transactions of the Institution of Naval Architecture, 98, pp. 443-463.

Comyn, M.I. 1985. Part of CIVE 679 Seminar on Offshore Structural Engineering. Department of Civil Engineering, University of Alberta, Edmonton, Alberta., pp. G1-G25.

Gagnon, D.P. and Kennedy, D.J.L., 1987. The Ultimate Strength of Partial Joint Penetration Groove Welds. Presented at the 1987 Annual Conference of the Canadian Society for Civil Engineering, Montreal, Quebec. May 19-22, pp. 533-554.

Hooke, R., 1970. Post-Elastic Deflection Prediction of Plates. Journal of the Structural Division, American Society of Civil Engineers, 96 (ST4), pp. 757-771.

Hooke, R., 1969. An Approximate Analysis of the Large Deflexion Behaviour of Clamped, Uniformly Loaded, Rectangular Plates. Journal of Mechanical Engineering Science, 11, pp. 256-268.

Hosford, W.E. and Caddell, R.M., 1983. Metal Forming, Mechanics and Metallurgy. Prentice Hall Inc., Inglewood Cliffs, N.J., 330 pp.

Hughes, O.F. 1981. Design of laterally loaded plating - uniform pressure loads. Journal of Ship Research, 25 (2), pp.77-89.

Ingerslev, A., 1923. The Strength of Rectangular Slabs. J. Inst. Struct. Eng., 1(1), January, pp. 3-14.

Johansen, K.W., 1943. Brudlinieteorier, Gjellerups Forlag, Copenhagen, July, 191 pp. ("Yield Line Theory," translated by Cement and Concrete Association, London, 1962, 181 pp.)

Johansen, K.W., 1946. Pladenformler, Polyteknisk Forening, Copenhagen, 186 pp. ("Yield Line Formulae for Slabs," translated by Cement and Concrete Association, London, 1972, 106 pp.)

Jones, N., 1976. Plastic Behaviour of Ship Structures. Presented at the annual meeting of the Society of Naval Architects and Marine Engineers, November, pp. 115-145.

Jones, N., and Walters, R.M., 1971. Large Deflections of Rectangular Plates. Journal of Ship Research, 15(2), June, pp. 164-171 and p. 288.

Kennedy, S.J. and Cheng, J.J.R., 1992(a). Behaviour of Transversely Loaded Steel-Concrete Composite Plates: Experimental Program and Test Results. Canadian Journal of Civil Engineering, 19(2), pp. 323-335.

Kennedy, S.J. and Cheng, J.J.R., 1992(b). Behaviour of Transversely Loaded Steel-Concrete Composite Plates: Analyses and Design Applications. Canadian Journal of Civil Engineering, 19(2), pp. 336-348.

Kennedy, D.J.L. and Hafez, M.A., 1984. End Plate Connections for Steel Beams. Canadian Journal of Civil Engineering, 11(2), pp. 139-149.

Lay, M.G. 1982. Structural Steel Fundamentals - a Metallurgical Primer. Australian Road Research Board, Nunawading, Victoria, Australia, 241 p.

Levy, S., 1942. Square Plate With Clamped Edges Under Normal Pressure Producing Large Deflections. N.A.C.A. Report No. 740.

MacGregor, C.W., 1940. The Tension Test. Symposium on Significance of the Tension Test. Proceedings: American Society for Testing and Materials, 40, pp. 508-534.

Matic, P. and Jolles, M.I. 1987. The Influence of Weld Metal Properties, Weld Geometry and Applied Load on Weld System Performance. NRL Memo. Report No. 5987, Fracture Mechanics Section, Naval Research Laboratory, Washington, D.C., 40 p.

McDermott, J.F., Kline, R.G., Jones, Jr., E.L., Manier, E.L., Maniar, N.M. and Chiang, W.P., 1974. Tanker Structural Analysis for Minor Collisions. Transactions, The Society of Naval Architects and Marine Engineers, 82, pp. 382-414.

Ratzlaff, K.P., Gagnon, D.P. and Kennedy, D.J.L. 1988. An investigation of Poisson's ratio for steel in the inelastic range. Presented at the 1988 Annual Conference of the Canadian Society for Civil Engineering, Calgary, Alberta. May 23-27, pp. 764-784.

Ratzlaff, K.P. and Kennedy, D.J.L, 1986. Behaviour and Ultimate Strength of Transversely Loaded Continuous Steel Plates. Canadian Journal of Civil Engineering, 13(1), pp. 76-85.

Ratzlaff, K.P. and Kennedy, D.J.L, 1985. Analysis of Continuous Steel Plates Subjected to Uniform Transverse Loads. Canadian Journal of Civil Engineering, 12(3), pp.685-699.

Taylor, J.S.W., 1986. An Experimental Investigation of the Behaviour of Flat Rectangular Plates Under the Action of Combined In-Plane and Lateral Loading. Experimental Stress Analysis (Proceedings of the VIIIth International Conference on Experimental Stress Analysis, Amsterdam, The Netherlands, May 12-16, 1986), edited by H. Wieringa, 637 pp.

Timoshenko, S., 1940. Theory of Plates and Shells. 1st. Edition. McGraw-HIll Book Company, London, England.

Vitovec, F.H., 1989. Private Communication.

Vitovec, F.H., 1984. Private Communication.

Way, S., 1938. Uniformly Loaded, Clamped, Rectangular Plates With Large Deflections. Proceedings of the 5th International Congress of Applied Mechanics, Cambridge Massachusetts, p. 123.

Young, A.G., 1959. Ship Plating Loaded Beyond the Elastic Limit. Transactions of the Institution of Naval Architecture, 10, pp. 143-165.

APPENDIX A

The relationships proposed by Ratzlaff and Kennedy (1986) for a membrane subject to fluid pressure relating the membrane deflection, maximum stress, strain, the edge inclination, to the fluid pressure and the material properties are derived here.

Figure A.1(a) is a free body diagram of the half-width of a unit length of plate with zero aspect ratio subject to fluid pressure and assumed to have constant curvature from the point of zero curvature, point Z, to the mid-width. The angle θ is the membrane edge inclination. Consider Fig. A.1(b), a free body diagram of the central circular portion from point Z to the mid-width, extending over a horizontal distance of $L/2 - d \sin\theta$. The strain arising from the extension of the plate under fluid pressure due to the membrane force, S, is

[A.1a] $$\varepsilon_s = \frac{L_f - L_o}{L_o}, \text{ or}$$

[A.1b] $$\varepsilon_s = \frac{\dfrac{\theta\pi L_o}{180 \sin\theta} - L_o}{L_o}, \text{ or}$$

[A.1c] $$\varepsilon_s = \frac{\theta\pi}{180 \sin\theta} - 1, \text{ or}$$

[A.1d] $$\frac{\sin\theta}{\theta} = \frac{\pi}{180\,(1 + \varepsilon_s)}$$

where q is expressed in degrees. Summing forces in the vertical direction gives

$$[\text{A.2a}] \qquad q\left(\frac{L}{2} - d\sin\theta\right) = V = S\sin\theta, \text{ or}$$

$$[\text{A.2b}] \qquad q = \frac{\sigma_s h \sin\theta}{(1 - \nu_s^2)\left(\frac{L}{2} - d\sin\theta\right)}$$

when S is replaced by $\sigma_s h/(1-\nu_s^2)$ which takes into account the state of plane strain (zero straining in the longitudinal direction). Summing moments about point Z and summing forces in the horizontal direction give, respectively,

$$[\text{A.3}] \qquad Q\cdot\frac{\frac{L}{2} - d\sin\theta}{2\cos\frac{\theta}{2}} = S\cdot W_m, \text{ and}$$

$$[\text{A.4}] \qquad Q\cdot\sin\left(\frac{\theta}{2}\right) + S\cos\theta - S = 0$$

and combining [A.3] and [A.4] gives

$$[\text{A.5}] \qquad W_m = \frac{\left(\frac{L}{2} - d\sin\theta\right)(1-\cos\theta)}{\sin\theta} = \left(\frac{L}{2} - d\sin\theta\right)\frac{\sqrt{1-\cos\theta}}{\sqrt{1+\cos\theta}}$$

Consider the free body diagram of Fig. A.1(c). The fluid pressure is indicated by its horizontal and vertical components. Assuming that the strain distribution at the cross section through point O and K is linear with an average axial strain, ε_p, equal to that due to the axial force P_o when the maximum strain due to bending and axial forces equals ε_u at point K, the radius of curvature is

[A.6] $$\rho_c = \frac{h\ (1 + \varepsilon_p)}{2\ (\varepsilon_u - \varepsilon_p)}$$

For simplicity, assuming that the centre line of the deformed plate shape can be described by a cubic function, the minimum radius of curvature corresponding to the maximum bending strains at the plate edge is found from geometry to be

[A.7] $$\rho_{min} = \frac{d\ \cos\theta}{2}$$

McDermott et al. (1974) also used a cubic function to describe the geometry at the plate edge when analyzing hull damages from ship collisions. They suggested that it was a reasonable and simple way in which to approximate the change in curvature from zero to a maximum value at the edge.

The eccentricity, e, of the maximum membrane force, S, can be shown to be

[A.8] $$e = \frac{d\ \sin^2\theta}{3}$$

Summing moments about point O and considering centre-line dimensions, the moment at the edge is

[A.9] $$M_o = S \cdot e$$

when the contribution to the moment of the fluid pressure is neglected (This moment is only of the order of 1% of the moment Se).

The axial force, P_o, is

[A.10] $$P_o = S \cdot \cos\theta$$

when neglecting the horizontal component of the fluid pressure.

Setting ρ_{min} of [A.7] equal to ρ_c of [A.6] gives

[A.11] $$d = \frac{h\ (1 + \varepsilon_p)}{\cos\theta\ (\varepsilon_u - \varepsilon_p)}$$

and substituting [A.11] in [A.8] gives

[A.12] $$e = \frac{h \sin^2\theta\ (1 + \varepsilon_p)}{3 \cos\theta\ (\varepsilon_u - \varepsilon_p)}$$

By replacing the expression for d of [A.11] and for e of [A.12] in [A.9], the edge moment becomes

[A.13] $$M_o = \frac{Sh \sin^2\theta\ (1 + \varepsilon_p)}{3 \cos\theta\ (\varepsilon_u - \varepsilon_p)}$$

For plane strain conditions for a unit length of plate, the

maximum membrane force corresponding to uniaxial stress-strain conditions (σ,ε_s) is

[A.14] $$S = \frac{\sigma_s h}{(1 - \nu_s^2)}$$

Substituting [A.14] in [A.13] gives

[A.15] $$M_o = \frac{\sigma_s h \sin^2\theta\ (1 + \varepsilon_p)}{3 \cos\theta\ (\varepsilon_u - \varepsilon_p)\ (1 - \nu_s^2)}$$

and similarly for [A10]

[A.16] $$P_o = \frac{\sigma_s h \cos\theta}{(1 - \nu_s^2)}$$

The coexisting axial load and moment at the edge are given by the interaction equation,

$$[A.17] \qquad \frac{M_o}{M_u} + \left(\frac{P_o}{P_u}\right)^2 = 1$$

based on full plasticity. Because the strains are exceptionally large, M_u and P_u are determined using σ_u, the ultimate tensile strength, and an inelastic strain ratio of 0.50. Substituting M_o and P_o of [A.15] and [A.16], respectively, in [A.17] gives

$$[A.18] \qquad \left[\frac{\sigma_s}{\sigma_u}\right]\left[\frac{4\ \sin^2\theta\ (1 + \varepsilon_p)\ (1 - \nu_p^2)}{3\ \cos\theta\ (\varepsilon_u - \varepsilon_p)\ (1 - \nu_s^2)}\right] + \left[\frac{\sigma_s}{\sigma_u}\right]^2 \frac{(1 - \nu_p^2)^2}{(1 - \nu_s^2)^2} \cos^2\theta = 1$$

This equation, describing the relationship among the maximum membrane stress and the edge inclination is based on the material properties of the plate, σ_s, σ_u, ε_u, ε_p, ν_s, and ν_p.

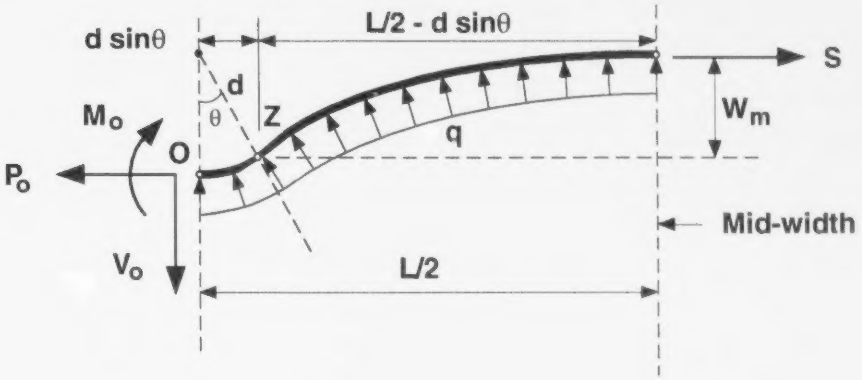
d sinθ
L/2 - d sinθ
S
d
θ
M_o
Z
W_m
q
O
P_o
Mid-width
V_o
L/2

Figure A.1(a) Free body diagram of half-width of plate under fluid pressure

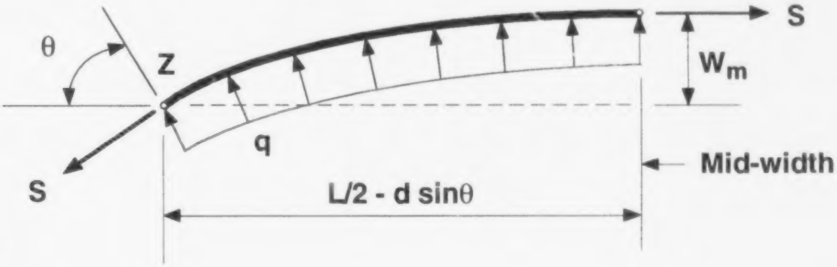
θ
Z
S
W_m
q
S
Mid-width
L/2 - d sinθ

Figure A.1(b) Free body diagram of membrane under fluid pressure

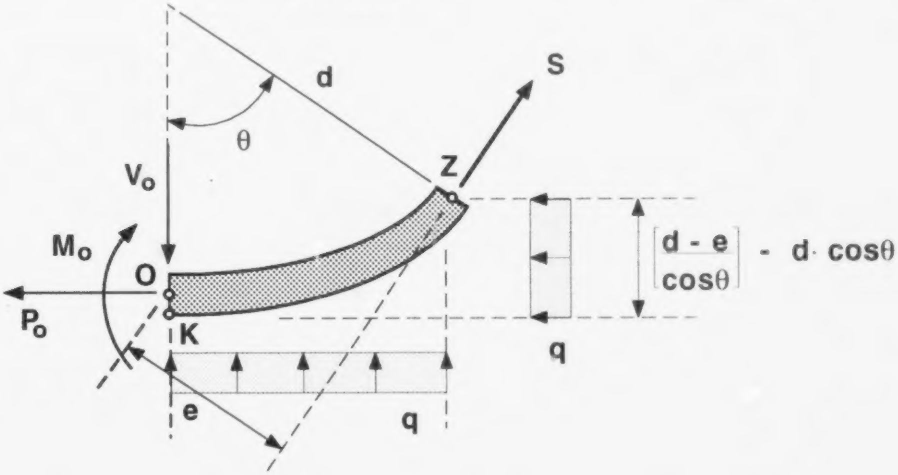
d
S
θ
V_o
Z
M_o
O
(d - e)/cosθ - d·cosθ
P_o
K
q
e
q

Figure A.1(c) Free body diagram of plate at edge